Conjugated organic diradicals and polyradicals: electronic structure and photophysics

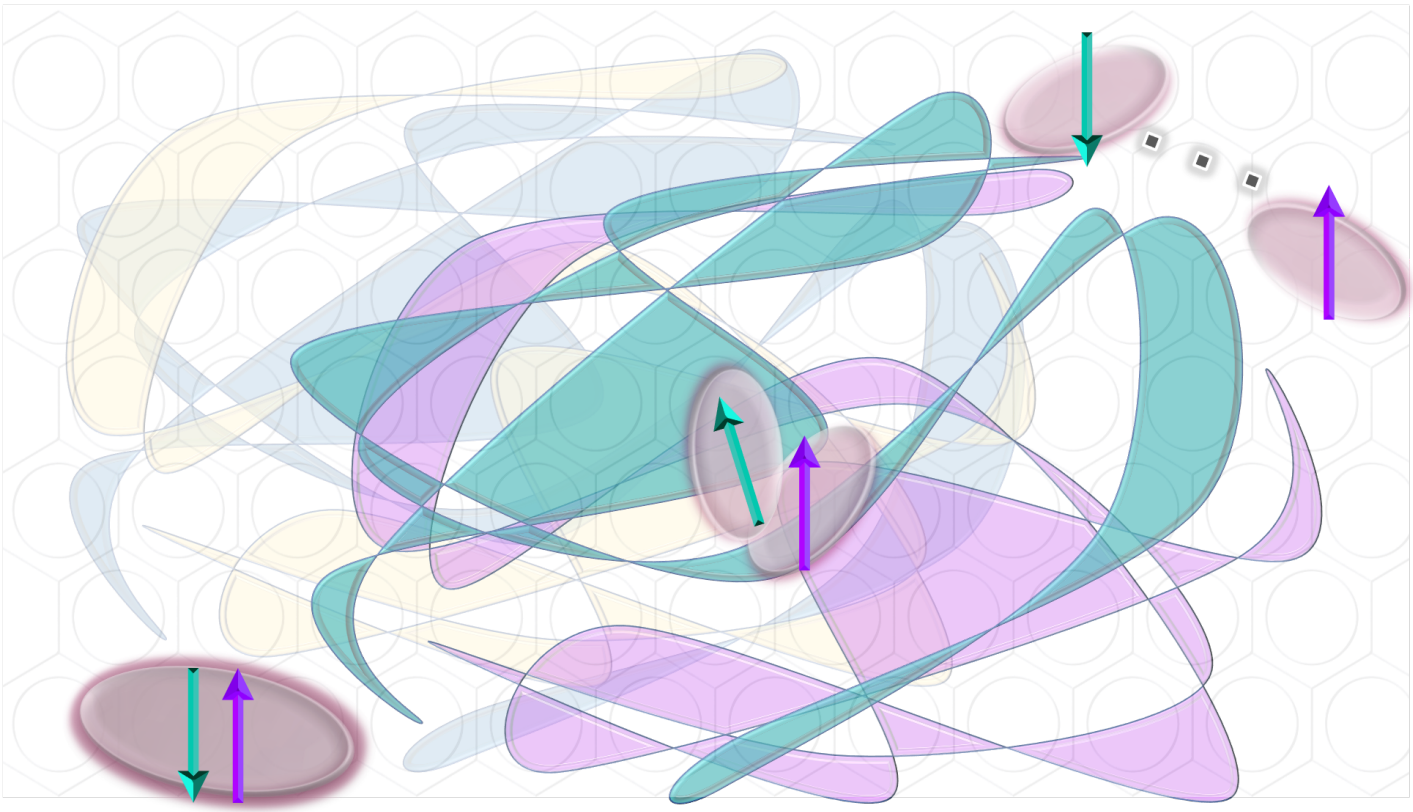

María Eugenia Sandoval-Salinas

Universitat de Barcelona

UNIVERSITAT DE BARCELONA

Universitat de Barcelona
Facultat de Química

Programa de Doctorat en Química Teòrica I Modelització Computacional

Conjugated organic radicals and polyradicals: electronic structure and photophysics

Presents:
María Eugenia Sandoval-Salinas

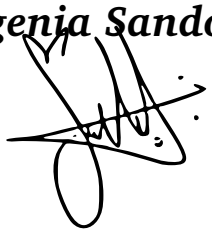

PhD supervisor:
Dr. David Casanova Casas

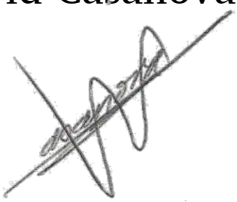

PhD tutor:
Prof. Pedro Alemany I Cahner

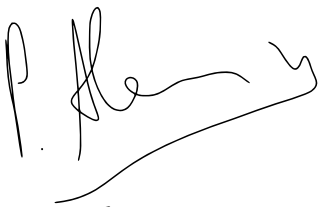

February 2021

The work presented in this thesis was carried out at the Donostia International Physics Center (DIPC) under the direction of Dr. David Casanova with the computational resources and the technical support of the Institut de Química Teòrica i Computacional of the Universitat de Barcelona (IQTCUB), Servicios Generales de Investigación (SGIker) of the Euskal Herriko Unibersitatea, and the Computational Center of the DIPC.

This research was funded by the "Consejo Nacional de Ciencia y Tecnología" (CONACyT-México) under a Ph.D. fellowship (Ref. No. 591700) and the projects No. CTQ2016-80955-P and PID2019-109555GB-I00 of the "Ministerio de Economía y Competitividad" of España.

Eterna compañia

En esa estrella radiante y luminosa,
que contemplo en noches despejadas y claras,
¡ahí estás tú!
A pesar de la muerte y del tiempo transcurrido,
¡¡¡sigues conmigo!!!

Martha Elena Salinas Huerta

Acknowledgements

Han pasado casi cuatro años desde que llegué a Donostia, y un poco menos de empezar el doctorado. No es fácil plasmarlos en palabras de agradecimiento, no porque no me sienta agradecida con todo lo que he tenido en estos años, simplemente creo que las palabras no alcanzan.

Dejar mi país, mi casa, mis amigos, mi familia, mi "vida" por un (largo) tiempo no ha sido siempre fácil. Así que, lo primero es agradecer a toda mi familia por su infinito apoyo y espera. Especialmente, a Paty, Eloy, Sandrita, Lili y Rodrigo, que a pesar de la distancia siempre han estado conmigo.

Al Dr. Casanova por su guía y toda la ciencia compartida, sobre todo por enseñarme como desvelar los misterios que la envuelven. Al Prof. Jesus Ugalde por abrirme las puertas de su grupo. Y también a la gente de la UB, no compartimos mucho tiempo, pero estoy profundamente agradecida con ustedes por su ayuda (Clàudia, Pere, Miquel, y, claro, Efrem por la matrícula... y la beca). Mercé, gracias por la paciencia y orientación con la burocracia.

Besides my supervisor, I would like to thank the members of my thesis committee, the professors Fabrizia Negri, Carles E. Curutchet Barat, Frédéric Castet, Jesus Ugalde, M. Carmen Sousa Romero, Joaquin Barroso and Julia Contreras for accepting to be part of my jury and evaluate my work.

Naturalmente, a todo el increíble grupo de Kimika Kuantikoa (KK) de Donostia: Eli, Elena, Eloy, Txema (sin ti muchos de mis cálculos no hubieran ido a ningún lado), Uranga, Xabi, Txoni, Abel (que has contribuido a desarrollar mi trabajo), Mitxelena, David de Sancho y Edu (quizá no lo recuerdas, pero antes de venir ya me habías ayudado) gracias a todos (TODOS) por la compañia, las charlas y buenos momentos. Also, to the In Silico Photochemistry group, Basile, Antonio, Lea, Emmanuel, and (aunty) V, thanks for making me one of yours in Durham. I would have liked to come back but ... you know, COVID19. También a la gente fuera del grupo que hicieron mi día a día más feliz: Cris, Sofia, Jorge, Raúl y Sergi. Por supuesto, a los miembros del pisu zahar berria, vaya confinamiento nos tocó, pero lo he pasado genial con ustedes!

Mario Piris, tú eres especial y lo sabes, te extrañaré. Mau, que se preocupaba

por mi salud física, pues dió por perdida la mental, y Rafa que desde el principio siempre estuviste ahí.

Elisa, Vero y mis Monserrats (la petita Irene i Mireieta), ha sido un placer conocerlas, simplemente no podría imaginar mis años aquí sin ustedes. Las quiero muchísimo chicas!!

Aarón, Matteo y Carmelito, el tiempo ha ido un poco en contra, pero he disfrutado mucho con ustedes. Claire ... you know, thanks for this little time and all the things you taught me, y te lo digo Merci mademoiselle!

David (Casanova), creo que no tendré palabras para acabar de agradecerte todo lo que, en los diferentes ámbitos, has hecho por mí, gracias por tanto!

Siempre agradeceré el lugar que me han dado sin conocerme y, sobre todo, después de hacerlo.

Gracias! Eskerrik asko!! Moltes gracies!!!

Abstract

The principal aim of this thesis is the accurate modelling of the electronic structure of organic diradical and polyradical molecules. Stable organic compounds exhibiting (poly)radical character have emerged as appealing materials in a wide range of opto-electronic applications and establishing structure-(di)radical character relationships to tune their electronic, magnetic, and optical properties is a necessary step for the design of new compounds with improved tunable radical character. The organic molecules investigated differ in chemical nature and topology and, in turn, in their associated electronic/magnetic features, so as to investigate a range of commonly used compounds in the field of organic electronics. The description of the selected systems has been achieved using a combination of rules based on graphic representation with quantum mechanical methods, namely Density Functional Theory (DFT), Restricted Active Space Spin-Flip (RAS-SF) and Spin-Flip Time-Dependent DFT (SF-TD-DFT). In particular, RAS-SF is systematically used to properly describe the highly correlated nature of the ground state of the diradical compounds under study. Beyond its ability to deal with multiconfigurational character of the wave function, this method can be applied to large systems at a very reasonable computational cost without compromising on the accuracy of the results. The theoretical work presented in this thesis has been carried out in close collaboration with experimental and theoretical groups.

First, triangular nanographene are investigated and shown to present an increased spin multiplicity in their ground state upon heteroatom substitution or hydrogen saturation, hence providing the possibility to design stable radical compounds with tunable radical character. The relationship between molecular topology was further investigated with linear and cyclic acenes that present a diradical and tetraradical character, respectively, that increases with the size of the system. I then focus on a series of organic oligomers, namely oligothiophene and poly-*p*-phenylene derivatives, whose radical character can be respectively induced and controlled via external stimuli, oxidation for the former and temperature for the latter. Upon increasing the size of the systems, a larger polyradical character can be achieved and was here investigated with three series of macrocycles with high polyradical character, from triradicals to decaradicaloids (up to 10 radical centers), a feature

particularly interesting for spintronic devices and molecular magnets. The properties of this open-shell compounds are as diverse as surprising; among others, AWA (annulenes-within-annulenes) super ring, characterized here in collaboration with experimental groups for the first time, exhibit a global aromaticity in relation with the radical interaction in each of the annulenes and is governed by both Hückel's and Baird's aromaticity rules simultaneously. A further step is done in the final part of this work that addresses the singlet fission (SF) process, considered as an alternative to increase the efficiency of solar cells, and possible use of a spiroconjugated system able to hold radical character as a SF molecule. More specifically, the commonly used model to describe SF, which involved five electronic states, is extended to double excitations for evaluating the possible contribution of dark states to the overall process. The feasibility of SF within spiroconjugated systems is then demonstrated and shown to involve charge transfer states, indicating that other photophysical processes are also accessible.

Contents

Abstract vi

1 How to (and why) read this thesis 1

2 Introduction 6

2.1 Diradicals . . . 6

2.1.1 What is a radical? and a diradical? . . . 6

2.1.2 Classes of diradicals . . . 7

2.1.2.1 Localized and delocalized diradicals . . . 7

2.1.3 Electronic states of diradicals . . . 9

2.1.3.1 Diradicaloids: between closed-shell and diradicals . . . 10

2.1.4 Characterization of diradicaloids . . . 12

2.1.4.1 Clar's sextet rule . . . 12

2.1.4.2 Ovchinnikov's rule . . . 13

2.1.5 Triradicals and beyond . . . 14

Bibliography . . . 16

3 Electronic structure methods and computational tools 18

3.1 The Schrödinger Equation . . . 18

3.2 Electronic Structure Approximations . . . 19

3.2.1 Density Functional Theory . . . 19

3.2.1.1 Constrained-DFT . . . 21

3.2.2 Time-dependent density functional theory . . . 21

3.2.3 Spin-flip methods . . . 22

3.2.3.1 Restricted active space - spin flip . . . 24
3.2.3.2 Spin flip time-dependent density functional theory . 26
3.3 Computational tools for the characterization of electronic states . . . 26
3.3.1 Diradical and polyradical character indices . . . 26
3.3.2 Unpaired number of electrons . . . 27
3.3.2.1 Fragment-based wave function analysis . . . 27
Bibliography . . . 29

4 Polycyclic aromatic hydrocarbon diradicals 32
4.1 Triangular Graphene Nanofragments . . . 33
4.1.1 Pristine phenalenyl and triangulene . . . 34
4.1.2 B-doped and N-doped TGNF . . . 37
4.1.2.1 Phenalenyl derivatives . . . 38
4.1.2.2 Triangulene derivatives . . . 41
4.1.3 Hydrogenated TGNF . . . 44
4.2 Diradical character in cyclic and linear acenes . . . 46
4.2.1 Linear acenes . . . 50
4.2.2 Cyclic acenes . . . 51
4.3 Appendix . . . 56
4.3.1 Computational details . . . 56
4.3.1.1 Triangular graphene nanofragments . . . 56
4.3.1.2 Cyclic and linear acenes . . . 57
Bibliography . . . 57

5 Anionic and cationic oligomer diradicals 64
5.1 Thieno[3,4-c]pyrrole-4,6-dione oligothiophene . . . 66
5.1.1 Monoanionic species . . . 67
5.1.2 Dianionic species: Bipolaron vs polaron-pair . . . 71
5.1.3 Spectroscopic features . . . 74
5.2 Diamino Oligophenyl Dication . . . 77
5.2.1 Origin of the diradical character . . . 78

5.2.2 **The PB-PAT^{+2} $\leftrightarrow$ DD-PAT^{+2}** conversion 81
5.3 Appendix 84
5.3.1 Computational details 84
5.3.1.1 OTPD$_n$ 84
5.3.1.2 PAT^{+2} 84
Bibliography 85

6 Organic macrostructures with polyradical character **91**
6.1 Organic Macrocycles with polyradical Character 92
6.1.1 π-conjugation: [n]annulene analogs 98
6.1.2 Global aromaticity of **[8]MC** and **[10]MC** 102
6.2 Fluorenyl dendrons 108
6.3 Appendix 114
Bibliography 115

7 Singlet fission **121**
7.1 Singlet fission in a nutshell 122
7.1.1 Singlet fission chromophores 123
7.1.1.1 Class I 124
7.1.1.2 Class II 124
7.1.1.3 Class III 125
7.2 Five-state model 125
7.2.1 Electronic states 125
7.2.1.1 Singlet excited states 125
7.2.1.2 Charge transfer states 126
7.2.1.3 The triplet-pair state 126
7.3 Seven-state model 128
7.3.1 Electronic couplings with the D state 129
7.3.2 Singlet fission couplings 131
7.3.3 Singlet fission dynamics with D state 136
7.4 Appendix 144

7.4.1 Computational details . . . 144
Bibliography . . . 144

8 Spiroconjugated dimers **149**

8.1 Spiroconjugated dimers in singlet fission . . . 150
8.1.1 Chromophores pro-spiro . . . 150
8.1.2 Spiroconjugated **DBP1** dimer . . . 156
8.1.2.1 Electronic states of *spiro*-**DBP1** . . . 157
8.1.2.2 Singlet fission mechanism . . . 160
8.1.3 Vibronic couplings . . . 163
8.1.3.1 Low-energy vibrational modes . . . 163
8.1.3.2 High-energy vibrational modes . . . 166
8.2 Spin orbit charge transfer - intersystem crossing in spiroconjugated dimers . . . 168
8.2.1 Spiro[bisanthracene]dione analogues . . . 170
8.2.2 Photophysics of Spiro[bisanthracene]dione . . . 171
8.2.3 Spin-orbit coupling . . . 175
8.2.3.1 A brief experimental background . . . 175
8.3 Spiroconjugation of a diradicaloid-pair . . . 177
8.4 Appendix . . . 181
8.4.1 Computational details . . . 181
8.4.1.1 Spiroconjugated dimers in singlet fission . . . 181
8.4.1.2 SOCT-IC . . . 182
8.4.1.3 spiro-DBP2 . . . 182
Bibliography . . . 183

9 General conclusions **190**

10 Full list of publications **192**

Chapter 1

How to (and why) read this thesis

It is not my intention to imitate Cortázar's masterpiece "Rayuela" (Hopscotch) providing a table of instructions to read this thesis. However, while there is no hidden mystery in the organization of its chapters, it seems appropriate to introduce them in a naturally evolutionary way, exposing the objectives pursued at each step.

The main aim of the research presented in this thesis consists in the understanding of the electronic structure of organic diradical and polyradical molecules. Through the study of organic systems with different radical natures, this work also intends to help in the design of new materials with improved tunable magnetic properties for applications in the wide field of organic electronics.

From a more personal perspective, the final aim of my Ph.D. in the group of Dr. Casanova is twofold, namely acquiring expertise in the study of electronic structure properties of complex systems and developing competences in the use of appropriate quantum chemistry methods and computational tools for the rationalization of experimental measurements.

This manuscript is structured as follows:
In Chapter 2, I provide the general background theory and concepts about diradicals, and how to characterize them from a theoretical point of view. Following that, I present in Chapter 3 a very broad overview of the theoretical methods and computational tools used to achieve the specific objectives set for the study of the systems considered in this thesis.

In Chapters 4-8, the diradical character of the organic systems investigated is described and discussed from a structure-electronic properties relationship perspective in the context of their potential applications. While the systems considered purposely differ in terms of chemical nature, topology, and associated electronic/magnetic features, all chapters share common objectives:

- Determine the diradical (polyradical) character of the ground state of the

systems under study.

- Identify the structure-diradical character relationships.
- Propose an interpretation of the experimental observations (when experimental data is available) at the electronic and molecular levels.
- Assess the robustness and quality of computational methods.

Among the zoo of existing graphene nanostructures, phenalenyl, triangulene and acenes are well-known representative examples of small organic molecules with open-shell character. In Chapter 4, the modulation of their magnetic properties as a function of structural and chemical modifications, namely size, shape, heteroatom substitution, and connectivity, is theoretically investigated. Particular objectives of this chapter are:

- Compare the open-shell nature of the ground state in hydrocarbons with different structure.
- Determine the role that topology plays in the nature of their radical character.
- Identify the origin of the synthetic challenge they represent.
- Explore a way to modulate the radical character in small triangular graphene nanostructures.

Results included in this chapter are published in:

- **M. E. Sandoval-Salinas**, A. Carreras, D. Casanova, "Triangular graphene nanofragments: open-shell character and doping", *Phys. Chem. Chem. Phys.*, 2019, 21, 9069-9076.
- A. Perez-Guardiola^{+}, **M. E. Sandoval-Salinas**$^{+}$, D. Casanova, E. San Fabián, A. J. José Pérez-Jiménez, J. C. Sancho-Garcia, "The role of topology in organic molecules: origin and comparison of the radical character in linear and cyclic oligoacenes and related oligomers", *Phys. Chem. Chem. Phys.*, 2018, 20, 7112-7124.

In Chapter 5, the rise of diradical character by means of reduction/oxidation of a family of closed-shell oligomers was studied, as well as the modulation of diradical character of a poly-p-phenylene via external stimuli. In both cases, experimental data was available and all the calculations have the final purpose to explain the spectroscopic features triggered by the change in the diradical character of the systems, and particularly:

- Describe the electronic structure of the ground state of organic oligomers to explain the origin of the magnetic properties determined experimentally.
- Interpret the spectroscopic features in light of electronic structure calculations of the excited states.
- Propose an explanation of the relative stability between conformers.

Results included in this chapter are published in:

- D. Yuan, S. Medina, P. Mayorga, L. Ren, **M. E. Sandoval-Salinas**, S. J. Grabowski, D. Casanova, X. Zhu, J. Casado, "Thieno[3,4-c]pyrrole-4,6-dione oligothiophenes have two crossed paths for electron delocalization", *Chem. Eur. J.*, 2018, 24, 13523-13534.
- S. Medina, P. Mayorga, **M. E. Sandoval-Salinas**, T. Li, F. J. Ramírez, D. Casanova, X. Wang and J. Casado, "Isomerism, diradical signature, and raman spectroscopy: underlying connections in diamino oligophenyl dications", *ChemPhysChem* 2018, 19, 1465-1470.

Beyond diradical (or tetraradical) character, systems with a large number of radical centers are particularly appealing candidates for use in spintronic devices and molecular magnets. In Chapter 6, series of macrostructures with high polyradical character are studied in collaboration with experimental groups. The objectives in this chapter are:

- Describe the radical-radical interaction in macrostructures.
- Identify the origin of their inherent features at the electronic level.
- Prove the performance of common methods in the description of complex (big and largely correlated) systems.

Results included in this chapter are published in:

- Y. Ni, **M. E. Sandoval-Salinas**, T. Tanaka, H. Phan, T. S. Herng, T. Y. Gopalakrishna, J. Ding, A. Osuka, D. Casanova, J. Wu, "[n]Cyclo-para-biphenylmethine polyradicaloids: [n]annulene analogues and unusual valence tautomerization", *Chem*, 2019, 5, 108-121.
- C. Liu, **M. E. Sandoval-Salinas**, Y. Hong, T. Y. Gopalakrishna, H. Pan, N. Aratani, T. S. Herng, J. Ding, H. Yamada, D. Kim, D. Casanova, J. Wu, "Macrocyclic polyradicaloids with unusual super-ring structure and global aromaticity",*Chem*, 2018, 4, 1-10.

- J. Wang, G. Kim, **M. E. Sandoval-Salinas**, H. Phan, T. Y. Gopalakrishna, X. Lu, D. Casanova, D. Kim, J. Wu, "Stable 2D anti-ferromagnetically coupled fluorenyl radical dendrons", *Chem. Sci.*, 2018, 9, 3395-3400.

The first three results chapters focused on the description of the radical character of molecular systems in relation to their shape, size and other structural and chemical features. In order to go further, the two final chapters address a concrete photophysical process, namely singlet fission, through the study of a spiroconjugated system able to hold radical character. Notably, the singlet fission process has been extensively investigated as an alternative to increase the efficiency of solar cells. In Chapter 7, a revision of the fundamental aspects of singlet fission theory is presented, as well as an extension of the widely accepted five-(electronic)state model by inclusion of doubly excited states. The objectives of this chapter are:

- Understand the principles of singlet fission mechanism.
- Establish the structural and energetic conditions that facilitate doubly excited state to take part in the singlet fission mechanism.
- Estimate the impact of the double excitations in the singlet fission processes.

Results included in this chapter are published in:

- **M. E. Sandoval-Salinas**, D. Casanova, "The doubly excited state in singlet fission", *ChemPhotoChem*, accepted, DOI: 10.1002/cptc.202000211.

Finally, Chapter 8 presents the in-depth investigation of spiroconjugated systems within the context of singlet fission. The specific objectives of this chapter are:

- Describe the electronic excited states of pro-spiro chromophores.
- Examine the effect of the spiroconjugation on the excited states presence and ordering.
- Evaluate the suitability of studied systems to carry out singlet fission.
- Understand the electronic structure of the nature of the spiro conjugation.
- Propose the singlet fission mechanism that spiro-systems can undertake.
- Identify the effect of the structural deformations triggered by representative normal mode vibrations.
- Explore the suitability of spiro-systems to carry out ISC.

- Analyse the effect of the spiro conjugation on the radical character of the spiroconjugated system.

Results included in this chapter are published in:

- **M. E. Sandoval-Salinas**, A. Carreras, J. Casado, D. Casanova, "Singlet fission in spiroconjugated dimers", *J. Chem. Phys.*, 2019, 150, 204306.
- M LV^{+}, Y. Yu^{+}, **M. E. Sandoval-Salinas**$^{+}$, J. Xu, Z. Lie, D. Casanova, Y. Yang, J. Chen, "Engineering the charge-transfer state to facilitate spin-orbit charge transfer intersystem crossing in spirobis[anthracene]diones", *Angew. Chem. Int. Ed.*, 2020, 59, 22179.
- S. Rivero^{+}, R. Shang^{+}, **M. E. Sandoval-Salinas**$^{+}$, H. Hamada, K. Nakabayashi, S. Ohkoshi. D. Casanova, E. Nakamura, J. Casado, "A spiro-driven tetraradical", submitted.

The results chapters are organized under the following scheme: first the system/process of interest is briefly introduced in the context of the optoelectronic field in relation with their radical properties; then, the main results are unfolded to smoothly reach particular conclusions that set the basis to continue with the discussion; finally, the computational details are explained. At the end of this dissertation, the general conclusions of this work are summarized.

Chapter 2

Introduction

2.1 Diradicals

In the Chemistry world, the terms *radical* and *diradical* are commonly associated with the idea of instability and high reactivity. Nevertheless, they have been extensively explored for more than one century and synthetic routes, stabilization techniques and characterization methods are nowadays well known. Organic diradicals are promising systems to be applied as main components in optoelectronic, photovoltaic, and magnetic devices.(1; 2; 3; 4)

2.1.1 What is a radical? and a diradical?

A radical or free radical is defined as a chemical entity with one unpaired electron. Depending on the atom that holds the unpaired electron, radicals are named as carbon-, nitrogen-, oxygen- or metal-centered. Also, they can be classified as σ- or π-radicals if the singly occupied orbital has considerable σ or π character.(5) The formation of radicals is usually associated with reaction intermediates or unstable products of bond cleavage. Due to the presence of the unpaired electron, radicals are highly reactive species with a very short lifetime. The understanding, detection, and characterization of radicals are crucial in organic synthesis. For instance, polymerization reactions are carried out mostly via radicals.(6; 4) They also play a key role in (several) biological processes such as the cellular oxidation, among others.

The first successful isolation of a radical molecule was achieved more than 100 years ago when Gomberg reported the observation of the triphenylmethyl radical (TM, Figure 2.1).(7; 8; 9) In this molecule, three phenyl moieties are connected through one sp^2 carbon (radical). Despite the sterical protection provided by the phenyl groups to the radical center, TM is a highly reactive species. Thenceforth, constant modifications of the TM backbone have been performed to improve its

stability and potentiate its practical applications. Gomberg's pioneering work paved the way for an extensive field of research that is still being explored nowadays.

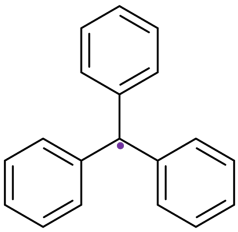

Figure 2.1: Structure of the triphenylmethyl (TM) radical.

However, even before the observation of the monoradicals, the high reactivity in some alternated compounds with even number of electrons has been explained considering the idea of two unpaired electrons.(10; 11; 12) This kind of systems, where two radicals interact across the molecular scaffold, are better known as diradicals or biradicals.(5) Although both terms have been used indistinctly through the years, they are not equivalent: while in a diradical there is a measurable interaction between unpaired electrons that determines the spin multiplicity of their ground state (singlet or triplet), there is no interaction in a biradical and unpaired electrons act as two independent doublets.(2) In this thesis, I focus my interest on diradicals. They are described as molecules with two unpaired electrons occupying two degenerate orbitals,(3; 2; 4) and are extremely important in the understanding of chemical reactivity, the nature of chemical bonding, or in biological processes.

2.1.2 Classes of diradicals

In the literature, several ways exist to classify diradicals, all of them having some points in common. Hereafter, I follow the classification used by M. Abe.(2)

2.1.2.1 Localized and delocalized diradicals

Intuitively, localized diradicals are those in which the unpaired electrons can be found over specific atoms. They can be generated by homolytic bond-cleavage and then change their spin multiplicity (singlet $\rightleftharpoons$ triplet) by intersystem crossing. Localized triplet diradicals have long lifetimes(2) and their chemistry has been more extensively investigated than the one of singlet localized diradicals. In Figure 2.2a, some examples of localized diradicals are shown.

On the contrary, delocalized diradicals are part of a π-conjugated system and the unpaired electrons cannot be associated to a particular atom (Figure 2.2b). These are classified as triplet antiaromatic or Kekulé and non-Kekulé diradicals.

- Antiaromatic delocalized diradicals:

  $4n\pi$-annulenes are antiaromatic in their ground state according to the Hückel's rule but aromatic in their first excited triplet state, as explained by Baird in 1972.(13) This aromaticity allows the delocalization of the two electrons of the triplet (Figure 2.2e).

- Kekulé delocalized diradicals:

  Kekulé delocalized diradicals are those presenting two resonance structures: aromatic and quinoidal (Figure 2.2c). While the Lewis structure of the aromatic form has to be drawn with two unpaired electrons (spin-triplet ground state), the bond alternation in the quinoidal form permits all electrons to be paired in a "closed-shell" (CS) configuration (spin-singlet ground state). Normally, the ground state holds a singlet spin multiplicity, but the preferred formation of aromatic rings brings about the presence of unpaired electrons. The typical interconversion energy between quinoidal-aromatic (singlet-triplet) conformers is $\Delta E_{ST} = 8-30$ kcal/mol, making these compounds quite reactive even when they possess a singlet ground state.

- Non-Kekulé delocalized diradicals:

  In these systems, no resonance structures without unpaired electrons can be drawn (Figure 2.2d). More specifically, in a localized orbital representation, if both frontier orbitals can be represented over the same group of atoms, they are termed non-disjoint non-Kekulé diradicals and the electron repulsion between both electrons favors the triplet state over the singlet. If there is no shared atom in the radical orbitals, they are disjoint non-Kekulé diradicals.

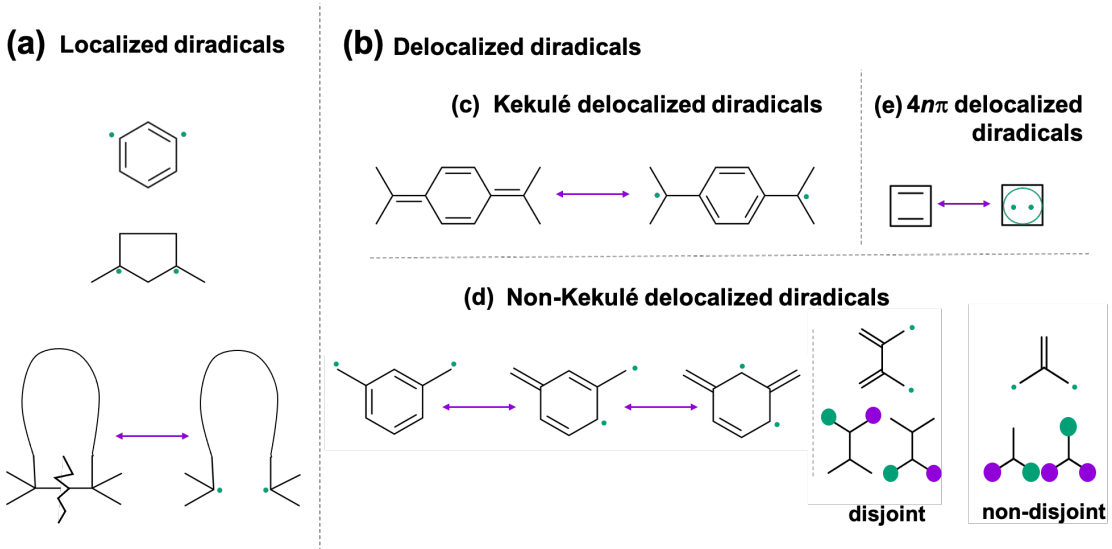

Figure 2.2: Classes of diradicals. Localized (a), delocalized (b), Kekulé delocalized (c), non-Kekulé delocalized, and disjoint and non-disjoint delocalized (d) diradicals.

2.1.3 Electronic states of diradicals

To properly describe the electronic structure of diradicals and rationalize their properties, it is necessary to recall their definition: "two electrons occupying two degenerate orbitals". In a model of two electrons in two degenerate orbitals based on the previous definition, it is possible to form six electronic configurations (Figure 2.3), which can be used to generate the three microstates (M_s) of one triplet and three singlet states.(4; 14)

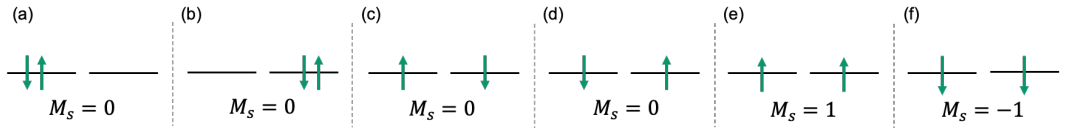

Figure 2.3: Electronic configurations and the projection of the total spin, M_s, that can be obtained by the distribution of two electrons in two degenerate orbitals.

Configurations (a) and (b) of Figure 2.3 are two closed-shell singlets, (e) and (f) are the $M_s = 1$ and $M_S = -1$ components of the triplet, respectively, and, the linear combination of (c) and (d) gives rise to the $M_s = 0$ spin projection of the triplet and the open-shell singlet.

From these determinants, 6 wave functions are written, corresponding to singlet (Ψ_n^s) and triplet (Ψ_n^t) states ($n = 1 - 3$) as:

$$\Psi_1^s = \frac{1}{2}[\phi_1^2 - \phi_2^2](\alpha\beta - \beta\alpha), \tag{2.1}$$

$$\Psi_2^s = \frac{1}{2}[\phi_1^2 + \phi_2^2](\alpha\beta - \beta\alpha), \tag{2.2}$$

$$\Psi_3^s = \frac{1}{2}(\phi_1\phi_2 + \phi_2\phi_1)(\alpha\beta - \beta\alpha), \tag{2.3}$$

$$\Psi_1^t = \frac{1}{2}(\phi_1\phi_2 - \phi_2\phi_1)(\alpha\beta + \beta\alpha), \tag{2.4}$$

$$\Psi_2^t = \frac{1}{\sqrt{2}}(\phi_1\phi_2 - \phi_2\phi_1)(\alpha\alpha), \tag{2.5}$$

$$\Psi_3^t = \frac{1}{\sqrt{2}}(\phi_1\phi_2 - \phi_2\phi_1)(\beta\beta), \tag{2.6}$$

where $\phi_i\phi_j$ is the spatial part of the wave function of electrons 1 and 2 in the i and j orbitals and α/β the spin of each particle. Equation 2.1 and 2.2 are the "closed-shell" singlets, in which the wave functions are written as the contribution of both (a) and (b) determinants.

The description of the ground state of diradical systems is given by the energy relationship between these singlet and triplet states. The energy of the Ψ_3^s (herein named as open-shell singlet) can be expressed as:

$$E_{os} = h_1 + h_2 + J_{12} + K_{12}, \tag{2.7}$$

where h_i is the monoelectronic energy in the orbital i, J_{ij} is the Coulomb integral ($J_{ij} = \int\int \phi_i^2(1)\frac{e^2}{r_{12}}\phi_j^2(2)dr_1dr_2$), that counts for the repulsion between electrons 1 and 2 localized in the same orbital, and K_{ij} is the exchange integral, $K_{ij} = \int\int \phi_i(1)\phi_j(1)\frac{e^2}{r_{12}}\phi_i(2)\phi_j(2)dr_1dr_2$.

The energy of the triplet, expressed in the same terms, is:

$$E_t = h_1 + h_2 + J_{12} - K_{12}. \tag{2.8}$$

Notably, the only difference between Equation 2.7 and 2.8 is the sign of the exchange integral K_{12}. Due to the symmetry (antisymmetry) of the spacial wave function of the singlet (triplet), the probability of having two electrons together rises (vanishes) and the electronic energy increases (decreases) by K_{12}, which is always a positive term. Accordingly, the energy gap between the two lowest states of a diradical is dictated by:

$$E_{os} - E_t = 2K_{12}, \tag{2.9}$$

where the energy of the triplet is lower than the OS by $2K_{12}$. This is in good agreement with the Pauli exclusion principle that prevents two electrons with the same spin from getting close and lowers their repulsion eventually resulting in the Hund's rule favoring the triplet stabilization.

On the other hand, the energy of the closed-shell states (Equation 2.1 and 2.2) is expressed as:

$$E_{cs_\pm} = h_1 + h_2 + \frac{J_{11} + J_{22}}{2} \pm K_{12}, \tag{2.10}$$

in which the energy splitting between both CS states is determined by the contribution of K_{12}. The addition or subtraction of the last term on the right side of Equation 2.10 correspond to the energy of Ψ_1^s and Ψ_2^s, labeled as cs_+ or cs_-, respectively. The energy gap is $E_{cs_+} - E_{cs_-} = 2K_{12}$. The energy relation between the lowest closed-shell (cs_-) and open-shell singlet is:

$$E_{os} - E_{cs_-} = J_{12} - \frac{J_{11} + J_{22}}{2} + 2K_{12}. \tag{2.11}$$

Consequently, the final ordering of states depends strongly on the magnitude of K_{12}. However, it is important to remark that this condition is established for perfectly degenerate orbitals and considering that they are exactly the same in both states. In the presence of small (moderate) perturbations, Equations 2.9 and 2.11 are not entirely satisfied and the order of states can change, allowing the observation of both singlet and triplet ground state diradicals.

2.1.3.1 Diradicaloids: between closed-shell and diradicals

When the degeneracy of i and j orbitals in Equations 2.1 - 2.6 is lifted, their respective occupations are not equally probable anymore. The probability of hav-

ing two electrons in the energetically higher orbital is low and the latter is then referred to as the Lowest-Unoccupied-Molecular-Orbital (LUMO), while the lower-lying orbital have a higher probability of being populated and is referred to as the Highest-Occupied-Molecular-Orbital (HOMO). Hence, in the wave function of both closed-shell singlets, one configuration can be neglected, assuming that both electrons are either in the HOMO or in the LUMO, and state energies can be expressed as:

$$E_0 = 2h_H + J_{HH}, \tag{2.12}$$

$$E_D = 2h_L + J_{LL}, \tag{2.13}$$

where the i and j indices have been replaced by H and L, referring to HOMO and LUMO orbitals, respectively. The subscripts correspond to the usual name for the ground state (S_0) and to the double excitation to the LUMO orbital (here labeled as D). Under the same approach of non-degenerate orbitals, the open-shell singlet and the triplet wave functions preserve their form and E_{os} and E_t can be written as:

$$E_{os} = h_H + h_L + J_{HL} + K_{HL}, \tag{2.14}$$

$$E_t = h_H + h_L + J_{HL} - K_{HL}. \tag{2.15}$$

According to the orbital splitting, two situations can be described. If the energy gap between orbitals is large, $h_L >> h_H$, the wave functions are not mixing and E_{os} and E_t are higher than E_{S_0}. Then, the overall picture corresponds to a closed-shell system with closed-shell ground state, the lowest excited triplet lying $2K_{hl}$ below the first excited singlet (HOMO-LUMO excitation) and the doubly excited state being higher in energy. However, if the energy gap between HOMO and LUMO is quite small, the probability of finding one or two electrons in the LUMO increases significantly and both closed-shell configurations must be considered to determine the properties of the ground state.

Rewriting Equation 2.1 as a configuration interaction (CI):

$$\Psi_1^s = C_1\phi_H^2 - C_2\phi_L^2, \tag{2.16}$$

where C_1 and C_2 are the coefficients that represent the weight of each configuration in the ground state wave function. Large C_1/C_2 are indicative of the closed-shell character of the system; as it decreases, the diradical character increases up to a value of 1, for which the system is a perfect diradical. The triplet state is then the first excited state, but lies very low in energy due to the small HOMO-LUMO gap, and might be degenerate with the singlet or, even, the ground state.

Systems in the situation between closed-shell and perfect diradicals are named *diradicaloids* (or diradical-like) and can be defined as molecules with two electrons

occupying two quasi-degenerate orbitals. Interestingly, most of the organic systems with diradical character studied as candidates for optoelectonic or photovoltaic applications are indeed diradicaloids.

2.1.4 Characterization of diradicaloids

The diradical character is not an observable and thus cannot be quantified directly, neither theoretically or experimentally. Several quantities have been defined to characterize diradicals and diradicaloids: i) the singlet-triplet energy gap (ΔE_{ST}), in order to establish the multiplicity of the ground state and the interaction between both radicals ($2K_{12}$); ii) the HOMO-to-LUMO energy gap, to determine the degeneration of frontier molecular orbitals; and iii) the effective occupation of these orbitals.

ΔE_{ST} can be approximated by twice the exchange integral ($2K_{12}$), which is the measurement of the electron-electron repulsion between two radicals. If $2K_{12}$ is equal to zero, the system is twice a radical (like two non-interacting doublets), which is the case of biradicals, as aforementioned. When $2K_{12}$ is different from zero, the radical interaction can be classified as antiferromagnetic (singlet ground state) or ferromagnetic (triplet ground state) if $2K_{12} < 0$ or > 0, respectively. While, in a perfect diradical there is one electron occupaying each orbital, there are 2 and 0 electrons in HOMO and LUMO orbitals, respectively, in the CS configuration.

Reliable characterization of diradicals needs robust electronic structure methods. Nevertheless, some useful rules can be used to describe diradicals and diradicaloids in a very basic way through graphical representation such as the Ovchinnikov's rule and the Clar's sextet rule.

2.1.4.1 Clar's sextet rule

In benzene rings, two equivalent forms with three localized double bonds are in resonance (cyclohexatriene), identified as Kekulé resonance structures. By superposition of both structures, a Clar's sextet is formed, *i.e.*, the benzene ring in which 6π-electrons are delocalized (Figure 2.4a). Benzene is more stable than cyclohexatriene owing to the effect of aromaticity.(15) The formation of Clar's sextets explains the effect of the aromaticity in extended benzenoid systems (named as alternant polycyclic aromatic hydrocarbons or simply PAHs).(16) Clar's rule establishes that the resonance structure with the largest number of aromatic rings is the one that contributes the most to the electronic structure character of the system.(15) The extra stabilization in such structures is the result of having an "extra" aromatic ring.

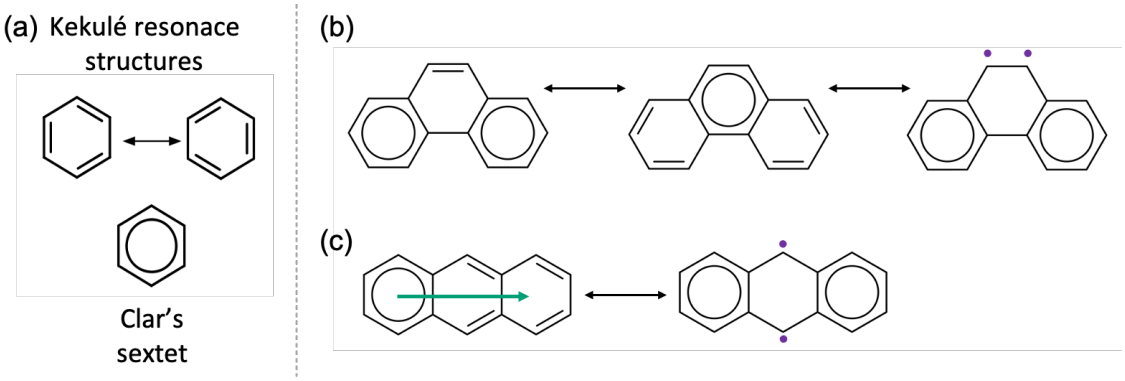

Figure 2.4: Benzene resonance structures and the Clar's sextet, which is represented as a circle inside the six-membered ring (a). Resonance structures of phenanthrene (b) and anthracene (c) with their Clar's sextets. The green arrow represents a Clar's sextet that can be localized in either one of the three benzene rings.

For a given PAH, Kekulé and non-Kekulé structures (forms with absence and presence of unpaired electrons, respectively) can be drawn. In the case of radicals and diradicals, the non-Kekulé forms are the ones with the largest number of Clar's sextets. Following the Clar's rule, they have a critical role in the description of these systems,(12) in which the instability induced by the unpaired electrons is compensated by the aromaticity gain. For instance, Figure 2.4 shows the resonance structures with their respective Clar's sextets for phenanthrene (b) and anthracene (c), PAHs with three fused benzene rings. Two Clar's sextets can be drawn in each structure, localized in the rings at the molecular end, which leads to having two unpaired electrons in the central benzene ring of each PAH. In phenanthrene, the presence of two radicals is largely unfavorable and these electrons can form a π-bond and have a closed-shell configuration, stabilizing the system. On the other hand, radicals in anthracene can not be bonded together or with adjacent atoms. The three equivalent closed-shell structures have the biggest influence in its electronic structure, but a fairly small diradical character can be expected. In this way, the (potential) radical character of PAHs can be predicted by the Clar's rule.

2.1.4.2 Ovchinnikov's rule

In alternant systems, as PAHs, simple models like Ovchinnikov's(17) rule can be used to predict the ground state spin multiplicity. According to this rule, atoms of a system can be classified in two types, labelled generically N and N^* (Equation 2.17), in such an arrangement that N atoms are surrounded only by N^* atoms and vice versa. Preferred ground state spin is predicted as the half of the difference between

the number of carbon atoms belonging to N or N^* types (opposite lattices).

$$S = \frac{|N - N^*|}{2}. \tag{2.17}$$

A special situation occurs when the number of N and N^* is not the same (Figure 2.5c), which results in systems holding a high-spin ground state. This rule has been employed to predict the spin multiplicity of a lot of aromatic systems, as well as in the engineering of structures with high spin-multiplicity state.

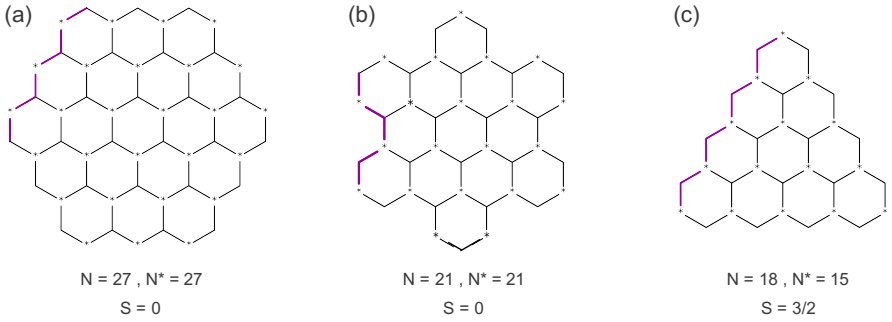

Figure 2.5: PAHs with different shapes and edges. N^* and N are the number of carbon atoms in each sublattice within the Ovchinnikov's rule. (a) Hexagonal PAH with singlet ground state; (b) armchair-edged hexagonal PAH with singlet ground state; and (c) triangular PAH with quartet ground state.

More formally, Lieb's theorem asserts that the ground state-multiplicity of a bipartite lattice system is obtained from the Equation 2.17.(18) In the organic chemistry context, the Ovchinnikov's rule is equivalent to the Lieb's theorem.

2.1.5 Triradicals and beyond

Molecules with an odd number of electrons inevitably have unpaired electrons. The diradical concept for the case of two electrons in two degenerate orbitals can be generalized to tri-, tetra-, pentaradicals, etc, and so on, for systems with a larger number of unpaired electrons. While there is an extensive number of examples of organic monoradicals and diradicals in the literature, the chemistry of triradicals (and beyond) has been less explored due to the increased instability associated with the increase of the number of unpaired electrons. Nevertheless, in the past few years fascinating examples of organic polyradicals have been designed, synthesized and characterized. For a couple of decades, Rajca and his group developed the concept of magnetic clusters, systems in which a core of high spin-multiplicity is growing in branches that couple diradicals in a polymeric way. With this strategy, the maximum spin-multiplicity achieved was $S \approx 5000$.(19) These systems with very large

polyradical character are particularly attractive for applications as supermagnets and insulating spin glasses.

Bibliography

[1] X. Hu, W. Wang, D. Wang, and Y. Zheng, "The electronic applications of stable diradicaloids: present and future," *J. Mater. Chem. C*, vol. 6, pp. 11232–11242, 2018.

[2] M. Abe, "Diradicals," *Chemical Reviews*, vol. 113, no. 9, pp. 7011–7088, 2013.

[3] A. Rajca, "Organic diradicals and polyradicals: From spin coupling to magnetism," *Chemical Reviews*, vol. 94, no. 4, pp. 871–893, 1994.

[4] T. Stuyver, B. Chen, T. Zeng, P. Geerlings, F. De Proft, and R. Hoffmann, "Do diradicals behave kike radicals?," *Chemical Reviews*, vol. 119, no. 21, pp. 11291–11351, 2019.

[5] I. U. of Pure and A. Chemistry, "Iupac compendium of chemical terminology – the gold book," 2009.

[6] I. Ratera and J. Veciana, "Playing with organic radicals as building blocks for functional molecular materials," *Chem. Soc. Rev.*, vol. 41, pp. 303–349, 2012.

[7] M. Gomberg, "An instance of trivalent carbon: triphenylmethyl," *Journal of the American Chemical Society*, vol. 22, no. 11, pp. 757–771, 1900.

[8] M. Gomberg, "On triphenylchlormethane," *Journal of the American Chemical Society*, vol. 23, no. 2, pp. 109–110, 1901.

[9] M. Gomberg, "Organic radicals," *Chemical Reviews*, vol. 1, no. 1, pp. 91–141, 1924.

[10] J. Thiele and H. Balhorn, "Ueber einen chinoïden kohlenwasserstoff," *Berichte der deutschen chemischen Gesellschaft*, vol. 37, no. 2, pp. 1463–1470, 1904.

[11] E. Müller and H. Pfanz, "Über biradikaloide terphenylderivate," *Berichte der deutschen chemischen Gesellschaft (A and B Series)*, vol. 74, no. 6, pp. 1051–1074, 1941.

[12] C.-N. Yeh and J.-D. Chai, "Role of kekulé and non-kekulé structures in the radical character of alternant polycyclic aromatic hydrocarbons: a tao-dft study," *Scientific Reports*, vol. 6, no. 1, p. 30562, 2016.

[13] N. C. Baird, "Quantum organic photochemistry. ii. resonance and aromaticity in the lowest $3\pi - \pi^*$ state of cyclic hydrocarbons," *Journal of the American Chemical Society*, vol. 94, no. 14, pp. 4941–4948, 1972.

[14] L. V. Slipchenko and A. I. Krylov, "Singlet-triplet gaps in diradicals by the spin-flip approach: A benchmark study," *The Journal of Chemical Physics*, vol. 117, no. 10, pp. 4694–4708, 2002.

[15] M. Solà, "Forty years of clar's aromatic π-sextet rule," *Frontiers in chemistry*, vol. 1, pp. 22–22, 2013.

[16] R. G. Harvey, "Environmental chemistry of pahs," in *PAHs and related compounds*, pp. 1–54, Springer, 1998.

[17] A. A. Ovchinnikov, "Multiplicity of the ground state of large alternant organic molecules with conjugated bonds," *Theor. Chim. Acta*, vol. 47, no. 4, pp. 297–304, 1978.

[18] E. H. Lieb, "Two theorems on the hubbard model," *Phys. Rev. Lett.*, vol. 62, pp. 1201–1204, 1989.

[19] A. Rajca, "The physical organic chemistry of very high-spin polyradicals," *Advances in Physical Organic Chemistry*, vol. 40, pp. 153–199, 2005.

Chapter 3

Electronic structure methods and computational tools

> The underlying physical laws necessary for the mathematical theory of a large part of physics and the whole of chemistry are thus completely known, and the difficult is only that the exact solution of these laws leads to equations much too complicated to be soluble.
>
> (P.A.M. Dirac, 1929)

This chapter sets the general quantum chemistry framework for the study of the electronic structure of molecular systems. In the following, I introduce and briefly describe an non-exhaustive list of electronic structure approximations for the calculation of electronic states and their properties, focusing on those employed in the results chapters of this thesis.

3.1 The Schrödinger Equation

Quantum chemistry focuses on the description of all the physical and chemical properties of atoms and molecules. The complete characterization of a system can be achieved using the Schrödinger equation,(1) which without relativistic effects is expressed as:

$$\hat{H}\Psi(\mathbf{r},t) = i\hbar\frac{\delta\Psi(\mathbf{r},t)}{\delta t}, \tag{3.1}$$

where $\hat{H}$ is the well-known Hamiltonian operator, whose eigenvalue is the energy of the system. As the wave function Ψ depends on the position ($\mathbf{r}$) of the particles and time (t) evolution, it is named the *time-dependent Schrödinger equation*. If the Hamiltonian does not have any dependence on time, Equation 3.1 can be written as:

$$\hat{H}\Psi(\mathbf{r})F(t) = \Psi(\mathbf{r})i\hbar\frac{\delta F}{\delta t}, \tag{3.2}$$

where F is the only term in which the time is involved, and $\Psi(\mathbf{r})$ depends only on the spatial coordinates. By keeping only the spatial term, the *time-independent* Schrödinger equation is written as:

$$\hat{H}\Psi(\mathbf{r}) = E\Psi(\mathbf{r}). \tag{3.3}$$

In quantum chemistry and molecular physics, $\hat{H}$ in Equation 3.3 corresponds to the molecular (or atomic) Hamiltonian. Under the Born-Oppenheimer approximation, atomic and electronic coordinates are treated separately and the electronic Schrödinger equation is expressed as:

$$\hat{H}_e(\mathbf{r}, \mathbf{R})\phi(\mathbf{r}; \mathbf{R}) = E_e(\mathbf{R})\phi(\mathbf{r}; \mathbf{R}), \tag{3.4}$$

where $\mathbf{r}$ and $\mathbf{R}$ are the electronic and atomic coordinates, respectively. The electronic wave function $\phi(\mathbf{r}; \mathbf{R})$ and its energy $E_e(\mathbf{R})$ depend parametrically on $\mathbf{R}$ and the electronic Hamiltonian takes the form:

$$\hat{H}_e(\mathbf{r}, \mathbf{R}) = \hat{T}_e(\mathbf{r}) + \hat{V}_{eN}(\mathbf{r}, \mathbf{R}) + \hat{V}_{ee}(\mathbf{r}), \tag{3.5}$$

where $\hat{T}_e$ is the electronic kinetic energy operator, $\hat{V}_{eN}$ accounts for the attractive interaction between nuclei and electrons, and $\hat{V}_{ee}$ for the repulsive electron-electron interactions.

In principle, all the information necessary to fully describe the electronic structure of a molecular system is provided by solving the electronic Schrödinger equation. In practice, this is a complicated task due to the large number of variables, and Equation 3.4 can only be solved exactly for a couple of systems (hydrogen and hydrogen-like).

3.2 Electronic Structure Approximations

The need to solve the Schrödinger equation for poly-atomic systems lead to the development of several quantum chemistry methods based either on the wave function (Hartree-Fock and post-Hartree-Fock methods, *e.g.* Møler-Plesset perturbation theory (MP), configuration interaction (CI), multiconfigurational self-consistent field (MCSCF), couple cluster (CC), etc) or based on the electronic density (density functional theory, density matrix functionals).

3.2.1 Density Functional Theory

Within the Density functional theory (DFT), the Schrödinger equation can be solved in terms of the electronic density (ρ) avoiding the construction of the wave function of

a N-electron system. The main premise of DFT is that the energy and all properties of a given system can be determined as a functional of ρ. This affirmation, known as the 1^{st} theorem of Hohenberg and Kohn, also establishes that there is a unique external potential (v) determined by each ρ. The electronic density depends (only) on the spatial coordinates $\mathbf{r}$, hereafter the density will be written as $\rho(\mathbf{r})$. Hence, within the DFT framework, the energy and all properties of the system are expressed as a *functional* of the density (a functional is defined as a function of a function) and can be written as:

$$E[\rho] = T[\rho(\mathbf{r})] + V_{ne}[\rho(\mathbf{r})] + V_{ee}[\rho(\mathbf{r})] \tag{3.6}$$

$$V_{ne}[\rho] = \int \rho(\mathbf{r}) v(\mathbf{r}) d\mathbf{r}. \tag{3.7}$$

The total energy of a system (Equation 3.6) includes the kinetic energy ($T[\rho(\mathbf{r})]$), electron-electron ($V_{ee}[\rho(\mathbf{r})]$), and nuclei-electron ($V_{ne}[\rho(\mathbf{r})]$) interaction energies.

The second Hohenberg and Kohn's theorem ensures the existence of an "exact" ρ (ρ_0) that minimizes the electronic energy of the ground state of the system. Despite the importance of this theorem, the general expressions of $T[\rho(\mathbf{r})]$ and $V_{ee}[\rho(\mathbf{r})]$ in Equation 3.6 are unknown, and in practice the description of the ground state electron density relies on further approximations.

Kohn and Sham (KS) established the most used approach in quantum chemistry to solve the Equation 3.6. Their method states that the density of a real system can be mapped to a single determinant wave function constructed by the Kohn-Sham orbitals $\psi_i(\mathbf{r})$ (orbitals of a system of non-interacting electrons), in such way that the density of the real system is:

$$\rho(\mathbf{r}) = \rho_s(\mathbf{r}) = \sum_{i}^{N} |\psi_i|^2(\mathbf{r}), \tag{3.8}$$

and the electronic energy of the real system is defined as:

$$E[\rho(\mathbf{r})] = V_{ne}[\rho(\mathbf{r})] + T_s[\rho(\mathbf{r})] + J[\rho(\mathbf{r})] + E_{XC}[\rho(\mathbf{r})], \tag{3.9}$$

where, $T_s[\rho]$ is the kinetic energy of a system of non-interacting electrons, $J[\rho]$ is the Coulomb interaction energy, and $E_{XC}[\rho]$ is the exchange and correlation energy (the key quantity of DFT), which is defined as the difference between the "real" energy of the system and the KS one.

DFT-KS is formulated as an exact method, which with the correct terms yields the exact description of an N-electrons system. Despite all the terms in Equation 3.9 can be known, the practical limitation is that the exact exchange-correlation functional is unknown. In this sense, numerous attempts in the search for the exact E_{XC} have been done since the birth of KS-DF. These approximations can

be classified as the those based on local density (LDA), generalized gradient of the density (GGA), its derivatives of higher order (*meta*GGA) and, hybrid functionals that combine pure density functionals with exact exchange. Owing to the large quantity of available functionals in quantum chemistry, a wide range of topics can be addressed by using DFT in the chemistry, physics, biology, etc. areas. However, DFT does not always offer the "correct" description for the correct reasons, as the use of of parameters to counterbalance the lack of exact functional can lead to cancellation of errors and, as a consequence, can lead to meaningless results.

3.2.1.1 Constrained-DFT

In certain cases, it can be desirable to solve the KS equations under some physical constraints to the electron density. For instance, it might be interesting to restrict the net spin density of the system over some specific atoms, or to enforce different amounts of electron density on different spatial regions, such as over electron donor and withdrawing groups in push-pull systems. The constrained-DFT (C-DFT)(2) formalism corresponds to the minimization of the total energy under a constraint, in which a Lagrange multiplier λ is used to build a functional W as:

$$W[\rho, \lambda] = \min_{\rho} \max_{\lambda} [E[\rho(\mathbf{r})] + \lambda(\int_{\Omega} \rho(\mathbf{r}) d^3r - N)]. \tag{3.10}$$

For a given restriction with N value in a Ω space, the energy of the whole system is computed by adding the energy of the constraint to the energy of the system without constraints ($E[\rho(\mathbf{r})]$). The density satisfies the constraints but is also the one that minimizes the total energy of the system. Under the Becke's partition(3), the charge or spin population on atom A is weighted as a function of its distance from the nucleus by w_A (1 close to the nucleus of atom A and 0 close to the nucleus of any other atom), and defined as:

$$N_A = \int w_A^{Becke}(\mathbf{r}) \rho(\mathbf{r}) d^3r. \tag{3.11}$$

Therefore, several constraints over both, charge and spin, can be fulfilled simultaneously in the ground state. Despite its limitations and range of applicability, C-DFT has shown to be a valuable tool to describe charge-transfer states and spin localization.(4)

3.2.2 Time-dependent density functional theory

Time-dependent density functional theory (TD-DFT) is the analog of DFT to deal with excited states.(5; 6) The Runge-Gross theorem is the equivalent of the first

Hohenberg and Kohn's theorem, it relies on the existence of a one-to-one mapping between time-dependent electron density and the time-dependent external potential of an N-electron system that corresponds to a time-dependent Schrödinger equation.(7; 8)

The excitation energies (ω) in TD-DFT can generally be obtained as the solution of:

$$\begin{pmatrix} \mathbf{A} & \mathbf{B} \\ \mathbf{B} & \mathbf{A} \end{pmatrix} \begin{pmatrix} \mathbf{X} \\ \mathbf{Y} \end{pmatrix} = \omega \begin{pmatrix} \mathbf{1} & \mathbf{0} \\ \mathbf{0} & \mathbf{-1} \end{pmatrix} \begin{pmatrix} \mathbf{X} \\ \mathbf{Y} \end{pmatrix}. \tag{3.12}$$

In the linear-response framework (LR-TD-DFT)(9), this equation is known as the Casida's equation and represents one of the most used methods to obtain the TD-DFT energies.(5) Since the matrix (**A**-**B**) is positive definite for real orbitals, it can be simplified as:

$$(\mathbf{A}-\mathbf{B})^{1/2}(\mathbf{A}+\mathbf{B})(\mathbf{A}-\mathbf{B})^{1/2}\mathbf{Z} = \omega^2\mathbf{Z}, \tag{3.13}$$

where $\mathbf{Z} = (\mathbf{A}-\mathbf{B})^{-1/2}(\mathbf{X}+\mathbf{Y})$ contains the information about occupied orbitals rotating into virtual orbitals. Matrices **A** and **B** depend on the exchange-correlation functional used.

Further approximation to the Casida's equation is the Tamm-Dancoff approximation (TDA) in which the Equation 3.13 is simplify to $\mathbf{AX} = \omega\mathbf{X}$, neglecting the de-excitation contributions to the energy. Although, TDA is a simplification of TD-DFT, the results qualitatively compare with the LR-DFT ones.

TD-DFT is formally an exact theory that, provided one uses the universal exchange-correlation functional, can describe all excitations of a system. However, in practice, the explicit form of the functional is unknown. Under the adiabatic approximation,(10) TD-DFT cannot deal with multiple excitations and non-adiabatic effects, *e.g.*, conical intersections, are wrongly predicted.(11) Additionally, standard functionals are unable to recover the correct $\frac{1}{r}$ asymptotic behavior of electronic interactions,(12) which prevents the proper description of electronic transitions with weak hole/electron overlap, like in charge transfer excitations or Rydberg states.(4; 13) Schemes to address this problem have been proposed by modeling the decay of the exchange-correlation potential at short- and long-range separately.(14) In this approximation, the short-range exchange is treated with a local potential, while the long-range expression is represented by the "exact" exchange term.(13)

3.2.3 Spin-flip methods

An appropriate method to describe the ground state of strongly correlated systems, such as diradicals and polyradicals, must be able to deal with degeneracies and near-

degeneracies. In principle, non-dynamic (strong) correlation induce the needed for a multi-configurational ansatz that can be treated by multireference methodologies, where the ground state is described as the combination of two or more (semi-)equally important configurations (from the definition of diradicals, these methods offer an adequate scheme to characterize them). The complete active space-self consistent field (CASSCF)(15) method is one of the most extensively used methodologies to deal with non-dynamic correlation. Instantaneous (dynamic) electron correlation effect can be added a posteriori by means of multireference perturbation theory, *e.g.*, CASPT2.(16; 17) The main "problem" with these methodologies lies in their substantial computational cost, which makes them prohibitive in the study of medium to large size molecules.

As an alternative that allows the inclusion of both, dynamic and non-dynamic correlation, a family of methods based on the spin-flip operator was proposed to obtain a multi-configurational description through a single-reference ansatz.(18) The spin-flip (SF) approach was formally developed in 2001(19; 20) within the equation-of-motion (EOM) formalism to address the multi-configurational problems arising in the proper description of homolytic bond cleavage. In a given molecule with singlet ground state that is splitted in two fragments, each fragment takes one electron of the broken bond. At the equilibrium distance, one configuration might be enough to describe the system, that is, the closed-shell singlet configuration with two electrons in the bonding orbital. On the other hand, when the bond is elongated, the electronic population of the antibonding orbital gains importance in the description of the ground state of the system. At dissociation, (at least) two configurations are necessary to describe the electronic structure of the lowest singlet. On the other hand, these correlation effects are less important in the triplet state, which is well described by a single configuration along the entire bond dissociation.(19; 20) According to this, SF methodologies use a well-behaved high-spin configuration as a reference to construct correlated wave functions. From the high-spin reference, *e.g.*, the $M_s = 1$ of triplet, the target states are obtained by the action of an excitation operator flipping the spin of one electron, $\alpha \rightarrow \beta$:

$$|\Psi\rangle = \hat{R}^{SF} |\phi_0\rangle \,, \tag{3.14}$$

where $\hat{R}^{SF}$ is the SF excitation operator connecting the ϕ_0 (reference) state to the target state Ψ. Excitation operator $\hat{R}^{SF}$ can be expanded as a linear combination of creation and annihilation operators, as:

$$\hat{R}^{SF} = \sum_{l} \hat{R}^{SF}_{l} = \sum_{ia} r^{a}_{i} a^{\dagger}_{\beta} i_{\alpha} + \frac{1}{2!} \sum_{ijab} r^{ab}_{ij} a^{\dagger}_{\beta} b^{\dagger}_{\sigma} i_{\alpha} j_{\sigma} ... \tag{3.15}$$

where $\sigma = \alpha, \beta$. Truncation of Equation 3.15 to different levels of excitations give rise to an hierarchy of SF methods. From application of the SF operator over the

high-spin reference, a triplet for instance ($M_s = +1$), final states are those with $M_s = 0$, *i.e.*, singlets and triplets in Figure 3.1.

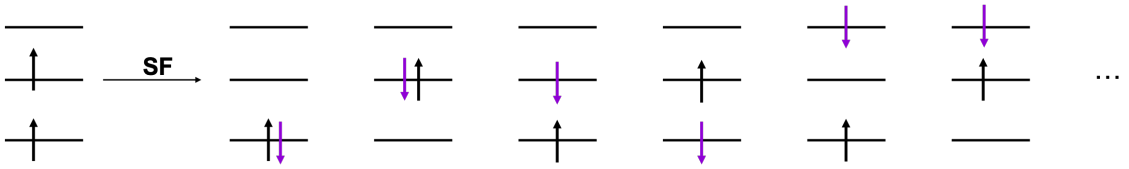

Figure 3.1: Target states obtained from the application of the SF operator (Equation 3.15) over a triplet reference of a system with two electrons in three orbitals. Figure adapted from reference (18).

Since its formulation in 2001, SF methods have been developed on top of well established wave function methodologies and in the DFT framework.(21) Spin-flip methodologies have been extensively used in the rationalization of bond-breaking process, determination of the diradical (polyradical) character, evaluation of non-linear optical properties, and description of photophysical processes as singlet fission.

3.2.3.1 Restricted active space - spin flip

The expansion in Equation 3.15 can be rearranged in series of excitation levels. In this way an active space where all possible configurations involving n_e electrons can be defined. Similarly to CASSCF methods, electrons included in the active space are those with higher reactivity, or more important in the description of the molecular electronic structure. By extension, two more spaces can be defined, one containing double occupied orbitals with less reactive electrons called occupied space; while the other one groups the virtual orbitals, and is referred to as the virtual subspace. Within the restricted active space (RAS), these spaces are considered as the RAS I, RAS II (active, A) and RAS III, see Figure 3.2a. In these terms, the spin flip operator is expressed as:

$$\hat{R}^{SF} = \sum_{\lambda \in A} \hat{R}_\lambda^{\Delta M_s = -n} + \sum_{\lambda \in h} \hat{R}_\lambda^{\Delta M_s = -n} + \sum_{\lambda \in p} \hat{R}_\lambda^{\Delta M_s = -n} + \sum_{\lambda \in hp}^{\Delta M_s = -n} \hat{R}_\lambda^{\Delta M_s = -n} + ..., \quad (3.16)$$

where configurations in $\sum_{\lambda \in h} \hat{R}_\lambda^{\Delta M_s = -n}$ are excitations from one doubly occupied orbital in RAS I space to the active space, and configurations in $\sum_{\lambda \in p} \hat{R}_\lambda^{\Delta M_s = -n}$ corresponds to excitations from the active space to one empty orbital of the RAS III space.

In this manner, the SF operator defines the RAS-SF method.(22; 23) In general, the active space is determined by the high-spin reference and the number of spins flipping; then, in a RAS-nSF calculation with ($2n$+1)-tuplet high spin reference, the minimum active space should contain $2n$ electrons and $2n$ spin-orbitals. RAS-SF is

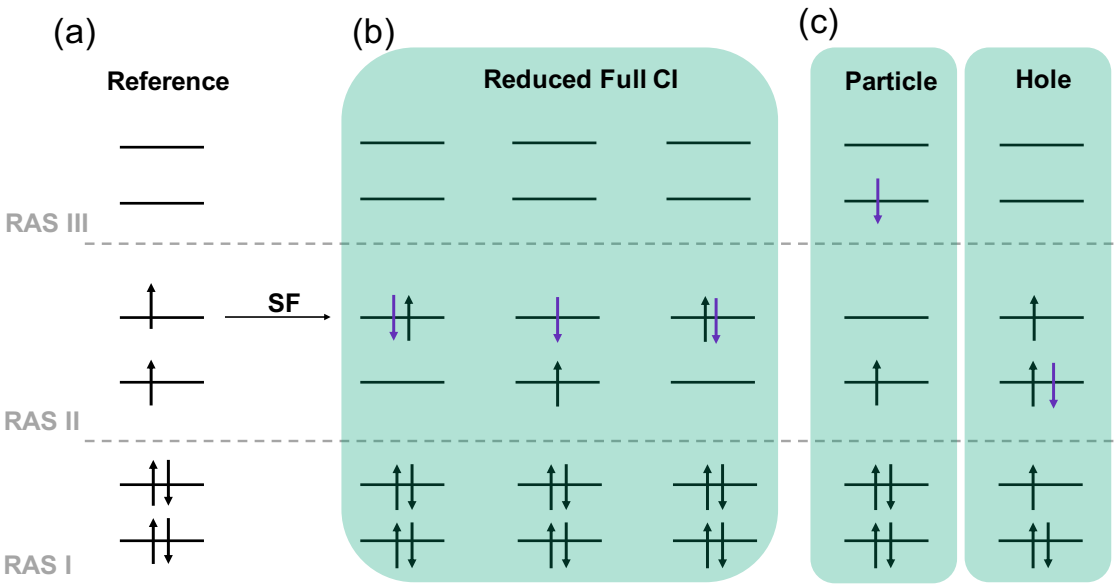

Figure 3.2: Schematic RAS-2SF subspaces partitioning, with 2 orbitals in the active space and a triplet as high spin reference (a). Resulting configurations in the active (b), and hole and particle spaces (c). Figure adapted from reference (22).

a single-reference method, which allows excitations illustrated in Figure 3.1. Within the *hole* and *particle* approximation in RAS-nSF, Equation 3.16 is truncated after the third term on the right side. The first one represents the full configuration interaction within the active space (Figure 3.2b), while the second and third ones allow monoexcitations out of the active space, as illustrated in Figure 3.2c. As a consequence, the spin completeness of the method is ensured, which in general is a problem for SF methodologies.(18)

RASn-SF represents a good compromise for dealing with non-dynamic correlation in (quite) large systems with an affordable computational cost. As demonstrated in this thesis (and in a large quantity of examples in the literature(24; 23)), RAS-nSF method is successfully used to characterize diradicals (polyradicals) and different excited state processes as singlet fission. Despite the advantages of RAS-SF method (and RAS-CI methos in general), one of its better-recognized deficiencies is the lack of dynamic correlation. In 2018, D. Casanova(25) proposed an hybrid method (RAS-srDFT) as a way to include dynamic correlation in RAS-CI methods, which consists in splitting the Coulomb operator (electron-electron repulsion, $\hat{V}_{ee}$) in long ($\hat{V}_{ee}^{lr,\mu}$) and short-range ($\hat{V}_{ee}^{sr,\mu}$) components. While the long-range is approximated by the wave function, the short-range term is provided by DFT. The energy of RAS-srDFT is obtained as:

$$E^{\mathrm{WFT}-sr\mathrm{DFT}} = \min_{\Psi^\mu}[\langle\Psi^\mu|\,\hat{T} + \hat{V}_{ne} + \hat{V}_{ee}^{lr,\mu}\,|\Psi^\mu\rangle + E_{Hxc}^{sr,\mu}[\rho]], \tag{3.17}$$

where the RAS-SF wave function is mixed with DFT short-range exchange-correlation

term to include dynamic correlation in RAS-CI methods.

3.2.3.2 Spin flip time-dependent density functional theory

The spin flip methodology has also been introduced in the framework of time-dependent density functional theory (SF-TD-DFT) to address some of the drawbacks of LR-TD-DFT such as the inability to treat states in which the adiabatic coupling is important.

The best performance of SF-TD-DFT predicting singlet-triplet energy gaps in diradicaloids is obtained with functionals with large amount of HF exchange like BHHLYP(26) or PBE50(27) (with 50% HF exchange).

3.3 Computational tools for the characterization of electronic states

Besides the computation of electronic states of molecules and their relative energies, the rationalization of their physical and chemical properties requires a detailed description of their electronic structure nature. In addition to the calculation of properties through well-defined operators, some useful descriptors can be established to describe non-observable properties, *e.g.*, the radical character, which is the core of this thesis. In the following, I explain the indices that I will use to describe the radical nature of the systems explored in the next chapters.

3.3.1 Diradical and polyradical character indices

Probably the most extensively used indices to quantify the di- and polyradical character of electronic states are the Yamaguchi ones.(28) Thy are based on the electronic occupation of the natural orbitals and defined as:

$$y_i = n_{\mathrm{LUNO}+i}. \tag{3.18}$$

Since $HONO\text{-}i$ + LUNO+$i = 2$, y_i represents a measure of the electrons missing in HOMO $- i$ for being doubly occupied. Then, y_i can take values between 0 and 1 and, when $y_i = 0, \forall i$ the system is closed-shell, while $y_i = 1$ represents a perfect (di or tri, tetra or penta, etc) radical. Concretely, for compounds with even number of electrons, y_0 is the index related to the diradical character, y_1 to the tetraradical character, y_2 to the hexaradical character, and so on. Polyradical character in systems with odd number of electrons are triradical (y_0), pentaradical (y_1), heptaradical (y_2), etc.

3.3.2 Unpaired number of electrons

In open-shell systems, the number of unpaired electron is a relevant quantity offering clues regarding the presence of diradicals or beyond. For instance, a singlet state with two unpaired electrons can be classified as a singlet diradical.

In any electronic state, the number of electrons can be computed by means of the occupation number of the natural orbitals (in the cases treated in this thesis, they are obtained from the one-particle density matrix extracted from RAS-SF calculations). The linear Head-Gordon equation(29) to quantify the number of unpaired electrons in a system is:

$$\mathrm{N}_u = \sum_i (1 - \mathrm{abs}(1 - n_i)), \tag{3.19}$$

where, n_i is the natural occupation number of the natural orbital i. n_i can take values between 0 and 2; in the extremes, $n_i = 0$ (2), the orbital i is totally empty (doubly occupied) and does not contribute to N_u. If $n_i = 1$, there is just one electron in such orbital that can be associated to an orbital holding a radical.

The spatial distribution of the unpaired electrons can be obtained through the graphical representation of N_u, that is, the fractional orbital density (FOD, as the graphical tool developed within the DFT framework).(30; 31)

$$\rho^{FOD}(\mathbf{r}) = \sum_i^M (\delta_1 - \delta_2 f_i)|\phi_i(\mathbf{r})|^2, \tag{3.20}$$

which by integration over all the space gives the N_u value (Equation 3.19).

3.3.2.1 Fragment-based wave function analysis

In the study of photophysical processes in dimers or aggregates, it is important to determine the electronic character of the excited states and the contribution of monomers to the collective properties. To describe the adiabatic excited states of the complex in terms of the diabatic states in the monomers, I used an approach developed by Luzanov, Casanova and Krylov,(32; 33) in which the wave function of the dimer or (oligomer) is computed and then deconstructed in terms of the individual chromophores under a super-molecule scheme. In the case of RAS-SF, the canonical orbitals obtained from the SCF procedure are localized in fragments before the correlated calculation takes place. The total wave function is written as:

$$|\Psi\rangle = |\Psi^{LE}\rangle + |\Psi^{ME}\rangle + |\Psi^{CT}\rangle\,. \tag{3.21}$$

Every term on the right side of Equation 3.21 is determined by means of charge and spin cumulants identifying unambiguously local excitations (LE), charge transfer states (CT), and multiple excitation (ME).

Localized excitations in a dimer can be written in term of specific contributions from each monomer as:

$$|\Psi^{LE}\rangle = c_A\,|A^*B\rangle + c_B\,|AB^*\rangle\,, \tag{3.22}$$

where A^*B are all possible combinations of A in an excited state and B in the ground state (or the opposite AB^*). In the same way charge resonance configurations are weighted as:

$$|\Psi^{CR}\rangle = t_{AB}\,|A^+B^-\rangle + t_{BA}\,|A^-B^+\rangle\,. \tag{3.23}$$

Finally, states in which both monomers are simultaneously excited giving rise to multiexcitations are described as:

$$|\Psi^{ME}\rangle = d_{AB}\,|A^*B^*\rangle\,. \tag{3.24}$$

By the combination of Equations 3.22, 3.23 and 3.24 in Equation 3.21 every adiabatic state can be expressed in terms of diabatic states:

$$|\Psi\rangle = c_A\,|A^*B\rangle + c_B\,|AB^*\rangle + t_{AB}\,|A^+B^-\rangle + t_{BA}\,|A^-B^+\rangle + d_{AB}\,|A^*B^*\rangle\,, \tag{3.25}$$

where $|c_A|^2+|c_B|^2+|t_{AB}|^2+|t_{BA}|^2+|d_{AB}|^2 = 1$ includes all the possible contribution of diabatic states to the adiabatic wave function.

Bibliography

[1] F. A. Berezin and M. Shubin, *The Schrödinger Equation*, vol. 66 9401131546. Springer Science Business Media, 2012.

[2] Q. Wu and T. V. Voorhis, "Constrained density functional theory and its application in long-range electron transfer," *J. Chem. Theory Comput.*, vol. 2, no. 3, pp. 765–774, 2006.

[3] A. D. Becke, "A multicenter numerical integration scheme for polyatomic molecules," *The Journal of Chemical Physics*, vol. 88, no. 4, pp. 2547–2553, 1988.

[4] B. Kaduk, T. Kowalczyk, and T. Van Voorhis, "Constrained density functional theory," *Chemical Reviews*, vol. 112, no. 1, pp. 321–370, 2012.

[5] M. E. Casida and M. Huix-Rotllant, "Progress in time-dependent density-functional theory," *Annual review of physical chemistry*, vol. 63, pp. 287–323, 2012.

[6] R. Van Leeuwen, "Key concepts in time-dependent density-functional theory," *International Journal of Modern Physics B*, vol. 15, no. 14, pp. 1969–2023, 2001.

[7] E. Runge and E. K. Gross, "Density-functional theory for time-dependent systems," *Physical Review Letters*, vol. 52, no. 12, p. 997, 1984.

[8] T.-c. Li and P.-q. Tong, "Hohenberg-kohn theorem for time-dependent ensembles," *Physical Review A*, vol. 31, no. 3, p. 1950, 1985.

[9] M. E. Casida, "Propagator corrections to adiabatic time-dependent density-functional theory linear response theory," *The Journal of chemical physics*, vol. 122, no. 5, p. 054111, 2005.

[10] J. I. Fuks, L. Lacombe, S. E. Nielsen, and N. T. Maitra, "Exploring non-adiabatic approximations to the exchange–correlation functional of tddft," *Physical Chemistry Chemical Physics*, vol. 20, no. 41, pp. 26145–26160, 2018.

[11] B. G. Levine, C. Ko, J. Quenneville, and T. J. MartÍnez, "Conical intersections and double excitations in time-dependent density functional theory," *Molecular Physics*, vol. 104, no. 5-7, pp. 1039–1051, 2006.

[12] T. Yanai, D. P. Tew, and N. C. Handy, "A new hybrid exchange-correlation functional using the coulomb-attenuating method (cam-b3lyp)," *Chemical Physics Letters*, vol. 393, no. 1, pp. 51–57, 2004.

[13] N. Kuritz, T. Stein, R. Baer, and L. Kronik, "Charge-transfer-like $\pi \rightarrow \pi^*$ excitations in time-dependent density functional theory: A conundrum and its solution," *Journal of chemical theory and computation*, vol. 7, no. 8, pp. 2408–2415, 2011.

[14] Y. Tawada, T. Tsuneda, S. Yanagisawa, T. Yanai, and K. Hirao, "A long-range-corrected time-dependent density functional theory," *The Journal of chemical physics*, vol. 120, no. 18, pp. 8425–8433, 2004.

[15] B. O. Roos, "The complete active space self-consistent field method and its applications in electronic structure calculations," *Advances in chemical physics*, vol. 69, pp. 399–445, 1987.

[16] K. Andersson, P. A. Malmqvist, B. O. Roos, A. J. Sadlej, and K. Wolinski, "Second-order perturbation theory with a casscf reference function," *The Journal of Physical Chemistry*, vol. 94, no. 14, pp. 5483–5488, 1990.

[17] M. Schreiber, M. R. Silva-Junior, S. P. A. Sauer, and W. Thiel, "Benchmarks for electronically excited states: Caspt2, cc2, ccsd, and cc3," *The Journal of Chemical Physics*, vol. 128, no. 13, p. 134110, 2008.

[18] D. Casanova and A. I. Krylov, "Spin-flip methods in quantum chemistry," *Phys. Chem. Chem. Phys.*, vol. 22, pp. 4326–4342, 2020.

[19] A. I. Krylov, "Size-consistent wave functions for bond-breaking: the equation-of-motion spin-flip model," *Chemical Physics Letters*, vol. 338, no. 4-6, pp. 375–384, 2001.

[20] A. I. Krylov, "Spin-flip configuration interaction: an electronic structure model that is both variational and size-consistent," *Chemical Physics Letters*, vol. 350, no. 5-6, pp. 522–530, 2001.

[21] Y. Shao, M. Head-Gordon, and A. I. Krylov, "The spin–flip approach within time-dependent density functional theory: Theory and applications to diradicals," *The Journal of chemical physics*, vol. 118, no. 11, pp. 4807–4818, 2003.

[22] D. Casanova and M. Head-Gordon, "Restricted active space spin-flip configuration interaction approach: theory, implementation and examples," *Phys. Chem. Chem. Phys.*, vol. 11, pp. 9779–9790, 2009.

[23] D. Casanova, "Efficient implementation of restricted active space configuration interaction with the hole and particle approximation," *J. Comput. Chem.*, vol. 34, no. 9, pp. 720–730, 2013.

[24] D. Casanova, "Electronic structure study of singlet fission in tetracene derivatives," *Journal of Chemical Theory and Computation*, vol. 10, no. 1, pp. 324–334, 2014.

[25] D. Casanova, "Short-range density functional correlation within the restricted active space ci method," *The Journal of Chemical Physics*, vol. 148, no. 12, p. 124118, 2018.

[26] A. Nakata, Y. Imamura, T. Otsuka, and H. Nakai, "Time-dependent density functional theory calculations for core-excited states: Assessment of standard exchange-correlation functionals and development of a novel hybrid functional," *The Journal of Chemical Physics*, vol. 124, no. 9, p. 094105, 2006.

[27] Y. A. Bernard, Y. Shao, and A. I. Krylov, "General formulation of spin-flip time-dependent density functional theory using non-collinear kernels: Theory, implementation, and benchmarks," *The Journal of Chemical Physics*, vol. 136, no. 20, p. 204103, 2012.

[28] K. Yamaguchi, *Self-Consistent Field: Theory and Applications*, pp. 727–828. Elsevier, 1990.

[29] M. Head-Gordon, "Characterizing unpaired electrons from the one-particle density matrix," *Chem. Phys. Lett.*, vol. 372, no. 3-4, pp. 508–511, 2003.

[30] C. A. Bauer, A. Hansen, and S. Grimme, "The fractional occupation number weighted density as a versatile analysis tool for molecules with a complicated electronic structure," *Chemistry–A European Journal*, vol. 23, no. 25, pp. 6150–6164, 2017.

[31] S. Grimme and A. Hansen, "A practicable real-space measure and visualization of static electron-correlation effects," *Angewandte Chemie International Edition*, vol. 54, no. 42, pp. 12308–12313, 2015.

[32] A. V. Luzanov, D. Casanova, X. Feng, and A. I. Krylov, "Quantifying charge resonance and multiexciton character in coupled chromophores by charge and spin cumulant analysis," *J. Chem. Phys.*, vol. 142, no. 22, p. 224104, 2015.

[33] D. Casanova and A. I. Krylov, "Quantifying local exciton, charge resonance, and multiexciton character in correlated wave functions of multichromophoric systems," *J. Chem. Phys.*, vol. 144, no. 1, p. 014102, 2016.

Chapter 4

Polycyclic aromatic hydrocarbon diradicals

Ever since its first experimental isolation in 2004(1), graphene has attracted immense interest among the scientific community, touted as a miracle material owing to its extraordinary physical and mechanical properties.(2; 3) Graphene can be viewed as an extended sheet of fused benzene rings. In this way, finite compounds with honeycomb-like structures can be considered as graphene derivatives, such as buckyballs, tubes, sheets and multidimensional graphene-fragments (0D, 1D and 2D, and 3D structures obtained as stacked graphene layers).(4; 5) In the nanoscale (1-100 nm), 2D-graphene fragments are known as graphene nanofragments or nanoflakes (GNFs), also referred as to alternant polycyclic aromatic hydrocarbons (PAHs).(6) The wide variety of shapes that graphene derivatives adopt, in particular GNFs, together with their emerging molecular properties make them a fancy research topic. Their value in diverse fields has been demonstrated: optoelectronics, photocatalysis, energy storage, medical and biological applications, environmental sciences, and quantum computing.(7; 8; 8; 9) Most of these applications are related to electronic and magnetic properties, and are dictated by the topology and edge shape together with the size of the nanostructure. For instance, in GNFs, the stability of the ground state is directly related to the geometrical arrangement of the benzene rings and the shape of their edges, zigzag or armchair, (Figure 4.1) modulate their electronic structure.(5) GNFs with an armchair edge are closed-shell systems, while zigzag-edged GNFs have open-shell configuration with potential to exhibit high-spin ground state. Open-shell GNFs are very interesting as the main component of optoelectronic devices but, as a consequence of their radical (radicaloid) nature, their synthesis is cumbersome and they show poor stability.

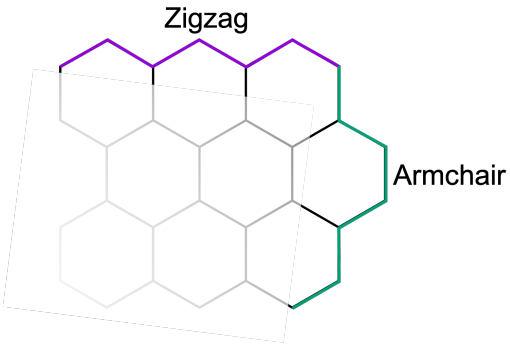

Figure 4.1: Armchair (green) and zigzag (purple) edges of a GNFs.

Through this chapter, I present the detailed electronic description of representative 1D and 2D GNF systems. The arising of radical character and its dependence on topology are rationalised in depth. First, a general picture is obtained by means of simple electronic structure analysis like Hückel model, Ovchinnikov's rule, and Clar's sextet rule(10) related to their classification as Kekulé and non-Kekulé structures. In a second time, powerful electronic structure calculations, namely, restricted active spin-flip method (RAS-SF), provide the appropriated description of the radical nature and correlation effects of these systems.

In the first section, the intricacies of the electronic properties of the smallest members of the triangular graphene nanofragments (TGNFs) family in their ground and low-lying excited states are fully unravelled. Radical and diradical nature of these systems is described and rationalized in detail. Additionally, the modulation of their electronic and magnetic properties is explored by means of selective boron or nitrogen substitution at carbon sites as well as by hydrogen saturation. The second part of the chapter explores the nature of electron-correlation effects in carbon nanobelts and linear oligoacenes.

4.1 Triangular Graphene Nanofragments

TGNFs consist in benzene rings fused following D_{3h} symmetry, with all edges exhibiting a zigzag pattern that allows them to hold open-shell character.(11) Analysis of the Clar's resonance structure of the small TGNFs shows the presence of at least one unpaired electron (Figure 4.2).(12) Consequently, they are considered as the smallest open-shell non-Kekulé systems, and it is expected that all members of this family possess a high-spin ground state. In the following, the smallest members of the family, phenalenyl (**1**) and triangulene (**2**), are considered to discuss the implications of their triangular shape and resultant topology over radical and diradical character. The modulation of their electronic structure is then addressed via inser-

tion of heteroatoms and hydrogenation.

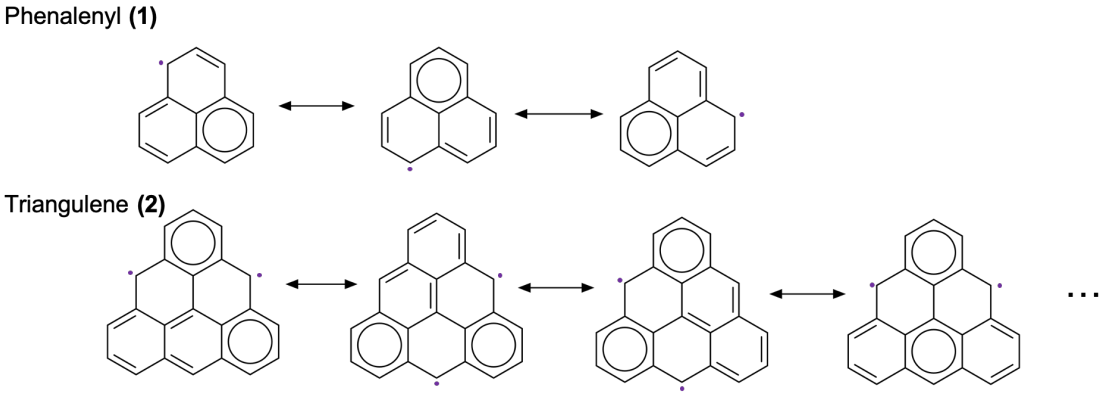

Figure 4.2: Clar's resonance structures in phenalenyl (**1**) and triangulene (**2**).

4.1.1 Pristine phenalenyl and triangulene

The smallest structure of the TGNF family, phenalenyl (**1**), is formed by three fused benzene rings sharing a central carbon atom and exhibits an odd number of electrons (13 π-electrons), thus inevitably resulting in a radical system. Ovchinnikov's rule predicts a spin-doublet ground state (Figure 4.3a). This prediction is supported by the Hückel model, which shows one unpaired electron in the $1^2A_1'$ ground state (Figure 4.3b).

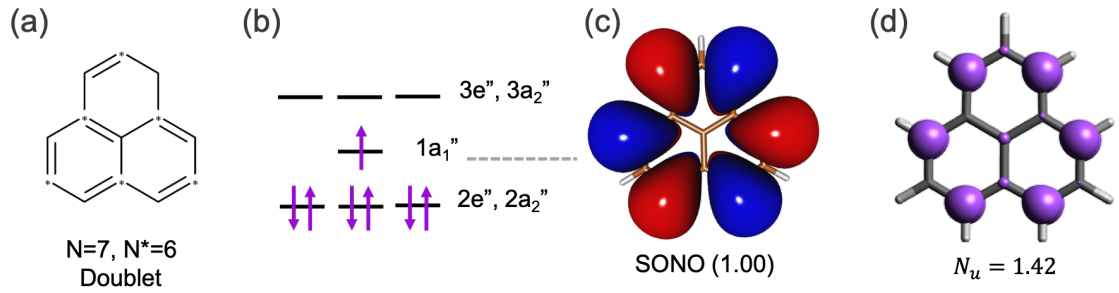

Figure 4.3: Characterization of the ground state of **1**. Ovchinnikov's rule prediction (a), Hückel diagram (b), Frontier Natural Orbital and occupation numbers (c), and FOD and number of unpaired electrons (d) of the ground state. (c) and (d) were computed at RAS-SF level.

The next non-Kekulé triangular PAH, triangulene (**2**), differs from **1** by the addition of an extra row of benzene rings. While the molecular symmetry is not altered, **2** possesses an even number of carbon atoms and 22 π-electrons. The Ovchinnikov's

rule and Hückel model predict a spin-triplet ground state ($1^3A_1'$, Figure 4.4a and b). The high-spin multiplicity of the ground state of **2** has been investigated theoretically and observed experimentally in its derivatives.(13; 14; 15; 16)

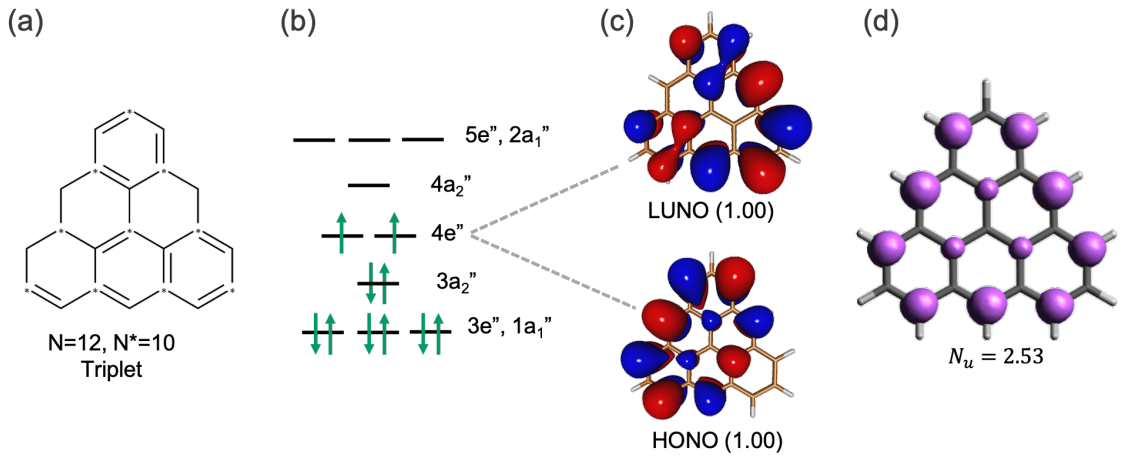

Figure 4.4: Characterization of the ground state of **2**. Ovchinnikov's rule prediction (a), Hückel diagram (b), Frontier Natural Orbital and occupation numbers (c), and FOD and number of unpaired electrons (d) of the ground state. (c) and (d) were computed at RAS-SF level.

It is interesting to notice that both Hückel MO energy diagrams present degeneration degrees beyond the one dictated by the molecular D_{3h} symmetry, *i.e.*, there are up to three degenerate π-orbitals, when the maximum dictated by molecular symmetry is two. Such triple degeneration is triggered by the symmetry of the Hückel Hamiltonian. By construction, only interactions with first neighbors are considered, and the Hamiltonian symmetry is consequently higher than the molecular one.(17) Nevertheless, orbital degeneracy is lifted when performing *ab initio* calculations.

The $2p_z$ orbital on the central carbon atom of **1** and **2** correspond to the A_2'' irreducible representation (D_{3h} point group). Then, this atom can only contribute to π-orbitals with that symmetry, *i.e.*, a_2'' molecular orbitals. In both systems, the electronic occupation of Hückel π-orbitals thus predicts the lack of unpaired electron density on the central atom, while $1a_1''$ and $4e''$ π-orbitals are singly occupied in **1** and **2** respectively (Figure 4.3b and 4.4b).

RAS-SF calculations provide further insights on the ground state radical nature of **1** and **2**. Singly occupied natural orbital (SONO) of **1**, depicted in Figure 4.3c, belongs to the A_1'' irreducible representation, as predicted by Hückel model, and is localized over the molecular edges. Qualitatively, the same picture is offered by the FOD of the $1^2A_1'$ state (Figure 4.3d). Similarly, the main contribution to the FOD,

and consequently to N_u, of **2** is given by HONO and LUNO shapes and occupation numbers (Figure 4.4c). Actually, both E'' irreducible representation are localized mostly over the edges of **2** with small contribution of inner carbons, apart from the central one. Straightforward comparison of FOD distribution of **1** and **2** with their respective Ovchinnikov's representation pointed out the bilattice-like motif of TGNFs, where carbon atoms on the sublattice with more C atoms contribute to the unpaired electron density (N in Figure 4.3a and 4.4a).

The lowest excited states of **1** correspond to $1^2E''$ and $1^2A_2''$ with vertical excitation energy of 2.95 and 3.29 eV, respectively (Table 4.1), in excellent agreement with MR-CI energies.(18) Doubly degenerate $1^2E''$ state corresponds to the promotion of the edge electrons ($2e'' \rightarrow 1a_1''$) whereas the $1^2A_2''$ state contains a partial displacement of central electrons to the molecular contour, as obtained from the $2a_2'' \rightarrow 1a_1''$ electronic excitation.

mol.	state	ΔE	N_u
1	$1^2A_1''$	-	1.42
	$1^2E''$	2.95	2.17
	$1^2A_2''$	3.29	1.87
2	$1^3A_2'$	-	2.53
	$1^1E'$	0.57	2.54
	$1^3E'$	2.82	3.44

Table 4.1: Low-lying states of **1** and **2**, energy gaps (in eV) and unpaired electron numbers (N_u) computed at the RAS-SF/6-311G(d,p) level.

Considering now compound **2**, the single electron occupation of the $4e''$ orbitals in **2** results in a four dimensional space with A_1', A_2' and E' symmetries. The antisymmetric spatial representation component of the direct product $E \otimes E$ corresponds to the ground state triplet ($1^3A_2'$), while A_1' and E' are linked to spin-singlet excited states (Table 4.1).

The energy gap to the lowest excited singlet of **2** ($1^1E'$) is computed at 0.57 eV, again in line with values obtained by means of other correlated methods (0.56-0.84 eV) (18; 16). This doubly degenerate singlet is mainly obtained as the $(3a_2'')^2(4e'')^2(4a_2'')^0$ configuration ($\sim 71\%$) with both states resulting from the single electronic occupation of $4e''$ orbitals. The fractional occupation density is mainly localized on the molecular edges (Figure 4.5), resembling qualitatively the one exhibited by the triplet ground state (Figure 4.4).

The triplet-triplet transition energy to the first excited triplet of **2** ($1^3E'$ state) is computed at 2.82 eV, and involves electronic configurations with the partial oc-

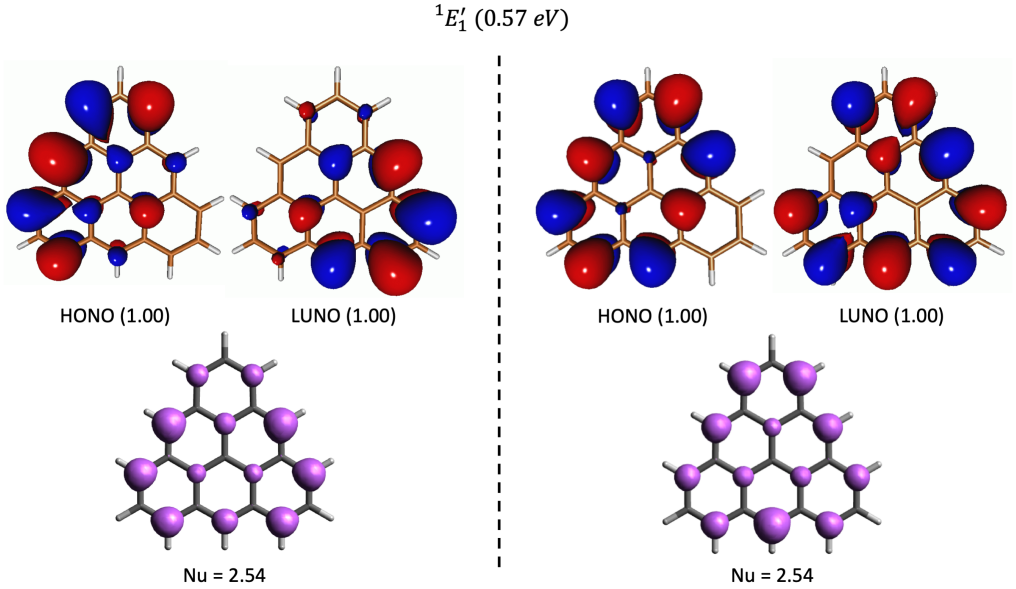

Figure 4.5: Frontier Natural Orbitals with their occupation numbers, and FOD and N_u of $^1E_1'$ state of **2**.

cupation of the $3a_2''$ and $4a_2''$ orbitals, meaning that the localization of the FOD on the central carbon is not symmetry forbidden for this state.

4.1.2 B-doped and N-doped TGNF

In light of the above characterization of **1** and **2**, doping of these systems by substitution of carbon atoms with electron-donating and electron-accepting elements can be envisioned as an efficient tool to tune their electronic and magnetic properties.(19) Notably, experimental methods devoted to the controlled substitution of carbon atoms by other species have been developed since the early studies on graphene, especially in the synthesis of N- and B-doped graphene.(20; 21; 22; 23; 24) It has also been evidenced that the electronic structure characteristics of these compounds not only depend on the dopant concentration but also on the doping symmetry pattern.(19)

Next, I explore the changes in the electronic properties of **1** and **2** upon replacing 1, 2, or 3 C sites with electron-donating (N atoms) or electron-accepting (B atoms) elements (Figure 4.6). In order to preserve the chemical composition at the edges, all substitutions were performed over the inner carbons.

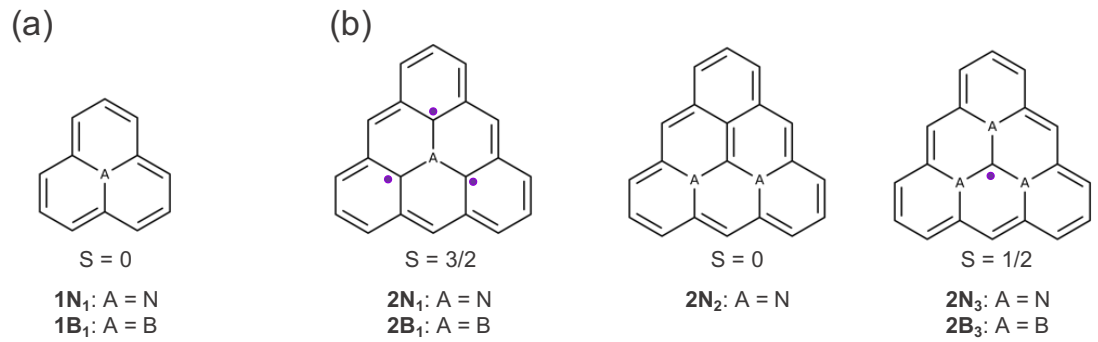

Figure 4.6: N- and B-doped derivatives of **1** (a) and **2** (b) systems with the spin predicted by Ovchinnikov's rule.

4.1.2.1 Phenalenyl derivatives

$\mathbf{1B}_1$ and $\mathbf{1N}_1$ are the monodoped derivatives of phenalenyl. While both systems conserve the D_{3h} symmetry of their pristine equivalent, the electronegativity difference of B and N atoms with respect to C results in slightly longer bond lengths in $\mathbf{1B}_1$ and shorter ones in $\mathbf{1N}_1$ (B-C > C-C > N-C).

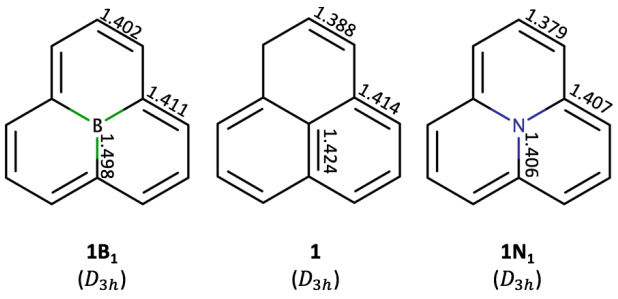

Figure 4.7: Bond lengths in Å in $\mathbf{1B}_1$ (left), **1** (center) and $\mathbf{1N}_1$ (right) systems.

The heteroatom substitution of the central carbon modifies the number of π-electrons with respect to **1**. In the application of the Ovchinnikov's rule to $\mathbf{1B}_1$ and $\mathbf{1N}_1$, the central site is not considered in the evaluation of carbon atoms belonging to opposite sublattices and ground state spin-singlet systems are predicted. However, this simplification cannot account for the electronic structure details of the doped systems, such as the diradical (or diradicaloid) character of the molecule that is dictated by the gap between occupied and virtual orbitals.

Since the $2p_z$ orbital of boron (nitrogen) is higher (lower) in energy than the carbon's counterpart, the a_2'' frontier π MOs are destabilized (stabilized) in $\mathbf{1B}_1$ ($\mathbf{1N}_1$), as obtained by the Hückel model (Figure 4.8). The energy shift of a_2'' orbitals

might eventually result in small HOMO-to-LUMO energy gaps inducing open-shell character to the ground state wave function.

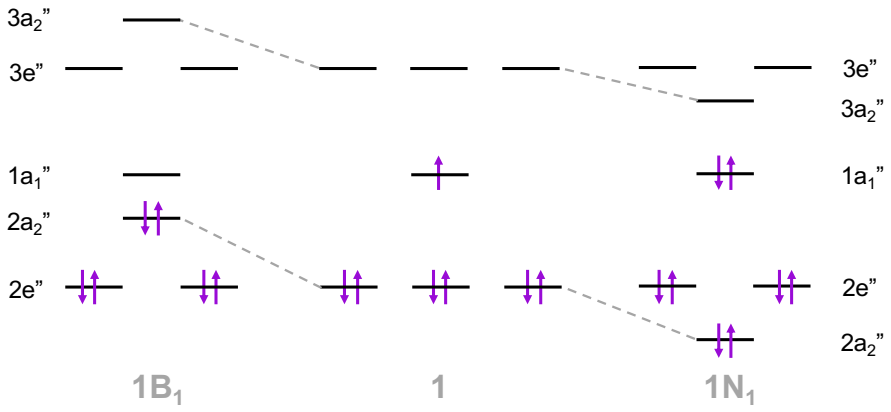

Figure 4.8: Hückel diagram of π-orbitals of $\mathbf{1N}_1$ and $\mathbf{1B}_1$.

Electronic structure calculations confirm the ground state spin-singlet nature of $\mathbf{1B}_1$ and $\mathbf{1N}_1$, and predict singlet-triplet energy differences smaller than 1 eV (Table 4.2). The quite small energy gap to the lowest triplet state suggest a partial open-shell character of molecular ground state singlets, both doped derivatives showing moderate diradical (or diradicaloid) character that approximately corresponds to half unpaired electron as measured by N_u values of 0.63 and 0.55 for $\mathbf{1B}_1$ and $\mathbf{1N}_1$, respectively. Differently to **1**, the unpaired electron density emerges, for the most part, from the fractional occupation of a_1'' and a_2'' orbitals. The moderate amount of unpaired electrons in substituted systems is almost equally distributed between all contour carbons with contributions from the central doping atom, especially in $\mathbf{1N}_1$ (Figure 4.9).

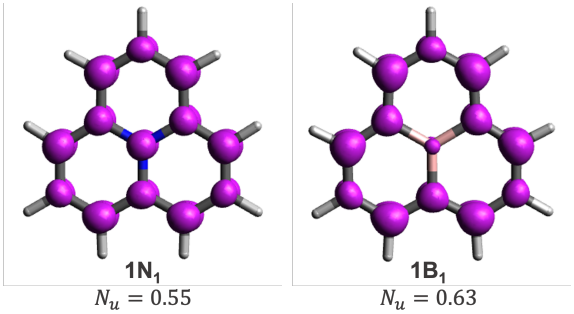

Figure 4.9: FOD of the ground state of $\mathbf{1N}_1$ and $\mathbf{1B}_1$.

The lowest excited singlet state of the doped phenalenyls is mainly obtained as the HOMO-to-LUMO single electron excitation ($a_1'' \rightarrow a_2''$ for $\mathbf{1B}_1$ and $a_2'' \rightarrow a_1''$ for $\mathbf{1N}_1$) and belongs to the same spatial symmetry as the lowest triplet (A_2' representation). The computed energy of $1^1A_2'$ is systematically lower than $1^3A_2'$, which is the inverse of the common singlet/triplet state ordering but can be rationalized as the result of two effects:

i) The weak HOMO/LUMO exchange, K_{hl}, expressed as:

$$K_{hl} \simeq \frac{E_S - E_T}{2}. \tag{4.1}$$

For both **1** derivatives, $\frac{\Delta E_{ST}}{2} \sim -0.06$ eV is computed at RAS-SF level. A better approximation of K_{hl} is obtained by the uncorrelated Single Excitation Configuration Interaction (CIS) method.(25; 26) At CIS/6-31G* level of theory, $K_{hl} = 0.14$ eV and 0.16 eV for $\mathbf{1B}_1$ and $\mathbf{1N}_1$, respectively. These small values are due to the poor spatial overlap between a_1'' and a_2'' orbitals as illustrated in the Figure 4.10.

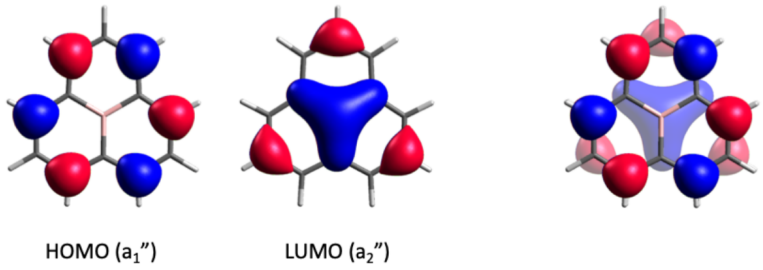

Figure 4.10: Frontier molecular orbitals (a_1'' and a_2'') of $\mathbf{1B}_1$ (left) and their superposition (right).

ii) Mixing of other configurations: the main configuration of $1^1A_2'$ and $1^3A_2'$ states corresponds to the single electron occupation of a_1'' and a_2'' orbitals ($\sim 85\%$). However, the wave function of the singlet state is mixed with other open-shell electronic configurations involving $3e''$ orbitals, helping to stabilize it with respect to the $1^3A_2'$ state (Table 4.2).

mol.	state	ΔE_{ST}	N_u	configuration	contributions (%)
$\mathbf{1B}_1$	$1^1A_2'$	0.66	2.40	$(2e'')^4(2a_2'')^1(1a_1'')^1(3e'')^0(3a_2'')^0$	84.13
				$(2e'')^3(2a_2'')^1(1a_1'')^1(3e'')^1(3a_2'')^0$	2.24
				$(2e'')^3(2a_2'')^1(1a_1'')^1(3e'')^1(3a_2'')^0$	2.24
	$1^3A_2'$	0.79	2.36	$(2e'')^4(2a_2'')^1(1a_1'')^1(3e'')^0(3a_2'')^0$	85.46
$\mathbf{1N}_1$	$1^1A_2'$	0.85	2.40	$(2e'')^4(2a_2'')^2(1a_1'')^1(3a_2'')^1(3e'')^0$	84.25
				$(2e'')^4(2a_2'')^1(1a_1'')^1(3a_2'')^1(3e'')^1$	2.10
				$(2e'')^3(2a_2'')^2(1a_1'')^1(3a_2'')^1(3e'')^1$	2.09
	$1^3A_2'$	0.96	2.36	$(2e'')^4(2a_2'')^2(1a_1'')^1(3a_2'')^1(3e'')^0$	85.76

Table 4.2: Low-lying states of **1** and **2**, energy gaps (in eV), unpaired electron numbers (N_u) and the main configuration contributions, computed at the RAS-SF/6-311G(d,p) level.

4.1.2.2 Triangulene derivatives

Triangulene allows different possible doping patterns, preserving its D_{3h} symmetry or not, by replacing one, two or three carbon sites (Figure 4.6b). The boron and nitrogen mono-substituted derivatives, $\mathbf{2B}_1$ and $\mathbf{2N}_1$, hold odd numbers of π-electrons. DFT results indicate a doublet ground state with adiabatic energy gaps to the quartet state (ΔE^{ad}_{DQ}) of 4.2 and 11.2 kcal/mol respectively, in disagreement with the Ovchinnikov's rule, which predicts a preference for the spin-quartet multiplicity.

Stabilization of the doublet state in $\mathbf{2B}_1$ and $\mathbf{2N}_1$ is driven by a Jahn-Teller distortion(27; 28; 29) that lowers the molecular symmetry to C_{2v}. The high-spin quartet of the D_{3h} geometry in both mono-doped species (predicted by the Ovchinnikov's rule as the ground state) is computed as the single electron occupation of a''_2 and e'' orbitals ($^4A''_2$), and lies slightly above the twofold degenerated doublet $^2E''$ state (Table 4.3). However, the D_{3h} arrangement is unstable upon certain structural deformations. The existence of a third order symmetry axis in TGNFs induces the presence of twofold degenerate electronic terms E, which are prompt to instabilities with respect to nuclear displacements that reduce the symmetry and remove the degeneracies.(30)

mol.	sym.	state	ΔE	N_u
$\mathbf{2B}_1$	D_{3h}	$1^2E''$	-	1.58
		$1^4A''_2$	0.15	3.03
$\mathbf{2B}_1$	C_{2v}	1^2B_2	-	1.47
		1^4A_2	0.32	3.03
$\mathbf{2N}_1$	D_{3h}	$1^2E''$	-	1.50
		$1^4A''_2$	0.06	3.02
$\mathbf{2N}_1$	C_{2v}	1^2B_2	-	1.49
		1^4A_2	0.25	3.02
$\mathbf{2B}_3$	D_{3h}	$1^2A''_2$	-	2.99
		$1^4A''_2$	1.40	3.25
$\mathbf{2N}_3$	D_{3h}	$1^2A''_2$	-	2.77
		$1^4A''_2$	2.06	4.72

Table 4.3: Vertical energy gaps (in eV) between low-lying states with different spin-multiplicities and unpaired electron numbers (N_u) of B- and N-doped triangulene derivatives computed at the RAS-SF/6-311G(d,p) level.

The Jahn-Teller active distortion modes able to split the spin doublet state must be different from the totally symmetric representation and must be contained

in the symmetric contribution of the direct self-product of the E'' representation. Therefore, Jahn-Teller distortions able to break the degeneracy of $^2E''$ states must follow an $S(e')$ mode. Structure modification upon the action of the $S(e')$ vibration breaks the degeneracy of e'' orbitals and allows e''/a_2'' orbital mixing. As a result, the doublet configuration is stabilized in the C_{2v} geometry with the unpaired electron occupying a b_2-orbital (Figure 4.11a). Moreover, the vertical gap to the spin-quartet state of $\mathbf{2B}_1$ and $\mathbf{2N}_1$ sensibly increases upon the $S(e')$ distortion towards the C_{2v} geometry (Figure 4.11b).

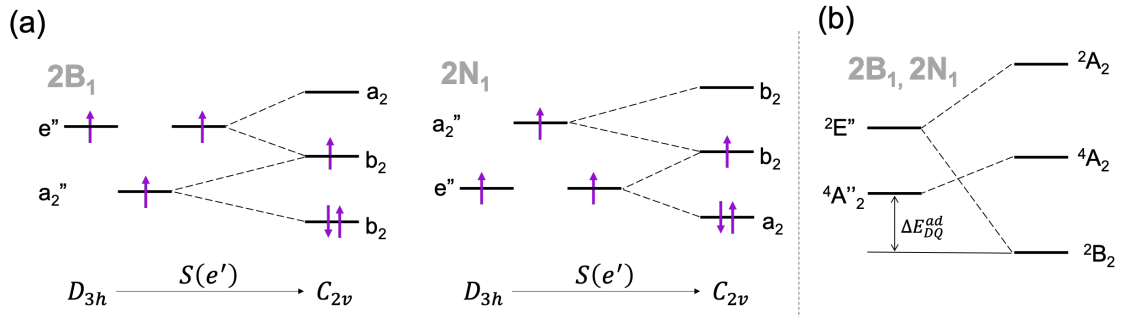

Figure 4.11: Qualitative representation of the $S(e^{'})$ distortion between the quartet (D_{3h}) and doublet (C_{2v}) optimized geometries of $\mathbf{2B}_1$ and $\mathbf{2N}_1$ (a), and state diagram of both monodoped triangulenes at each molecular symmetry (b).

Accordingly, while the unpaired electrons of the high-spin state symmetrically delocalizes over the entire π-system, the unpaired electron density of the ground state doublet (1^2B_2) in the mono-substituted triangulenes does not preserve the three fold symmetry, and delocalize the spin density on one of the triangle edges of $\mathbf{2B}_1$ and at one of the vertices in $\mathbf{2N}_1$ (Figure 4.12).

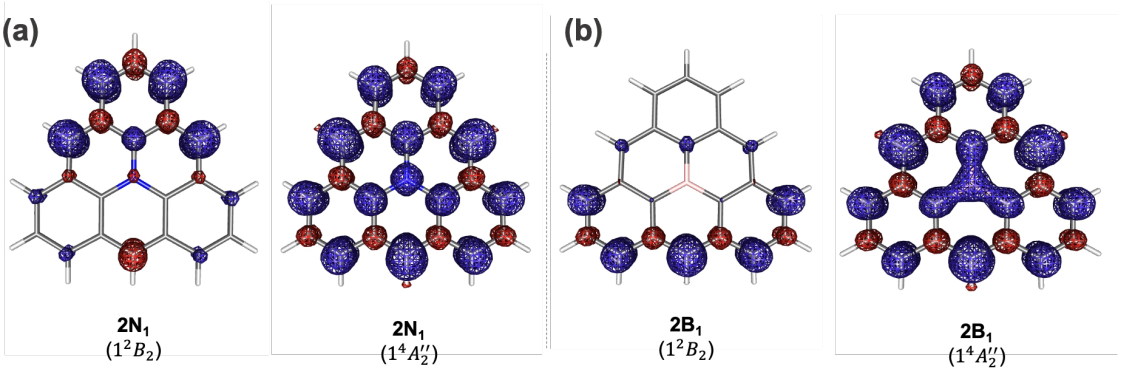

Figure 4.12: Spin densities of 1^2B_2 (C_{2v}) and $1^4A_2^{"}$ (D_{3h}) states of $\mathbf{2N}_1$ (a) and $\mathbf{2B}_1$ (b) in their respective optimized geometries.

Equivalently, the action of e'-symmetry Jahn-Teller distortion modes on **2** re-

sults in the splitting of the lowest $^1E'$ state. But, contrary to the situation in $\mathbf{2B}_1$ and $\mathbf{2N}_1$, such stabilization is not enough for the lowest spin-state to become the global minimum of the system ($\Delta E_{ST}^{ad} = -8.6$ kcal/mol).

The C_3-symmetric substitution of three carbon atoms by boron or nitrogen in $\mathbf{2B}_3$ and $\mathbf{2N}_3$, respectively, stabilizes the low-spin doublet state. Contrary to the mono-substituted species, $\mathbf{2B}_3$ and $\mathbf{2N}_3$ keep the overall D_{3h} molecular symmetry, since the unpaired electron lies on a (non-degenerate) a_2''-orbital. Characterization of their ground state radical character identifies one unpaired electron mainly localized on the central atom with small C_3-symmetrical contributions from the doping atoms and the carbons at the center of the triangle edges (Figure 4.13). Computed energy gaps to the quartet state are shown in Table 4.3.

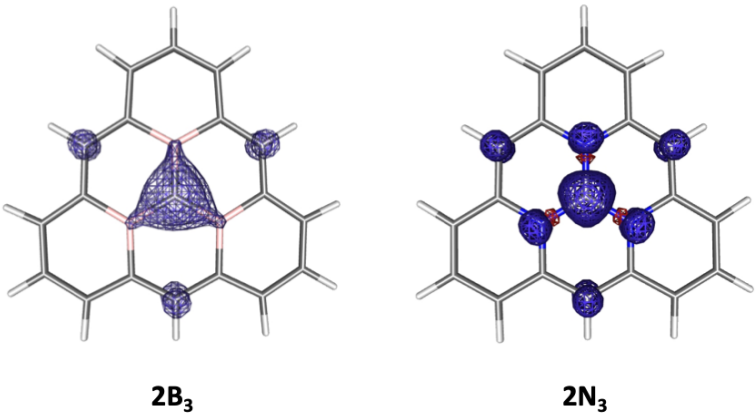

Figure 4.13: Spin densities of $\mathbf{2B}_3$ and $\mathbf{2N}_3$ doublet ground state.

Finally, we consider the non-symmetric doping of **2** by replacing two inner carbon atoms with nitrogen atoms ($\mathbf{2N}_2$). As shown in Figure 4.6, this substitution pattern implies the reduction of molecular symmetry to C_{2v} that results in the stabilization of the closed-shell configuration and, $\mathbf{2N}_2$ has a spin-singlet ground state with a weak diradical character identified by a quite small N_u value. Similarly to pristine triangulene, the unpaired electron density of $\mathbf{2N}_2$ is mainly localized over the molecular edges. Nevertheless, in this case all the inner atoms also exhibit radical character, mostly on the two doping atoms (Figure 4.14). The small diradical character of $\mathbf{2N}_2$ is in agreement with the rather large gap to the lowest triplet state, as presented in Table 4.3.

Therefore, we can conclude that doping of **1** and **2** with N and B results in the reduction of spin-multiplicity of the ground state for all the doping patterns investigated. By extrapolation to bigger members of TGNFs, symmetric and asymmetric substitution with heteroatoms offers a way to obtain stable larger graphene

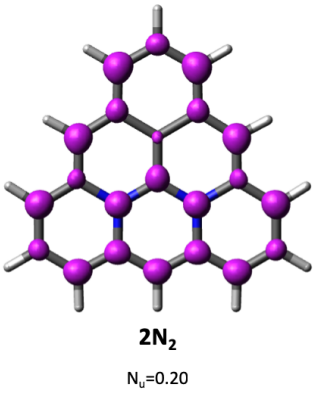

Figure 4.14: Ground state fractional occupied density (FOD) of $\mathbf{2N_2}$.

nanofragments with zigzag edges.

4.1.3 Hydrogenated TGNF

Selective hydrogen saturation of peripheral carbon positions according to Ovchinnikov's rule has been shown to constitute a simple and effective strategy in order to design high-spin states PAHs.(16) Here, we symmetrically hydrogenize three carbons of **1** and **2** (Figure 4.15a). The application of the Ovchinnikov's rule is done by removing the sp^3 carbon atoms and preserving only the conjugated system as illustrated in Figure 4.15b.

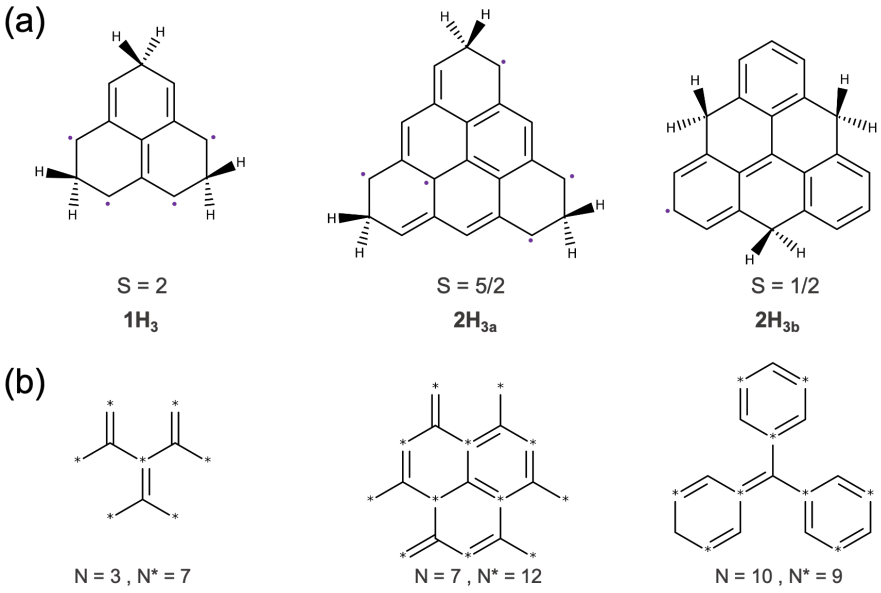

Figure 4.15: Hydrogenated derivatives of **1** and **2** (a) and their multiplicity predicted by Ovchinnikov's rule (b).

Saturation of the three vertices of **1** results in a triallyl-methane type product in

which the sp^3 atoms enforce molecular planarity with a D_{3h} symmetry. The topology of sp^2 sites in $\mathbf{1H}_3$ favors the high-spin stabilization, and its ground state corresponds to a spin-quintet state, $1^5A_1'$ (Table 4.4). The unpaired electron density at the ground state is distributed amongst the sp^2 atoms bonded to the CH_2 fragments and the central atom (Figure 4.16). The lowest doubly degenerate triplet and singlet states lie at 0.40 and 1.11 eV above the high-spin ground state, respectively, in very good agreement with accurate correlated *ab initio* and spin decontamination corrections of DFT energies.(16)

mol.	sym.	state	ΔE	N_u
$\mathbf{1H}_3$	D_{3h}	$1^5A_2'$	-	4.16
		$1^3E'$	0.40	4.09
		$1^1E'$	1.11	4.05
$\mathbf{2H}_{3a}$	D_{3h}	$1^6A_2''$	-	5.28
		$1^4E''$	0.26	4.79
		$1^2E''$	0.66	4.60
$\mathbf{2H}_{3b}$	D_{3h}	$1^2A_2''$	-	1.29
		$1^2E''$	3.16	1.82

Table 4.4: Vertical energy gaps (in eV) to the low-lying states with different spin-multiplicities and unpaired electron numbers (N_u) of H-saturated **1** and **2** derivatives computed at the RAS-SF/6-311G(d,p) level.

Similarly, hydrogenation of carbon atom at the vertices of **2** in $\mathbf{2H}_{3a}$ results in a high-spin ground state with five unpaired electrons, and with energy gaps to lower spin-multiplicities obtained from the spin-flip of one and two electrons of 0.26 and 0.66 eV, respectively. Contrarily, threefold saturation of **2** at the midpoint of the triangle edges ($\mathbf{2H}_{3b}$) reduces the imbalance between the number of carbons in each of the two sublattices, which stabilizes the low-spin (doublet) state (Table 4.4), giving rise to a planar triphenylmethane-like radical structure (Figure 4.15b).

Replacement of sp^2 by sp^3 carbon atoms in the peripherical positions of **1** and **2** provokes the rise of spin-multiplicity at ground state when done at the triangle's vertices. If the carbons at the midpoint of the triangle edges are hydrogenated, the diminution of the ground state multiplicity is predicted, suggesting a selective way to modulate the radical character of TGNFs by hydrogen saturation of peripherical carbon positions.

In summary, I have described the electronic structure of the doublet ground state of the phenalenyl molecule and the nature of its radical character arising from the single electron occupation of a a_1'' orbital delocalized at the molecular edges.

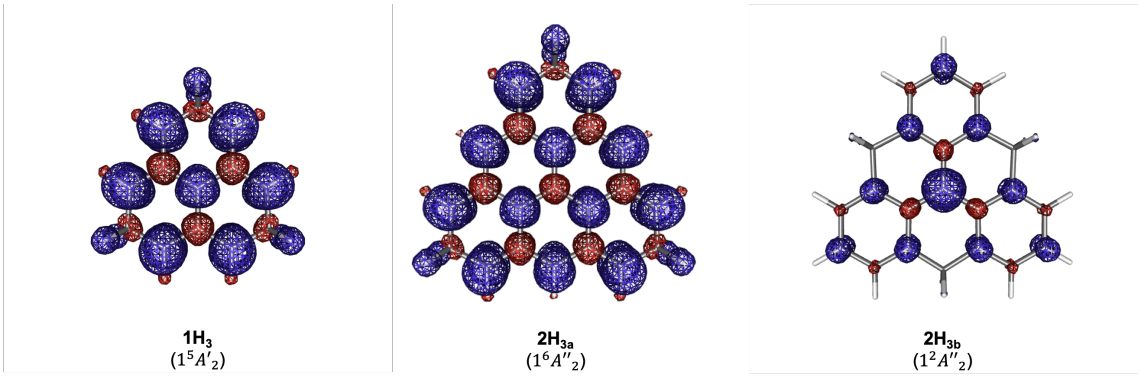

Figure 4.16: Spin density of hydrogenated derivative from **1** and **2**.

Similarly, the radical character of ground state triplet of triangulene is located at the carbon edges with no participation of the central and vertex sites. Substitution of the carbon atoms by boron or nitrogen can be used to tune the electronic and magnetic properties of TGNFs. The substitution symmetry pattern dictates the distribution of unpaired electrons and can be used to design TGNF ensembles with the desired properties. The fractional occupation of degenerate levels induces a Jahn-Teller distortion of mono-doped triangulene resulting in a stabilization of the doublet state, which cannot be taken into account by simple models such as Ovchinniko's rule. Selective saturation of carbon edge positions of **1** and **2** with hydrogen atoms also has a very strong impact on the ground state spin multiplicity, and hence provides another approach for the tuning of their magnetic properties.

4.2 Diradical character in cyclic and linear acenes

IUPAC Golden Book defines acenes as polycyclic aromatic hydrocarbons consisting of fused benzene rings in a rectilinear arrangement.(31) Cyclic acenes or cyclacenes (**[***n***]CC**) can be obtained by fusing the molecular ends of linear acenes (**[***n***]Ac**). In the context of the single-walled carbon nanotubes (SWCNT), **[***n***]CC** (also known as nanobelts) are important systems as they are considered as the smallest chemical unit to grow size-specific SWCNT.(32)

According to Ovchinnikov's rule, **[***n***]CC** and **[***n***]Ac**, presented in Figure 4.17a, are predicted to hold spin-singlet ground state since they have the same number of atoms in each sublattice. Even so, the presence of zigzag edges suggests the rise of open-shell properties, which is supported by the Clar's sextet rule. While only one Clar's sextet ring can be drawn in closed-shell structures of **[***n***]Ac**, no aromatic rings can be formed without unpaired electrons in **[***n***]CC** (Figure 4.17b). These observations point towards linear and cyclic acenes having slight diradical

character, at least. Furthermore, it is predicted that **[***n***]Ac** hold a softer diradical character than **[***n***]CC**.

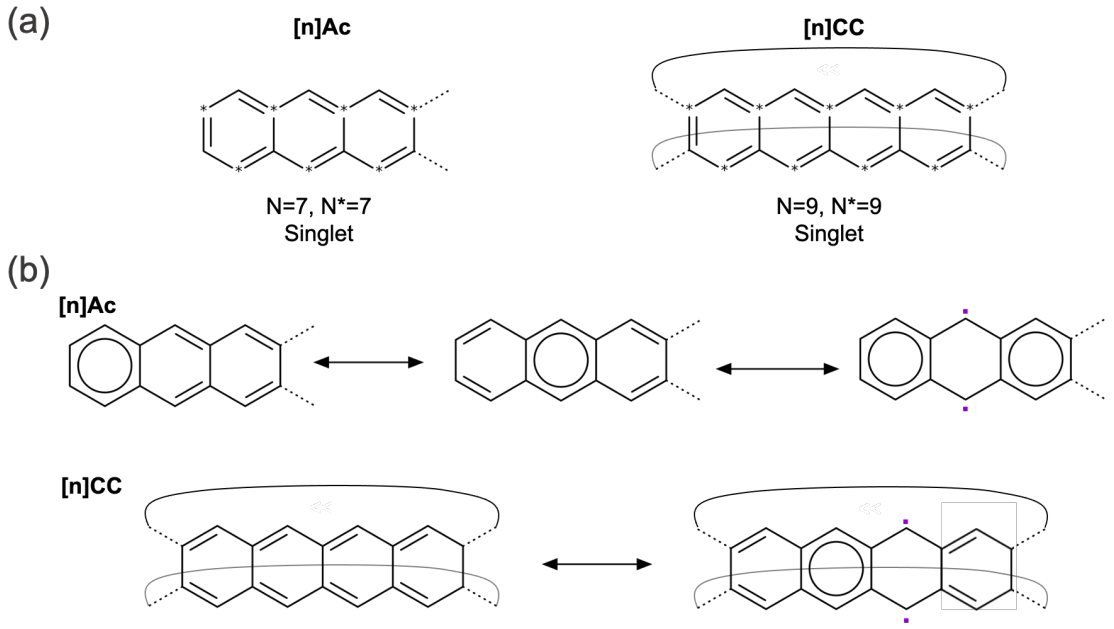

Figure 4.17: Ovchinnikov's rule applied to **[***n***]Ac** and **[n]**CC (a). Clar's resonate structures of **[***n***]Ac** and **[***n***]**CC (b).

At the beginning of the 50s decade, cyclic acenes with zigzag edges, were proposed and investigated theoretically.(33; 34) The first attempt to synthesize a zigzag-cyclic acene was reported in 1987, when Kohnke *et al.* tried to obtain duodecacyclacene.(35) Since then the synthesis of **[***n***]CC** has been widely attempted, yet with no success.(33) Recently, a carbon-nanobelt isomer of the [12]cyclophenacene has been isolated under standard conditions and characterized by X-ray diffraction by Povie *et al.*(36) Synthesis of linear acenes can be also challenging. The smallest pristine **[***n***]Ac** are stable under ambient conditions and commercially available (up to pentacene). In particular, tetracene and pentacene have been extensively used as component of organic thin film transistors, organic photovoltaics and solar cells.(37; 38; 39) Together with hexacene and its derivatives, they also have been tested as singlet fission molecules.(40; 41) In medium size linear acenes, from hexacene to nonacene, the synthesis of stable compounds at ambient conditions has not been achieved yet and special conditions are necessary to obtain them.(42; 43; 44; 45) Routes to prepare hexacene and heptacene consist mainly in the *in situ* generation of pristine acenes from its derivatives, which could be over metallic layers,(46) in solution,(47) under matrix isolation conditions,(48) or directly as part of a thin-film.(49) Nevertheless, crystalline hexacene can be stable for few days under ambient conditions but only in the dark.(50) Larger acenes can be photogenerated(51; 46) or

obtained on-surface(52; 53; 54) up to undecacene. Radical character in this family of compounds has been associated to the unstable behavior of cyclic acenes and medium to large linear acenes.

With that in mind, a series of increasing size **[*n*]CC**, with $n = 5 - 12$, was thoroughly studied and compared with the parent **[*n*]Ac** (from pentacene to dodecacene), so as to rationalise the relationship between topology and radical character.

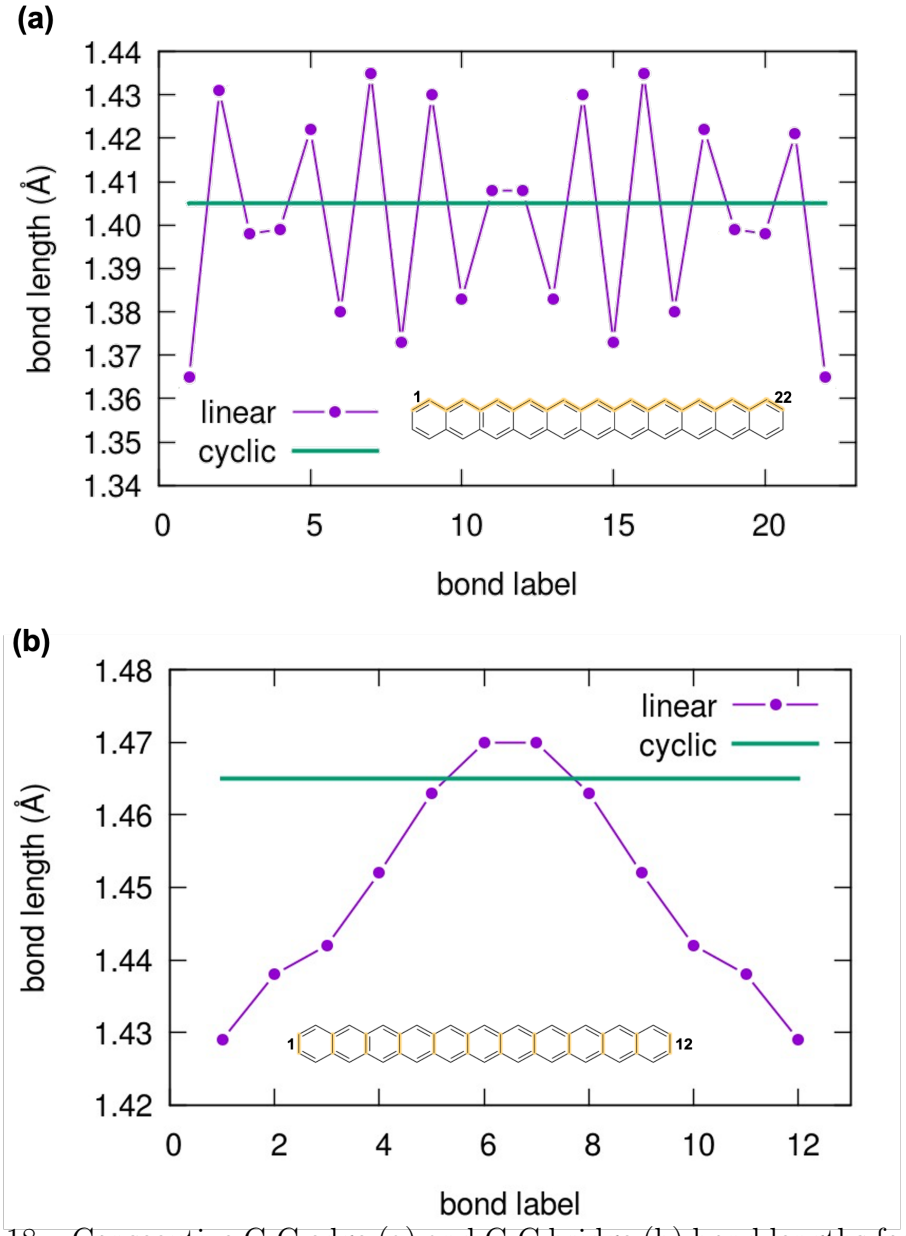

Figure 4.18: Consecutive C-C edge (a) and C-C bridge (b) bond lengths for **[11]Ac** and **[11]CC** oligoacenes. In the inset, both types of C-C bond are highlighted in yellow. Figure adapted from reference(55).

Geometrically, the effect of different contour conditions, in this particular case if the acenes are closed or not, *i.e.*, cyclic or linear acenes, significantly changes their symmetry. While **[*n*]Ac** have a D_{2h} symmetry in the ground state, the geometry of

the ground state of **[*n*]CC** belongs to the D_{nh} point group. As a consequence, all rings in **[*n*]CC** are equivalent. On the other hand, benzene rings at the extremities of **[*n*]Ac** are smaller than those in the molecular center. The resulting impact on their respective bond length alternation is presented in Figure 4.18, which shows the differences between linear and cyclic undecacene, **[11]Ac** and **[11]CC**. Two types of C-C bonds can be distinguished in these systems, namely edge and bridge ones, hereafter referred to as CC_e and CC_b, respectively (as illustrated in the inset of Figure 4.18a and b, respectively).

The CC_e along **[11]CC** are constant and amount to $\sim$ 1.41 Å, while they oscillate between 1.36-1.44 Å in **[11]Ac**. These C-C distances are close to the C-C bond lengths in benzene and graphite, *i.e.*, 1.38 Å and 1.42 Å, respectively.(56) The bridge (interchain) bond lengths CC_b of **[11]CC** ($\sim$ 1.47 Å) and **[11]Ac** (from 1.42 Å to 1.47 Å) are similar to the single bond length between two double bonds in butadiene, *i.e.*, single bond connecting two sp^2 carbons (1.46 Å).(56) This suggests that cyclic and linear acenes can be considered as two conjugated zigzag chains (top and bottom edges) that are covalently bound. Note that the central rings of **[*n*]Ac** exhibit similar CC_e and CC_b bonds as those of the **[*n*]CC** compounds.

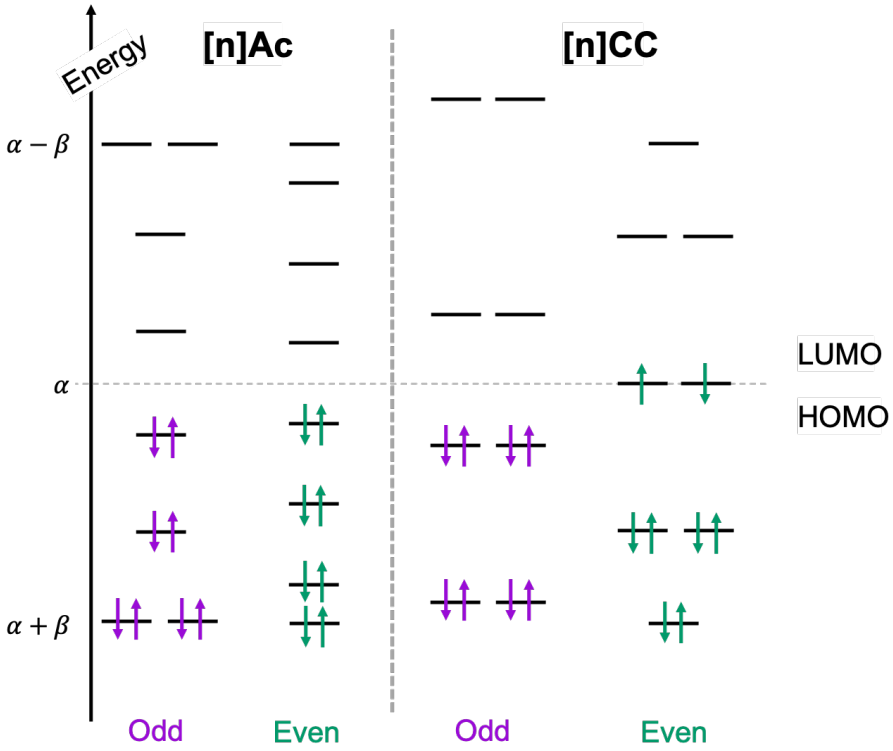

Figure 4.19: Hückel molecular orbital energy diagram around the Fermi energy level (E = α) for **[*n*]Ac** (left) and **[*n*]CC** (right) with an odd (n=5) and even (n=6) number of fused rings. Figure adapted from reference(55).

The Hückel model pointed out a main difference in the electronic structure of

both families as illustrated by their molecular orbital diagram, which helps to clarify the nature of radical character in **[*n*]Ac** and **[*n*]CC** (Figure 4.19). The HOMO-LUMO energy gap in **[*n*]Ac** decreases with the increase of the molecular size (*i.e*, diradical character increases with n). Similarly, the energy gap between occupied and virtual orbitals of **[*n*]CC** decreases constantly with molecular size. However, the degeneracy of frontier molecular orbitals depends on the number of fused rings. When n is odd, **[*n*]CC** hold a doubly degenerate HOMO and LUMO and, at very large n, the vanishing of the HOMO-LUMO energy gap and the emergence of the tetraradical character can be predicted. On the other hand, in even-**[*n*]CC**, two electrons located in two degenerate orbitals are predicted, suggesting a strong diradical character for these systems.

These elementary considerations evidence a strong relationship between topology and radical character of both linear and cyclic acenes. In-depth electronic structure characterization of these systems through wave function analysis is summarized for each family in the following subsections.

4.2.1 Linear acenes

As predicted by the Hückel model, the HOMO-LUMO energy gap diminishes from shorter to larger **[*n*]Ac**. In good agreement, the energy of first triplet excited state (characterized as the single HONO to LUNO transition computed within the RAS-SF framework) decreases with the increment of n (Table 4.5).

System	ΔE_{ST}^{vert}	HONO	LUNO	N_u
Pentacene	1.275	1.844	0.157	0.62
Hexacene	1.015	1.826	0.175	0.67
Heptacene	0.753	1.772	0.229	0.79
Octacene	0.360	1.598	0.403	1.17
Nonacene	0.237	1.462	0.538	1.46
Decacene	0.108	1.018	0.982	2.44
Undecacene	0.111	1.013	0.988	2.48
Dodecacene	0.120	1.058	0.943	2.42

Table 4.5: Vertical singlet-triplet energy gaps (in eV), natural orbital occupation and unpaired electron numbers (N_u) computed at the RAS-SF/6-31G(d) level of theory for the **[*n*]Ac** family.

The vertical singlet-triplet energy gap, $\Delta E_{ST}^{vert} = E(T_1) - E(S_0)$, of **[*n*]Ac** with $n = 10$ to $n = 12$ is very small, indicating a ground state singlet with a large diradical character, thus making them extremely reactive. N_u values and

the electronic occupation of HONO and LUNO support this finding (Table 4.5). More specifically, the occupation of the HONO decreases by transferring electronic population to the LUNO (and other higher virtual orbitals to a much lesser degree) as the oligoacenes grow in size; in the largest **[*n*]Ac** ($n = 10 - 12$) both orbitals are occupied in nearly 1 electron, which is reflected by their number of unpaired electron (N_u = 2.44, 2.48 and 2.42, respectively). The smooth increase of both LUNO occupation and N_u with the increment of n indicates the emergence of the diradicaloid character.

Frontier natural orbitals in **[*n*]Ac** are localized on C atoms that are not part of CC_b bonds (Figure 4.20). This observation is in good agreement with bond length behavior, since rings at molecular ends have aromatic-like structure, *i.e.*, are conjugated and with (quasi)closed-shell character. In the molecular center of **[*n*]Ac**, CC_b are maximum and the electronic interaction between top and bottom conjugated chains is minimised.

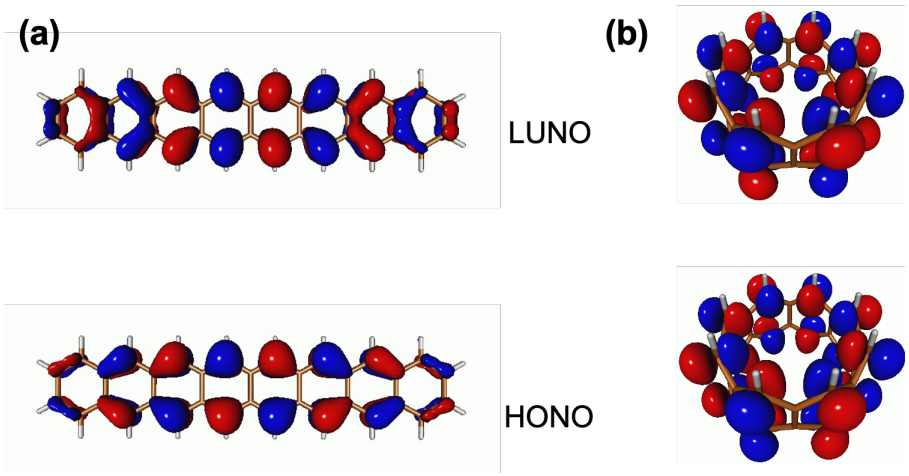

Figure 4.20: Frontier natural orbitals for **[8]Ac** (a) and **[8]CC** (b).

The origin of radical character of linear oligoacenes has been exposed. The results presented here suggest difficulties to synthesize and isolate larger acenes due to their high diradical character.

4.2.2 Cyclic acenes

The fundamental electronic differences between linear and cyclic acenes induced by topology were exposed by the Hücklel model. While frontier molecular orbitals in linear acenes are not degenerated and present an energy gap that decreases with n, the orbital distribution of **[*n*]CC** is different depending on whether the number of fused rings is odd or even.

As in linear compounds, only carbon atoms not participating in CC_b bonds

contribute to the natural orbitals, as illustrated in Figure 4.20. However, in contrast to linear acenes, the natural orbitals of **[*n*]CC** are homogeneously distributed over the hole molecule, in good agreement with the higher molecular symmetry and the constant value of CC_e and CC_b. Regarding the radical character, ΔE_{ST} decreases as n increases, indicating an increasing diradical character. As a consequence, the electronic occupation of LUNO orbital also augments, as well as N_u (Table 4.6).

[*n*]CC	ΔE_{ST}	ΔE_{SQ}	HONO-1	HONO	LUNO	LUNO+1	N_u
5	0.854	2.068	1.778	1.731	0.266	0.216	1.22
6	0.264	-	1.902	1.457	0.542	0.102	1.60
7	0.356	0.842	1.627	1.626	0.369	0.368	1.79
8	0.255	-	1.880	1.462	0.542	0.119	1.66
9	0.164	0.399	1.449	1.449	0.549	0.549	2.57
10	0.258	-	1.841	1.435	0.570	0.158	1.82
11	0.112	0.284	1.317	1.310	0.689	0.682	3.19
12	0.228	-	1.813	1.340	0.664	0.186	2.15

Table 4.6: Vertical singlet-triplet and singlet-quintet energy gaps (in eV), natural orbital occupation and number of unpaired electrons (N_u) at the RAS-SF/6-31G(d) level for **[n]CC**.

The evolution of ΔE_{ST} and N_u as a function of the number of fused benzene rings in **[*n*]Ac** and **[*n*]CC** is illustrated in Figure 4.21. While a constant trend to drop (rise) for ΔE_{ST} (N_u) can be seen within the **[*n*]Ac** family up to $n = 10$ (after which both remain stable), an odd-even effect is observed for the **[*n*]CC** family. This different behaviour of ΔE_{ST} and N_u for **[*n*]CC** with odd or even n can be related to the differences in their Hückel diagram (Figure 4.19) which suggest that their electronic structure is qualitatively different.

These results point out that **[*n*]CC** with odd and even number of fused rings are part of two separated families. Actually, when n is odd, N_u tends to four, indicating that they are tetraradicaloid systems, as indicated by the double degeneracy of the HOMO and LUMO in the Hückel model. Fractional occupation of frontier natural orbitals, from HONO-1 to LUNO+1, shows the simultaneous increment of the electronic population in LUNO and LUNO+1, while HONO and HONO-1 are being depopulated. Another way to describe the tetraradicaloid character of the odd systems is by the energy gap between singlet ground state and lowest quintet state, $\Delta E_{SQ} = E_{Q_1} - E_{S_0}$, which decreases concomitantly with ΔE_{ST} (Table 4.6). On the other hand, the natural orbital occupation number (HONO $\sim$ 1.4 and LUNO $\sim$ 0.6) and N_u (> 1.5) indicate the diradicaloid character of **[n]CC** with even number of rings.

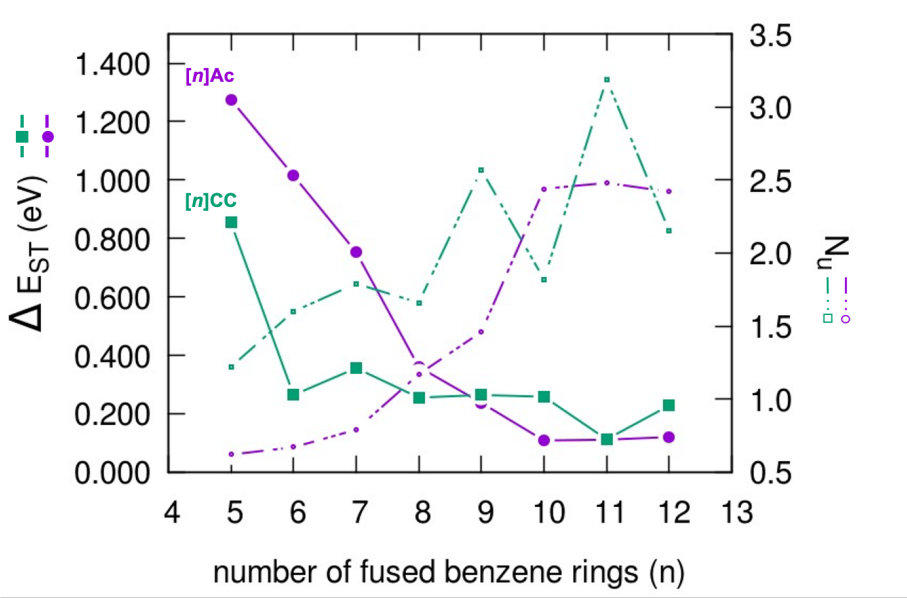

Figure 4.21: Singlet-triplet energy gap (continued lines) and N_u (discontinued lines) of **[n]CC** (green squares) and **[n]Ac** (purple circles).

Interestingly, the electronic structure of cyclic acenes with even number of benzene rings diverge from what is anticipated by the Hückel model as the energy degeneracy of HONO and LUNO is not observed. Similarly to what was observed in the previous section, the symmetry of the Hückel Hamiltonian is higher than the molecular symmetry. For example, HONO and LUNO of **[8]CC** (Figure 4.22a) correspond to the B_{2g} and B_{2u} irreducible representations of the D_{8h} point group and are predicted to be degenerate by the Hückel model. In electronic structure calculations, when not only interactions between first neighbours are considered, this orbital degeneracy is lifted.

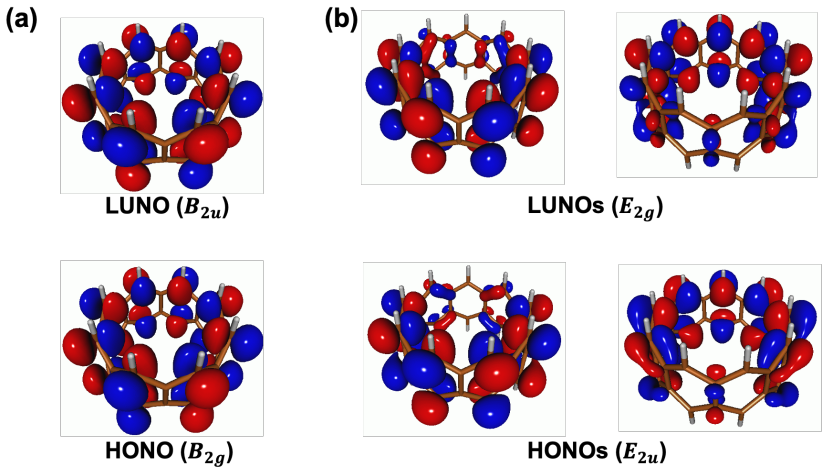

Figure 4.22: Frontier natural orbitals of **[8]CC** (a) and **[9]CC** (b). Figure adapted from reference (55).

Inspection of frontier natural orbitals in Figure 4.22 reveals the opposite interaction between top and bottom edges for odd- and even-**[***n***]CC**. When $n = 5, 7, 9$ and 11 the HONOs (LUNOs) corresponds to out-of-phase (in-phase) arrangement between π-orbitals, which is also observed in linear acenes. On the contrary, HONO (LUNO) of n-even **[***n***]CC** holds bonding (anti-bonding) interaction between unpaired electrons in top and bottom edges. This bonding (anti-bonding) interaction between top and bottom edges can be added to the Hückel Hamiltonian (γ in Figure 4.23), as a resulting in the decrease of the HOMO-LUMO gap in n-odd cyclacenes. On the other hand, it results in the breaking of the previously observed degeneracy in even-**[***n***]CC**. These results are in good agreement with the rapid increment of tetraradicaloid character of odd-**[***n***]CC** and explain why even-**[***n***]CC** are diradicaloids but not perfect diradicals.

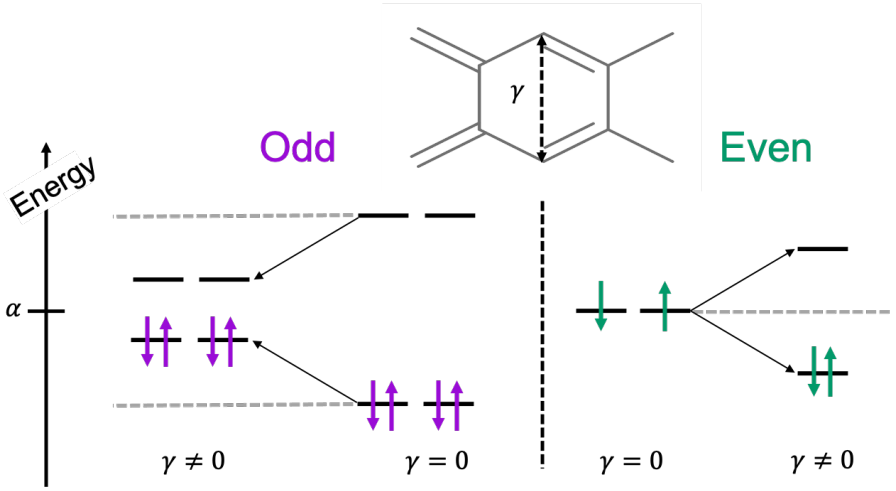

Figure 4.23: Effect of radical center interaction (γ) in the Hückel frontier orbitals for **[***n***]CC** with n-odd (left) and n-even (right). Figure adapted from reference(55).

Alternatively, the interaction between radical centers can be rationalised by the contribution of the ionic configuration to the wave function of the ground state using a simple model, two electrons in two orbitals, where one electron (radical) is localized over each ring, top or bottom edge in **[n]CC**. The ability of two radical centers to share electron density is measured by the ionic contributions that help to stabilize closed-shell configurations. As a consequence, strong interaction results in large HOMO-LUMO energy gaps and the diminution of the radical character. This radical-radical interaction can be described by deconstruction of the ground-state wave function of **[***n***]CC**, when n is even, in a fragment decomposition scheme (Subsection 3.3.2.1). Defined fragments, top (ϕ_t) and bottom (ϕ_b) are both radical cycles. The wave function of the full system in terms of covalent (cov) and ionic (ion) contributions is expressed as:

$$|\Psi\rangle = C_{cov}|\phi_u^{(1)}\phi_d^{(1)}\rangle + C_{ion}(|\phi_u^{(2)}\phi_d^{(0)}\rangle + |\phi_u^{(0)}\phi_d^{(2)}\rangle), \tag{4.2}$$

where (m) superindex indicates the number of electrons in each ring. The correlation between ionic contribution to ground-state wave function and ΔE_{ST} of **[**n**]CC**, $n = 6, 8, 10$ and 12 is displayed in Figure 4.24. In the simple model used here, the values in the graph have to be considered only qualitatively since fragment decomposition has been done with a small active space different from the one used to compute values reported in Table 4.6. Nevertheless, the correlation indicates the weak interaction between radical centers with ionic contributions to the wave function of less than 4%. It is noticeable that the presence of radical-radical interaction between centers (γ in Hückel model) controls and tunes the diradical character.

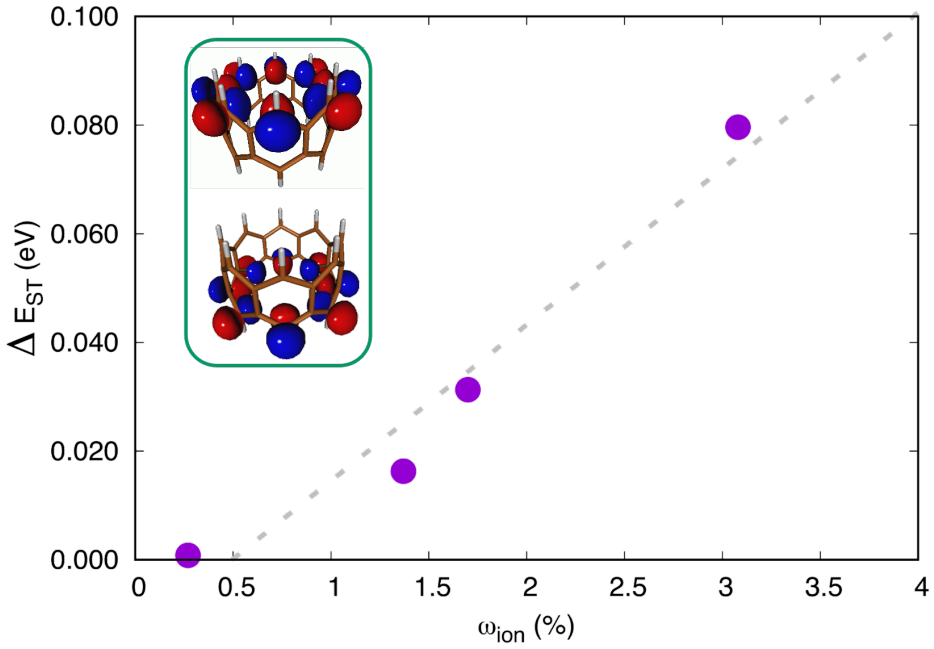

Figure 4.24: Correlation between ionic contributions ($\omega_{ion} = 100 \times |c_{ion}|^2$) and singlet–triplet energy gaps for the RAS-SF[2,2] ground state wave functions of **[**n**]CC** molecules with n-even. Inset shows fragment orbitals for the case with n = 8. Dashed line corresponds to the regression line and is only plotted for visual guidance. Figure adapted from reference(55).

To conclude, the relationship between the growing strength of the diradical character with the size of cyclic and lineal acenes and its dependence on the topology of both families was exposed here. Detailed analysis of the ground state of **[**n**]CC** allows us to unveil that their radical nature is different when are constituted by an odd and even number of fused benzene rings. n-even cyclacenes are diradicaloids, while n-odd ones can be regarded as tetraradicaloids.

4.3 Appendix

4.3.1 Computational details

Molecular geometries have been optimized in the framework of the density functional theory (DFT) with the M06-2X exchange-correlation functional.(57) Ground and low-lying excited electronic states have been computed by means of the restricted active space configuration interaction (RASCI) with the *hole* and *electron* approximation and the use of a spin-flip excitation operator.(58; 59) All π-orbitals were included in the calculation while core electrons orbitals were frozen, in this way excitations from σ-orbitals are not considered.

Radical and poly-radical character of electronic states have been evaluated through the representation of natural orbitals and the fractional occupation density. FODs have been plotted with a modified version of Avogrado (Version 1.2).(60) The number of unpaired electrons has been quantified by the Head-Gordon (N_u) metrics.(61) All calculations have been performed with the Q-Chem package.(62)

4.3.1.1 Triangular graphene nanofragments

All calculations for these systems were performed with the 6-311G(d,p) basis set. Detailed description of the orbital spaces employed for each system can be found in Table 4.7. Doped **1** and **2** derivatives have the same set of active orbitals in the RAS II space than the pristine counterpart.

TGNF	Symmetry	Spin reference	(Active) RAS II electrons	(Active) RAS II orbitals
1	D_{3h}	Doublet	7	$2e''$, $2a_2''$, $1a_1''$, $3e''$ and $3a_2''$
1N$_1$	D_{3h}	Triplet	8	$2e''$, $2a_2''$, $1a_1''$, $3e''$ and $3a_2''$
1B$_1$	D_{3h}	Triplet	6	$2e''$, $2a_2''$, $1a_1''$, $3a_2''$ and $3e''$
1H$_3$	D_{3h}	Quintet	8	$2e''$, $1a_1''$, $4a_2''$, $3e''$ and $4e''$
2	D_{3h}	Triplet	10	$3e''$, $1a_1''$, $3a_2''$, $4e''$, $4a_2''$, $5e''$ and $2a_1''$
2B$_1$	D_{3h}/C_{2v}	Quartet	3	$3a_2''$, $4e''$ and $4a_2''$
2B$_3$	D_{3h}	Quartet	7	$3e''$, $1a_1''$, $3a_2''$, $4e''$, $4a_2''$, $5e''$ and $2a_1''$
2N$_1$	D_{3h}/C_{c2v}	Quartet	5	$3a_2''$, $4e''$ and $4a_2''$
2N$_3$	D_{3h}	Quartet	13	$3e''$, $1a_1''$, $3a_2''$, $4e''$, $4a_2''$, $5e''$ and $2a_1''$
2H$_3a$	D_{3h}	Sextet	9	$3a_2''$, $1a_1'$, $4e''$, $5e''$, $4a_2''$, $2a_1''$ and $5a_2''$
2H$_3b$	D_{3h}	Doublet	5	$3e''$, $3a_2''$ and $3e''$
2N$_2$	C_{2v}	Singlet	4	$3a''2$, $4e''$ and $4a_2''$

Table 4.7: Active space parameter employed in the RAS-SF calculations.

4.3.1.2 Cyclic and linear acenes

Study over oligoacenes was carried out together with the theoretical group lead by Prof. Juan Carlos Sancho-Garcia from the University of Alicante.

RAS-SF calculations were performed over a set of geometries provided by the group of Prof. Sancho-Garcia (optimized and confirmed as a minimum in the ground state PES at M06-2X/6-31+G(d) level, using Gaussian09 package (63)). The active subspace of RAS-SF included 8 electrons in 8 π-orbitals, and the 6-31G(d) was used in all calculations. The high-spin reference was the triplet ROHF for n-even cyclic and linear acenes. For [n]CC with odd n, the lowest ROHF quintet was employed instead. Fragment decomposition of the RAS-SF ground state wave function of even [n]CC molecules has been done considering a RAS2 subspace with 2 electrons in 2 π-orbitals (as described in subsection 3.3.2.1). Molecular orbital energies for the Hückel model were obtained with $\alpha < 0$, $\beta = \alpha/10$ and $\gamma = \beta/5$ for the Coulomb and resonance integrals.

Bibliography

[1] K. S. Novoselov, A. K. Geim, S. V. Morozov, D. Jiang, Y. Zhang, S. V. Dubonos, I. V. Grigorieva, and A. A. Firsov, "Electric field effect in atomically thin carbon films," vol. 306, no. 5696, p. 666, 2004.

[2] B. Feringa, *Molecular Switches*. Wiley, 2001.

[3] W. Han, R. K. Kawakami, M. Gmitra, and J. Fabian, "Graphene spintronics," *Nature Nanotechnology*, vol. 9, p. 794, 2014.

[4] A. K. Geim and K. S. Novoselov, "The rise of graphene," *Nature Materials*, vol. 6, no. 3, pp. 183–191, 2007.

[5] W. L. Wang, S. Meng, and E. Kaxiras, "Graphene nanoflakes with large spin," *Nano Letters*, vol. 8, no. 1, pp. 241–245, 2008.

[6] X.-Y. Wang, X. Yao, and K. Müllen, "Polycyclic aromatic hydrocarbons in the graphene era," *Science China Chemistry*, vol. 62, no. 9, pp. 1099–1144, 2019.

[7] A. K. Geim, "Graphene: status and prospects," *Science*, vol. 324, no. 5934, pp. 1530–1534, 2009.

[8] F. J. García de Abajo, "Graphene plasmonics: Challenges and opportunities," *ACS Photonics*, vol. 1, pp. 135–152, 2014.

[9] M. J. Allen, V. C. Tung, and R. B. Kaner, "Honeycomb carbon: A review of graphene," *Chemical Reviews*, vol. 110, no. 1, pp. 132–145, 2010.

[10] M. Solà, "Forty years of clar's aromatic π-sextet rule," *Frontiers in chemistry*, vol. 1, pp. 22–22, 2013.

[11] M. Melle-Franco, "When 1 + 1 is odd," *Nature Nanotechnology*, vol. 12, no. 4, pp. 292–293, 2017.

[12] J. Zhang, M. Terrones, C. R. Park, R. Mukherjee, M. Monthioux, N. Koratkar, Y. S. Kim, R. Hurt, E. Frackowiak, T. Enoki, Y. Chen, Y. Chen, and A. Bianco, "Carbon science in 2016: status, challenges and perspectives," *Carbon*, vol. 98, pp. 708–732, 2016.

[13] Y. Morita, S. Suzuki, K. Sato, and T. Takui, "Synthetic organic spin chemistry for structurally well-defined open-shell graphene fragments," *Nature Chemistry*, vol. 3, no. 3, pp. 197–204, 2011.

[14] J. Inoue, K. Fukui, T. Kubo, S. Nakazawa, K. Sato, D. Shiomi, Y. Morita, K. Yamamoto, T. Takui, and K. Nakasuji, "The first detection of a clar's hydrocarbon, 2,6,10-tri-tert-butyltriangulene: A ground-state triplet of non-kekulé polynuclear benzenoid hydrocarbon," *Journal of the American Chemical Society*, vol. 123, no. 50, pp. 12702–12703, 2001.

[15] K. Fukui, J. Inoue, T. Kubo, S. Nakazawa, T. Aoki, Y. Morita, K. Yamamoto, K. Sato, D. Shiomi, K. Nakasuji, and T. Takui, "The first non-kekulé polynuclear aromatic high-spin hydrocarbon: Generation of a triangulene derivative and band structure calculation of triangulene-based high-spin hydrocarbons," *Synthetic Metals*, vol. 121, no. 1, pp. 1824–1825, 2001.

[16] G. Trtaquier, N. Suaud, and J. P. Malrieu, "Theoretical design of high-spin polycyclic hydrocarbons," *Chem. Eur. J.*, vol. 16, no. 29, pp. 8762–8772, 2010.

[17] J.-P. Malrieu and G. Trinquier, "Can a topological approach predict spin-symmetry breaking in conjugated hydrocarbons?," *The Journal of Physical Chemistry A*, vol. 120, no. 48, pp. 9564–9578, 2016.

[18] A. Das, T. Müller, F. Plasser, and H. Lischka, "Polyradical character of triangular non-kekuléstructures, zethrenes, p-quinodimethane-linked bisphenalenyl, and the clar goblet in comparison: An extended multireference study," *J. Phys. Chem. A*, vol. 120, no. 9, pp. 1625–1636, 2016.

[19] S. Casolo, R. Martinazzo, and G. F. Tantardini, "Band engineering in graphene with superlattices of substitutional defects," *J. Phys. Chem. C*, vol. 115, no. 8, pp. 3250–3256, 2011.

[20] L. S. Panchakarla, K. S. Subrahmanyam, S. K. Saha, A. Govindaraj, H. R. Krishnamurthy, U. V. Waghmare, and C. N. R. Rao, "Synthesis, structure, and properties of boron- and nitrogen-doped graphene," *Adv. Mater.*, vol. 21, no. 46, pp. 4726–4730, 2009.

[21] L. Ci, L. Song, C. Jin, D. Jariwala, D. Wu, Y. Li, A. Srivastava, Z. F. Wang, K. Storr, L. Balicas, F. Liu, and P. M. Ajayan, "Atomic layers of hybridized boron nitride and graphene domains," *Nature Mater.*, vol. 9, p. 430, 2010.

[22] R. B. Pontes, A. Fazzio, and G. M. Dalpian, "Barrier-free substitutional doping of graphene sheets with boron atoms: Ab initio calculations," *Phys. Rev. B*, vol. 79, p. 033412, 2009.

[23] B. Guo, Q. Liu, E. Chen, H. Zhu, L. Fang, and J. R. Gong, "Controllable n-doping of graphene," *Nano Lett.*, vol. 10, no. 12, pp. 4975–4980, 2010.

[24] J. C. Johannsen, S. Ulstrup, A. Crepaldi, F. Cilento, M. Zacchigna, J. A. Miwa, C. Cacho, R. T. Chapman, E. Springate, F. Fromm, C. Raidel, T. Seyller, P. D. C. King, F. Parmigiani, M. Grioni, and P. Hofmann, "Tunable carrier multiplication and cooling in graphene," *Nano Lett.*, vol. 15, no. 1, pp. 326–331, 2015.

[25] J. E. D. Bene, R. Ditchfield, and J. A. Pople, "Self [U+2010] consistent molecular orbital methods. x. molecular orbital studies of excited states with minimal and extended basis sets," *The Journal of Chemical Physics*, vol. 55, no. 5, pp. 2236–2241, 1971.

[26] J. B. Foresman, M. Head-Gordon, J. A. Pople, and M. J. Frisch, "Toward a systematic molecular orbital theory for excited states," *The Journal of Physical Chemistry*, vol. 96, no. 1, pp. 135–149, 1992.

[27] L. S. Bartell, "Molecular geometry: Bonded versus nonbonded interactions," *J. Chem. Educ.*, vol. 45, no. 12, p. 754, 1968.

[28] H. A. Jahn, "Stability of polyatomic molecules in degenerate electronic states. II. Spin degeneracy," *Proc. R. Soc. A*, vol. 164, no. 916, pp. 117–131, 1938.

[29] R. G. Pearson, "Symmetry rule for predicting molecular structures," *Journal of the American Chemical Society*, vol. 91, no. 18, pp. 4947–4955, 1969.

[30] I. B. Bersuker, "Modern aspects of the jahn-teller effect theory and applications to molecular problems," *Chemical Reviews*, vol. 101, no. 4, pp. 1067–1114, 2001.

[31] I. U. of Pure and A. Chemistry, "Iupac compendium of chemical terminology – the gold book," 2009.

[32] H. Omachi, T. Nakayama, E. Takahashi, Y. Segawa, and K. Itami, "Initiation of carbon nanotube growth by well-defined carbon nanorings," *Nature Chemistry*, vol. 5, no. 7, pp. 572–576, 2013.

[33] X. Lu and J. Wu, "After 60 years of efforts: The chemical synthesis of a carbon nanobelt," *Chem*, vol. 2, no. 5, pp. 619–620, 2017.

[34] H. Qu and C. Chi, "Synthetic chemistry of acenes and heteroacenes," *Current Organic Chemistry*, vol. 14, no. 18, pp. 2070–2108, 2010.

[35] F. H. Kohnke, A. M. Z. Slawin, J. F. Stoddart, and D. J. Williams, "Molecular belts and collars in the making: A hexaepoxyoctacosahydro[12]cyclacene derivative," *Angewandte Chemie International Edition in English*, vol. 26, no. 9, pp. 892–894, 1987.

[36] G. Povie, Y. Segawa, T. Nishihara, Y. Miyauchi, and K. Itami, "Synthesis of a carbon nanobelt," *Science*, vol. 356, no. 6334, p. 172, 2017.

[37] D. Lehnherr and R. R. Tykwinski, "Conjugated oligomers and polymers based on anthracene, tetracene, pentacene, naphthodithiophene, and anthradithiophene building blocks," *Australian Journal of Chemistry*, vol. 64, no. 7, pp. 919–929, 2011.

[38] H. Yamada, Y. Yamashita, M. Kikuchi, H. Watanabe, T. Okujima, H. Uno, T. Ogawa, K. Ohara, and N. Ono, "Photochemical synthesis of pentacene and its derivatives," *Chemistry–A European Journal*, vol. 11, no. 21, pp. 6212–6220, 2005.

[39] T. Okamoto and Z. Bao, "Synthesis of solution-soluble pentacene-containing conjugated copolymers," *Journal of the American Chemical Society*, vol. 129, no. 34, pp. 10308–10309, 2007.

[40] X. Wang, R. Wang, L. Shen, Z. Tang, C. Wen, B. Dong, H. Liu, C. Zhang, and X. Li, "Intramolecular singlet fission in a face-to-face stacked tetracene trimer," *Phys. Chem. Chem. Phys.*, vol. 20, pp. 6330–6336, 2018.

[41] S. N. Sanders, E. Kumarasamy, K. J. Fallon, M. Y. Sfeir, and L. M. Campos, "Singlet fission in a hexacene dimer: energetics dictate dynamics," *Chem. Sci.*, vol. 11, pp. 1079–1084, 2020.

[42] R. Mondal, B. K. Shah, and D. C. Neckers, "Photogeneration of heptacene in a polymer matrix," *Journal of the American Chemical Society*, vol. 128, no. 30, pp. 9612–9613, 2006.

[43] R. Einholz, T. Fang, R. Berger, P. Grüninger, A. Früh, T. Chassé, R. F. Fink, and H. F. Bettinger, "Heptacene: Characterization in solution, in the solid state, and in films," *Journal of the American Chemical Society*, vol. 139, no. 12, pp. 4435–4442, 2017.

[44] T. Jadhav, B. Dhokale, and R. Misra, "Aggregation induced emission and mechanochromism in tetraphenylethene substituted pyrazabole," *RSC advances*, vol. 5, no. 83, pp. 68187–68191, 2015.

[45] B. Purushothaman, M. Bruzek, S. R. Parkin, A.-F. Miller, and J. E. Anthony, "Synthesis and structural characterization of crystalline nonacenes," *Angewandte Chemie International Edition*, vol. 50, no. 31, pp. 7013–7017, 2011.

[46] J. Han, X. Liu, Y. Li, Z. Lou, M. Yi, H. Kong, and J. Luo, "New synthetic approaches for hexacene and its application in thin-film transistors," *Organic Chemistry Frontiers*, vol. 6, no. 16, pp. 2839–2843, 2019.

[47] B. Purushothaman, S. R. Parkin, and J. E. Anthony, "Synthesis and stability of soluble hexacenes," *Organic Letters*, vol. 12, no. 9, pp. 2060–2063, 2010.

[48] R. Mondal, C. Tönshoff, D. Khon, D. C. Neckers, and H. F. Bettinger, "Synthesis, stability, and photochemistry of pentacene, hexacene, and heptacene: A matrix isolation study," *Journal of the American Chemical Society*, vol. 131, no. 40, pp. 14281–14289, 2009.

[49] M. Watanabe, W.-T. Su, K.-Y. Chen, C.-T. Chien, T.-H. Chao, Y. J. Chang, S.-W. Liu, and T. J. Chow, "A soluble precursor of hexacene and its application in thin film transistors," *Chem. Commun.*, vol. 49, pp. 2240–2242, 2013.

[50] T. J. Chow, "Hexacene: Synthesis, properties and future perspectives," *The Chemical Record*, vol. 15, no. 6, pp. 1137–1139, 2015.

[51] C. Tönshoff and H. F. Bettinger, "Photogeneration of octacene and nonacene," *Angewandte Chemie International Edition*, vol. 49, no. 24, pp. 4125–4128, 2010.

[52] R. Zuzak, R. Dorel, M. Kolmer, M. Szymonski, S. Godlewski, and A. M. Echavarren, "Higher acenes by on-surface dehydrogenation: From heptacene to undecacene," *Angewandte Chemie International Edition*, vol. 57, no. 33, pp. 10500–10505, 2018.

[53] W. Chen, F. Yu, Q. Xu, G. Zhou, and Q. Zhang, "Recent progress in high linearly fused polycyclic conjugated hydrocarbons (pchs, n $>$ 6) with well-defined structures," *Advanced Science*, vol. 7, no. 12, p. 1903766, 2020.

[54] J. Krüger, F. García, F. Eisenhut, D. Skidin, J. M. Alonso, E. Guitián, D. Pérez, G. Cuniberti, F. Moresco, and D. Peña, "Decacene: On-surface generation," *Angewandte Chemie*, vol. 129, no. 39, pp. 12107–12110, 2017.

[55] A. Pérez-Guardiola, M. E. Sandoval-Salinas, D. Casanova, E. San-Fabián, A. J. Pérez-Jiménez, and J. C. Sancho-García, "The role of topology in organic molecules: origin and comparison of the radical character in linear and cyclic oligoacenes and related oligomers," *Phys. Chem. Chem. Phys.*, vol. 20, pp. 7112–7124, 2018.

[56] L. Pauling, *The Nature of the Chemical Bond*, vol. 260. Cornell university press Ithaca, NY, 1960.

[57] Y. Zhao and D. G. Truhlar, "The m06 suite of density functionals for main group thermochemistry, thermochemical kinetics, noncovalent interactions, excited states, and transition elements: two new functionals and systematic testing of four m06-class functionals and 12 other functionals," *Theoretical Chemistry Accounts*, vol. 120, no. 1, pp. 215–241, 2008.

[58] D. Casanova and M. Head-Gordon, "Restricted active space spin-flip configuration interaction approach: theory, implementation and examples," *Phys. Chem. Chem. Phys.*, vol. 11, pp. 9779–9790, 2009.

[59] D. Casanova, "Efficient implementation of restricted active space configuration interaction with the hole and particle approximation," *J. Comput. Chem.*, vol. 34, no. 9, pp. 720–730, 2013.

[60] M. D. Hanwell, D. E. Curtis, D. C. Lonie, T. Vandermeersch, E. Zurek, and G. R. Hutchison, "Avogadro: an advanced semantic chemical editor, visualization, and analysis platform," *J. Cheminf.*, vol. 4, no. 1, p. 17, 2012.

[61] M. Head-Gordon, "Characterizing unpaired electrons from the one-particle density matrix," *Chem. Phys. Lett.*, vol. 372, no. 3-4, pp. 508–511, 2003.

[62] Y. Shao, Z. Gan, E. Epifanovsky, A. T. B. Gilbert, M. Wormit, J. Kussmann, A. W. Lange, A. Behn, J. Deng, X. Feng, D. Ghosh, M. Goldey, P. R. Horn, L. D. Jacobson, I. Kaliman, R. Z. Khaliullin, T. Kus, A. Landau, J. Liu, E. I. Proynov, Y. M. Rhee, R. M. Richard, M. A. Rohrdanz, R. P. Steele, E. J. Sundstrom, H. L. Woodcock, P. M. Zimmerman, D. Zuev, B. Albrecht, E. Alguire, B. Austin, G. J. O. Beran, Y. A. Bernard, E. Berquist, K. Brandhorst, K. B. Bravaya, S. T. Brown, D. Casanova, C.-M. Chang, Y. Chen, S. H. Chien, K. D. Closser, D. L. Crittenden, M. Diedenhofen, R. A. DiStasio, H. Do, A. D. Dutoi, R. G. Edgar, S. Fatehi, L. Fusti-Molnar, A. Ghysels, A. Golubeva-Zadorozhnaya, J. Gomes, M. W. D. Hanson-Heine,

P. H. P. Harbach, A. W. Hauser, E. G. Hohenstein, Z. C. Holden, T.-C. Jagau, H. Ji, B. Kaduk, K. Khistyaev, J. Kim, J. Kim, R. A. King, P. Klunzinger, D. Kosenkov, T. Kowalczyk, C. M. Krauter, K. U. Lao, A. D. Laurent, K. V. Lawler, S. V. Levchenko, C. Y. Lin, F. Liu, E. Livshits, R. C. Lochan, A. Luenser, P. Manohar, S. F. Manzer, S.-P. Mao, N. Mardirossian, A. V. Marenich, S. A. Maurer, N. J. Mayhall, E. Neuscamman, C. M. Oana, R. Olivares-Amaya, D. P. O'Neill, J. A. Parkhill, T. M. Perrine, R. Peverati, A. Prociuk, D. R. Rehn, E. Rosta, N. J. Russ, S. M. Sharada, S. Sharma, D. W. Small, A. Sodt, T. Stein, D. Stuck, Y.-C. Su, A. J. W. Thom, T. Tsuchimochi, V. Vanovschi, L. Vogt, O. Vydrov, T. Wang, M. A. Watson, J. Wenzel, A. White, C. F. Williams, J. Yang, S. Yeganeh, S. R. Yost, Z.-Q. You, I. Y. Zhang, X. Zhang, Y. Zhao, B. R. Brooks, G. K. L. Chan, D. M. Chipman, C. J. Cramer, W. A. Goddard, M. S. Gordon, W. J. Hehre, A. Klamt, H. F. Schaefer, M. W. Schmidt, C. D. Sherrill, D. G. Truhlar, A. Warshel, X. Xu, A. Aspuru-Guzik, R. Baer, A. T. Bell, N. A. Besley, J.-D. Chai, A. Dreuw, B. D. Dunietz, T. R. Furlani, S. R. Gwaltney, C.-P. Hsu, Y. Jung, J. Kong, D. S. Lambrecht, W. Liang, C. Ochsenfeld, V. A. Rassolov, L. V. Slipchenko, J. E. Subotnik, T. Van Voorhis, J. M. Herbert, A. I. Krylov, P. M. W. Gill, and M. Head-Gordon, "Advances in molecular quantum chemistry contained in the q-chem 4 program package," *Mol. Phys.*, vol. 113, no. 2, pp. 184–215, 2015.

[63] M. J. Frisch, G. W. Trucks, H. B. Schlegel, G. E. Scuseria, M. A. Robb, J. R. Cheeseman, G. Scalmani, V. Barone, B. Mennucci, G. A. Petersson, H. Nakatsuji, M. Caricato, X. Li, H. P. Hratchian, A. F. Izmaylov, J. Bloino, G. Zheng, J. L. Sonnenberg, M. Hada, M. Ehara, K. Toyota, R. Fukuda, J. Hasegawa, M. Ishida, T. Nakajima, Y. Honda, O. Kitao, H. Nakai, T. Vreven, J. A. Montgomery, Jr., J. E. Peralta, F. Ogliaro, M. Bearpark, J. J. Heyd, E. Brothers, K. N. Kudin, V. N. Staroverov, R. Kobayashi, J. Normand, K. Raghavachari, A. Rendell, J. C. Burant, S. S. Iyengar, J. Tomasi, M. Cossi, N. Rega, J. M. Millam, M. Klene, J. E. Knox, J. B. Cross, V. Bakken, C. Adamo, J. Jaramillo, R. Gomperts, R. E. Stratmann, O. Yazyev, A. J. Austin, R. Cammi, C. Pomelli, J. W. Ochterski, R. L. Martin, K. Morokuma, V. G. Zakrzewski, G. A. Voth, P. Salvador, J. J. Dannenberg, S. Dapprich, A. D. Daniels, [U+FFFD] Farkas, J. B. Foresman, J. V. Ortiz, J. Cioslowski, and D. J. Fox, "Gaussian∼09 Revision E.01." Gaussian Inc. Wallingford CT 2009.

Chapter 5

Anionic and cationic oligomer diradicals

Conjugated organic polymers have been extensively investigated because of their promising magnetic, optical and electronic properties for applications in solar cells, charge carriers, energy storage, bioelectronics, or chemical sensors.(1; 2; 3; 4; 5) Polyvinylenes, polythiophenes, poly-*p*-phenylene, polyfluorene, polypyrrole, among others(6; 7; 8; 9; 10) are paramount examples of conjugated polymers. They exhibit electronic resonance between aromatic and quinoidal structures, as Figure 5.1 shows.

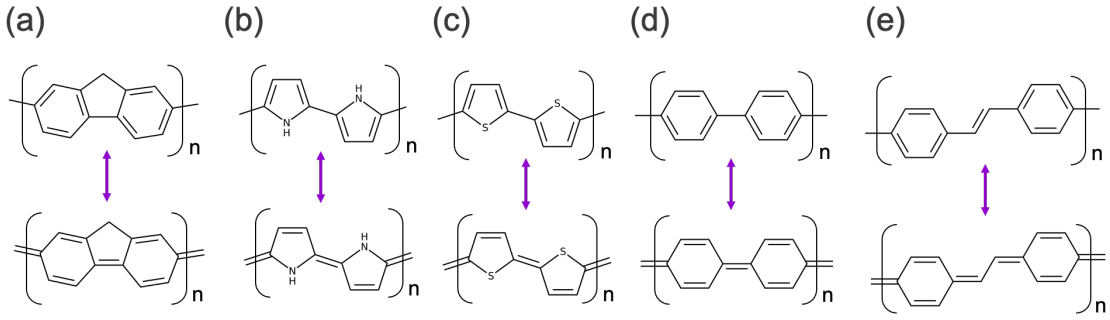

Figure 5.1: Polyfluorene (a), polypyrrole (b), polythiophene (c), poly-*p*-phenylene (d), polyvinylene (e) in aromatic (top) and quinoidal (bottom) structures.

A typical strategy to improve their electronic and magnetic properties consists in substituting the polymeric chains with electron donor and withdrawing groups. For instance, n-type (electron acceptor) and p-type (electron donor) polythiophenes have proved their excellent performance for decades(11; 12; 13; 14) in organic field-effect transistors,(4) organic light-emitting diodes, photovoltaic devices, batteries, solar cells,(15) etc.(16) and catalyst to solar energy utilization.(17) Notably, structural modifications, *e.g.*, functionalization of 3,4 positions or introduc-

tion of a copolymer between thiophene units, have been shown to modulate their features.(18; 19; 20; 21)

Modelling of the optoelectronic properties of polymers is commonly addressed using the so-called oligomer approach, which relies on the extrapolation of the properties of finite length oligomers to the polymer limit.(22) From a fundamental point of view, oligomers provide accurate structure-property relationships that are beneficial for the knowledge and understanding of the photomechanisms in polymers and for unraveling the design rules for the elaboration of new materials with enhanced functionalities.(23; 24; 25)

Stable organic oligomers with closed-shell (CS) singlet ground state, *i.e.*, large HOMO-LUMO energy gap, can be transformed into diradicals by adding or removing a pair of electrons. Double oxidation of the system may lead to the formation of a dication-diradical. If the HOMO to HOMO-1 energy gap is rather narrow, removing two electrons leads to a situation in which a pair of HOMO and LUMO are nearly degenerate and can share electronic population. Similarly, if the LUMO and LUMO+1 energy gap is small enough, the double reduction can lead to the partial occupancy of both HOMO and LUMO orbitals of the formed dianion. Thus a di-ionic diradicaloid species appears (Figure 5.2).

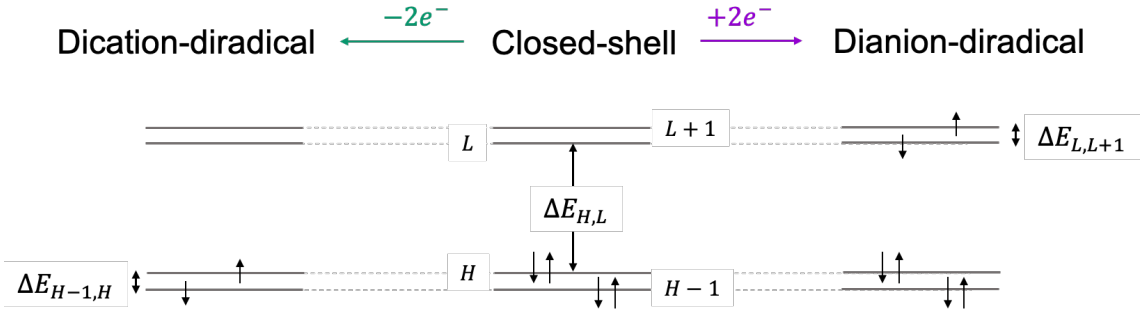

Figure 5.2: Dication (left) and dianion (right) diradical formation from a closed-shell structure (center) by double oxidation and reduction, respectively.

The present chapter is devoted to the exhaustive description of two organic diradical oligomers. The main goal is to unravel the origin of their diradical nature and what dictates their structural, photophysical, and spectroscopic features. In the first part, oligothiophene derivatives will be investigated. In the second part, the equilibrium between aromatic and quinoidal structures (and the associated variation of radical character) of a poly-*p*-phenylene derivative will be described in detail.

5.1 Thieno[3,4-c]pyrrole-4,6-dione oligothiophene

Thiophene based π-functional materials have been intensively investigated for their application in organic (opto)electronic devices. Recently, Zhu et al. developed a new low-bandgap copolymer combining n-type (electron acceptor) thieno[3,4-c]pyrrole-4,6-dione oligothiophenes (**TPD**) units with the quinoid-enhancing thieno[3 ,4-*b*]thiophene (T*b*T) moiety and a weakly electron-donating benzo[1,2-*b*:4,5b'] dithiophene (BDT),(20) which was successfully applied to polymeric solar cells demonstrating a power conversion efficiency over 9%.(26) In order to investigate the nature of TPD as an acceptor moitey, a new series of thieno[3,4-c]pyrrole-4,6-dione oligothiophenes, $\mathbf{OTPD}_n$ ($n = 2-6$, Figure 5.3b), was synthesized and characterized spectroscopically, and found to be able to stabilize both anions and dianions in their reduced forms. The properties of anions and dianions of oligothiophenes have been scarcely investigated, since oligothiophenes are better suited for the stabilization of positive charges than negative ones. The study of $\mathbf{OTPD}_n$ oligomers therefore represent a significant step towards understanding the oligothiophene anionic species.

In the following, I present a comprehensive computational investigation of the main electronic features of $\mathbf{OTPD}_n$ oligomers in their neutral, anionic and dianionic forms. Interestingly, these oligomers display a clear spatial opposition between the peripheral dione groups and the central oligothiophene array, which establish two separated electronic domains: one among the dione units and one among the thiophene moieties, referred to as interdione (IDn) and interthiophene (IT) π-conjugation paths (Figure 5.3b and c), respectively.

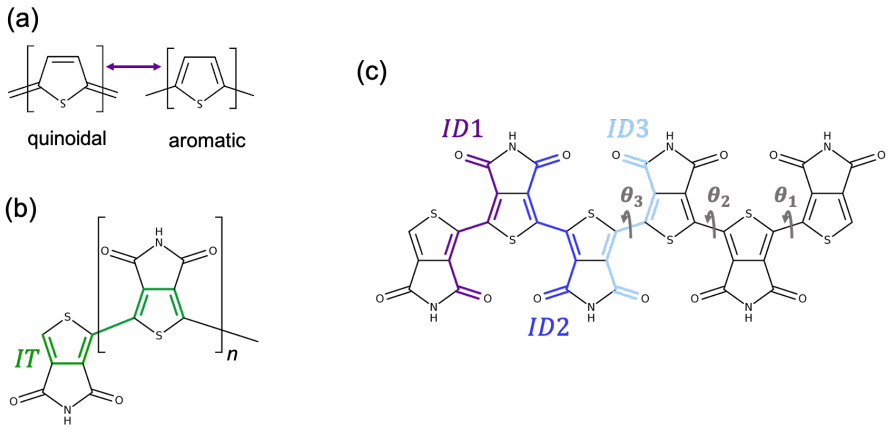

Figure 5.3: Quinoidal and aromatic forms in conjugated thiophene oligomers and polymers (a). Structure of $\mathbf{OTPD}_n$ with $n = 1-5$, interthiophene (IT) π-conjugation path indicated in green (b). Interdione (IDn) π-conjugation paths and the dihedral angle (θ) between adjacent thiophene units of **[OTPD**$_n$] oligomers (c).

5.1.1 Monoanionic species

The ground state molecular geometry of the **OTPD**$_n$ presents significant structural differences as a function of n (Table 5.1). Namely, the (quasi-)planarity of the backbone, measured by the dihedral angle (θ_n) between adjacent TPD units (Figure 5.3b), decreases as the system size increases, in agreement with what has been reported theoretically and experimentally for other substituted oligothiophenes.(27; 19; 28; 29) Despite the fluctuation of θ_n, conjugation along the thiophene backbone is not affected, as illustrated by the evolution of the bond length alternation of the IT path (BLA$_{IT}$ in Table 5.1), for which the largest decrease is found from the dimer to the trimer. Such change is associated with the downshift of the band assigned to the collective stretching of C-C bonds in the Raman spectra (as shown in reference(30), Figure 2) and can be understood as the result of the slight increase of the π-conjugation from **OTPD**$_2$ $\rightarrow$ **OTPD**$_6$. On the other hand, the BLA of the interdione conjugation path does not vary with the length of the oligomer.

species	BLA$_{IT}$	BLA$_{ID1}$	BLA$_{ID2}$	BLA$_{ID3}$	θ_1	θ_2	θ_3
OTPD$_2$	0.063	0.092	-	-	179.9	-	-
[OTPD$_2$**]**$^{-1}$	0.031	0.023	-	-	180.0	-	-
[OTPD$_2$**]**$^{-2}$	-0.003	-0.061	-	-	170.7	-	-
OTPD$_3$	0.052	0.091	-	-	171.2	-	-
[OTPD$_3$**]**$^{-1}$	0.028	0.048	-	-	171.2	-	-
[OTPD$_3$**]**$^{-2}$	0.017	0.011	-	-	165.2	-	-
OTPD$_4$	0.055	0.091	0.094	-	171.7	155.1	-
[OTPD$_4$**]**$^{-1}$	0.029	0.065	0.049	-	171.8	164.0	-
[OTPD$_4$**]**$^{-2}$	0.025	0.021	0.070	-	169.1	153.9	-
OTPD$_5$	0.050	0.091	0.092	-	172.1	158.0	-
[OTPD$_5$**]**$^{-1}$	0.029	0.073	0.057	-	171.8	165.4	-
[OTPD$_5$**]**$^{-2}$	0.026	0.027	0.071	-	170.4	155.8	-
OTPD$_6$	0.051	0.092	0.094	0.088	170.1	153.7	180.0
[OTPD$_6$**]**$^{-1}$	0.034	0.078	0.065	0.060	171.1	166.1	178.8
[OTPD$_6$**]**$^{-2}$	0.025	0.038	0.061	0.074	169.8	159.9	179.8

Table 5.1: Bond length alternation (in Å) of π-conjugation paths IT, $ID1-3$ and dihedral angles θ_{1-3}, as described in Figure 5.3.

Aromatic/quinoidal forms of the five-membered thiophene rings (Figure 5.3a)

can be described by the double-single bond alternation of the C-C bonds in the ring, where C=C-C=C (C-C=C-C) alternation pattern corresponds to the aromatic (quinoidal) structure. A visual representation is obtained by plotting the three bonds of their π-backbone and connecting them with a line. A Λ-shape line corresponds to an aromatic ring while a V-shape is indicative of a quinoidal structure. Figure 5.4 shows the bond length distribution of the π-conjugated backbone of $\mathbf{OTPD}_6$, where thiophene units have almost equivalent aromatic rings connected by C-C bonds of constant length.

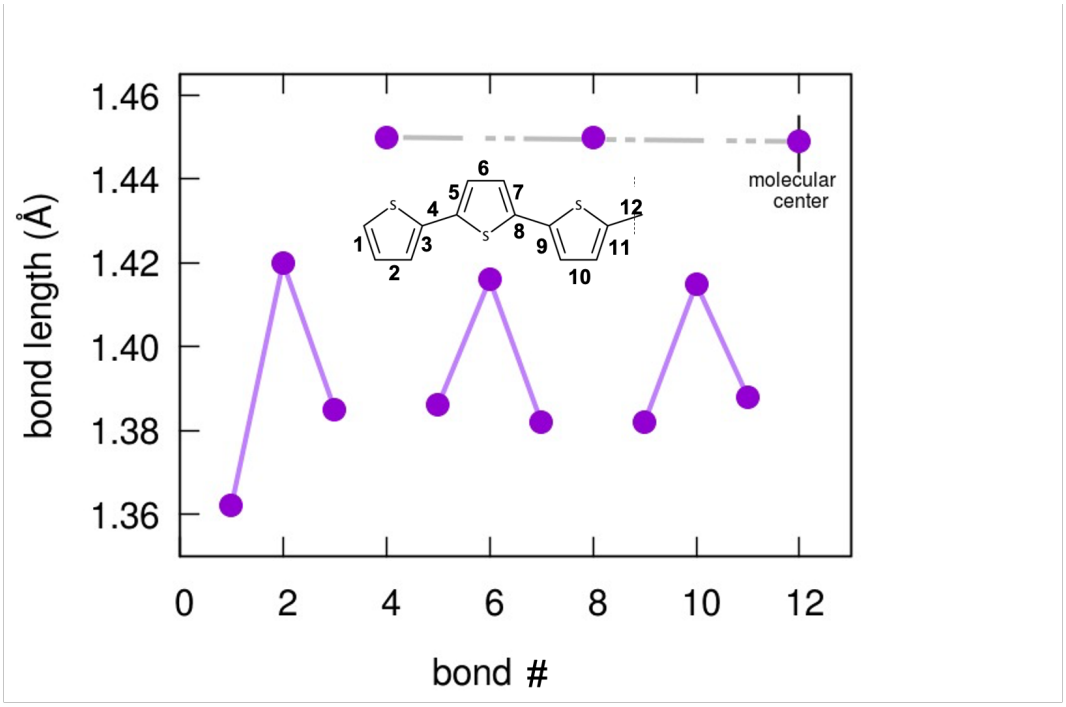

Figure 5.4: C-C bond lengths along the IT path of $\mathbf{OTPD}_6$. Purple lines connect the three C-C bond lengths within each thiophene ring, while the dashed gray line connects the interthiophene bond lengths. The bond labels of a half of $\mathbf{OTDP}_6$ are shown in the inset.

All $\mathbf{OTPD}_n$ oligomers exhibit a large HOMO-LUMO energy gap in their singlet ground state (Table 5.2), illustrating their closed-shell character. The substantial adiabatic energy gap to the lowest triplet further supports the closed-shell nature of the ground state.

The consecutive formation of the anion and dianion is observed by means of cyclic voltammetry measurements, with a very weak size-dependency of the reduction potentials, from -1.65 eV and -1.85 eV in the trimer to -1.38 eV and -1.55 eV in the hexamer (as shown in reference(30), Figure 4). This behaviour suggests that the dione group plays a key role in the stabilization of the injected charge by resonance between adjacent TPD units (IDn paths on Figure 5.3). It is noteworthy that the LUMO-LUMO+1 energy difference is rather small, suggesting a potential diradical character in the dianionic species.

OTPD$_n$	ΔE_{ST}	$\Delta E_{H,L}$	$\Delta E_{L,L+1}$
n = 2	48.1	88.5	20.1
n = 3	42.7	76.6	8.8
n = 4	39.9	70.9	8.8
n = 5	38.9	67.8	7.5
n = 6	38.0	65.3	6.9

Table 5.2: Adiabatic energy gaps in kcal mol^{-1} between closed-shell singlet and triplet states (ΔE_{ST}). $\Delta E_{H,L}$ ($\Delta E_{L,L+1}$) is the energy difference between HOMO (LUMO) and LUMO (LUMO+1) orbitals in the ground state geometry.

Single reduction of **OTPD**$_n$ leads to the formation of the monoanion mono-radicals **[OTPD**$_n$**]**$^{-1}$. The distribution of the excess charge over each thiophene unit is presented in Figure 5.5. The additional electron is shared equitably between monomers in **[OTPD**$_n$**]**$^{-1}$ with $n = 2 - 4$. More specifically, atomic charge analysis for the smallest oligomer suggests that the excess charge is located over oxygen atoms in dione groups and in resonance with the adjacent units through the inter-dione path (*IDn* in Figure 5.3c). As a result, there is an increment of the conjugation over the *IDn* path, *i.e.*, the BLA$_{IDn}$ decreases. When $n = 3$, the additional electron delocalizes over the two equivalent interdione paths. The presence of another dione group in the extreme thiophene unit explains the asymmetrical charge distribution. In the tetramer, excess of charges in oxygen atoms are in resonance only through the ID path between central units, and the charge is equally distributed. Finally, a moderate charge localization over the molecular center is observed for $n = 5$ and 6.

Structurally, a slight increase of the molecular planarity of the monoanionic oligomers is obtained, with an average dihedral angle (θ_2) of 165° (155° in neutral forms), while θ_1 and θ_3 barely change with respect to the neutral species (see Table 5.1). Structural stabilization of the additional charge translates into significant changes in the molecular bond lengths. Namely, BLA$_{IT}$ of **[OTPD***n***]**$^{-1}$ considerably decreases as compared to the neutral form. The BLA$_{ID}$ of monoanions is also lower, with a strong dependence on the oligomer size. Interestingly, the central units are the ones showing the smaller value of BLA$_{ID}$, meaning that the bond lengths along this path are more homogeneous and the π-conjugation increases by delocalization of additional charge. This result is in good agreement with what was observed by cyclic voltammetry, *i.e.*, that the charge is mainly stabilized by the dione group and has a weak dependence on the oligomer length.

A more detailed picture can be seen from the bond length distribution along the IT path as shown for **[OTDP**$_6$**]**$^{-1}$ in Figure 5.6. While thiophene units at the molecular ends are aromatic, this character gradually decreases towards the

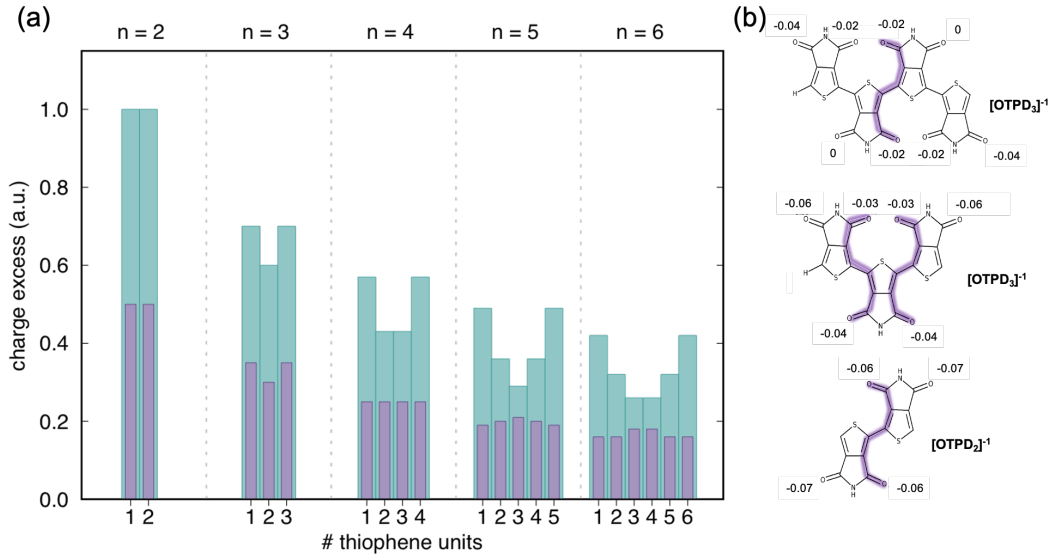

Figure 5.5: Distribution of the Mulliken charge over each thiophene unit in $\mathbf{OTPD}_n$ monoanions (purple bars) and dianions (green bars) (a). The ID path for $\mathbf{[OTPD}n\mathbf{]}^{-1}$ ($n = 2 - 4$) and atomic charge of O atom are illustrated (b).

central rings, along with a decrease of the interring distance. Comparison to the neutral $\mathbf{OTDP}_6$ (Figure 5.4) illustrates that the main geometrical effect of adding an electron is the gain in quinoidal character at the molecular center.

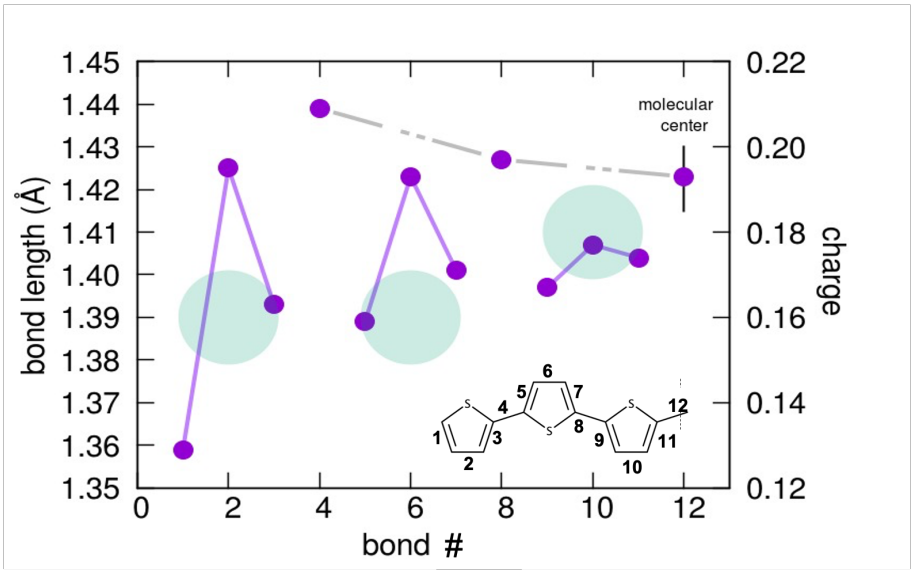

Figure 5.6: C-C bond lengths in the IT path of $\mathbf{[OTDP}_6\mathbf{]}^{-1}$. Purple lines connect the three C-C bond lengths within each thiophene ring, while the dashed gray line connects the interthiophene bond lengths. The bond labels of a half of $\mathbf{[OTDP}_6\mathbf{]}^{-1}$ are shown in the inset.

All these features are a clear indication that charge stabilization leads to a distortion of the geometry that confines the unpaired electron (the additional charge).

In 1985, Brédas(31) characterized this kind of charge localization in organic polymers and defined it as a polaron (as in solid materials), *i.e.*, a radical-ion associated with a lattice distortion. Since then, the formation of polarons has been mainly described in cationic oligomers, but it has been theoretically proven that monocations and monoanions of pristine oligothiophenes localize the charge in very similar manners.(32) In anion-radicals $\mathbf{[OTPD}_n\mathbf{]}^{-1}$ (up to 6 units at least), a polaron is localized over the molecular center.

5.1.2 Dianionic species: Bipolaron vs polaron-pair

Following the reduction of $\mathbf{[OTPD}_n\mathbf{]}^{-1}$ to $\mathbf{[OTPD}_n\mathbf{]}^{-2}$, we envision two possible situations: a) a bipolaron, in which two negative charges are confined together and associated with a single but strong geometrical distortion, and a closed-shell like structure; or b) a polaron-pair, as a result of the formation of two interacting polarons (localized radical-ion) leading to a diradical-dianionic species.(31)

The charge distribution over TPD units for $n = 2$ and 3 is simply twice the one observed in the monoanions, as a consequence of their small size. For larger dianionic oligothiophenes, namely $\mathbf{[OTPD}_{4-6}\mathbf{]}^{-2}$, both charges are symmetrically localized on the external units of the oligomer, as presented in Figure 5.5a.

Geometrical distortions of the dianions are summarized in Table 5.1. To offer a better interpretation of the results, I will focus on the oligomers with $n = 4 - 6$. In these larger oligothiophenes, the stabilization of a second electron reverts the planarization gained (θ_2) in the monoanionic structures, returning to the distortion exhibited by the neutral parents. BLA_{IT} is not significantly affected by the reduction of $\mathbf{[OTPD}_{4-6}\mathbf{]}^{-1}$, supporting the idea that the thiophene π-backbone plays a minor role in the charge stabilization. Interestingly, BLA_{ID2-3} increases, meaning that in these paths the π-conjugation is lower than in monoanions, but the opposite effect is observed across $ID1$, where conjugation significantly increases with a very weak dependence on the size of the system. These results indicate two equivalent geometrical deformations localized in each extreme of the molecule.

A better insight on the role of the interthiophene path is provided by the evolution of the C-C bond lengths of $\mathbf{[OTPD}_6\mathbf{]}^{-2}$ π-backbone (Figure 5.7). Thiophene rings at the extremities clearly exhibit the pattern classically associated to aromatic thiophene-rings, while the second thiophene unit shows a more quinoidal-like structure, before a partial recovery of aromaticity is found in the central thiophene ring. Accordingly, the interring bond length becomes larger towards the molecular center (more single bond character).

On the other hand, $\mathbf{[OTPD}_{2-3}\mathbf{]}^{-2}$ are very challenging systems whose small size leads to a severe structural deformation driven by the accomodation of two charges

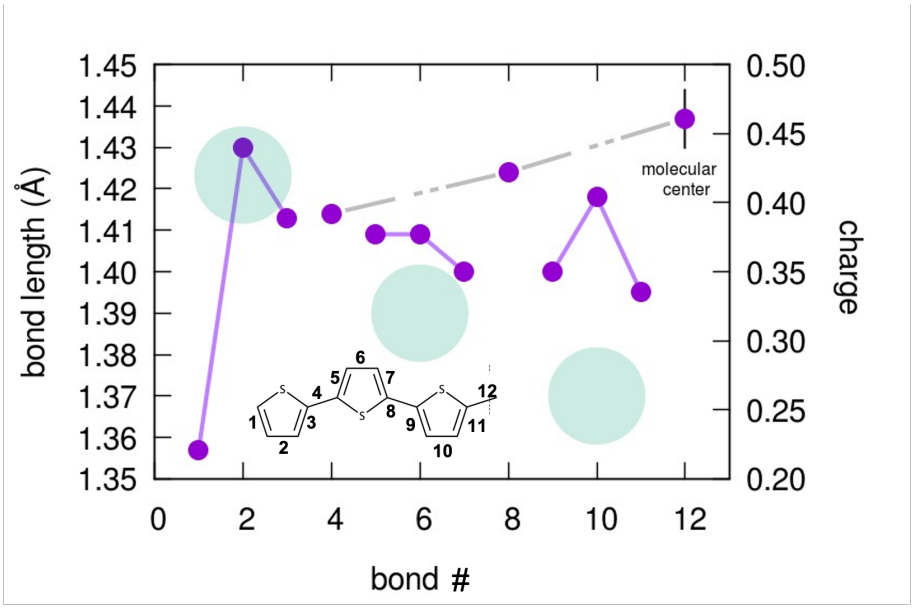

Figure 5.7: C-C bond lengths in the *IT* path of $\mathbf{[OTDP_6]}^{-2}$. Purple lines connect the three C-C bond lengths within each thiophene ring, while dashed gray line connects the interthiophene bond lengths. The bond labels of a half of $\mathbf{[OTDP_6]}^{-2}$ are shown in the inset.

in the system.

The small LUMO to LUMO+1 energy gap of the neutral oligomers suggests the formation of a dianion diradical by addition of two electrons. Indeed, the small $\Delta E_{L,L+1}$ in neutral $\mathbf{OTPD}_n$ allows the partial population of LUMO+1 when two electrons are added to the system, which induces the formation of two (quasi) degenerate HOMOs in $\mathbf{[OTPD}_n\mathbf{]}^{-2}$, see Table 5.2. Radical characterization of oligothiophene dianions is presented in Table 5.3. The adiabatic energy difference between open and closed-shell solutions (ΔE^{ad}_{OS-CS}) shows that all systems hold an open-shell (OS) singlet ground state. When $n = 2$, $\Delta E^{ad}_{OS-CS} = 0.04$ kcal mol^{-1} and $\mathbf{[OTPD_2]}^{-2}$ must be considered a closed-shell system. On the other hand, when $n = 6$, the CS solution is destabilized by 4.2 kcal mol^{-1} with respect to the OS one. This is reaffirmed by the adiabatic and vertical energy gaps between the open-shell singlet and the lowest triplet state, both decreasing substantially from $n = 2$ to $n = 4$. For $n = 4-6$, ΔE^{ad}_{OS-T} remains nearly constant. Based on these trends, it can be deduced that the lengthening of the oligomer will not result in an increase of the radical character (beyond the diradical). In fact, the quintet state, which represents an ideal tetraradical (4 unpaired electrons), is rather high in energy. Accordingly, the number of unpaired electrons is close to 2 ($n = 4-6$), meaning that they are not perfect diradicals, but can be appropriately named diradicaloids. Indeed, natural orbitals shown in Figure 5.8 evidence the presence of two weakly interacting radical moieties located over each molecular end, with electronic occupancy numbers approaching 1 as the molecular length increases.

$[\mathbf{OTPD}_n]^{-2}$	ΔE^{ad}_{OS-CS}	ΔE^{ad}_{OS-T}	$^{[a]}\Delta E^{ad}_{OS-T}$	$N_u^{[a]}$	ΔE^{vert}_{OS-Q}	ΔE_{int}
n = 2	∼0.0	13.6	21.3	0.47	77.0	92.04
n = 3	1.1	1.5	1.2	0.86	62.9	77.35
n = 4	2.2	0.4	0.7	1.61	48.4	66.72
n = 5	3.5	0.3	0.5	1.80	46.5	58.50
n = 6	4.2	0.4	0.3	1.84	44.4	52.22

Table 5.3: Adiabatic (ad) and vertical (vert) energy gaps in kcal mol^{-1}. $^{[a]}$ Computed at RAS-SF level. ΔE_{int} is the energy difference between the dianion and twice the monoanion.

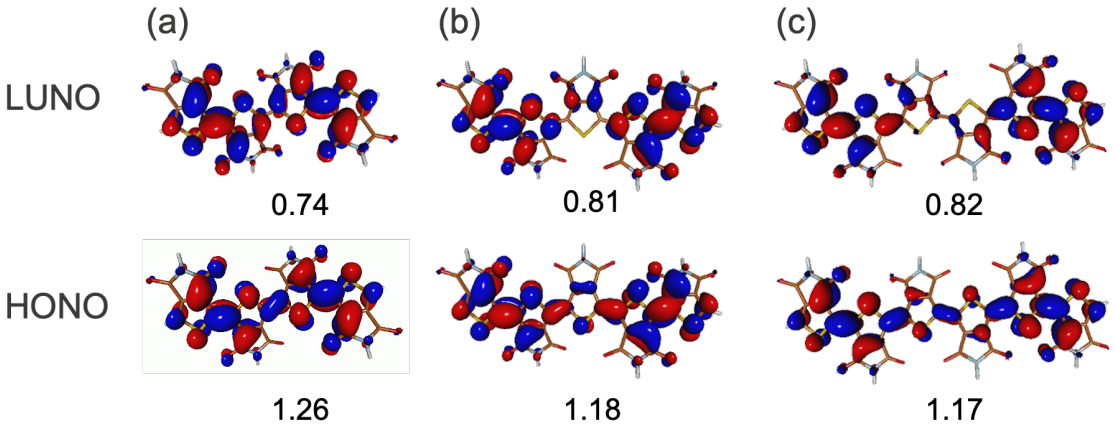

Figure 5.8: Frontier natural orbitals with their electronic occupation numbers for $[\mathbf{OTPD}_4]^{-2}$ (a), $[\mathbf{OTPD}_5]^{-2}$ (b), and $[\mathbf{OTPD}_6]^{-2}$ (c). Figure adapted from reference(30).

The interaction energy of the two radicals can be approximated as $\Delta E_{int} = \Delta E^{ad}_{di} - \Delta E^{ad}_{2mono}$, where the first term on the right side of the equation is the difference between the dianionic and the neutral compounds ($\Delta E^{ad}_{di} = E^{ad}_D - E^{ad}_N$), *i.e.*, the increment of energy from adding two electrons to the system. On the other hand, ΔE^{ad}_{2mono} is twice the energy gap between monoanionic and neutral compounds ($\Delta E^{ad}_{2mono} = 2(E^{ad}_M - E^{ad}_N)$) . Thus, ΔE_{int} approximates the difference of having either a diradicaloid or two "independent" radicals (twice a radical). As n increases, ΔE_{int} decreases, reproducing the dependence on the distance of the classical repulsion between two negative charges ($1/n \propto 1/\mathrm{R}$, Figure 5.9), in good agreement with the picture exposed by the natural orbitals.

Therefore, we conclude that the electronic structure of $[\mathbf{OTPD}_{4-6}]^{-2}$ can be described as a polaron-pair with two favorable conjugation routes: the interdione path

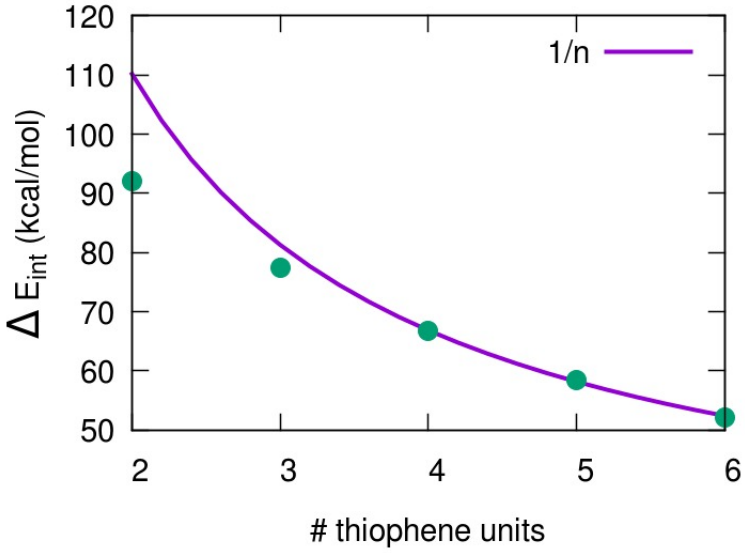

Figure 5.9: Adiabatic energy difference ΔE (kcal/mol) between dianion and twice the monoanion for $n = 2 - 6$. Purple line corresponds to the energy adjusted to a 1/n for $4 \leq n \leq 6$. Figure adapted from reference(30).

which stabilizes the total charge and the interthiophene-interdione path which modulates the diradical character. The small size and closed-shell nature of $\mathbf{[OTPD}_{2-3}\mathbf{]}^{-2}$ is not appropriate to classify them as bipolaron or polaron-pair.

5.1.3 Spectroscopic features

So far, the appearance of polaron, bipolaron, and polaron-pair derived from the consecutive reduction of oligothiopenes have been described here by means of the analysis of geometrical and electronic features. There is a considerable lack of information about the experimental characterization of n-doped oligothiophenes or their polaronic species with only few reports in the literature. Salzner et al.(32) carried out a computational study to investigate the spectroscopic properties of a series of monoanionic and monocationic pristine thiophene oligomers, concluding that the spectra of p- or n-doped species are virtually identical.

UV-VIS/NIR spectra of neutral, monoanion and dianion $\mathbf{OPTD}_n$ have been measured experimentally (as shown in reference(30), Figure 5) and interpreted by means of TD-DFT calculations presented hereafter, the most relevant data being collected in Table 5.4. In neutral oligothiophenes, the maximum of the main band of the absorption spectra is continuously redshifted from colorless (dimer) to strongly yellow-orange (hexamer), which is similar to the behaviour observed in unsubstituted thiophene oligomers.

	$\mathbf{OTPD}_n$	$[\mathbf{OTPD}_n]^{-1}$		$[\mathbf{OTPD}_n]^{-2}$	
n	S_1	S_1	S_2	S_1	S_2
2	347 (0.499)	981 (0.057)	414 (0.447)	-	846 (0.091)
3	402 (0.738)	1784 (0.076)	482 (0.658)	1635 (0.062)	438 (0.134)
4	441 (1.042)	1734 (0.213)	537 (0.954)	1534 (0.103)	601 (0.101)
5	459 (1.276)	1849 (0.365)	573 (1.196)	1879 (0.188)	542 (0.484)
6	475 (1.612)	1975 (0.567)	596 (1.432)	2089 (0.344)	557 (0.691)

Table 5.4: Wavelength (in nm) of the two lowest singlet-singlet vertical excitations for $\mathbf{OTPD}_n$, $[\mathbf{OTPD}_n]^{-1}$ and $[\mathbf{OTPD}_n]^{-2}$ (n = 2-6) computed at the B3LYP/6-31G(d,p) level. Values in parenthesis correspond to oscillator strengths.

The bathochromic shift measured in neutral oligothiophenes upon increasing n is nicely reproduced by our calculations with a gradual shift of the $S_0 \rightarrow S_1$ vertical transition as n increases, from 347 nm for $n = 2$ to 475 nm for $n = 6$. This transition is characterized by the electronic excitation from HOMO to LUMO, in line with what is expected for closed-shell π-conjugated systems.

Upon reduction of the $\mathbf{OTPD}_{3-6}$ oligomers, the absorption spectra exhibit two important bands due to their radical nature, namely a main absorption in the visible and a second broad weak one in the infrared. This is the typical two-bands pattern for the open-shell doublet of anions and cations of linear π-conjugated oligomers.(31) This is fully supported by our calculations, which characterize the bands of these open-shell anion radicals as two excitations that involve the doubly occupied, semi-occupied, and empty frontier molecular orbitals. The first band corresponds to the HOMO $\rightarrow$ LUMO transition, as in neutral compounds, but red-shifted from 347 nm to 414 nm when $n = 2$, and from 475 nm to 596 nm for $n = 6$. The second one involves the excitations SOMO $\rightarrow$ LUMO and HOMO $\rightarrow$ SOMO, with a transition intensity (approximated by the oscillator strength) that increases with the system size.

Similarly, UV-VIS spectra of dianions show a two-bands profile. $[\mathbf{OPTD}_{n=4-6}]^{-2}$ experimental band maxima were characterized at 580/1537 nm ($n = 4$), 569/1590 nm ($n = 5$), and 568/1707 nm ($n = 6$), blueshifted with respect to those of their respective anion radicals. This is typical of dicationic π-conjugated molecules, that discloses a polaron-pair structure,(33) while their dianions are typical closed-shell systems that exhibit a single absorption band in the optical spectrum.(31) The two-bands pattern in the absorption spectra of π-conjugated dianions has been reported in the case of oligofluorenes(34) and assigned to the presence and stabilization of segregated polarons. The separation of the bipolaron structure into two symmetrical polarons (polaron-pair) might justify the similitude of the spectra of radical anions

and polaron-pair dianions in $\mathbf{[OTPD}n\mathbf{]}^{-2}$ compounds.

TD-DFT results identify the main absorption band as the $\pi-\pi^*$ transition from the highest doubly occupied orbital to the lowest totally empty orbital. This band resembles the one in the monoanionic species although slightly blue-shifted. The low-energy broad band associated with the presence of radical species is located in the IR region, a little red-shifted with respect to the low-energy band of the monoanions, and arises from an excitation that involves the two SOMOs. This band is the main spectroscopic characteristic of polarons, in line with the polaron-pair characterization of $\mathbf{[OTPD}_{4-6}\mathbf{]}^{-2}$.

Figure 5.10 shows the simulated absorption spectrum of $\mathbf{[OTPD}_6\mathbf{]}^{-2}$, with assignment of the polaron-pair band and the molecular orbitals involved, as well as the $\pi-\pi^*$ transition. In contrast, the smaller members ($n = 2$ and $n = 3$) just exhibit one absorption band (HOMO-to-LUMO) due to their closed-shell nature.

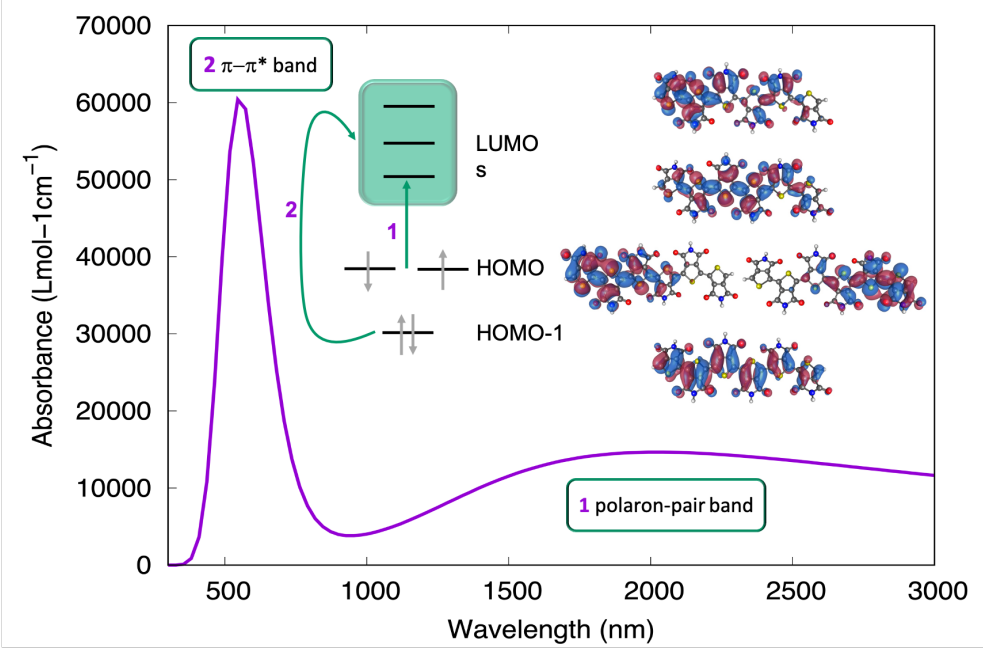

Figure 5.10: Absorption spectrum of the dianion $\mathbf{[OTPD}_6\mathbf{]}^{-2}$. Main orbital-to-orbital transitions are shown in the inset. Figure adapted from reference(30).

An important result of this study was the segmentation of the electronic structure of these $\mathbf{OTPD}_n$ oligomers, which provoked the stabilization of dianions as segregated anions or polaron-pair dianions placed in parallel (*i.e.,* in contrast to polaron-pairs in series, as described in oligofluorenes).(34) The existence of two paths of π-conjugation; i) between neighbor diones and ii) through the thiophene spine was pointed out. They allow interspins and through-bond interactions, which result in the existence of a singlet diradical ground state.

5.2 Diamino Oligophenyl Dication

The Thiele's,(35) Chichibabin's,(36; 37) and Muller's(38) hydrocarbons are the smallest members among the diradicals *p*-phenylene bridged oligomers. They have a singlet-ground state with a narrow singlet-triplet energy gap, and as Kekulé diradicals can be described by a superposition of open-shell (aromatic) and closed-shell (quinoidal) resonance structures (Figure 5.11). Typically, they are unstable molecules with no practical application. In order to understand their properties, stable derivatives have been synthesized and extensively studied.(39; 40; 41)

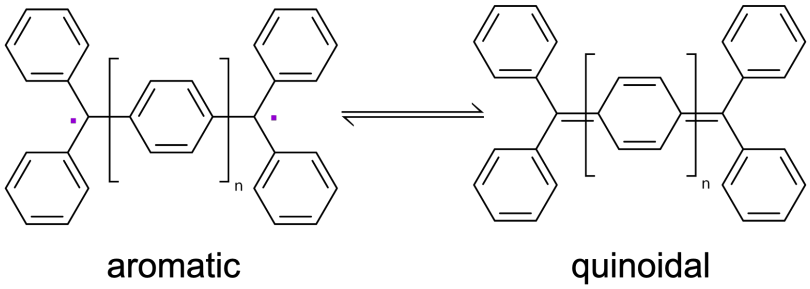

Figure 5.11: Aromatic (radical) and quinoidal (closed-shell) resonant forms of Thiele's (n = 1), Chichibabin's (n = 2) and Müller's (n = 3) hydrocarbons.

Recently, the formation of a bis(triarylamine) unit in each extreme of the *p*-phenylene bridge by substitution of the carbon centers with nitrogen atoms, and posterior generation of the dication, has been proved to be an efficient way to obtain stable diradicals analogous to the Thiele's series.(42; 40) Concretely, the stable 4,4'-di(bis(1,4-methylphenyl)amino)-*p*-terphenyl dication (named as $\mathbf{1}^{+2}$ in the original work, herein $\mathbf{PAT}^{+2}$), depicted in Figure 5.12, was synthesized in 2016 by Su et al.(43) Interestingly, its characterization by EPR spectroscopy, SQUID measurement and X-ray crystallography evidenced the equilibrium between two conformational isomers with singlet ground state, but different diradicaloid nature. The equilibrium between the two conformers is temperature dependent, which allows changing the diradical character of the system by heating/cooling. This feature is very promising in the design of stable materials that can "activate" their diradical character by external stimuli.

At low temperature (LT = 123 K), a distortion from planarity of the central ring of the bridge is observed. The associated singlet-triplet energy gap is determined by SQUID magnetic measurements to be 1.14 kcal/mol (400.57 cm^{-1}), suggesting a strong radical character.(43) This LT conformation can thus be referred to as a distorted diradical ($\mathbf{DD\text{-}PAT}^{+2}$). As the temperature is increased to 200 K (HT), a planar biradicaloid conformer is obtained, namely $\mathbf{PB\text{-}PAT}^{+2}$. As its name indicates it is a biradicaloid and a larger singlet-triplet energy gap of ΔE_{ST} = 2.37

kcal/mol (872.84 cm^{-1}) is observed (SQUID experiments) together with the full planarization of the terphenyl bridge.(43)

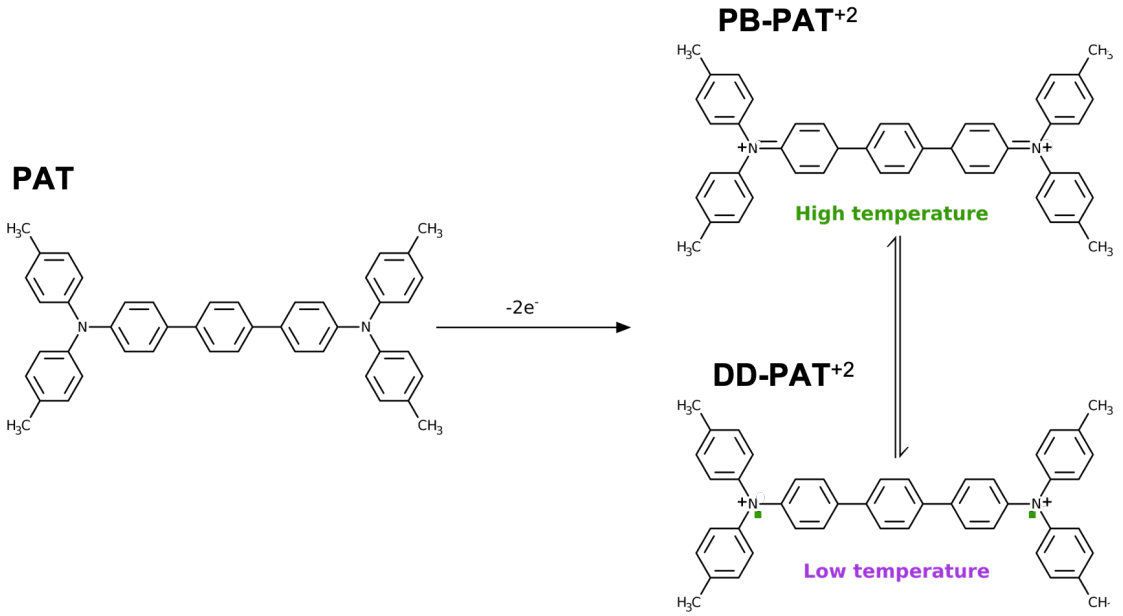

Figure 5.12: Neutral **PAT** with the resonance structures of $\mathbf{PAT}^{+2}$ at high and low temperatures. Figure adapted from reference(44).

In the following, the detailed description of the electronic structure of $\mathbf{PAT}^{+2}$ is presented, and the driving force of the interconversion mechanism between the two configurations unveiled.

5.2.1 Origin of the diradical character

PAT holds a closed-shell singlet ground state, in line with the large HOMO to LUMO energy gap with a smaller gap between HOMO and HOMO-1 of 0.91 eV. The removal of two electrons from **PAT** results in (quasi)degenerate HOMO-LUMO pair of orbitals, which is the origin of the diradical character of $\mathbf{PAT}^{+2}$. To get a balanced description of the diradical nature with accurate reproduction of experimental observations, $\mathbf{PAT}^{+2}$ conformers are characterized using DFT, RAS-SF and SF-TDDFT methods.

Small singlet-triplet energy gaps reported in Table 5.5 are in good agreement with experimental values. Furthermore, the experimentally measured relative diradical character (OS) is well reproduced by the computed diradical index (y_0), with a larger diradical index for $\mathbf{DD\text{-}PAT}^{+2}$ (0.84 against 0.65 for $\mathbf{PB\text{-}PAT}^{+2}$). $\mathbf{DD\text{-}PAT}^{+2}$ possesses roughly two singly-occupied orbitals (HONO occupation number is 1.16), and a large number of unpaired electrons (1.72). The N_u (1.36) and mod-

erate fractional occupancy of **PB-PAT**$^{+2}$ orbitals (HONO occupation number is 1.36) is indicative of its lower diradical character.

Structure	SF-TDDFT	RAS-SF	exp.^{a}	N_u	y_0
DD-PAT^{+2}	1.16	0.49	1.14	1.72	0.84
PB-PAT^{+2}	3.88	2.87	2.37	1.36	0.65

Table 5.5: Singlet-triplet energy gap (kcal/mol) for both conformers of **PAT**$^{+2}$. Number of unpaired electrons (N_u) and diradical index (y_0) were computed at RAS-SF level. Calculations were performed over the X-ray structures. ^{a} Experimental values were obtained from reference(43).

Interestingly, the distorted diradicaloid form (**DD-PAT**$^{+2}$) is obtained at low temperature, while the planarization of the bridge (**PB-PAT**$^{+2}$) is observed at higher temperature. This counterintuitive result indicates that the interconversion process and diradical formation is not entropy-driven. In order to understand the leading force of this transformation, the focus is first put on the rationalization of the structural parameters of both conformers.

In Table 5.6, the most relevant bond distances of crystal structures are compared with those obtained by geometrical relaxation at the DFT level. The terphenyl moiety has two kinds of nonequivalent benzene rings, referred to as A (at each side) and B (the central ring) hereafter. BLA_X is the bond length alternation in each ring. N-Ar is the N-C bond length at the bisphenylamino (BPA) unit, and N-$C_{terphenyl}$ is the distance between the *p*-terphenyl bridge and the BPA moiety. Overall, computational results agree well with the experimental data. The most important discrepancies are observed in the overestimation of the quinoidal character of the B ring in **PB-PAT**$^{+2}$, as well as in the prediction of a larger θ angle by DFT for both conformers. These differences can be explained by the absence in the calculations of the structural constraints inherent to the crystal environment.

In **PB-PAT**$^{+2}$, N-Ar and N-$C_{terphenyl}$ bond lengths correspond to single and double bonds, respectively. While BLA_A and BLA_B are virtually identical in DFT optimized geometries, rings A and B are clearly different in the crystal structure. At LT, the N-Ar and N-$C_{terphenyl}$ bond lengths of **DD-PAT**$^{+2}$ are quite homogeneous. In addition, both kind of rings possess an aromatic structure and are linked by a single bond (k, which compares well with the standard single bond between two carbons sp^2 in butadiene). The distortion of the central benzene is slightly overestimated, again most likely due to the absence of the constraints imposed by the crystal packing, but remains in quite good agreement with the X-ray structure. Molecular length, measured as the distance between N atoms, is shorter in **PB-PAT**$^{+2}$ (by Å) indicating a more quinoidized structure. For the sake of comparison,

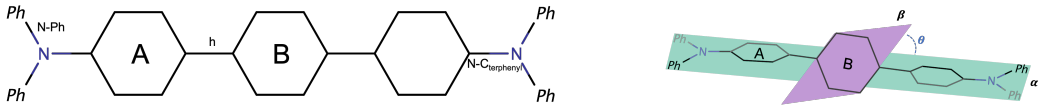

Structure	N-Ph	N-$C_{terphenyl}$	h	BLA_A	BLA_B	θ (^{o})	Charge BPA	Charge A	Charge B
[a]**PB-PAT**$^{+2}$	1.430	1.366	1.466	0.053	0.022	3.78	-	-	
PB-PAT^{+2}	1.433	1.346	1.423	0.075	0.076	9.58	0.51	0.35	0.30
[a]**DD-PAT**$^{+2}$	1.414	1.392	1.468	0.031	0.023	26.76	-	-	-
DD-PAT^{+2}	1.404	1.412	1.479	0.020	0.014	35.73	0.74	0.20	0.13
PAT	1.422	1.417	1.482	0.015	0.015	35.18	-	-	-

Table 5.6: Main geometrical parameters of **PB-PAT**$^{+2}$ and **DD-PAT**$^{+2}$ optimized geometries at UCAM-B3LYP/6-31G* level. BLA_A is the bond length alternation of the ring A whereas BLA_B is from ring B. Charges are computed under Mulliken approximation. BLA were calculated as is indicated in the appendix. [a]X-ray structural data were obtained from reference(43). The bond lengths, Å, are defined in the figure.

PAT was optimized at the same level of theory as the two dicationic conformers. The ground state minimum presents a distorted structure in which all the rings are rather aromatic (see Table 5.6). Geometrically, it is more similar to **DD-PAT**$^{+2}$ than to **PB-PAT**$^{+2}$.

Mulliken analysis for the two forms of **PAT**$^{+2}$ locates the positive excess charge mainly on the BPA units, with small (medium) contribution over the A rings in **DD-PAT**$^{+2}$ (**PB-PAT**$^{+2}$). This suggests that the charge and unpaired electron density is stabilized mainly over BPA moieties and towards the A rings of the *p*-terphenyl bridge, see Table 5.6.

Frontier natural orbitals, Figure 5.13, are mostly localized over the nitrogen atom of the BPA moiety and the side ring of the terphenyl (A). Disruption of the π-conjugation can be attributed to the loss of planarity along the bridge. The interaction between radical centers is larger in **PB-PAT**$^{+2}$, as the distortion between A and B rings is smaller than in **DD-PAT**$^{+2}$.

The singlet-ground state of **PAT**$^{+2}$ can be rationalized as a consequence of the antiferromagnetic interaction between radical centers, stronger at high temperature when the system is more planar, giving an overall moderate diradical character. At low temperature the radical-radical interaction is weaker and the singlet-triplet gap is rather small so that both states, singlet and triplet, are in equilibrium.

Quinoidal/aromatic-like rings, radical character, and charge distribution together offer a complete picture of the electronic structure nature of each conformer

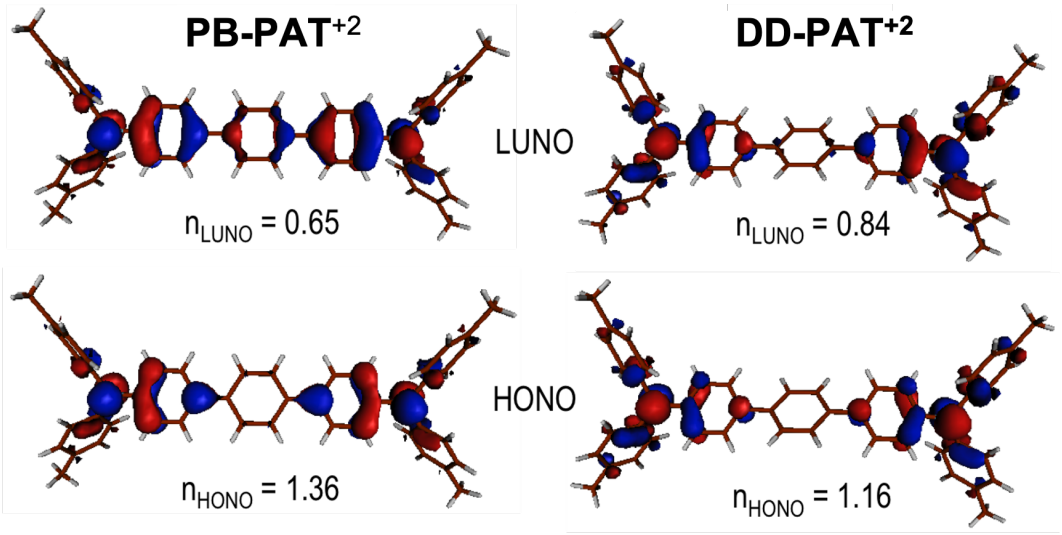

Figure 5.13: Frontier natural orbitals and their electronic occupancy of **PAT**$^{+2}$ conformers. Figure adapted from reference(44).

of **PAT**$^{+2}$ and explain their fundamental differences.

5.2.2 The PB-PAT^{+2} $\leftrightarrow$ DD-PAT^{+2} conversion

In order to explain the relative stability of both **PAT**$^{+2}$ conformers, it is crucial to take into account the steric strain within the phenyl rings of the *p*-terphenyl unit. To analyze the stability provided by the aromatic/quinoidal-like conjugation through the bridge, adiabatic singlet-triplet energy gaps of smaller oligophenylene, namely, *p*-phenyl (N=1) and *p*-biphenyl (N=2), were computed at their respective distorted and planar conformations. Adiabatic singlet-triplet energy gap when N = 1 shows the stabilization of the closed-shell (quinoidal-like) form over triplet conformation (aromatic structure) by 2.03 kcal/mol. By addition of one more ring, *p*-biphenyl bridge can either adopt the planar or the distorted geometry in both, aromatic (triplet) and quinoidal-like (CS) structures. The lowest energy conformation in the singlet and triplet states exhibits a θ dihedral angle of $\sim 36°$. Interestingly, the triplet state is more stable than the CS configuration in both planar and distorted conformations ($\Delta E_{ST,\theta=0°} = -7.78$ kcal/mol, and $\Delta E_{ST,\theta=36°} =$ -9.76 kcal/mol). This result can be associated with the stabilization provided by the aromaticity of the *p*-biphenyl in the triplet state, since both benzene rings hold a Clar's sextet. Indeed, the significant hydrogen repulsion in the planar conformation can be counterbalanced by the aromaticity, so that the diradical structure (triplet state) is favoured over the closed-shell form (singlet). Upon distortion of the bridge ($\theta_0 \rightarrow \theta_{\sim 36}$), the steric repulsion within the *p*-biphenyl benzene rings lowers and the triplet state is further stabilized by $\sim$ 2 kcal/mol with respect to the planar

conformation. The distorted closed-shell structure is the most unstable situation due to its tendency to break the double bond between benzene rings (similar to the ethylene torsion). In summary, the relative energies of the four conformations follow the trend: $E(CS_{\theta\sim36^\circ}) \gg E(CS_{\theta=0^\circ}) > E(T_{\theta=0^\circ}) > E(T_{\theta\sim36^\circ})$.

These results indicate that the distortion of the central ring of the *p*-terphenyl bridge is the key structural parameter that governs magnetic properties in the equilibrium between the low and high temperature **PAT**$^{+2}$ conformers. As mentioned beforehand, conversion between the two isomers is not entropy driven: what is then the driving force behind the interconversion mechanism? To address the interconversion between **PB-PAT**$^{+2}$ and **DD-PAT**$^{+2}$, the torsional potential for the dihedral angle θ is computed at the RAS-SF level for the two conformers, as presented in Figure 5.14. These energy profiles are obtained by rigid scans of the torsion, *i.e.*, single point energy calculation with all internal coordinates fixed to their equilibrium values besides θ, which is scanned between -25° and 45° by steps of 5°.

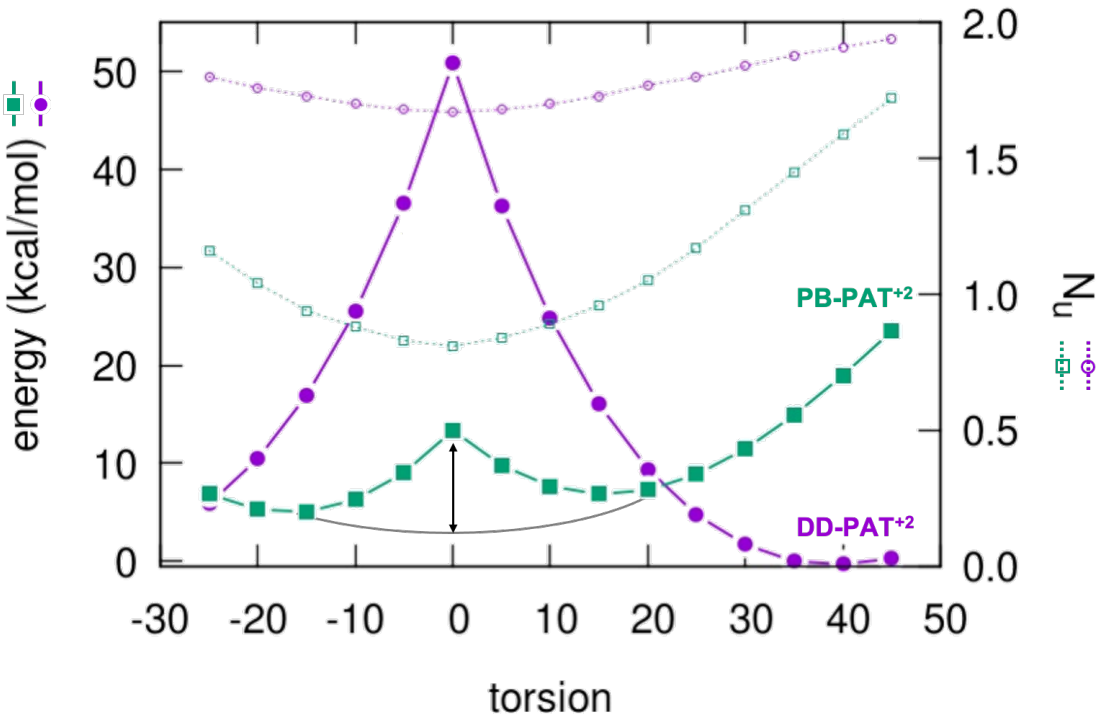

Figure 5.14: Energy profiles and N_u for the **PB-PAT**$^{+2}$ (green squares) and **DD-PAT**$^{+2}$ (purple circles) molecular torsion model. Vertical arrow represents the energy associated with the steric hindrance in **PB-PAT**$^{+2}$. Note that, due to numerical approximations, energy profiles are not symmetrical. Figure adapted from reference(44).

The most stable conformation is found for **DD-PAT**$^{+2}$ at $\theta \sim 35^\circ$. From this geometry, the gradual planarization of the *p*-terphenyl entails the loss of stability due

to the increase of steric hindrance (the potential energy curve reaches a maximum when the bridge is perfectly planar). On the other hand, the minimum of **PB-PAT**$^{+2}$ is found at $\theta \sim 15°$, almost 5 kcal/mol above the **DD-PAT**$^{+2}$ minimum, in good agreement with DFT calculations that predict an energy difference between the two minima of 5.4 kcal/mol.

The geometry in which the bridge is perfectly planar might be anticipated to be the minimum of **PB-PAT**$^{+2}$. Nevertheless, an energy peak is obtained for $\theta = 0°$, which can be interpreted as the consequence of the steric effect between the hydrogens of contiguous phenyls in the terphenyl unit (estimated about 5 kcal/mol as indicated in by the vertical arrow in 5.14). The crossing point between **PB-PAT**$^{+2}$ and **DD-PAT**$^{+2}$ curves locates approximately at $\theta = 23°$. The path connecting both minima, from **DD-PAT**$^{+2}$ to **PB-PAT**$^{+2}$, presents a barrier towards the molecular planarization, *i.e.*, the energy increases due to steric effects up to $\sim 23°$, where a pseudo-Jahn-Teller distortion might be correlated with the increment of energy by the gain of local symmetry (at the *p*-terphenyl core). Once passed the crossing point, to stabilize the planar biradicaloid conformation, the quinoidal structure arises through the formation of a π-bond and the reduction of the diradical character, quantified in Figure 5.14 as the decrease of the N_u from $\theta \sim 23° \rightarrow 15°$ (**PB-PAT**$^{+2}$ minimum). The stability provided by the high symmetrical conformation of **PAT**$^{+2}$ at high temperature is compensated, and exceeded, by the contribution from the aromaticity recovered in the central ring and the lower internal *p*-terphenyl steric strain at low temperature conformation.

The entropy should increase with temperature, enabling the population of rotational conformers, as already well described for the oligophenylenes family.(45) The so called "bond stretching isomerism" establishes that breaking of a σ-bond and subsequent stabilization of a diradical is obtained as the effect of a pseudo Jahn-Teller distortion (reduction of the local symmetry to stabilize the energy) when temperature decreases. In other words, bond formation is promoted by heating the system. In **PAT**$^{+2}$ conformers, the quinoidal-like configuration of **PB-PAT**$^{+2}$ can be understood as the partial formation of a π-bond (N-$C_{terphenyl}$ bond holds a double bond character) as the temperature increases, in such a way that the radical character is decreased, as shown in Figure 5.14 with the diminution of N_u towards $\theta = 0°$.

To summarize, the interconversion between the two isomers can be understood as a dynamic process fueled by thermal energy. At low temperature, steric congestion dominates and the equilibrium structure exhibits a *p*-terphenyl core distortion together with the associated sacrifice of a π-bond. On the other hand, this bond can be formed by heating as the energy gained is invested into keeping the geometry planar. Finally, the origin of the small interconversion barrier between conformers with different radical character was rationalized. Equilibrium between the two forms

of **PAT**$^{+2}$ can be tuned by using bridges of different nature and length, hence modifying its topology or electronic structure nature. Thus, the singlet-triplet energy gap of **PAT**$^{+2}$ is thermally controllable in the solid state.

5.3 Appendix

5.3.1 Computational details

Geometry optimizations of **OTPD**$_n$ and **PAT** have been performed within the density functional theory (DFT) framework with the unrestricted B3LYP(46) and CAM-B3LYP(47) exchange-correlation functionals, respectively. Basis set of double-ζ quality with polarization functions were used, namely 6-31G(d) for **OTPD**$_n$ and 6-31G(d,p) for **PAT**. Optimized geometries were identified as true local minima with no imaginary frequencies within the harmonic approximation. UV/VIS/NIR spectra were calculated using TD-DFT method at the same level of theory. All calculations were performed with Q-Chem package.(48)

5.3.1.1 OTPD$_n$

RAS-SF calculations were performed with 4 electrons in 4 orbitals in the active space with triplet high-spin as reference.

5.3.1.2 PAT^{+2}

Raman spectra were simulated within the harmonic approximation by convolution of Lorentzian functions with a half-with at half maximum (HWHM) of 10 cm^{-1}. Computed vibrational frequencies were scaled by a constant factor of 0.96.(49)

RAS-SF calculations were performed including 2 electrons in 2 π-orbitals as the active space (RAS2) with the ROHF triplet high-spin as reference.

The BLA of benzene rings of the *p*-terphenyl are defined as the difference between the average of the lengths of longitudinal bonds (a, c, d, f in ring A, and i, k in ring B) and transverse bonds (e and b in ring A, and j in B) in each ring. The bond lengths used to calculate the BLA in Table 5.6 are presented in Table 5.7.

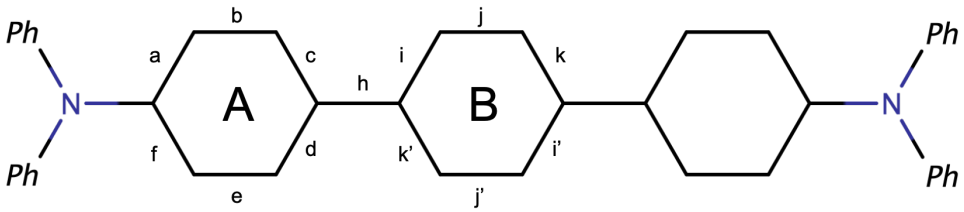

Structure	Average a, c, d and f	Average b and e	Average j	Bond h
[a]**PB-1**$^{+2}$	1.415	1.362	1.396	1.374
PB-1^{+2}	1.433	1.358	1.434	1.358
[a]**DD-1**$^{+2}$	1.407	1.376	1.402	1.379
DD-1^{+2}	1.402	1.382	1.399	1.387
1	1.405	1.390	1.406	1.391

Table 5.7: Average of transverse a, c, d and f (i and k) and longitudinal b and e (j) bonds of the A (B) ring for high and low temperature conformers at DFT and [a]X-ray(43) structure.

Bibliography

[1] T. Skotheim and J. Reynolds, *Conjugated Polymers: Theory, Synthesis, Properties, and Characterization*. Handbook of Conducting Polymers, Fourth Edition, CRC Press, 2006.

[2] J. F. Mike and J. L. Lutkenhaus, "Recent advances in conjugated polymer energy storage," *Journal of Polymer Science Part B: Polymer Physics*, vol. 51, no. 7, pp. 468–480, 2013.

[3] Y. Li and Y. Zou, "Conjugated polymer photovoltaic materials with broad absorption band and high charge carrier mobility," *Advanced Materials*, vol. 20, no. 15, pp. 2952–2958, 2008.

[4] K. P. P. D. S. Rahman, M.A. and Y. B. Shim, "Electrochemical sensors based on organic conjugated polymers," *Sensors*, vol. 8, no. 1, pp. 118–141, 2008.

[5] J. M. Warman, M. P. de Haas, G. Dicker, F. C. Grozema, J. Piris, and M. G. Debije, "Charge mobilities in organic semiconducting materials determined by pulse-radiolysis time-resolved microwave conductivity: π-bond-conjugated polymers versus π- π-stacked discotics," *Chemistry of materials*, vol. 16, no. 23, pp. 4600–4609, 2004.

[6] J. H. Burroughes, D. D. C. Bradley, A. R. Brown, R. N. Marks, K. Mackay, R. H. Friend, P. L. Burns, and A. B. Holmes, "Light-emitting diodes based on conjugated polymers," *Nature*, vol. 347, no. 6293, pp. 539–541, 1990.

[7] P. Wang, S. Lin, Z. Lin, M. D. Peeks, T. Van Voorhis, and T. M. Swager, "A semiconducting conjugated radical polymer: Ambipolar redox activity and faraday effect," *Journal of the American Chemical Society*, vol. 140, no. 34, pp. 10881–10889, 2018.

[8] N. K. Guimard, N. Gomez, and C. E. Schmidt, "Conducting polymers in biomedical engineering," *Progress in Polymer Science*, vol. 32, no. 8, pp. 876–921, 2007.

[9] M. Leclerc, "Polyfluorenes: Twenty years of progress," *Journal of Polymer Science Part A: Polymer Chemistry*, vol. 39, no. 17, pp. 2867–2873, 2001.

[10] T. Granier, E. L. Thomas, D. R. Gagnon, F. E. Karasz, and R. W. Lenz, "Structure investigation of poly(p-phenylene vinylene)," *Journal of Polymer Science Part B: Polymer Physics*, vol. 24, no. 12, pp. 2793–2804, 1986.

[11] J. Roncali, "Conjugated poly(thiophenes): synthesis, functionalization, and applications," *Chemical Reviews*, vol. 92, no. 4, pp. 711–738, 1992.

[12] J. Roncali, "Conjugated poly(thiophenes): synthesis, functionalization, and applications," *Chemical Reviews*, vol. 92, no. 4, pp. 711–738, 1992.

[13] J. Roncali, "Chapter 3. linear Ï[U+0080]-conjugated systems with tailored electronic properties," *Annu. Rep. Prog. Chem., Sect. C: Phys. Chem.*, vol. 95, pp. 47–88, 1999.

[14] G. Schopf and G. Koßmehl, *Polythiophenes - Electrically Conductive Polymers*. Advances in Polymer Science.

[15] S. Inal, J. Rivnay, A.-O. Suiu, G. G. Malliaras, and I. McCulloch, "Conjugated polymers in bioelectronics," *Accounts of Chemical Research*, vol. 51, no. 6, pp. 1368–1376, 2018.

[16] W. Zhou, K. Hernández-Burgos, S. E. Burkhardt, H. Qian, and H. D. Abruña, "Synthesis and electrochemical and computational analysis of two new families of thiophene-carbonyl molecules," *The Journal of Physical Chemistry C*, vol. 117, no. 12, pp. 6022–6032, 2013.

[17] G. Zhang, Z.-A. Lan, and X. Wang, "Conjugated polymers: Catalysts for photocatalytic hydrogen evolution," *Angewandte Chemie International Edition*, vol. 55, no. 51, pp. 15712–15727, 2016.

[18] S. Xu, Z. Zhou, H. Fan, L. Ren, F. Liu, X. Zhu, and T. P. Russell, "An electron-rich 2-alkylthieno[3,4-b]thiophene building block with excellent electronic and morphological tunability for high-performance small-molecule solar cells," *J. Mater. Chem. A*, vol. 4, pp. 17354–17362, 2016.

[19] C. Zhang and X. Zhu, "Thieno[3,4-b]thiophene-based novel small-molecule optoelectronic materials," *Accounts of Chemical Research*, vol. 50, no. 6, pp. 1342–1350, 2017.

[20] C. Zhang, H. Li, J. Wang, Y. Zhang, Y. Qiao, D. Huang, C.-a. Di, X. Zhan, X. Zhu, and D. Zhu, "Low-bandgap thieno[3,4-c]pyrrole-4,6-dione-polymers for high-performance solar cells with significantly enhanced photocurrents," *J. Mater. Chem. A*, vol. 3, pp. 11194–11198, 2015.

[21] E.-K. Lee, M. Y. Lee, A. Choi, J.-Y. Kim, O. Y. Kweon, J.-H. Kim, J. Y. Jung, T.-J. Shin, J. H. Oh, J.-I. Park, and S. Y. Lee, "Phenyl derivative of dibenzothiopheno[6,5-b:6′,5′-f]thieno[3,2-b]thiophene (dph-dbttt): High thermally durable organic semiconductor for high-performance organic field-effect transistors," *Advanced Electronic Materials*, vol. 3, no. 10, p. 1700142, 2017.

[22] K. Müllen and G. Klarner, *Electronic Materials: The Oligomer Approach*. 2007.

[23] M.-S. Kang, J. H. Kim, J. Won, and Y. S. Kang, "Oligomer approaches for solid-state dye-sensitized solar cells employing polymer electrolytes," *The Journal of Physical Chemistry C*, vol. 111, no. 13, pp. 5222–5228, 2007.

[24] P. F. Van Hutten, V. V. Krasnikov, and G. Hadziioannou, "A model oligomer approach to light-emitting semiconducting polymers," *Accounts of Chemical Research*, vol. 32, no. 3, pp. 257–265, 1999.

[25] J. L. Segura, N. Martín, and D. M. Guldi, "Materials for organic solar cells: the c60/π-conjugated oligomer approach," *Chem. Soc. Rev.*, vol. 34, pp. 31–47, 2005.

[26] W. Li, B. Guo, C. Chang, X. Guo, M. Zhang, and Y. Li, "Efficient polymer solar cells based on a copolymer of meta-alkoxy-phenyl-substituted benzodithiophene and thieno[3,4-b]thiophene," *J. Mater. Chem. A*, vol. 4, pp. 10135–10141, 2016.

[27] F. Costanzo, D. Tonelli, G. Scalmani, and J. Cornil, "Theoretical investigation of the electronic and optical properties of oligothiophenes upon methyl, thiol, and thiomethyl substitutions," *Polymer*, vol. 47, no. 19, pp. 6692–6697, 2006.

[28] S. M. Bouzzine, S. Bouzakraoui, M. Bouachrine, and M. Hamidi, "Density functional theory (b3lyp/6-31g*) study of oligothiophenes in their aromatic

and polaronic states," *Journal of Molecular Structure: THEOCHEM*, vol. 726, no. 1, pp. 271–276, 2005.

[29] T. Vikramaditya, M. Saisudhakar, and K. Sumithra, "Electronic structure of -oligothiophenes with various substituents," *Journal of Molecular Structure*, vol. 1081, pp. 114–123, 2015.

[30] D. Yuan, S. Medina Rivero, P. Mayorga Burrezo, L. Ren, M. E. Sandoval-Salinas, S. J. Grabowski, D. Casanova, X. Zhu, and J. Casado, "Thieno[3,4-c]pyrrole-4,6-dione oligothiophenes have two crossed paths for electron delocalization," *Chemistry –A European Journal*, vol. 24, no. 51, pp. 13523–13534, 2018.

[31] J. L. Bredas and G. B. Street, "Polarons, bipolarons, and solitons in conducting polymers," *Accounts of Chemical Research*, vol. 18, no. 10, pp. 309–315, 1985.

[32] F. Alkan and U. Salzner, "Theoretical investigation of excited states of oligothiophene anions," *The Journal of Physical Chemistry A*, vol. 112, no. 27, pp. 6053–6058, 2008.

[33] S. R. González, Y. Ie, Y. Aso, J. T. López Navarrete, and J. Casado, "The frontiers of quinoidal stability in long oligothiophenes: Raman spectra of dicationic polaron pairs," *Journal of the American Chemical Society*, vol. 133, no. 41, pp. 16350–16353, 2011.

[34] L. Zaikowski, P. Kaur, C. Gelfond, E. Selvaggio, S. Asaoka, Q. Wu, H.-C. Chen, N. Takeda, A. R. Cook, A. Yang, J. Rosanelli, and J. R. Miller, "Polarons, bipolarons, and side-by-side polarons in reduction of oligofluorenes," *Journal of the American Chemical Society*, vol. 134, no. 26, pp. 10852–10863, 2012.

[35] J. Thiele and H. Balhorn, "Ueber einen chinoïden kohlenwasserstoff," *Berichte der deutschen chemischen Gesellschaft*, vol. 37, no. 2, pp. 1463–1470, 1904.

[36] A. E. Tschitschibabin, "Über einige phenylierte derivate des p, p-ditolyls," *Berichte der deutschen chemischen Gesellschaft*, vol. 40, no. 2, pp. 1810–1819, 1907.

[37] L. K. Montgomery, J. C. Huffman, E. A. Jurczak, and M. P. Grendze, "The molecular structures of thiele's and chichibabin's hydrocarbons," *Journal of the American Chemical Society*, vol. 108, no. 19, pp. 6004–6011, 1986.

[38] E. Müller and H. Pfanz, "Über biradikaloide terphenylderivate," *Berichte der deutschen chemischen Gesellschaft (A and B Series)*, vol. 74, no. 6, pp. 1051–1074, 1941.

[39] M. Abe, "Diradicals," *Chemical Reviews*, vol. 113, no. 9, pp. 7011–7088, 2013.

[40] G. Tan and X. Wang, "Isolable bis(triarylamine) dications: Analogues of thiele's, chichibabin's, and müller's hydrocarbons," *Accounts of Chemical Research*, vol. 50, no. 8, pp. 1997–2006, 2017.

[41] A. Maiti, S. Chandra, B. Sarkar, and A. Jana, "Acyclic diaminocarbene-based thiele, chichibabin, and m"

[42] Y. Su, X. Wang, Y. Li, Y. Song, Y. Sui, and X. Wang, "Nitrogen analogues of thiele's hydrocarbon," *Angewandte Chemie International Edition*, vol. 54, no. 5, pp. 1634–1637, 2015.

[43] Y. Su, X. Wang, L. Wang, Z. Zhang, X. Wang, Y. Song, and P. P. Power, "Thermally controlling the singlet-triplet energy gap of a diradical in the solid state," *Chem. Sci.*, vol. 7, pp. 6514–6518, 2016.

[44] S. Medina Rivero, P. Mayorga Burrezo, M. E. Sandoval-Salinas, T. Li, F. J. Ramírez, D. Casanova, X. Wang, and J. Casado, "Isomerism, diradical signature, and raman spectroscopy: underlying connections in diamino oligophenyl dications," *ChemPhysChem*, vol. 19, no. 12, pp. 1465–1470, 2018.

[45] J. D. Honeycutt and H. C. Andersen, "Molecular dynamics study of melting and freezing of small lennard-jones clusters," *The Journal of Physical Chemistry*, vol. 91, no. 19, pp. 4950–4963, 1987.

[46] A. D. Becke, "Density-functional thermochemistry. iii. the role of exact exchange," *The Journal of Chemical Physics*, vol. 98, no. 7, pp. 5648–5652, 1993.

[47] T. Yanai, D. P. Tew, and N. C. Handy, "A new hybrid exchange-correlation functional using the coulomb-attenuating method (cam-b3lyp)," *Chemical Physics Letters*, vol. 393, no. 1, pp. 51–57, 2004.

[48] Y. Shao, Z. Gan, E. Epifanovsky, A. T. B. Gilbert, M. Wormit, J. Kussmann, A. W. Lange, A. Behn, J. Deng, X. Feng, D. Ghosh, M. Goldey, P. R. Horn, L. D. Jacobson, I. Kaliman, R. Z. Khaliullin, T. Kus, A. Landau, J. Liu, E. I. Proynov, Y. M. Rhee, R. M. Richard, M. A. Rohrdanz, R. P. Steele, E. J. Sundstrom, H. L. Woodcock, P. M. Zimmerman, D. Zuev, B. Albrecht, E. Alguire, B. Austin, G. J. O. Beran, Y. A. Bernard, E. Berquist, K. Brandhorst, K. B. Bravaya, S. T. Brown, D. Casanova, C.-M. Chang, Y. Chen, S. H. Chien, K. D. Closser, D. L. Crittenden, M. Diedenhofen, R. A. DiStasio, H. Do, A. D. Dutoi, R. G. Edgar, S. Fatehi, L. Fusti-Molnar, A. Ghysels, A. Golubeva-Zadorozhnaya, J. Gomes, M. W. D. Hanson-Heine, P. H. P. Harbach, A. W. Hauser, E. G. Hohenstein, Z. C. Holden, T.-C. Jagau,

H. Ji, B. Kaduk, K. Khistyaev, J. Kim, J. Kim, R. A. King, P. Klunzinger, D. Kosenkov, T. Kowalczyk, C. M. Krauter, K. U. Lao, A. D. Laurent, K. V. Lawler, S. V. Levchenko, C. Y. Lin, F. Liu, E. Livshits, R. C. Lochan, A. Luenser, P. Manohar, S. F. Manzer, S.-P. Mao, N. Mardirossian, A. V. Marenich, S. A. Maurer, N. J. Mayhall, E. Neuscamman, C. M. Oana, R. Olivares-Amaya, D. P. O'Neill, J. A. Parkhill, T. M. Perrine, R. Peverati, A. Prociuk, D. R. Rehn, E. Rosta, N. J. Russ, S. M. Sharada, S. Sharma, D. W. Small, A. Sodt, T. Stein, D. Stuck, Y.-C. Su, A. J. W. Thom, T. Tsuchimochi, V. Vanovschi, L. Vogt, O. Vydrov, T. Wang, M. A. Watson, J. Wenzel, A. White, C. F. Williams, J. Yang, S. Yeganeh, S. R. Yost, Z.-Q. You, I. Y. Zhang, X. Zhang, Y. Zhao, B. R. Brooks, G. K. L. Chan, D. M. Chipman, C. J. Cramer, W. A. Goddard, M. S. Gordon, W. J. Hehre, A. Klamt, H. F. Schaefer, M. W. Schmidt, C. D. Sherrill, D. G. Truhlar, A. Warshel, X. Xu, A. Aspuru-Guzik, R. Baer, A. T. Bell, N. A. Besley, J.-D. Chai, A. Dreuw, B. D. Dunietz, T. R. Furlani, S. R. Gwaltney, C.-P. Hsu, Y. Jung, J. Kong, D. S. Lambrecht, W. Liang, C. Ochsenfeld, V. A. Rassolov, L. V. Slipchenko, J. E. Subotnik, T. Van Voorhis, J. M. Herbert, A. I. Krylov, P. M. W. Gill, and M. Head-Gordon, "Advances in molecular quantum chemistry contained in the q-chem 4 program package," *Mol. Phys.*, vol. 113, no. 2, pp. 184–215, 2015.

[49] A. P. Scott and L. Radom, "Harmonic vibrational frequencies: an evaluation of hartree- fock, møller- plesset, quadratic configuration interaction, density functional theory, and semiempirical scale factors," *The Journal of Physical Chemistry*, vol. 100, no. 41, pp. 16502–16513, 1996.

Chapter 6

Organic macrostructures with polyradical character

As outlined in Chapters 4 and 5, small to medium size organic radicaloids have been extensively used in the development of emerging technologies in miscellaneous fields, from light/energy generation, transport and storage to medical and biological sciences.(1; 2; 3; 4) Their performance in such applications can be significantly improved by increasing their radical character. In other words, materials with more than two radical centers (*i.e.*, polyradicals) could be valuable for applications based on magnetic, electronic, and optical properties.(5; 6) Moreover, the nature of the interaction between radical sites guides the potential utilization of these polyradicals; for instance, ferromagnetic interaction is important for organic magnets,(7) while the anti-ferromagnetic one can improve electronic conjugation between radicals.(8; 9)

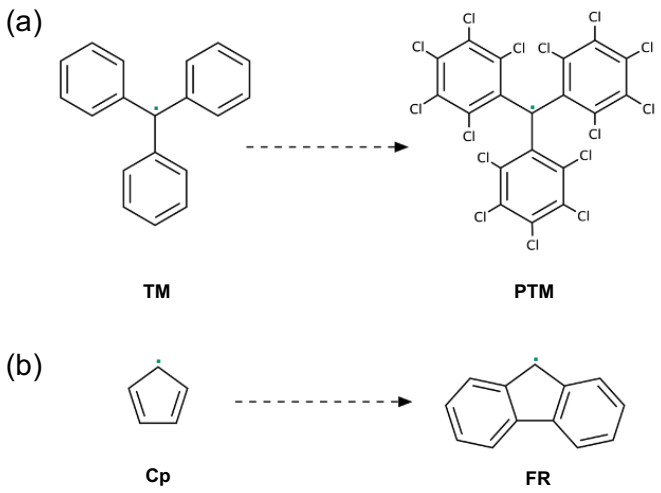

Figure 6.1: Structure of tripehenylmethyl, **TM**, radical and its polychlorated derivative, **PTM**, (a). Structure of the cyclopentadienyl ring, **Cp**, and the extended aromatic system fluorenyl, **FR** (b).

Despite the constant research efforts and development of new synthetic routes, the production of stable polyradical materials is still not straightforward nowadays. Nevertheless, small organic radicals can be experimentally obtained and applied thanks to stabilization techniques. A well-known example is the polychlorotriphenylmethyl (**PTM**) radical, derivative of the **TM** mono-radical, where phenyl rings are totally or partially chlorinated (Figure 6.1a). Steric strain provided by the presence of Cl atoms at *ortho* position forces the phenyl rings to adopt a propeller-like conformation, that sterically protects the methyl radical site providing in turn an improved stability and long life-times.(10; 11) Another paramount example of carbon-radicals stabilized by protection with bulky groups is the cyclopentadienyl ring (**Cp**), Figure 6.1. Stabilization of the unpaired electron can be improved by the extension of the π-conjugation around the radical center. For instance, the benzannulation, as in fluorenyl radical (**FR**, Figura 6.1b), is a common way to effectively hyper-conjugate and delocalize the spin through the system. **FR** is a widely exploited frame in the design of radical macrostructures(12; 13) owing to its ability to be easily stabilized by kinetic blocking of the 9-position with a bulky group. Given their stability, these moieties are key to the development of larger systems with high-spin ground state or polyradical character. These radical centers are fused together or connected by means of rigid or flexible organic linkers to produce macroestructures with a large diversity of topological arrangements (linear, macrocyclic, polymeric, and the so-called spin clusters, that is branched polyradicals).(10; 6; 12; 14) For instance, recently, 3D motifs have been constructed as the ensemble of multiple radical units.(15; 16; 17)

In this chapter, I will describe stable macrostructures with polyradicaloid character constructed as the assembly of **FR** and **PTM** radical moieties. The relation between connectivity and the nature of the radical interactions (ferromagnetic or antiferromagnetic) is studied here, rationalizing their strong open-shell nature. Finally, molecular and electronic properties induced by the radical character will be investigated from a computational point of view by means of correlated electronic structure methods, as required by the nature of the systems. The series of systems reported hereafter have been synthesized and experimentally characterized by the group of Prof. Jishan Wu from the National University of Singapore.

6.1 Organic Macrocycles with polyradical Character

This section focuses on the study of three families of macrocycles (Figure 6.2). [n]cyclo-*para*-biphenylmethines (**[n]CPBM**) with $n = 3 - 8$ are formed by n *p*-diphenyl units connected through a methine carbon, giving rise in each one of the

vertices to a radical site that is protected by an anthracene derivative. As described in the previous chapter, due to the steric hindrance between benzene rings, the *p*-phenyl bridges allows the modulation of the overall radical character through the equilibrium between aromatic and quinoidal-like forms. Similar structures are shown by **[*n*]PTM** macrocycles, where $n = 3-6$ units of **PTM** radical are linked together by an ethynylene moiety that provides molecular rigidity and avoid steric hindrance between polychlorated phenyls due to larger distance between radical centers (compared with **[*n*]CPBM**). Finally, **[8]MC** and **[10]MC** are coronnene-like cycles of fused alternated 5- and 6-membered carbon rings, resulting in an arrangement of n fluorenyl radical-like units. Structurally, all these macrocycles are able to hold a large number of radicals, *i.e*, to be polyradicals. Concretely, they are potential triradicals up to decaradicals according to the value of n. While experimentally, every potential radical site is protected with a bulky group, these groups were reduced (in **[n]CPBM**) or replaced by hydrogen atoms (in **[n]MC**) for computational reasons.

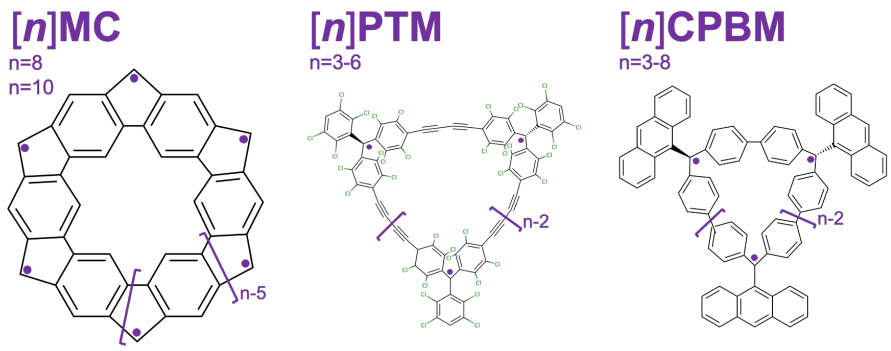

Figure 6.2: Structure of macrocyclic families studied here: **[*n*]MC** with $n = 8$ and 10, **[*n*]PTM** with $n = 3-6$, and **[*n*]CPBM** with $n = 3-8$. Purple dots indicate the radical centers.

Geometrical minima were determined by means of DFT theory. **[*n*]MC** are very rigid structures with well defined molecular symmetry. The larger, **[10]MC**, is a flat macrocycle with D_{2h} symmetry (in good agreement with the X-ray structure) and spin-triplet ground state, while **[8]MC** holds a singlet ground state, and the ring tension suppresses molecular planarity, favouring a bowl-shape structure with C_{2v} molecular symmetry (Figure 6.3a). **[*n*]PTM** with $n = 3$ and $n = 5$ have a doublet ground state, while $n = 4$ ground state is a singlet, and with $n = 6$, the ground state multiplicity is the triplet. The distance between radical centers in **[n]PTM** slightly increases with n, ($\sim$ 14.40, 15.09, 15.26, and 15.30 Å, for $n = 3-6$, respectively). Ethynylene bridges are aligned in a (pseudo)planar macrocycle for $n = 3-5$, but the largest member of the family, **[6]PTM**, adopts a boat-shaped conformation, similar to the one observed in cyclohexane (Figure 6.3b). **[*n*]CPBM** hold low-spin multiplicity ground states, *i.e.*, they are doublets if n is odd, and singlets when n is even. The relative orientation of the phenyl rings results from an interplay

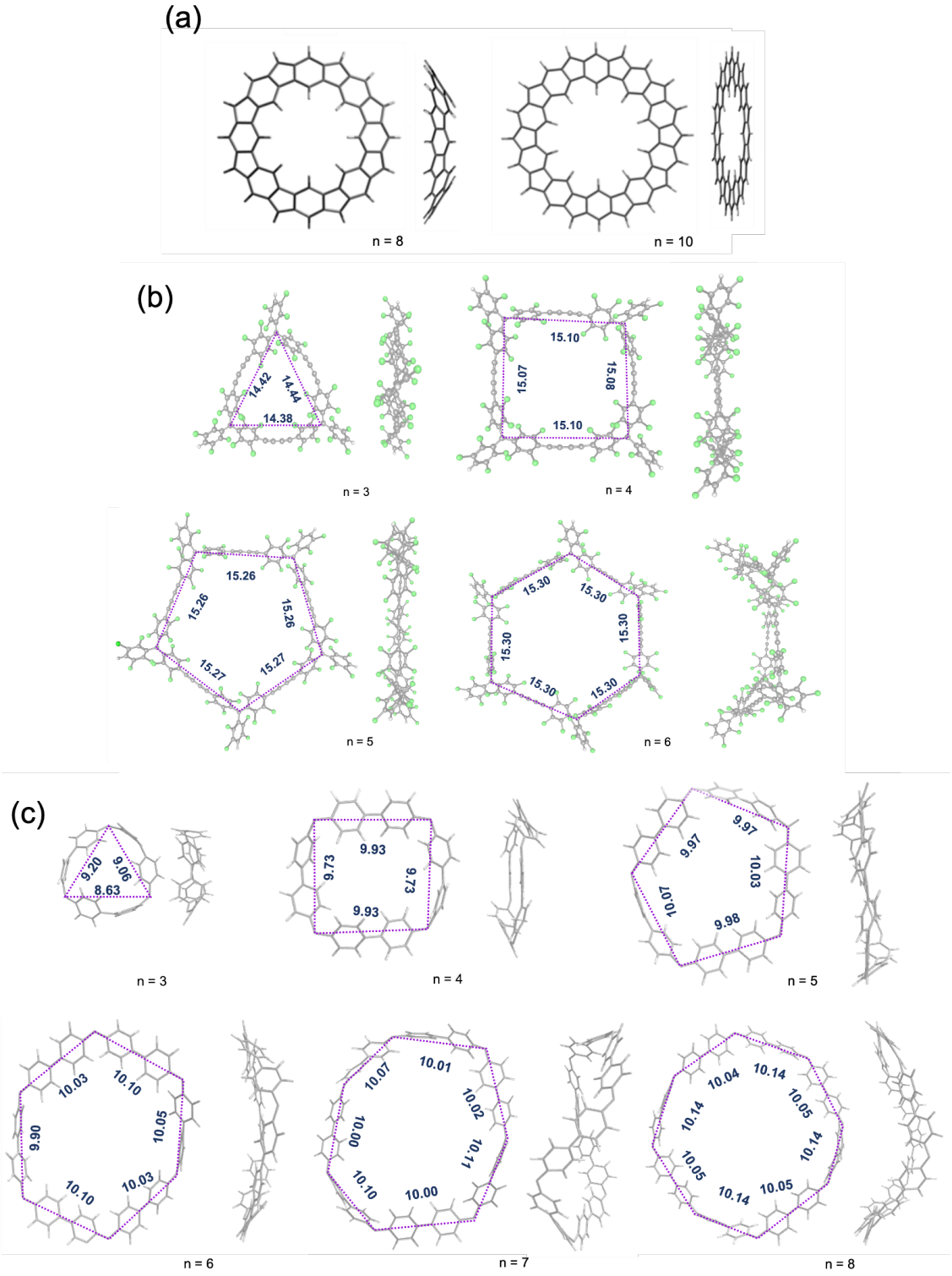

Figure 6.3: Top and side view of the optimized structures and radical-radical distance of **[*n*]MC** (a), **[*n*]PTM** (b), and **[*n*]CPBM** (c). Figures (a) and (c) are adapted from reference(18) and reference(19), respectively.

between repulsion within each individual bridge and with the contiguous bridges. As a result, **[3]CPBM** has a highly tensed bowl-shaped structure with nonequivalent distances between radical centers (9.20, 9.06 and 8.63 Å). The tetramer exhibits an almost flat rectangular conformation, which nicely reproduces the crystalline distorted-C_2 geometry with distances between neighboring methyl sites of 9.56 and 9.91 Å computed as 9.73 and 9.93 Å, respectively. As the size of the system increases, the structure of the macrocycle is distorted to a boat-shape for $n = 6$, a tub-like conformation for $n = 8$ (as in the cyclooctatetraene), and the twisted 8-figure for $n = 7$ (Figure 6.3c). Increase of the radical-radical distance suggests the weakness of the coupling between radicals in **[n]PTM** and **[n]CPBM** macrocycles with increasing values of n.

The polyradicaloid character of these macrocycles is summarized in Table 6.1. Descriptors, namely, $\Delta E_{gs,es}$ (energy gap from ground state to first excited state of higher multiplicity), y_n and N_u, were computed with RAS-SF method, the active space and high-spin multiplicity are system dependent. Note that radical index y_i is obtained as the LUNO+i occupation: when n is odd, y_0 (LUNO), y_1 (LUNO+1), y_2 (LUNO+2), y_3 (LUNO+3) and y_4 (LUNO+4) are the tri, penta, hepta, nona and undecaradicaloid characters, respectively, while for even values of n y_0, y_2, y_3, y_4 and y_5 are the di, tetra, hexa, octa and decaradicaloid index.

[n]	State	Energy	N_u	y_0	y_1	y_2	y_3	y_4
[n]CPBM								
3	Doublet	0.000	1.70	0.35	-	-	-	-
	Quartet	4.186	3.00		-	-	-	-
4	Singlet	0.000	2.95	0.75	0.73	-	-	-
	Triplet	3.396	3.47			-	-	-
	Quintet	6.956	4.00			-	-	-
5	Doublet	0.000	3.94	0.74	0.73	-	-	-
	Quartet	3.395	4.51			-	-	-
	Sextet	6.971	5.00			-	-	-
6	Singlet	0.000	4.61	0.82	0.75	0.73	-	-
	Triplet	1.632	4.98				-	-
	Septet	8.200	6.00				-	-
7	Doublet	0.000	5.42	0.75	0.74	0.72	-	-
	Quartet	3.252	5.93				-	-
	Octet	10.390	7.00				-	-
8	Singlet	0.000	5.93	0.76	0.75	0.73	0.73	-
	Triplet	3.074	6.44					-

Continued on next page

[n]	State	Energy	N_u	y_0	y_1	y_2	y_3	y_4
	Nonet	13.248	8.00					-
[n]PTM								
3	Doublet	0.0000	3.00	1.00	-	-	-	-
	Quartet	0.0000	3.00		-	-	-	-
4	Singlet	0.0000	3.99	1.00	1.00	-	-	-
	Triplet	0.0003	3.99			-	-	-
	Quintet	0.0007	4.00			-	-	-
5	Doublet	0.0000	4.98	1.00	1.00	-	-	-
	Quartet	0.0008	4.99			-	-	-
	Sextet	0.0016	5.00			-	-	-
6	Singlet	0.0001	5.95	1.00	0.99	0.99	-	-
	Triplet	0.0000	5.95				-	-
	Septet	0.0261	6.00				-	-
[n]MC								
8	Singlet	0.0	4.85	0.73	0.58	0.58	0.50	-
	Triplet	2.7						-
	Nonet	20.6	8.00					-
10	Singlet	0.4	7.08					
	Triplet	0.0	7.04	0.97	0.94	0.57	0.52	0.51
	11-et	22.8	10.00					

Table 6.1 Relative energies of ground state and excited states with lowest and maximum multiplicity (according to n) of **[n]CPBM**, **[n]PTM** and **[n]MC**. Energy is in kcal/mol, N_u represents the number of unpaired electrons, and y_i is the ith radical index of the ground state.

In the ground state, these macrocycles are characterized by large N_u and y_i values, as well as small energy gaps between ground state and lowest-lying excited state of different multiplicity. **[8]MC** is a singlet octaradicaloid ($y_3 = 0.50$) with 4.85 unpaired electrons. In the triplet ground state, **[10]MC** has large y_i values up to $y_4 = 0.51$ ($y_1 = 0.97$, $y_2 = 0.94$, and $y_3 = 0.57$), meaning that it possesses moderate decaradicaloid character. In fact, **[10]MC** was the first stable (finite) organic decaradicaloid system reported at the moment of its synthesis and characterization (2018).

In **[n]CPBM**, the polyradical character is moderate, with 1.70, 2.95, 3.94,

4.61, 5.42 and 5.93 unpaired electrons for $n = 3 - 8$, respectively, and states of the highest multiplicities computed at ≈ 13 kcal/mol with respect to the ground state. Experimental measurements by SQUID give energy gaps between ground state and states with higher multiplicity of less than 4 kcal/mol.

[n]PTM	ΔE	Spin configuration
[3]PTM		
	0.000	α, β, α
	0.066	β, α, β
	0.066	α, α, α
[4]PTM		
	0.000	$\alpha, \beta, \alpha, \beta$
	0.077	$\alpha, \alpha, \beta, \beta$
	0.154	$\alpha, \alpha, \alpha, \alpha$
[5]PTM		
	0.000	$\beta, \alpha, \beta, \alpha, \beta$
	0.182	$\alpha, \alpha, \alpha, \alpha, \alpha$
	0.581	$\alpha, \alpha, \alpha, \alpha, \beta$
[6]PTM		
	0.000	$\alpha, \beta, \alpha, \beta, \alpha\beta$
	0.172	$\alpha, \beta, \alpha, \alpha, \beta, \alpha$
	0.320	$\alpha, \alpha, \beta, \beta, \alpha, \beta$
	0.940	$\alpha, \alpha, \alpha, \alpha, \alpha, \alpha$

Table 6.2: Energy gap between different spin configurations (kcal/mol) computed with the C-DFT method.

There are $\sim n$ unpaired electrons in **[n]PTM**, and a quasi-degeneration between states with different multiplicities, resulting in an ambiguous ground state spin. To further explore and analyze this situation, specific spin configurations at the ground state geometry were computed by imposing one electron to be localized over each one of the n **PTM** radical centers as presented in Table 6.2. Notice that in **[3]PTM**, the energy of configuration β, α, β is not equal to α, β, α because the sides of the triangle are not equivalent. The imposed spin constraints split the energy of the states of different multiplicities, but with rather small energy gaps ($\Delta E < 1$ kcal/mol). Considering the cyclic arrangement of **[n]PTM** and **[n]CPBM**, the interradical coupling can be approximated by $\Delta E_{S,T} = 2J$ ($\Delta_{D,Q} = 3J$) for even (odd) radical sites.(14) J values of ≈ 1.5 kcal/mol and $J \approx 0$ kcal/mol are computed for **[n]CPBM** and **[n]PTM**, respectively, indicating the weak to very weak AFM

coupling in these macrocycles. Delocalization of the unpaired electrons in **[*n*]MC** prevents the characterization of low-lying states of different spin multiplicities with an effective spin Hamiltonian, and I did not attempt to define a coupling interaction constant in these systems.

In summary, macrocycles of these families can be regarded as *n*-radicaloid (from tri up to decaradicaloid) with a weak to medium AFM coupling between radical centers that favors a low-spin ground state multiplicity. It is remarkable that all of them are stable under ambient conditions.

6.1.1 π-conjugation: [*n*]annulene analogs

The large number of radical sites in addition to the π-conjugation along the backbone favors the delocalization of the electronic density over the whole cycle. This is reflected by i) the formation of alternated aromatic-quinoidal-like structure within the *p*-phenyl units of **[*n*]CPBM** and, ii) the single-double bond alternation in **[*n*]MC** extending over both edges of the macrocycles. Differently, the presence of the ethynylene group in the bridge of **[*n*]PTM** gives rise to an equilibrium between single-triple bond alternation and the cumulene conjugation. On the other hand, the benzene rings in these macrocycles tend to form Clar's sextets and recover their local aromaticity, leading to the presence of unpaired electrons and the rise of polyradical character. Equilibrium between quinoidal and local aromatic structures of **[8]MC**, **[4]CPBM** and **[4]PTM** are illustrated in Figure 6.4.

Due to their geometry and conjugation, **[*n*]CPBM** and **[*n*]PTM** could be thought as large-size annulenes with *n* sides to which the aromatic basic rules apply. Namely, if there are (4n+2)π-electrons, annulenes are classified as aromatic according to the Hückel's rule and tend to delocalize their π electrons over the whole cycle. But, if there are 4nπ-electrons in the system, annulenes are then considered antiaromatic and avoid electron delocalization. The interconversion between both valence isomers in annulenes can occur via polyradical transition state(20; 21), and can be experimentally detected if the rate constant is slow. This process is called "valence tautomerization" and involves the breaking and posterior formation of double bonds. As a consequence, the valence tautomerization goes through an intermediate with unpaired electrons. Despite the big efforts to characterize it, this process remains experimentally unobserved, presumably due to the presence of small reaction barriers.

Particularly, **[4]CPBM**, where two opposite sides of the macrocycle hold quinoidal-like structure and the other two are aromatic (illustrated with the radical-radical distance in Figure 6.3b), can be compared with the cyclobutadiene (CBD) structure. In the ground state, CBD has two clearly localized double bonds con-

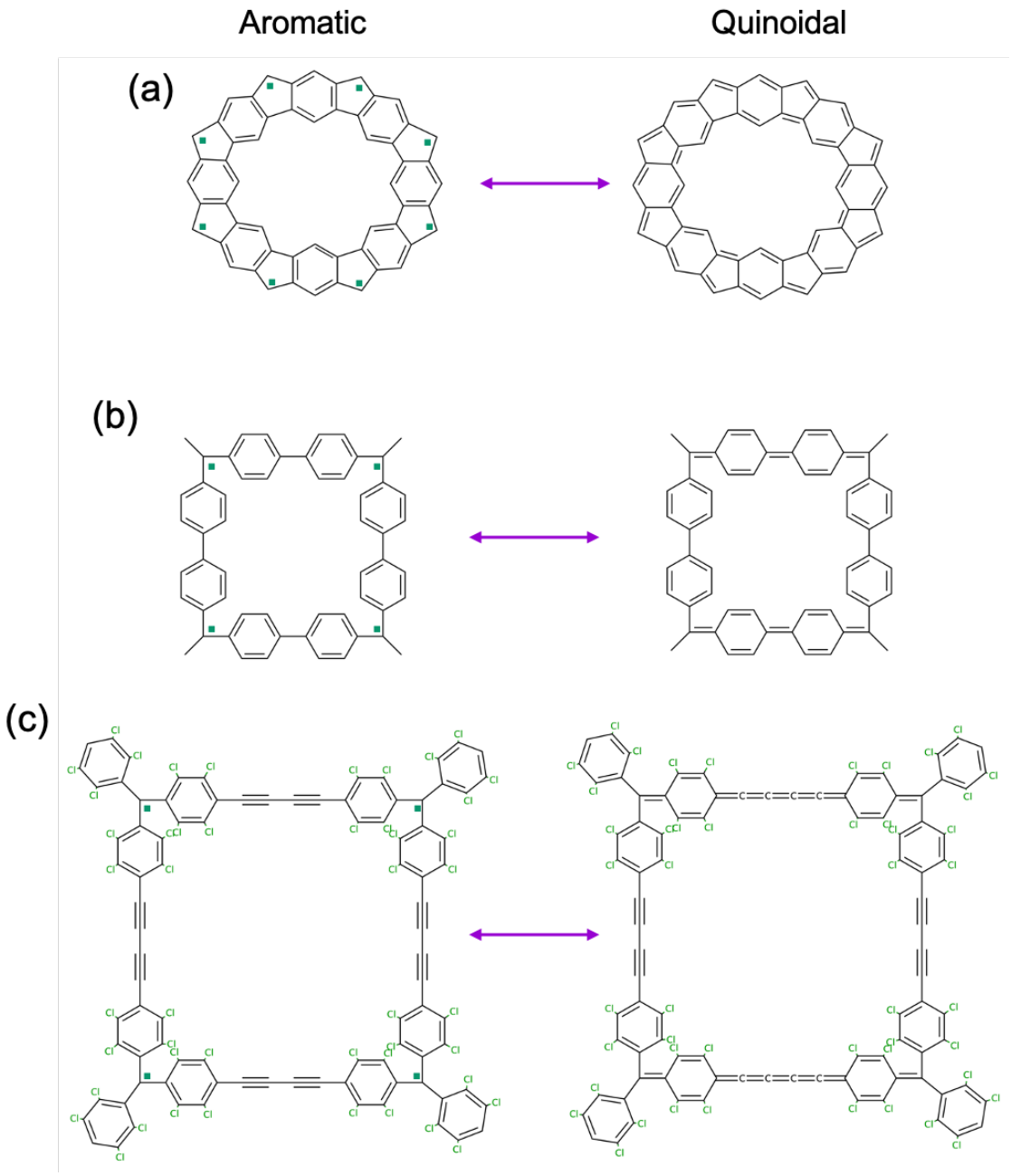

Figure 6.4: Equilibrium between quinoidal and local aromatic structures of **[8]MC** (a), **[4]CPBM** (b) and **[4]PTM** (c).

nected by two single bonds and is thus the smallest antiaromatic annulene (with 4π-electrons). The valence tautomerization of CBD is an ultrafast process with a transition state theoretically predicted as a square diradical.(21; 22) **[4]CPBM** has 36π-electrons, and it can be thought as an antiaromatic annulene. Its size and the large number of bonds that must be broken and formed in the valence tautomerization, in addition to the loss of local aromaticity in 4 benzene rings, increase significantly the barrier of the process and make it experimentally detectable by

variable-temperature (VT)-NMR measurements.

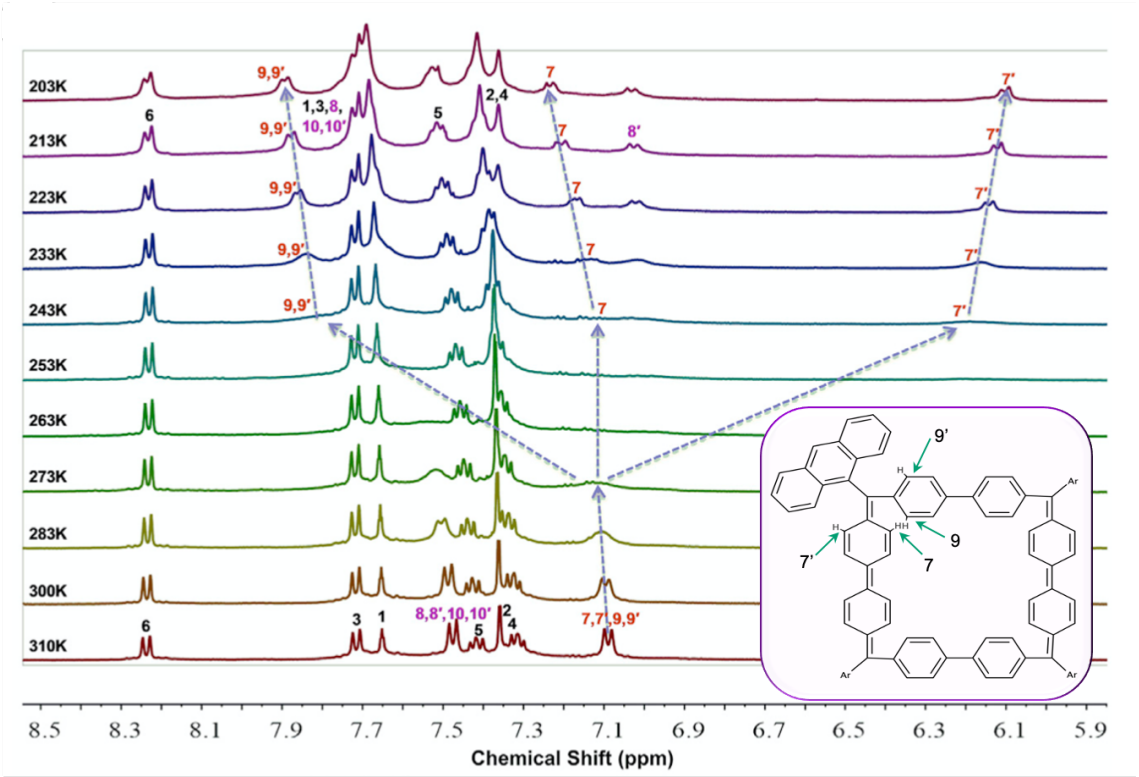

Figure 6.5: VT-NMR spectra of the aromatic region of **[4]CPBM**. The arrows show the splitting of the protons 7, 7' , 9, and 9' at low temperature. Hydrogen atoms labeled as 7, 7', 9 and 9' are shown in the inset. Figure adapted from reference(19).

Experimentally, the process was followed by the evolution of the chemical shift of the NMR of the non-equivalent hydrogen atoms of benzene rings in the *p*-diphenyl bridges of **[4]CPBM**. Spectrum at 310 K (Figure 6.5) shows two signals, suggesting that there are just two kinds of hydrogen atoms in the macrocycle backbone. The first one corresponds to those close to the bulky protector group (7, 7', 9 and 9' in Figure 6.5) and the other one to hydrogen in the centre of each side (8, 8', 10 and 10'). This is an indication of the very fast interconversion between quinoidal and aromatic structures. By cooling the sample, the signals are broadened and they coalesce at 263 K. Then, around 243 K, the signals of 7, 7', 9 and 9' split in three groups, which means that the bridges are not equivalent anymore. In quinoidal-like sides of the "annulene", the signal of hydrogen in position 7' (closest to the anthracene group) is clearly different from the hydrogen atom labeled as 7 (in the "internal" side of the macrocycle). The atoms in the same positions (7 and 7') of aromatic bridges remain equivalent due to the ability of the benzene ring to rotate (quinoidal bridge is rigid and six-membered rings cannot rotate). The interconversion energy barrier of the valence tautomerization was determined to be $\sim$ 11.2 kcal/mol,(19) slightly lower than the barrier in smaller annulenes. For instance, the cyclooctatetraene the

experimental barrier was determined as $\sim$ 13 kcal/mol.(20)

Theoretically, the transition state between valence isomers of **[4]CPBM** was computed as a global antiaromatic C_4 structure, found 7.1 kcal/mol higher in energy than the C_2 ground state (Figure 6.6). In the transition state geometry, all four sides of **[4]CPBM** are equivalent, meaning that the four benzene rings localized in two opposite sides of the macrocycle in C_2 geometry have lost their aromatic sextet and now contribute with 4 π-electrons each to the whole ring. As a consequence, the transition state is globally antiaromatic with $4n\pi$-electrons.

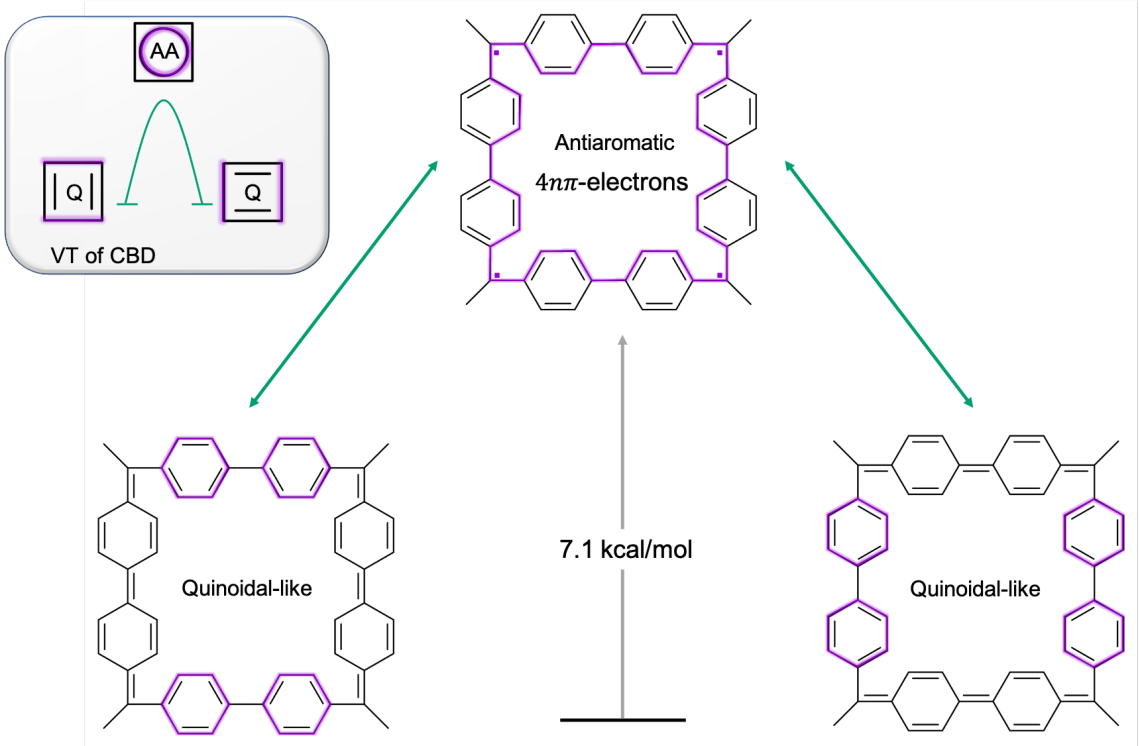

Figure 6.6: Valence tautomerization of **[4]CPBM**. Two quinoidal-like structures are connected through an antiaromatic transition state by a energy barrier of 7.1 kcal/mol. Local aromatic benzene rings of quinoidal-like structures and antiaromatic ring of transition state are highlighted in purple. For comparison the same process of CBD is represented. AA = antiaromatic, Q = quinoidal. Figure adapted from reference(19).

Experimentally, the tautomerization of **[n]CPBM** with $n = 6$ and $n = 8$ is not observed, indicating that the interconversion barrier must be too small to be detected. Hence, **[4]CPBM** represents a rare example of annulene-like system carrying out a detectable valence tautomerization process.(19)

6.1.2 Global aromaticity of [8]MC and [10]MC

Coronoid-like molecules (as **[*n*]MC**) are cyclic compositions of fused benzene rings that can be drawn as an alternation of aromatic rings with Clar's sextet and 5-membered carbon rings or as the union of two peripheral singlet-double bond chains ([*n*]annulenes) one inside of the other, covalently linked by single bonds, *i.e.*, with no conjugation between both annulenes. These structures have been named annulene-whitin-an-annulene (AWA) super ring and were proposed for the first time in 1966 with the synthesis of corannulene(23; 24), see Figure 6.7a. However, the AWA concept was discarded by theoretical calculations showing that inner-outer annulenes are not decoupled as there is at least one double bond linking them.(24) Lately, kekulene(25; 26) was proposed theoretically with an AWA structure consisting of an [18]annulene within an [30]annulene (Figure 6.7b); its synthesis in 1978 proved that its structure is dominated by the presence of Clar's rings. Since then, constant efforts have been dedicated to the design of macrocycles with the AWA structure. One approach proposed to (at least partially) prevent the formation of aromatic benzene consist in alternating five and six membered rings so as to promote the annulene formation.(27) However, a truly AWA super ring structure has not yet been found.

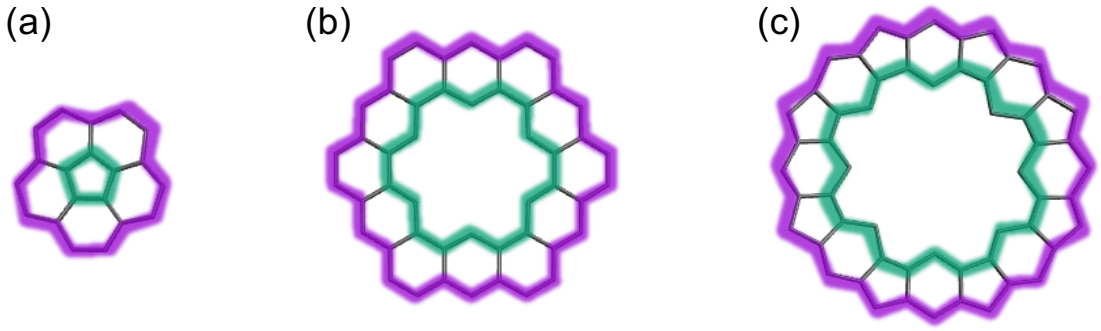

Figure 6.7: Examples of first predicted AWA structures: corannulene (a) and kekulene (b). AWA structure of **[8]MC** (c).

The close inspection of the quinoidal structure (Figure 6.4a) of **[8]MC** shows the absence of Clar's sextets and the formation of two, "in" and "out", disconnected annulenes. More specifically, **[*n*]MC** outer and inner rings present a single-double bond alternation pattern and are connected by single bonds ($\sim$ 1.46Å). To further characterize the conjugated systems in the singlet (triplet) ground state of **[8]MC** (**[10]MC**), I have performed induced current density (ACID) calculations at the (U)B3LYP/6-31G(d,p) level of theory. In both macrocycles, ACID plots show two fully decoupled ring current circuits (Figure 6.8a) localized over the annulenes of the macrocycle. These results suggest the formation of truly AWA super-ring structures:

[8]MC and **[10]MC** are characterized as [24]annulene-within-an-[32]annulene and [30]annulene-within-an-[40]annulene super-ring structures, respectively.

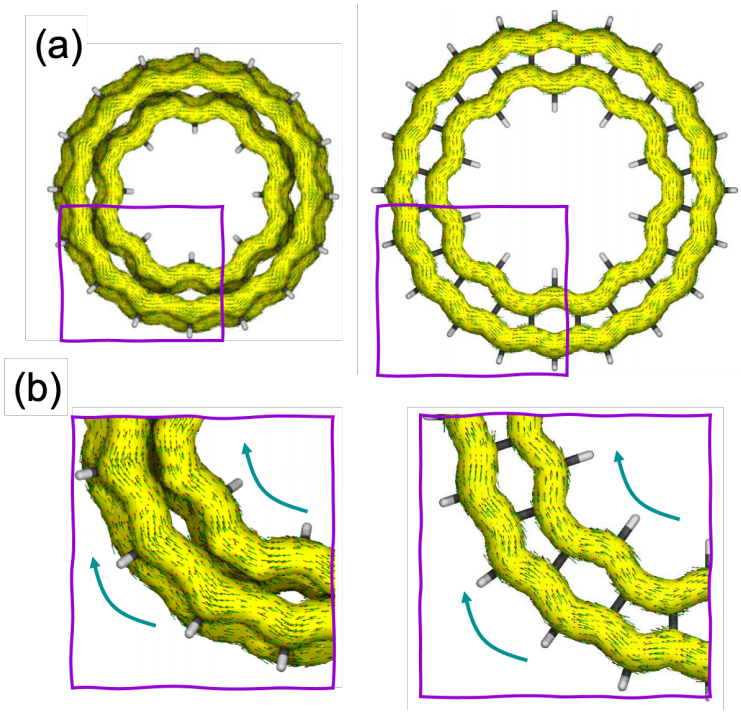

Figure 6.8: ACID current of **[8]MC** (left) and **[10]MC** (right) in their ground state conformation, singlet and triplet, respectively (a). Green arrows are clockwise direction and represent the diamagnetic current in each cycle (b). Figure adapted from reference(18).

[8]MC, as the combination of [24] and [32] annulenes, has 56 π-electrons and should be classified as an antiaromatic system ($4n\pi$ with n = 14). Surprisingly, a current flow in the ACID plots shows opposite aromaticity with an unexpected clockwise diamagnetic current flow in both inner and outer annulenes that corresponds to an aromatic system (Figure 6.8b). **[8]MC** is thus a [24]annulene-within-an[32]annulene with unusual local and global aromaticity.

On the other hand, as the internal ring in **[10]MC** has $(4n+2)\pi$-electrons and the external one $4n\pi$-electrons. **[10]MC** possesses $(4n+2)\pi$-electrons. Nevertheless, it is worth remembering that since the ground state of **[10]MC** is a triplet, Baird's rule should be applied to predict the aromaticity of the system. Under Baird's rule, the lowest-lying triplet exhibit aromatic (antiaromatic) character if there are $4n\pi((4n+2)\pi)$-electrons; hence, this macrocycle should be expected to be antiaromatic.

Experimentally, the ^{1}NMR spectra of **[8]MC** shows two signals that can be associated to hydrogen atoms of the outer and inner annulene rings, named *a* and *b*, respectively (Figure 6.9). Spectra were recorded at temperatures ranging between

298 and 233 K, showing a central group of bands associated with the protons of the bulky protector group, and two small side peaks at low and high field that presumably correspond to hydrogen of the inner and outer rings, respectively, the latter being better defined at low temperature. Differently from the NMR spectrum of **[4]CPBM**, the broadening observed by heating is characteristic of open-shell singlet diradicaloids and not of the change of the chemical nature of hydrogen atoms. Our calculations nicely reproduce the ^{1}H NMR spectrum, showing one signal for the eight *b* protons at very high field (δ = -24.06 - -24.10 ppm) that corresponds to the protons of the inner ring. The other signal, for all eight hydrogens of the outer ring, was found at very low field (δ = 14.80 - 14.78). Therefore, **[8]MC** can be regarded as a highly aromatic system. On the other hand, **[10]MC** is ^{1}H NMR silent due to its triplet ground state.

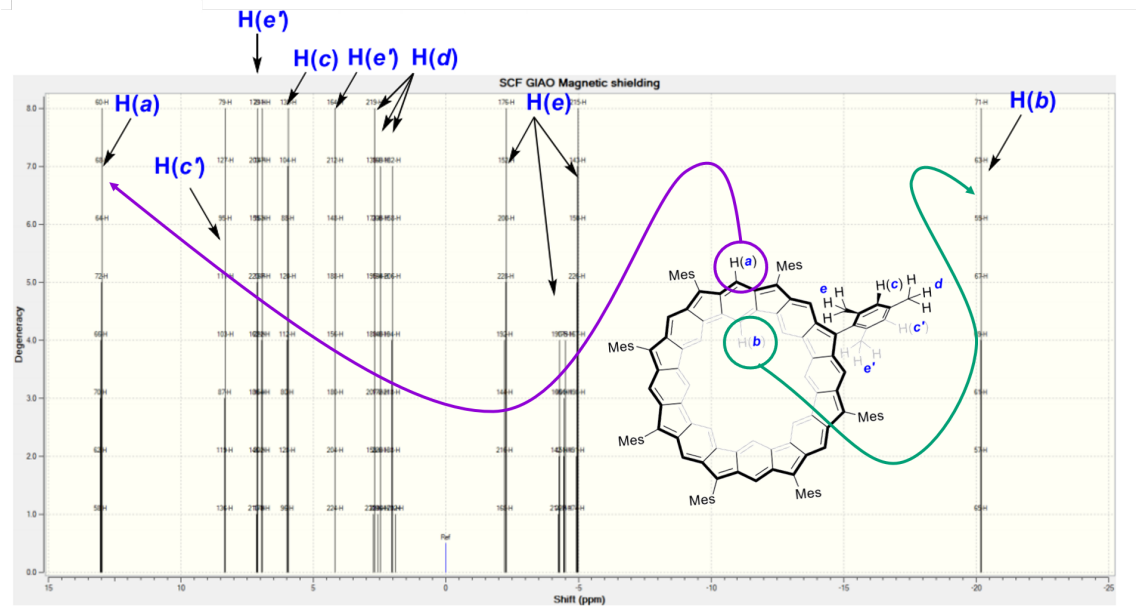

Figure 6.9: Calculated (restricted) 1H NMR spectrum (B3LYP/6-31G(d,p)-GIAO) based on the optimized geometry. The hydrogen labels of **[8]MC** are indicated in the inset. The bowl pointing from the inner hub to the outer rim through the paper. Protons e and c point to the concave side, while protons e' and c' point to the convex side. Figure adapted from reference(18).

In order to rationalize the unusual global aromaticity of both macrocycles, based on their AWA properties we can consider the whole macrocycle as the sum of two individual parts (inner and outer rings). Hence, the "adiabatic" state (describing **[*n*]MC**) can be understood as the combination of "diabatic" states with well defined charge and spin on each annulene. Within this approximation, the aromaticity of **[8]MC** can be explained by two alternative electronic structures: i) one annulene gives two electrons to the other one, then both are (4n+2)π-electrons

systems and therefore aromatic singlets (Hückel's rule); or, ii) each annulene holds a triplet (diradical) ground state and is aromatic according to the Baird's rule. To that end, constrained DFT (C-DFT) calculations were performed with restrictions imposed to inner and outer annulenes, resulting in the following "in/out" annulenes configurations: S/S, T/T, 1+/1-, 1-/1+, 2+/2- and 2-/2+. The main idea is to provide energetic arguments to discern which conformations can stabilize the total wave function.

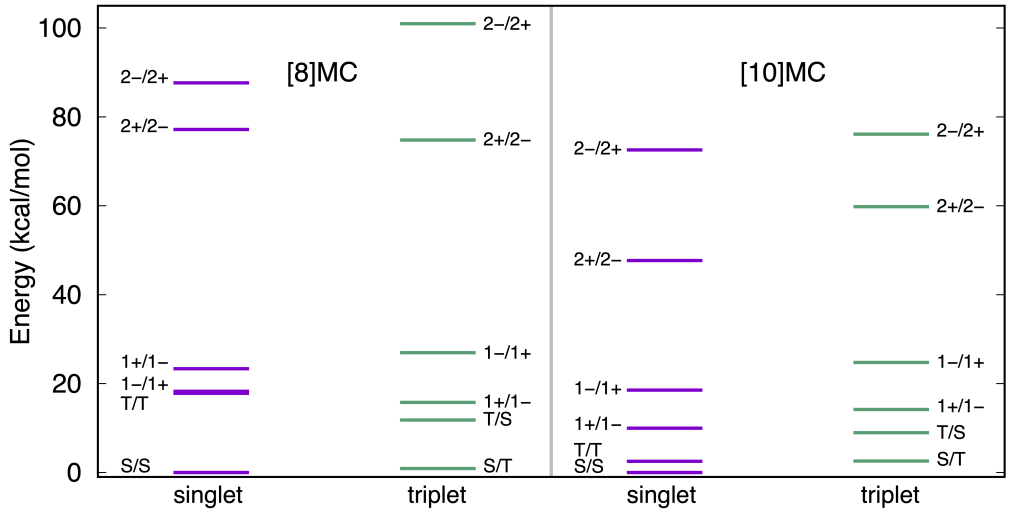

Figure 6.10: State energy diagram for the diabatic states of **[8]MC** and **[10]MC** molecules computed with C-DFT. All energies are given with respect to the lowest singlet or triplet state. State labels correspond to the restriction on inner/outer annulene rings, respectively. S/S = singlet/singlet, T/T = triplet/triplet, 1-/1+ = anion/cation, 1+/1- = cation/anion; 2-/2+ = dianion/dication, 2+/2- = dication/dianion. Figure adapted from reference(18).

The relative energy ordering of each pair of diabatic states (Figure 6.10) indicates that 2+/2- and 2-/2+ states are much higher in energy than S/S, T/T, 1+/1- and 1-/1+. Consequently, the participation of dianionic states in the total wave function is expected to be insignificant. This excludes the option of having two $(4n+2)\pi$ annulenes with singlet ground state exhibiting Hückel aromaticity. Hence, the second case has to be considered to explain the global aromaticity of **[8]MC**, that is, both annulenes are open-shell (computed as triplet) ground state, *i.e.*, diradicals, with aromatic properties according to the Baird's rule. The presence of two open-shell annulenes agrees very well with the high polyradical character of this macrocycle and the number of unpaired electrons (N_u = 4.85, Table 6.1) and explains the flow currents observed in ACID plots.

The ground state triplet of **[10]MC** can be described as the combination of singlet and triplet annulenes with 30 and 40 π-electrons. The lowest energy contri-

bution is the S/T state, and ACID plot reveal their clockwise current flow, like this both aromaticity rules are satisfied simultaneously, inner ring is an aromatic singlet (Hückel) and the outer ring is an aromatic triplet (Baird's rule). These results confirms its super-aromatic AWA structure.

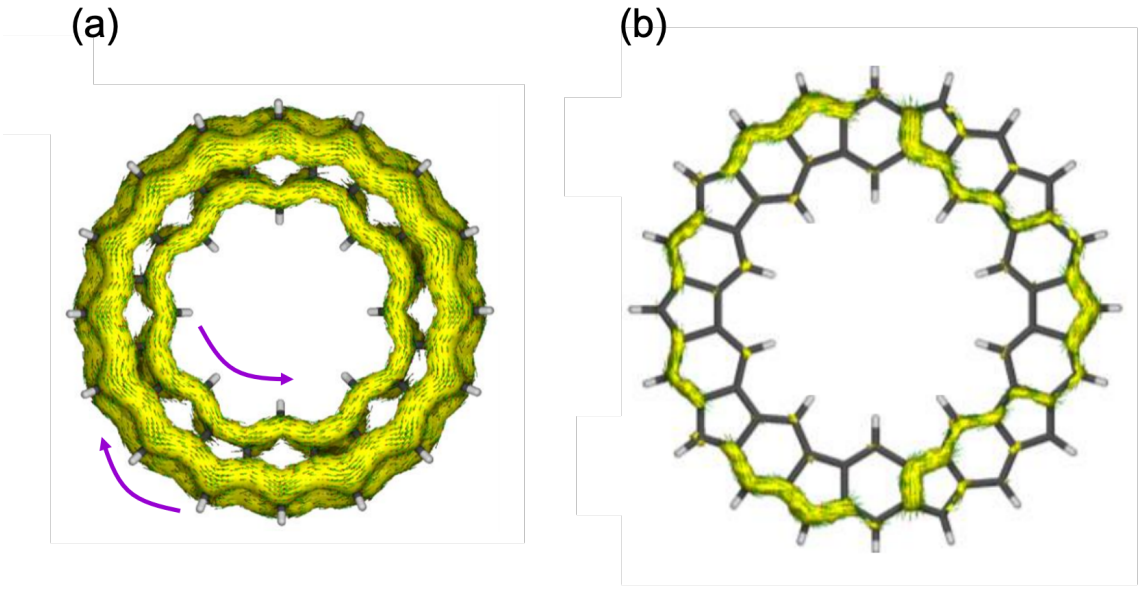

Figure 6.11: ACID current of **[8]MC** (a) and **[10]MC** (b) in their first excited state conformation, triplet and singlet, respectively. Green arrow is clockwise direction and represent the diamagnetic current, purple arrow is counter clockwise direction and represent the paramagnetic current of the rings. Figure adapted from reference(18).

The ACID plots of the lowest-lying excited states of **[n]MC** shows antiaromatic ($n = 8$) and non-aromatic ($n = 10$) features. Again, their wave function can be rationalized by the contributions of the diabatic states of each ring to the adiabatic state of the macrocycle. The first triplet excited state of **[8]MC** is mainly the S/T combination of states and it must be understood as an antiaromatic [24]annulene with singlet state (Hückel rule) within an aromatic diradicaloid with 4nπ-electrons (Baird's rule). This combination of states is in good agreement with the counter-clockwise paramagnetic (inner) and clockwise diamagnetic (outer) current flow observed in the ACID plot (Figure 6.11a). The lowest-lying excited state of **[10]MC** is a singlet with no current flow and therefore a non-aromatic system; this might be seen as the result of the aromatic-antiaromatic cancellation (Figure 6.11b). S/S and T/T are close in energy and to differentiating them is not straightforward. Nevertheless, both configurations combine one (4n+2)π and one 4nπ-annulenes, *i.e*, one aromatic and one antiaromatic rings under both Hückel and Baird rules.

Ring model	Spin multiplicity	Charge	α-elec	β-elec	Global
[8]MC_in	S	0	12 (AA)	12 (AA)	AA
[8]MC_in	T	0	13 (A)	11 (A)	A
[8]MC_in	D	-1	13 (A)	12 (AA)	NA
[8]MC_in	D	+1	12 (AA)	11 (A)	NA
[8]MC_in	S	-2	13 (A)	13 (A)	A
[8]MC_in	T	+2	11 (A)	11 (A)	A
[8]MC_out	S	0	16 (AA)	16 (AA)	AA
[8]MC_out	T	0	17 (A)	15 (A)	A
[8]MC_out	D	-1	17 (A)	16 (AA)	NA
[8]MC_out	D	+1	16 (AA)	15 (A)	NA
[8]MC_out	S	-2	17 (A)	17 (A)	A
[8]MC_out	T	+2	15 (A)	15 (A)	A
[10]MC_in	S	0	15 (A)	15 (A)	A
[10]MC_in	T	0	16 (AA)	14 (AA)	AA
[10]MC_in	D	-1	16 (AA)	15 (A)	NA
[10]MC_in	D	+1	15 (A)	14 (AA)	NA
[10]MC_in	S	-2	16 (AA)	16 (AA)	AA
[10]MC_in	T	+2	14 (AA)	14 (AA)	AA
[10]MC_out	S	0	20 (AA)	20 (AA)	AA
[10]MC_out	T	0	21 (A)	19 (A)	A
[10]MC_out	D	-1	21 (A)	20 (AA)	NA
[10]MC_out	D	+1	20 (NA)	19 (A)	NA
[10]MC_out	S	-2	21 (A)	21 (A)	A
[10]MC_out	T	+2	19 (A)	19 (A)	A

Table 6.3: Contributions to the global aromaticity from α and β π-electrons for each diabatic state of inner (_in) and outer (_out) rings of **[8]MC** and **[10]MC** molecules. S = singlet (closed-shell), D = doublet, T = triplet, A = aromatic, AA = antiaromatic, NA = no aromatic (cancellation between α and β).

Finally, the ionic configurations (1-/1+ and 1+/1-) are low in energy, and can be considered as a minor contribution to the polyradical character of these macrocycles. However, differently from the singlet and triplet states, there is no a well-established rule to determine the aromaticity of doublet states. Mandado et al. suggested an extension to the Baird's rule in order to evaluate the aromaticity as the sum of separate contributions from α and β π-electrons.(28) To this end, we deconstructed the macrocycles as the inner and outer annulenes (**[X]MC**_in or _out), and applied

the "extended Baird's rule", the prediction of which are summarized in Table 6.3.

Anionic annulenes have no aromatic character and thus do not contribute to the global aromaticity of the macrocycles. These results are also in good agreement with the contributions given by the energetic ordering of C-DFT configurations, showing that the singlet of **[8]MC** can be aromatic only from the combination of triple(inner)-triplet(outer) rings. While the sharing of 2 electrons also leads to global aromaticity in a singlet, this contribution can be neglected on the basis of energy considerations. Similarly, the singlet(inner)-triplet(outer) is the only one that gives an aromatic triplet.

It is necessary to stress the qualitative character of these results. They should be used only to distinguish between two extreme situations. The entire complexity of these macrocycles is dictated by their multiconfigurational character and cannot be recovered by C-DFT calculation.

6.2 Fluorenyl dendrons

Etymologically, the term dendrimer comes from the Greek words *dendron* (tree) and *mero* (part), meaning "the part of a tree". Actually, their structure resembles snowflakes or treetops.(29) More specifically, they are polymers growing up in branched arrangements surrounding a core. The number of units in the polymer determines the generation of dendrimers and dendrons: a core with one layer constitutes a dendrimer of first generation, while it is a dendrimer of second generation when the core has two layers, and so on up to generation "n" (Figure 6.12).(30; 29; 31) The physical properties associated with the structure, *i.e.*, viscosity, flexibility, solubility, and density distribution can be modulated by the nature of the end group, leading to possible applications in a huge number of fields, from medicine as drug carrier agents, tumor sensors or contrast agents for bioimaging, etc.(31; 32) to photoelectronic material science as light-harvesting systems or emitting polymers LEDs.(31; 29; 33)

Over the past decades, the group of Prof. Rajca has worked extensively in the design and synthesis of dendritic radicals (also referred to as spin clusters), which exhibit a massive number of radical sites with very strong ferromagnetic interaction between them, consequently holding an impressive ground state spin multiplicities (up to 500), yet with low stabilities.(6) No evidence of stable radical or polyradical dendrons and dendrimers was available in the literature before 2018, when the present investigation was published.(34)

The expansion of the polyradical macrostructures in branches (following the dendritic arrangement) using the fluorenyl radical (**FR**) as building block is explored

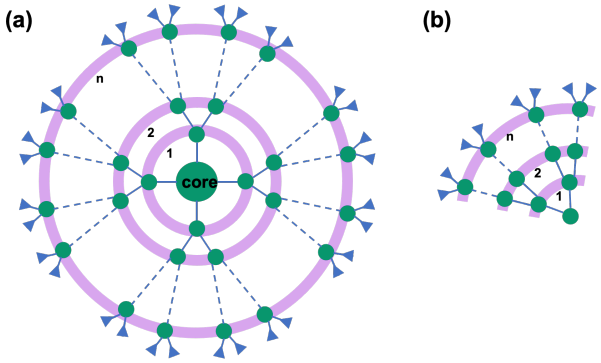

Figure 6.12: General structure of a dendrimer (a) and dendron (b). Central green circle is the core, and the small ones represent branching units. Blue triangles are the end group. Each generation is indicated by purple circles and labeled as first (1), second (2), or n-*th* (n).

here. The first generation of fluorenyl radical monodendron, **FR-G1**, is built by connecting two fluorenyl moieties through 9-position to the *central* **FR** in 3,6-positions. By expanding **FR-G1** with one more layer using the same pattern, the dendron radical of second generation **FR-G2** is obtained. The 9-position of the central fluorenyl moiety is kinetically blocked by a bulky 9-(3,5-di*tert*-butylphenyl)anthryl and 3,6-positions of the outer units are blocked by 4-*tert*-butylphenyl groups, as a result both dendrons are stable. Experimentally, half-life of **FR-G1** and **FR-G2** has been determined upon exposure to air and light ambient conditions by UV/VIS/NIR spectroscopy. **FR-G1** has a half-life of 6 days, while the lifetime of the larger **FR-G2** is shorter, lasting a bit more than 4 days.(34)

The connectivity of **FR** units in **FR-G1** and **FR-G2** allows the formation of quinoidal and aromatic forms (Figure 6.13): In latter case, all six-membered carbon rings preserve their aromatic sextets. On the other hand, the formation of *para*-quinodimethane-like bonds between fluorenyl units in one or two of the branches of **FR-G1** and **FR-G2**, respectively, leads to the quinoidal-like structure of these fluorenyl dendrimers. Additionally, an intermediate situation can be drawn for **FR-G2** in which one branch has aromatic features and the other presents some quinoidal character. Aromatic and quinoidal forms stabilize the open- and closed-shell configurations, respectively. In the aromatic structure, the number of "free" radicals and the multiplicity is expected to be maximized; in this case, **FR-G1** has 3 radical centers, and **FR-G2** can stabilize up to 7 unpaired electrons. The ground state of **FR-G1** is predicted to be a doublet (D_0), while **FR-G2** has a quartet (Q_0) ground state. In these minima, the bond length between fluorenyl units does not correspond to a double bond (**FR-G1** = 1.46, 1.467 Å and **FR-G2** = 1.463, 1.467, 1.468, 1.465, 1.467, 1.467 Å). This suggests that the aromaticity of the benzene rings is preserved in both dendrons (Figure 6.13 right) and they are open-shell systems.

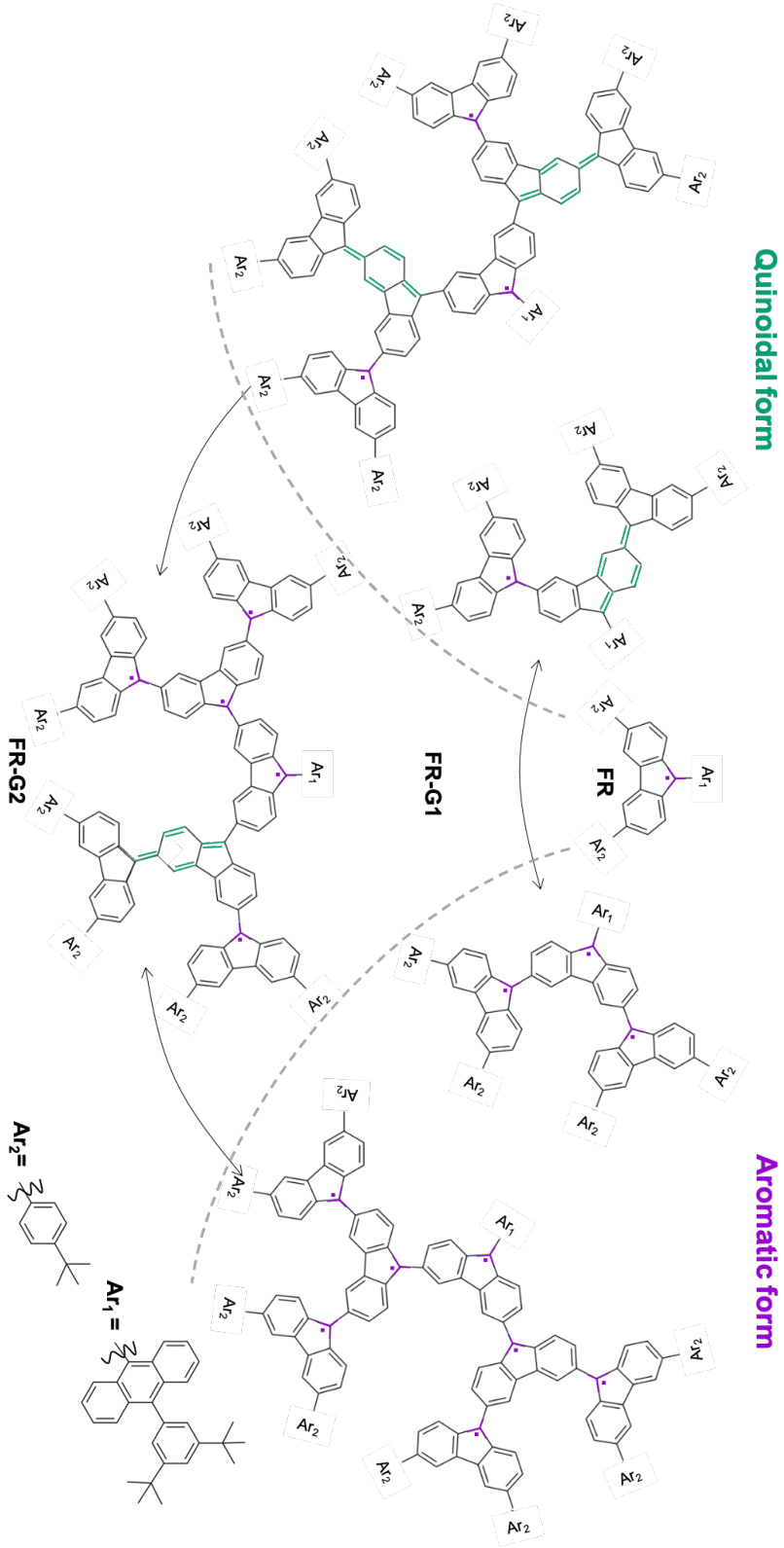

Figure 6.13: Structure of fluorenyl radical (**FR**) surrounded by the first generation flourenyl radical mono-dendron (**FR-G1**) and the second generation fluorenyl radical mono-dendron (**FR-G2**). Quinoidal bonds are indicated in green and radical sites in purple. Figure adapted from reference(34).

The radical characterization of minimum energy structures is summarized in Table 6.4. The doublet ground state of **FR-G1** with close to 2 effective unpaired electrons is computed 8.19 kcal/mol below the first excited quartet. The quartet ground state of **FR-G2** has more than 5 effective unpaired electrons. The lowest-lying doublet state is computed just 0.78 kcal/mol higher in energy than Q_0. Computational description of both systems is in good agreement with the doublet-quartet energy gaps of **FR-G1** ($\Delta E_{D-Q} = -3.9$ kcal mol^{-1}) and **FR-G2** ($\Delta E_{D-Q} = 0.2$ kcal mol^{-1}) obtained from electron spin resonance (ESR) experiments.

FR-Gn	Multiplicity	Energy	N_u	n_{SONO-3}	n_{SONO-2}	n_{SONO-1}	n_{SONO}	n_{SONO+1}	n_{SONO+2}	n_{SONO+3}
FR-G1	Doublet	0.00	1.82	-	-	1.63	1.00	0.37	-	-
	Quartet	8.19	3.08	-	-	1.00	1.00	1.00	-	-
FR-G2	Quartet	0.00	5.23	1.50	1.42	1.00	1.00	1.00	0.58	0.50
	Doublet	0.78	4.71	1.64	1.42	1.12	1.00	0.88	0.58	0.36

Table 6.4: Characterization of lowest doublet and quartet states of **FR-G1** and **FR-G2**. Energy is in kcal/mol, N_u represents the number of unpaired electrons, $n_{SONO\pm i}$ is the electronic occupation of the semioccupied natural orbital i.

The interaction between radicals in these systems can be modeled by means of the effective spin Hamiltonian:

$$H = -2J \sum_{i<j} S_i S_j, \tag{6.1}$$

where J is the radical-radical interaction energy and $S_i S_j$ are the interaction between spins in two centers.

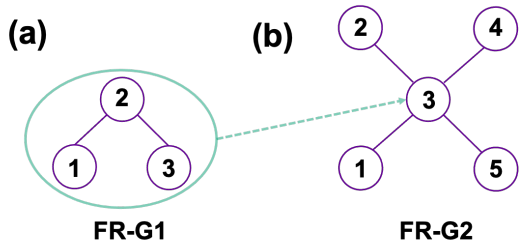

Figure 6.14: Radical-radical interaction models for **FR-G1** (a) and **FR-G2** (b). Figure adapted from reference(34).

FR-G1 follows a linear arrangement of three radical sites (Figure 6.14a) in which $H = -2J(S_1S_2 + S_2S_3)$ and $-2J = \Delta E_{D-Q}$, so that $J \approx -4.10$ kcal/mol. In **FR-G2** a star-like model is employed, in which one central radical site interacts with the peripheral ones (Figure 6.14b). It is important to notice that this model assumes the antiferromagnetic interaction of three radicals in the molecular center, *i.e.*, site 3 in Figure 6.14b is equivalent 6.14a. The effective Hamiltonian is then written as $H = -2J(S_3S_2 + S_3S_1 + S_3S_4 + S_3S_5)$ with $J = \Delta E_{Q-D} = -0.78$ kcal/mol.

From this analysis, the coupling between unpaired electrons in these systems can be classified as moderate antiferromagnetic.

Orbital diagram of the dominant configuration of the ground state of both molecules is depicted in Figure 6.15. (Note: Graphical representation and energy diagrams correspond to molecular orbitals obtained from the ROHF high-spin configuration, while electronic orbital occupancy was obtained at RAS-SF level, as reported in Table 6.4). Semi-occupied molecular orbitals are delocalized through-

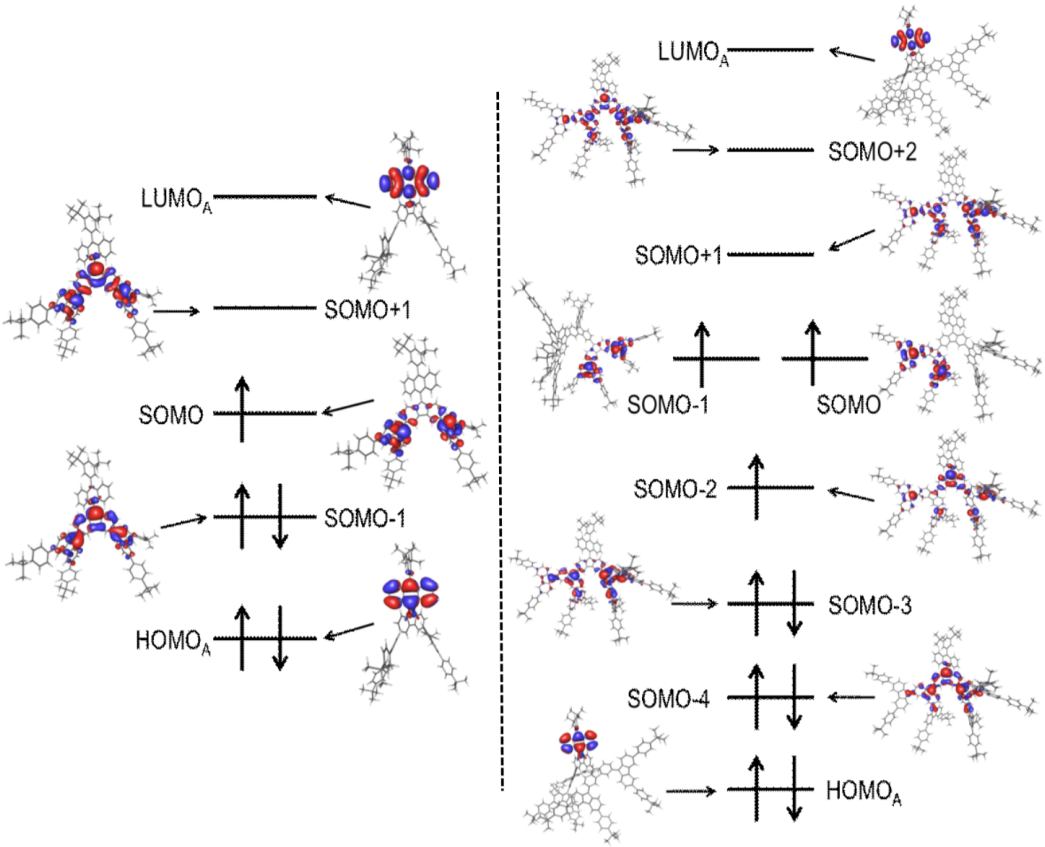

Figure 6.15: Ground state molecular orbital diagram of **FR-G1** (left) and **FR-G2** (right). Figure taken from reference(34).

out at least two neighbouring fluorenyl moieties. Accordingly, spin density of the doublet (quartet) ground state of **FR-G1** (**FR-G2**) is spread homogeneously over the whole fluorenyl core, illustrating the two-dimensional π-conjugation through the branches. Most of the spin density is localized at the 9-position carbons, *i.e.* the radical sites in the cyclopentadienyl radicals (Figure 6.16).

Electronic occupation of the lowest unoccupied natural orbital (Table 6.4) allows the characterization of the polyradical character of **FR-G1** and **FR-G2**. While **FR-G1** shows moderate triradical character, as indicated by $y_0 = 0.37$, **FR-G2** can be regarded as an heptaradicaloid, with $y_0 = 1.00$, $y_1 = 0.58$, and $y_2 = 0.50$.

All data exposed so far strengthen the description of the moderate AFM exchange interaction between fluorenyl units in both polyradicaloid dendrons. **FR-G1**

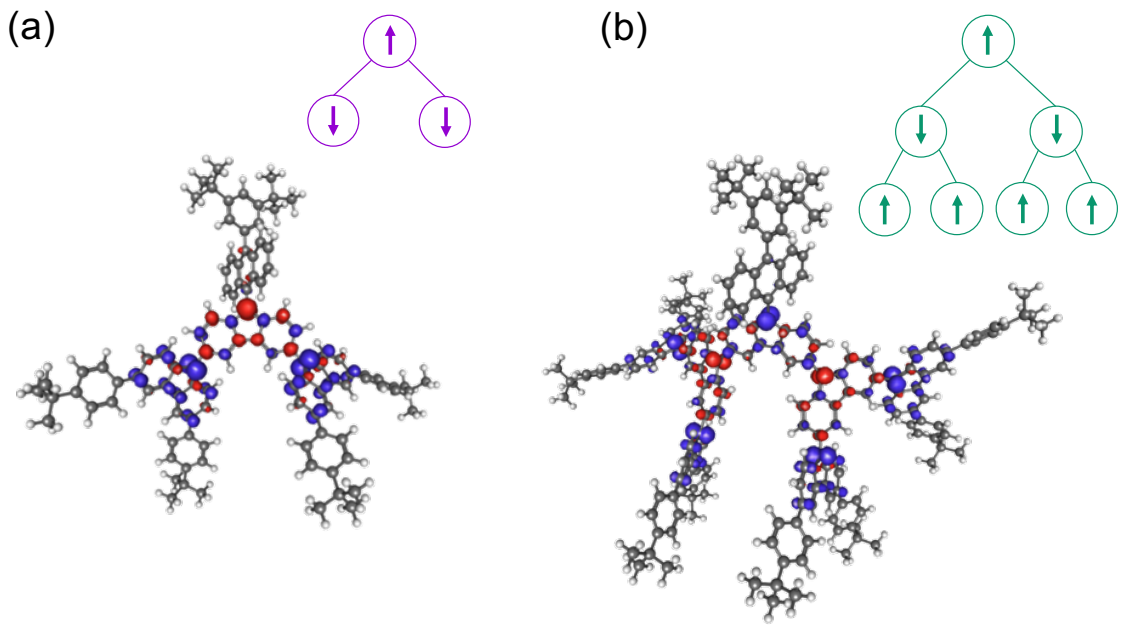

Figure 6.16: Spin density distribution of **FR-G1** (a) and **FR-G2** (b) computed at their respective ground states (doublet and quartet) at the UB3LYP/6-31G* level of theory. Figure adapted from reference(34).

and **FR-G2** thus represent the first class of two-dimentionally AFM coupled dendritic polyradicaloids of first and second generation.

Moderate polyradical character allows to get states of different multiplicities in a rather narrow window of energy. The main configuration of D_0 (doublet ground state) of **FR-G1** is represented in the orbital diagram shown in Figure 6.15. D_1 (excitation energy 5.26 kcal/mol and $N_u = 2.08$) and Q_1 states correspond to single electron excitation from D_0 within the SOMO-1, SOMO and SOMO+1 space, as indicated in Table 6.4 ($n_{SONO\pm i}$).

Excited states in Table 6.4 can be understood as the result of radical-radical interactions with energies approximated as:

$$E(D_0) = J, \tag{6.2}$$

$$E(D_1) = 0, \tag{6.3}$$

$$E(Q_1) = -J. \tag{6.4}$$

Likewise, Q_0 of **FR-G2** mainly corresponds to the single electron occupation of SOMO-1, SOMO and SOMO+1, as displayed in Figure 6.15, as well as D_1. Similarly, D_2 to D_4 and Q_2 to Q_3 are obtained as the single excitation from D_1 or Q_0 state, respectively, involving orbitals from SOMO-2 to SOMO+2. D_5 and D_6 are

excitations from D_2, D_3 and D_4 configurations involving the entire set of SOMOs (Table 6.5). Due to the moderate AFM coupling, all low-lying states exhibit high N_u values. The octuplet state is found at higher energies with transitions involving orbitals localized on the anthracene moieties.

State	Energy	N_u	n_{SONO-3}	n_{SONO-2}	n_{SONO-1}	n_{SONO}	n_{SONO+1}	n_{SONO+2}	n_{SONO+3}
Q_0	0.00	5.23	1.50	1.42	1.00	1.00	1.00	0.58	0.50
D_1	0.78	4.71	1.64	1.42	1.12	1.00	0.88	0.58	0.36
D_2	2.47	4.32	1.62	1.54	1.22	1.00	0.78	0.46	0.38
D_3	2.65	4.38	1.60	1.52	1.22	1.00	0.78	0.48	0.40
D_4	2.77	4.90	1.47	1.37	1.24	1.00	0.75	0.63	0.53
Q_1	6.04	5.50	1.43	1.24	1.10	1.00	0.89	0.76	0.57
Q_2	6.09	5.68	1.37	1.22	1.10	1.00	0.90	0.78	0.63
Q_3	6.11	5.59	1.41	1.26	1.06	1.00	0.93	0.74	0.59
D_5	6.32	5.08	1.61	1.37	1.01	0.99	0.99	0.63	0.39
D_6	6.53	5.56	1.43	1.22	1.10	1.00	0.90	0.78	0.56
O_1	58.18	7.00	1.00	1.00	1.00	1.00	1.00	1.00	1.00

Table 6.5: Calculated relative vertical energies (kcal/mol) of **FR-G2** for different spin states, and the number of unpaired electrons (N_u) and electronic occupation of SONOs at the quartet ground state (n_{SONO-3}, n_{SONO-2}, n_{SONO-1}, n_{SONO}, n_{SONO+1}, n_{SONO+2}, and n_{SONO+3}).

Another significant result to highlight is the moderate AFM coupling demonstrated by all the macrostructures, despite their connectivity. AFM allows them to be stable open shell systems with a large number of accessible excited states.

6.3 Appendix

In order to determine the ground state geometry, adiabatic energies for all possible ground state spin multiplicity of **[*n*]CPBM**, **[*n*]PTM** were computed with the Q-Chem package(35) and whit Gaussian 09 package(36) for **[*n*]MC**. All of them with the (restricted and unrestricted) B3LYP(37) functional and the basis set 6-31G(d). The molecular geometries of **FR-Gn** were supplied by the collaborators of the National University of Singapore, obtained at the UB3LYP/6-31G(d,p) level with Gaussian 09 package.

Polyradical character was analysed by the number of unpaired electrons (N_u),(38) electronic occupation of natural orbitals (y_0)(39), and the vertical energy energy gap between lowest states of different multiplicity computed using the RAS-SF method with the basis set 6-31G*. The active subspace, RAS II, for all the systems is detailed in the Table 6.6.

System	n	RAS I [e,o]	RAS II [e,o]	RAS III [e,o]	High spin reference
[n]CPBM	3	[6,3]	[3,3]	[0,3]	quartet
	4	[8,4]	[4,4]	[0,4]	quintet
	5	[10,5]	[5,5]	[0,5]	sextet
	6	[12,6]	[6,6]	[0,6]	septet
	7	[14,7]	[7,7]	[0,7]	octet
	8	[16,8]	[8,8]	[0,8]	nonet
[n]PTM	3	[0,0]	[3,3]	[0,0]	quartet
	4	[0,0]	[4,4]	[0,0]	quintet
	5	[0,0]	[5,5]	[0,0]	sextet
	6	[0,0]	[6,6]	[0,0]	septet
[n]MC	8	-	[8,8]	-	nonet
	10	-	[10,10]	-	11-et
FR-Gn	1	-	[5,5]	-	quartet
	2	-	[9,9]	-	octet

Table 6.6: Subspaces parameters employed in the RAS-SF calculations. RAS I and III of **FR-G1** (**FR-G2**) includes all the electrons and orbitals presents within a range of ±0.55 (±0.30) Hartrees below and above the RAS II subspace, while for **[n]MC** all π-orbitals were included in RAS I and RAS III subspaces.

Constrained-DFT (C-DFT) methodology was used by forcing a $\pm\frac{1}{2}$ spin in each radical center of **[n]PTM**, at the B3LYP/6-31G(d) level of theory. In the case of the in/out model of **[n]MC**, both, spin and charge, were fixed in the inner and outer annulenes and computed at the B3LYP/6-31G(d,p) level.

The energy barrier of the VT of **[4]CPBM** was computed with the 6-311G(d,p) basis set.

Anisotropy of the induced current density (ACID) plots (iso-value = 0.04) of **[n]MC** were computed at (U)B3LYP/6-31G(d,p) level employing only the π-orbitals, by using the method developed by Herges.(40)

Spin densities of **FR-Gn** were obtained at the DFT level (UB3LYP) and with the 6-31G(d) basis set.

Bibliography

[1] X. Wan, X. Lv, G. He, A. Yu, and Y. Chen, "Synthesis of neutral stable polyradicals and their application on photovoltaic devices," *European Polymer Journal*, vol. 47, no. 5, pp. 1018–1030, 2011.

[2] D. A. Wilcox, V. Agarkar, S. Mukherjee, and B. W. Boudouris, "Stable radical materials for energy applications," *Annual Review of Chemical and Biomolecular Engineering*, vol. 9, no. 1, pp. 83–103, 2018.

[3] A. Caminade, C. Turrin, R. Laurent, A. Ouali, and B. Delavaux-Nicot, *Dendrimers: Towards catalytic, material and biomedical uses*. Wiley, 2011.

[4] K. Zhang, M. J. Monteiro, and Z. Jia, "Stable organic radical polymers: synthesis and applications," *Polym. Chem.*, vol. 7, pp. 5589–5614, 2016.

[5] A. Rajca, "Organic diradicals and polyradicals: From spin coupling to magnetism," *Chemical Reviews*, vol. 94, no. 4, pp. 871–893, 1994.

[6] A. Rajca, "The physical organic chemistry of very high-spin polyradicals," *Advances in Physical Organic Chemistry*, vol. 40, pp. 153–199, 2005.

[7] N. M. Gallagher, A. Olankitwanit, and A. Rajca, "High-spin organic molecules," *The Journal of organic chemistry*, vol. 80, no. 3, pp. 1291–1298, 2015.

[8] M. Abe, "Diradicals," *Chemical Reviews*, vol. 113, no. 9, pp. 7011–7088, 2013.

[9] M. Nakano, *Excitation energies and properties of open-shell singlet molecules: applications to a new class of molecules for nonlinear optics and singlet fission*. Springer, 2014.

[10] I. Ratera and J. Veciana, "Playing with organic radicals as building blocks for functional molecular materials," *Chem. Soc. Rev.*, vol. 41, pp. 303–349, 2012.

[11] J. Guasch, X. Fontrodona, I. Ratera, C. Rovira, and J. Veciana, "The perchlorotriphenylmethyl (PTM) radical," *Acta Crystallographica Section C*, vol. 69, no. 3, pp. 255–257, 2013.

[12] X. Lu, S. Lee, J. O. Kim, T. Y. Gopalakrishna, H. Phan, T. S. Herng, Z. Lim, Z. Zeng, J. Ding, D. Kim, and J. Wu, "Stable 3,6-linked fluorenyl radical oligomers with intramolecular antiferromagnetic coupling and polyradical characters," *Journal of the American Chemical Society*, vol. 138, no. 39, pp. 13048–13058, 2016.

[13] Y. Tian, K. Uchida, H. Kurata, Y. Hirao, T. Nishiuchi, and T. Kubo, "Design and synthesis of new stable fluorenyl-based radicals," *Journal of the American Chemical Society*, vol. 136, no. 36, pp. 12784–12793, 2014.

[14] X. Lu, S. Lee, Y. Hong, H. Phan, T. Y. Gopalakrishna, T. S. Herng, T. Tanaka, M. E. Sandoval-Salinas, W. Zeng, J. Ding, D. Casanova, A. Osuka, D. Kim, and J. Wu, "Fluorenyl based macrocyclic polyradicaloids," *Journal of the American Chemical Society*, vol. 139, no. 37, pp. 13173–13183, 2017.

[15] S. Wu, M. Li, H. Phan, D. Wang, T. S. Herng, J. Ding, Z. Lu, and J. Wu, "Toward two-dimensional -conjugated covalent organic radical frameworks," *Angewandte Chemie International Edition*, vol. 57, no. 27, pp. 8007–8011, 2018.

[16] L. Yuan, Y. Han, T. Tao, H. Phan, and C. Chi, "Formation of a macrocycles-in-a-macrocycle superstructure with all-gauche conformation by reversible radical association," *Angewandte Chemie International Edition*, vol. 57, no. 29, pp. 9023–9027, 2018.

[17] Y. Ni, T. Y. Gopalakrishna, H. Phan, T. Kim, T. S. Herng, Y. Han, T. Tao, J. Ding, D. Kim, and J. Wu, "3d global aromaticity in a fully conjugated diradicaloid cage at different oxidation states," *Nature Chemistry*, vol. 12, no. 3, pp. 242–248, 2020.

[18] C. Liu, M. E. Sandoval-Salinas, Y. Hong, T. Y. Gopalakrishna, H. Phan, N. Aratani, T. S. Herng, J. Ding, H. Yamada, D. Kim, D. Casanova, and J. Wu, "Macrocyclic polyradicaloids with unusual super-ring structure and global aromaticity," *Chem*, vol. 4, no. 7, pp. 1586–1595, 2018.

[19] Y. Ni, M. E. Sandoval-Salinas, T. Tanaka, H. Phan, T. S. Herng, T. Y. Gopalakrishna, J. Ding, A. Osuka, D. Casanova, and J. Wu, "[n]cyclo-para-biphenylmethine polyradicaloids: [n]annulene analogs and unusual valence tautomerization," *Chem*, vol. 5, no. 1, pp. 108–121, 2019.

[20] J. Oth, "Conformational mobility and fast bond shift in the annulenes," *Pure and Applied Chemistry*, vol. 25, no. 3, pp. 573–622, 1971.

[21] R. A. Moss, R. R. Sauers, R. S. Sheridan, J. Tian, and P. S. Zuev, "Carbon tunneling in the ring expansion of noradamantylchlorocarbene," *Journal of the American Chemical Society*, vol. 126, no. 33, pp. 10196–10197, 2004.

[22] H. Irngartinger, N. Riegler, K.-D. Malsch, K.-A. Schneider, and G. Maier, "Structure of tetra-*tert*-butylcyclobutadiene," *Angewandte Chemie International Edition in English*, vol. 19, no. 3, pp. 211–212, 1980.

[23] W. E. Barth and R. G. Lawton, "Dibenzo[ghi,mno]fluoranthene.," *Journal of the American Chemical Society*, vol. 88, no. 2, pp. 380–381, 1966.

[24] E. Steiner, P. W. Fowler, and L. W. Jenneskens, "Counter-rotating ring currents in coronene and corannulene," *Angewandte Chemie International Edition*, vol. 40, no. 2, pp. 362–366, 2001.

[25] J. Aihara, "Is superaromaticity a fact or an artifact? the kekulene problem," *Journal of the American Chemical Society*, vol. 114, no. 3, pp. 865–868, 1992.

[26] J. C. Buttrick and B. T. King, "Kekulenes, cycloarenes, and heterocycloarenes: Addressing electronic structure and aromaticity through experiments and calculations," *Chemical Society Reviews*, vol. 46, no. 1, pp. 7–20, 2017.

[27] F. Diederich and H. A. Staab, "Benzenoid versus annulenoid aromaticity: synthesis and properties of kekulene," *Angewandte Chemie International Edition in English*, vol. 17, no. 5, pp. 372–374, 1978.

[28] M. Mandado, A. M. Graña, and I. Pérez-Juste, "Aromaticity in spin-polarized systems: Can rings be simultaneously alpha aromatic and beta antiaromatic?," *The Journal of Chemical Physics*, vol. 129, no. 16, p. 164114, 2008.

[29] F. Vögtle, S. Gestermann, R. Hesse, H. Schwierz, and B. Windisch, "Functional dendrimers," *Progress in Polymer Science*, vol. 25, no. 7, pp. 987–1041, 2000.

[30] C. C. Lee, J. A. MacKay, J. M. J. Fréchet, and F. C. Szoka, "Designing dendrimers for biological applications," *Nature Biotechnology*, vol. 23, no. 12, pp. 1517–1526, 2005.

[31] S. M. Grayson and J. M. J. Fréchet, "Convergent dendrons and dendrimers: from synthesis to applications," *Chemical Reviews*, vol. 101, no. 12, pp. 3819–3868, 2001.

[32] K. T. Al-Jamal, C. Ramaswamy, and A. T. Florence, "Supramolecular structures from dendrons and dendrimers," *Advanced Drug Delivery Reviews*, vol. 57, no. 15, pp. 2238–2270, 2005.

[33] A. Adronov and J. M. J. Fréchet, "Light-harvesting dendrimers," *Chemical Communications*, pp. 1701–1710, 2000.

[34] J. Wang, G. Kim, M. E. Sandoval-Salinas, H. Phan, T. Y. Gopalakrishna, X. Lu, D. Casanova, D. Kim, and J. Wu, "Stable 2d anti-ferromagnetically coupled fluorenyl radical dendrons," *Chemical Science*, vol. 9, pp. 3395–3400, 2018.

[35] Y. Shao, Z. Gan, E. Epifanovsky, A. T. B. Gilbert, M. Wormit, J. Kussmann, A. W. Lange, A. Behn, J. Deng, X. Feng, D. Ghosh, M. Goldey, P. R. Horn, L. D. Jacobson, I. Kaliman, R. Z. Khaliullin, T. Kus, A. Landau, J. Liu, E. I. Proynov, Y. M. Rhee, R. M. Richard, M. A. Rohrdanz, R. P. Steele, E. J. Sundstrom, H. L. Woodcock, P. M. Zimmerman, D. Zuev, B. Albrecht, E. Alguire, B. Austin, G. J. O. Beran, Y. A. Bernard, E. Berquist, K. Brandhorst, K. B. Bravaya, S. T. Brown, D. Casanova, C.-M. Chang, Y. Chen, S. H. Chien, K. D. Closser, D. L. Crittenden, M. Diedenhofen, R. A. DiStasio, H. Do, A. D. Dutoi, R. G. Edgar, S. Fatehi, L. Fusti-Molnar,

A. Ghysels, A. Golubeva-Zadorozhnaya, J. Gomes, M. W. D. Hanson-Heine, P. H. P. Harbach, A. W. Hauser, E. G. Hohenstein, Z. C. Holden, T.-C. Jagau, H. Ji, B. Kaduk, K. Khistyaev, J. Kim, J. Kim, R. A. King, P. Klunzinger, D. Kosenkov, T. Kowalczyk, C. M. Krauter, K. U. Lao, A. D. Laurent, K. V. Lawler, S. V. Levchenko, C. Y. Lin, F. Liu, E. Livshits, R. C. Lochan, A. Luenser, P. Manohar, S. F. Manzer, S.-P. Mao, N. Mardirossian, A. V. Marenich, S. A. Maurer, N. J. Mayhall, E. Neuscamman, C. M. Oana, R. Olivares-Amaya, D. P. O'Neill, J. A. Parkhill, T. M. Perrine, R. Peverati, A. Prociuk, D. R. Rehn, E. Rosta, N. J. Russ, S. M. Sharada, S. Sharma, D. W. Small, A. Sodt, T. Stein, D. Stuck, Y.-C. Su, A. J. W. Thom, T. Tsuchimochi, V. Vanovschi, L. Vogt, O. Vydrov, T. Wang, M. A. Watson, J. Wenzel, A. White, C. F. Williams, J. Yang, S. Yeganeh, S. R. Yost, Z.-Q. You, I. Y. Zhang, X. Zhang, Y. Zhao, B. R. Brooks, G. K. L. Chan, D. M. Chipman, C. J. Cramer, W. A. Goddard, M. S. Gordon, W. J. Hehre, A. Klamt, H. F. Schaefer, M. W. Schmidt, C. D. Sherrill, D. G. Truhlar, A. Warshel, X. Xu, A. Aspuru-Guzik, R. Baer, A. T. Bell, N. A. Besley, J.-D. Chai, A. Dreuw, B. D. Dunietz, T. R. Furlani, S. R. Gwaltney, C.-P. Hsu, Y. Jung, J. Kong, D. S. Lambrecht, W. Liang, C. Ochsenfeld, V. A. Rassolov, L. V. Slipchenko, J. E. Subotnik, T. Van Voorhis, J. M. Herbert, A. I. Krylov, P. M. W. Gill, and M. Head-Gordon, "Advances in molecular quantum chemistry contained in the q-chem 4 program package," *Mol. Phys.*, vol. 113, no. 2, pp. 184–215, 2015.

[36] M. J. Frisch, G. W. Trucks, H. B. Schlegel, G. E. Scuseria, M. A. Robb, J. R. Cheeseman, G. Scalmani, V. Barone, B. Mennucci, G. A. Petersson, H. Nakatsuji, M. Caricato, X. Li, H. P. Hratchian, A. F. Izmaylov, J. Bloino, G. Zheng, J. L. Sonnenberg, M. Hada, M. Ehara, K. Toyota, R. Fukuda, J. Hasegawa, M. Ishida, T. Nakajima, Y. Honda, O. Kitao, H. Nakai, T. Vreven, J. A. Montgomery, Jr., J. E. Peralta, F. Ogliaro, M. Bearpark, J. J. Heyd, E. Brothers, K. N. Kudin, V. N. Staroverov, R. Kobayashi, J. Normand, K. Raghavachari, A. Rendell, J. C. Burant, S. S. Iyengar, J. Tomasi, M. Cossi, N. Rega, J. M. Millam, M. Klene, J. E. Knox, J. B. Cross, V. Bakken, C. Adamo, J. Jaramillo, R. Gomperts, R. E. Stratmann, O. Yazyev, A. J. Austin, R. Cammi, C. Pomelli, J. W. Ochterski, R. L. Martin, K. Morokuma, V. G. Zakrzewski, G. A. Voth, P. Salvador, J. J. Dannenberg, S. Dapprich, A. D. Daniels, [U+FFFD] Farkas, J. B. Foresman, J. V. Ortiz, J. Cioslowski, and D. J. Fox, "Gaussian∼09 Revision E.01." Gaussian Inc. Wallingford CT 2009.

[37] A. D. Becke, "Density-functional thermochemistry. iii. the role of exact exchange," *The Journal of Chemical Physics*, vol. 98, no. 7, pp. 5648–5652, 1993.

[38] M. Head-Gordon, "Characterizing unpaired electrons from the one-particle density matrix," *Chem. Phys. Lett.*, vol. 372, no. 3-4, pp. 508–511, 2003.

[39] K. Yamaguchi, *Self-Consistent Field: Theory and Applications*, pp. 727–828. Elsevier, 1990.

[40] D. Geuenich, K. Hess, F. Köhler, and R. Herges, "Anisotropy of the induced current density (acid), a general method to quantify and visualize electronic delocalization," *Chemical Reviews*, vol. 105, no. 10, pp. 3758–3772, 2005.

Chapter 7

Singlet fission

Singlet fission (SF) is a photophysical process in which one singlet exciton shares its energy with a molecule in the ground state, yielding the formation of two triplet excitons. The SF concept dates back to the observation of the triplet states in anthracene crystals in 1965.(1) Later on, the mechanism was also evidenced in crystalline tetracene.(2) Since that discovery, theoretical efforts were done to develop a model to explain the kinetics of the process,(3; 4; 5) while experimental studies focused on deepening the understanding of the mechanism and exploring new materials.(6) Despite, the interesting advances in the field during the decade of 1990, the interest for SF gain a lot of attention until the early 2000s, when Hanna and Nozik suggested SF as a possible strategy to overcome the efficiency barrier in solar-cells.(7; 8) Since then, extensive theoretical and experimental work has been done in order to provide a detailed understanding of the mechanisms ruling the SF process.(9; 10; 11) In particular, the role and properties of the electronic states involved, the potential underlying mechanisms, and the energetic conditions, among others, have being extensively explored by computational investigations. Besides these fundamental aspects, computational efforts have also focused on the theoretical modelling of organic materials able to undergo SF efficiently, and design of systems with improved capabilities for integration in solar cell devices. Experimentally, solar cells incorporating SF materials have reached above 100% of external quantum yield efficiency and up to 200% of internal quantum efficiency.(12; 13)

In this chapter, I will expose the basic concepts necessary to understand the singlet fission process and define in detail the well-accepted five-state model. Finally, I will show how the expansion of this model by considering the role of two more states not only can shed light on the mechanistic aspect of SF but also can help in the rational design of new efficient singlet fission chromophores.

7.1 Singlet fission in a nutshell

SF is a down conversion process in which the excitation energy of one singlet exciton is shared to produce two "independent" triplet excitons.(10; 11) The singlet fission process can be described in two steps as follows:

$$S^* \rightleftharpoons {}^1TT \rightleftharpoons T_1 + T_1. \tag{7.1}$$

The first step starts from the singlet exciton and ends with the formation of the multiexcitonic state (^{1}TT). The second step consist in the decoupling of the triplet-triplet pair.

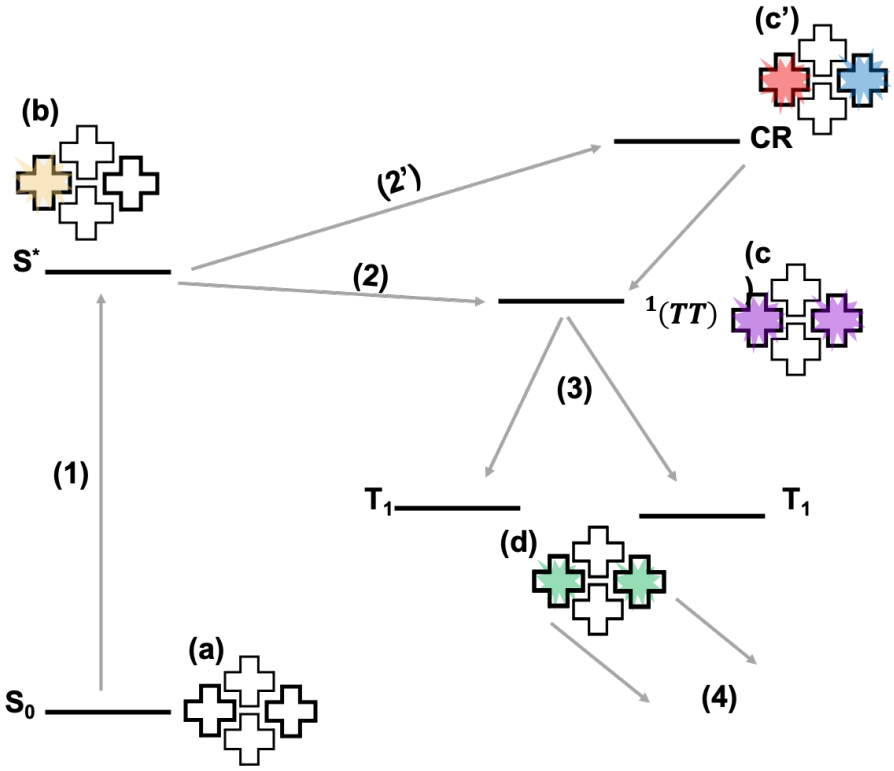

Figure 7.1: Overview of the singlet fission process. Ground state (a), excitation (1), optical exciton (b), relaxation (2), triplet-pair state (c), charge separation (2'), charge transfer states (c'), fission (3), independent triplets (d), diffusion (4). Figure adapted from reference(14).

The whole process can be described as the succession of several photophysical events, as illustrated in Figure 7.1. The activation is usually, but not only, achieved by the absorption of one photon leading to the singlet excitation; then, the multiexcitonic state is formed through an internal conversion process since the triplet-triplet state is coupled as an overall singlet. Then, by the fission of this state, two triplets localized over different monomers are generated and, in excited systems, migration through neighbour chromophores can occur. The SF process requires some energetic

conditions to be fulfilled:

$$E(S_1) \geq 2E(T_1). \tag{7.2}$$

The thermodynamic condition establishes that the energy of the singlet exciton should be at least twice the energy of the triplet (Equation 7.2) to ensure the exothermicity of the whole process. The second requirement is the kinetic condition says that the S_1 level should be slightly above twice the energy of T_1, *i.e.*, $E(S_1)$ - $2E(T_1) \sim 0$. Note that when the energy of S_1 is slightly lower than $2T_1$, SF has been observed to be carried out as an endothermic process in tetracene crystals.(2)

$$E(T_2) > 2E(T_1), \tag{7.3}$$

$$E(Q_1) > 2E(T_1). \tag{7.4}$$

Equation 7.3 and 7.4 have to be fulfilled to avoid the undesirable triplet-triplet recombination event. Concretely, the energy of the second triplet (T_2) must be higher than twice the energy of T_1 to discard the triplet-triplet recombination to the triplet manifold. The population of Q_1 is not often observed due to the high energy of this state, and can be related to the tetraradical character of the SF chromophore, which is detrimental to the process.

In addition to the state energies of the monomer, the spatial arrangement of the chromophores is crucial. The relative position and orientation of π-conjugated systems within molecular aggregates affects the energy of S_1, giving rise to accessible deactivation paths competing with SF. It has been observed that covalently linked dimers are beneficial to modulate the electronic interaction between monomers by imposing restrictions to their relative orientation without affecting their photophysical properties.(15; 16; 10)

7.1.1 Singlet fission chromophores

One of the main research axes in the field is the design of new chromophores to enhance the efficiency of singlet fission. Organic molecules with very small to moderate diradical character have been proved to fulfil the energetic requirements of SF. This is the case of polyacenes which have been extensively explored as SF materials, more specifically tetracene and pentacene and their derivatives (according to our calculations reported in Chapter 4, they hold a low-moderate diradicaloid character).

The minimum unit to model SF is a dimer, so as to have a system that can localize both triplets separately. Nevertheless, the properties of the monomer, *i.e.*, relative energy of excited states, absorption coefficients, structure, radical character, and chemical photostability, have to be considered first in order to have a chromophore appropriate for SF.

There are three main classes of organic chromophores that can be found in the literature, classified according to the ordering of excited singlet states (Figure 7.2).

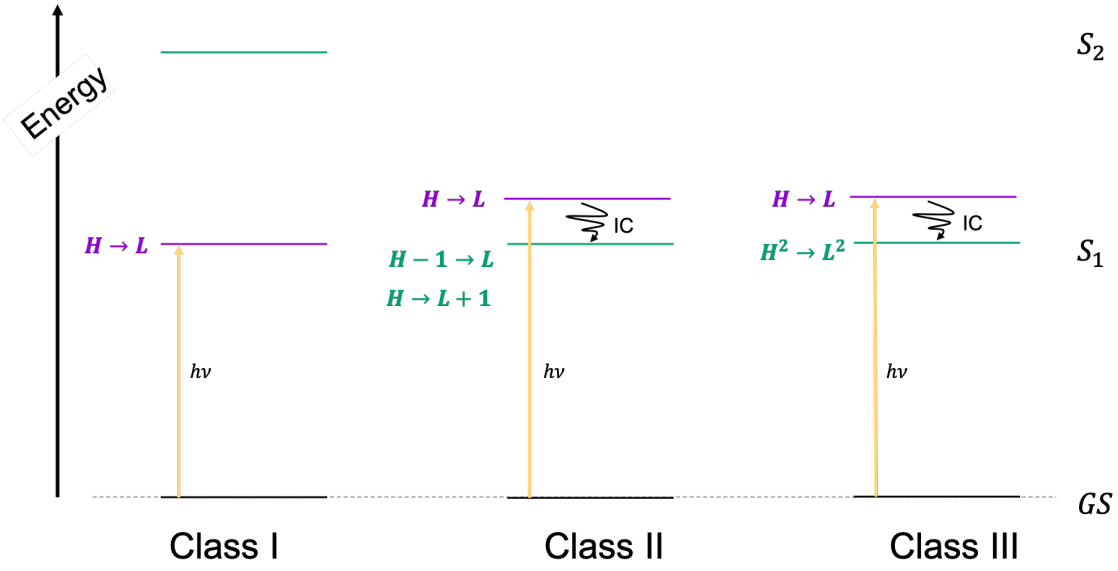

Figure 7.2: Excited state diagram of singlet fission chromophores of class I (left), II (center) and III (right). H = HOMO, L= LUMO, IC = internal conversion. Figure adapted from reference(10).

7.1.1.1 Class I

In this class of chromophores, the lowest excited singlet state corresponds to the optical transition, which is characterized as the HOMO-to-LUMO excitation. Other singlet excited states are considerably higher in energy, avoiding mixing or additional decay channels. Compounds in this class hold a closed-shell configuration. Tetracene, anthracene and perylene are chromophores belonging to this class that have been investigated to carry out singlet fission.

7.1.1.2 Class II

The optically allowed excitation is to the S_2 state in chromophores of class II. The electronic configuration of S_1 corresponds to the linear combination to the HOMO-1-to-LUMO and HOMO-to-LUMO+1 excitations. S_1 is energetically found slightly below S_2, and can be populated by an internal conversion process. SF chromophores of this class are naphthalene, pyrene and phenanthrene, among others.

7.1.1.3 Class III

In chromophores of class III, as in those of class II, the second excited singlet is the optically allowed one, while the energy gap with respect to the S_1 state is quite small. S_2 involves HOMO-to-LUMO transition and S_1 is characterized as the double excitation $HOMO^2$-to-$LUMO^2$. This doubly excited state is very common in π-conjugated systems like polyenes, where ^1B_u and ^1A_g excited states are almost degenerated.

For all classes, the relative energy of T_1 and S_1 have to fulfil the Equation 7.2. Energy splitting between both states can be approximated to twice the HOMO-LUMO exchange integral ($\Delta E_{ST} \approx 2K_{hl}$), and hence depends on the repulsion of two electrons located in different orbitals whose magnitude is related to the spatial overlap of HOMO and LUMO. There are two main manners to tune ΔE_{ST} and open the gap between S_1 and T_1: **i**) by destabilization of S_1 (increment of K_{hl}) in class I, since in closed-shell molecules the $\Delta E_{S_1T_1}$ is smaller than $\Delta E_{S_0T_1}$; this can be achieved by means of inclusion of heteroatom or increasing the size of the conjugated system. **ii**) by stabilization of the T_1 state, *i.e.*, decreasing $\Delta E_{S_0T_1}$ by inducing low to moderate diradical character in chromophores of class I and III.(10) Systems with strong diradical character are detrimental for the SF efficiency, since SF becomes too exothermic, resulting in a large energy loss in the fission process.

7.2 Five-state model

Normally, within the dimer model, the first step of the SF process is described within a five-state model, including the singlet excited state (S_1S_0 or S_0S_1), and the multiexcitonic state (^{1}TT), as indicated in Equation 7.1. Additionally, charge transfer states are included as potential intermediates or states assisting the process.

7.2.1 Electronic states

7.2.1.1 Singlet excited states

The S_1 state is assumed to be the lowest excited singlet state of the SF chromophore, usually described by the HOMO-to-LUMO transition. Within the SF context, it is expected that if the optical state is not the lowest one, S_1 will be populated before the fission through internal conversion. Still, a small possibility exists that higher singlets (S_n) can undergo SF.

7.2.1.2 Charge transfer states

First, it is important to clarify the difference between charge transfer (CT) and charge resonance (CR) states. Both kind of states are related to the exchange of electrons to form the cation/anion (CA or AC) pair. CT refers to the formal migration of one electron from one monomer to the other, while CR indicates the presence of charged configurations in the wave function, but does not imply the formation of charged chromophores. In other words, it is possible to describe the CR state as the linear combination of CT states. The big impact of these states on SF process has been extensively studied and the most common SF mechanism is the one mediated by charge transfer states.(16)

7.2.1.3 The triplet-pair state

The core of the singlet fission reaction is the formation of the multiexcitonic triplet-pair state (^{1}TT). According to the coupling of two angular moments, the triplet-pair leads to the formation of 9 microstates, ^{1}TT (1), ^{3}TT (3), and ^{5}TT (5). The most relevant in SF is the one corresponding to the triplet-pair coupled as an overall singlet, making SF allowed by spin symmetry rules as no change of multiplicity occurs between S_1S_0 and ^{1}TT states. Normally, ^{1}TT is more stable than ^{3}TT and ^{5}TT, and the extra stabilization can be described as the energy needed to dissociate two triplets, specifically:

$$E_b \approx {}^5TT - {}^1TT, \tag{7.5}$$

where ^{5}TT is the triplet-pair coupled as an overall quintet and can be understood as 4 unpaired electrons (two on each triplet), while ^{1}TT has a larger tendency to mix with other configurations (as local excitations or charge transfer states).

This triplet-pair state was first computationally characterized through wave function based methods.(17; 18) Later on, it was experimentally detected by Chan and collaborators(19) as a SF intermediate. Since then, the nature and properties of the coupled double triplet state have been largely investigated both experimentally and theoretically by several authors.(20; 16; 18; 21)

The minimal configuration space necessary to describe the S_1S_0, S_0S_1, AC, CT, and ^{1}TT states must contain the two frontier orbitals (HOMO and LUMO) of the two monomers. Low-lying excited singlet states of molecular dimers can be built in terms of local excitations to S_1 and ionic configurations corresponding to the cation-anion (CA) and anion-cation (AC) charge transfer (CT) states, and the triplet-pair state (^{1}TT). In the HOMO/LUMO frozen orbital approximation for

equivalent homodimers,(10) these diabatic states are expressed as:

$$|\mathrm{S_1S_0}\rangle = \frac{1}{\sqrt{2}}\left(|h_A\bar{l}_A h_B\bar{h}_B\rangle + |l_A\bar{h}_A h_B\bar{h}_B\rangle\right), \tag{7.6}$$

$$|\mathrm{S_0S_1}\rangle = \frac{1}{\sqrt{2}}\left(|h_A\bar{h}_A h_B\bar{l}_B\rangle + |h_A\bar{h}_A l_B\bar{h}_B\rangle\right), \tag{7.7}$$

$$|\mathrm{CA}\rangle = \frac{1}{\sqrt{2}}\left(|h_A\bar{l}_B h_B\bar{h}_B\rangle + |l_B\bar{h}_A h_B\bar{h}_B\rangle\right), \tag{7.8}$$

$$|\mathrm{AC}\rangle = \frac{1}{\sqrt{2}}\left(|h_A\bar{h}_A l_A\bar{h}_B\rangle + |h_A\bar{h}_A h_B\bar{l}_A\rangle\right), \tag{7.9}$$

$$\begin{aligned}|^1\mathrm{TT}\rangle = \frac{1}{\sqrt{3}}[&|h_A l_A\bar{h}_B\bar{l}_B\rangle + |\bar{h}_A\bar{l}_A h_B l_B\rangle \\ &- \frac{1}{2}\left(|h_A\bar{l}_A h_B\bar{l}_B\rangle + |l_A\bar{h}_A l_B\bar{h}_B\rangle - |h_A\bar{l}_A l_B\bar{h}_B\rangle - |l_A\bar{h}_A h_B\bar{l}_B\rangle\right)],\end{aligned} \tag{7.10}$$

where h_X (l_X) is the HOMO (LUMO) of molecule X, the upper bar indicates spin-β orbital. The exciton Hamiltonian in the basis of orthonormal diabatic states is expressed as:

$$H_{ex} = \sum_{I\leq J} |I\rangle H_{IJ}\langle J|, \tag{7.11}$$

where $H_{IJ} \equiv \langle I|\hat{H}|J\rangle$ are defined as the electronic energies ($I = J$) and couplings ($I \neq J$). The electronic coupling between the five electronic states is:

$$\langle \mathrm{S_1S_0}|\hat{H}|^1\mathrm{TT}\rangle = \sqrt{\frac{3}{2}}\left[(l_A h_B|l_A l_B) - (l_B h_A|h_A h_B)\right], \tag{7.12}$$

$$\langle \mathrm{S_1S_0}|\hat{H}|\mathrm{S_0S_1}\rangle = 2(l_A h_A|l_B h_B) - (l_A l_B|h_A h_B), \tag{7.13}$$

$$\langle \mathrm{S_1S_0}|\hat{H}|\mathrm{CA}\rangle = (l_A|\hat{F}|l_B) + 2(h_A l_B|h_A l_A) - (h_A h_A|l_A l_B), \tag{7.14}$$

$$\langle \mathrm{S_1S_0}|\hat{H}|\mathrm{AC}\rangle = -(h_A|\hat{F}|h_B) + 2(h_A l_B|h_B l_B) - (h_A h_B|l_B l_B), \tag{7.15}$$

$$\langle ^1\mathrm{TT}|\hat{H}|\mathrm{AC}\rangle = \sqrt{\frac{3}{2}}\left[(l_A|\hat{F}|h_B) + (l_A h_B|l_B l_B) - (l_A h_B|h_A h_A)\right], \tag{7.16}$$

$$\langle \mathrm{CA}|\hat{H}|\mathrm{AC}\rangle = 2(l_B h_A|l_A h_B) - (l_A l_B|h_A h_B), \tag{7.17}$$

where orthonormal orbitals have been considered ($\langle i|j\rangle = \delta_{ij}$), $(i|\hat{F}|j)$ is the Fock matrix element between orbitals i and j, and $(ij|kl)$ is a two-electron interaction integral written as:

$$(ij|kl) = \int \phi_i^*(\mathbf{r}_1)\phi_j(\mathbf{r}_1)\frac{1}{r_{12}}\phi_k^*(\mathbf{r}_2)\phi_l(\mathbf{r}_2)\mathrm{d}\mathbf{r}_1\mathrm{d}\mathbf{r}_2. \tag{7.18}$$

Notice that for symmetric homodimers $\langle IJ|\hat{H}|KL\rangle = \langle JI|\hat{H}|LK\rangle$, with $|IJ\rangle$ corresponding to any of the diabatic states of the dimer built as the coupling of monomeric states $|I\rangle$ and $|J\rangle$ in Equations 7.6-7.10.

In the following, I use the co-planar ethylene dimer as a model system. The conformational space considered corresponds to the two ethylene molecules stacked

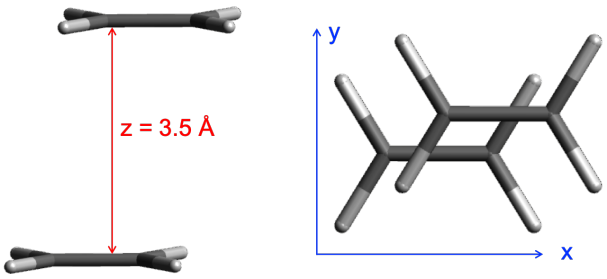

Figure 7.3: Side (left) and top (right) views of the co-planar ethylene dimer employed in this work. Vertical intermolecular distance ($z = 3.5$ Å) indicated in red.

at 3.5 Å with different relative in-plane displacements along the long and short molecular axes (Figure 7.3).

Computed electronic couplings for the co-planar conformational space of the ethylene dimer (Figure 7.4) are in very good agreement to similar calculations performed by Smith and Michl.(22) The coupling between S_1S_0 (and S_0S_1) with ^{1}TT state, which is optimal at the alternate disposition along the bond axis (x coordinate), is 1-2 orders of magnitude smaller than those of S_1S_0 or ^{1}TT to charge separated configurations (540-740 meV absolute maxima), since the latter contain single electron Fock matrix elements (Equations 7.14-7.16), while the (direct) interaction is obtained as the difference between two bielectronic integrals (Equation 7.12). Such strong coupling of the initial and final states to charge separation state, is the driving force for CT-mediated singlet fission mechanism invoked in numerous studies.(23; 24; 14; 25)

7.3 Seven-state model

Beyond the extensively studied states, S_1S_0, ^{1}TT, T_1 and CT, in organic conjugated molecules other electronic states can be close in energy and available to be populated and play an active or secondary role in the SF process. Such is the case of chromophores in class III, in which the doubly excited (dark) state is almost degenerated to the bright state. The dark state has been characterized to be mainly the double excitation from HOMO-to-LUMO and becomes the lowest excited state in polyenes larger than butadiene.(26; 27) Herein, this state is named doubly excited state ("D state"). Within the framework of SF, it is important to stress the difference between the D ($HOMO^2 \rightarrow LUMO^2$) and the ^{1}TT states, even when both are not optically active (dark states), and D state has been described as a coupled triplet-pair,(28; 29; 30) its triplet-triplet electronic coupling is significantly larger than the coupling between triplets in ^{1}TT state. Moreover, while ^{1}TT exists as a state delocalized over at least two choromopores, D state is a monomeric dou-

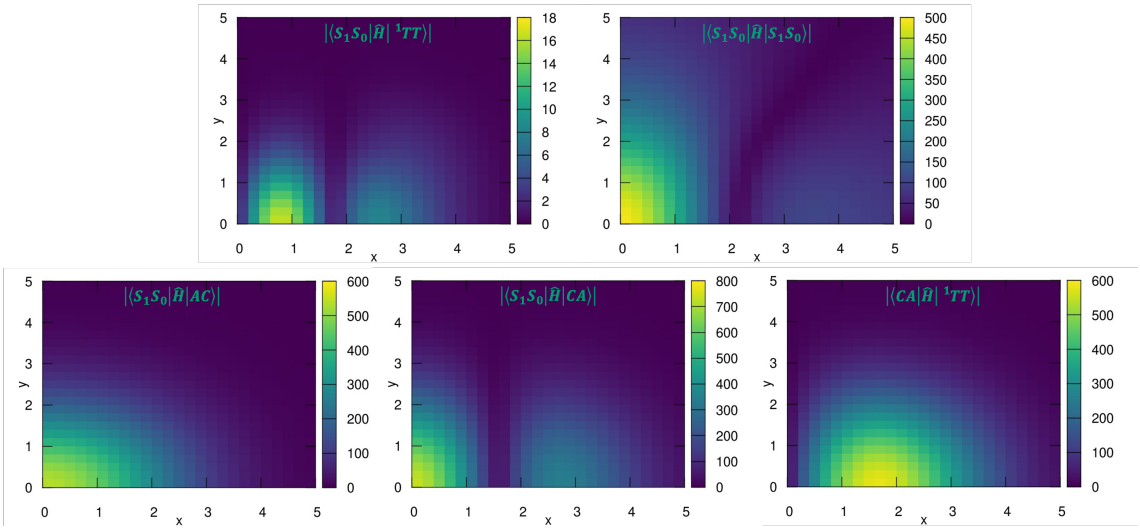

Figure 7.4: Absolute electronic couplings (in meV) between S_1S_0, ^{1}TT, CA, and AC diabats for the stacked ethylene dimer computed at a constant vertical separation ($z = 3.5$ Å) and different longitudinal (x in Å) and horizontal (y in Å) displacements as shown in Figure 7.3.

bly excited state. Its participation in the SF mechanism was suggested to occur in pentacene,(17) although this possibility was later disregarded by means of experimental measurements(31; 32) and accurate electronic structure calculations(24) indicating that the optical state lies below the dark state.

Here an extension of the SF model (previous section) is presented by the inclusion of the D state. The possible role in the ^{1}TT formation: i) direct when D is the lowest excited state; or ii) as a mediator when D is a higher state, is explored by means of the analysis of the electronic couplings and the time evolution of excited states.

7.3.1 Electronic couplings with the *D* state

Within the simple model of SF states described in previous section (HOMO and LUMO of each monomer), the DS_0 and S_0D states, monomeric HOMO to LUMO double excitation, are expressed as:

$$|\mathrm{DS_0}\rangle = |l_A\bar{l}_A h_B\bar{h}_B\rangle, \tag{7.19}$$

$$|\mathrm{S_0D}\rangle = |h_A\bar{h}_A l_B\bar{l}_B\rangle. \tag{7.20}$$

The energy of the D state under this approximation is computed as $E(\mathrm{DS_0}) \approx E(\mathrm{D}) + E(\mathrm{S_0})$, and $E(^1\mathrm{TT}) \approx 2E(\mathrm{T_1})$, and the relative energy of $D\mathrm{S_0}$ with respect

to ^{1}TT and S_1S_0 is then:

$$E(\mathrm{DS_0}) - E(\mathrm{S_1S_0}) \approx \varepsilon_l - \varepsilon_h - 3(ll|hh) + (ll|ll), \tag{7.21}$$

$$E(\mathrm{DS_0}) - E(^1\mathrm{TT}) \approx (ll|ll) - (hh|hh) + 2\left[(ll|hh) + (lh|lh)\right]. \tag{7.22}$$

The variables used here follow the definition and nomenclature as in Equation 7.18. Within the HOMO-LUMO model, the electronic couplings between SF states (Equations 7.6-7.10) and D state can be calculated as:

$$\langle \mathrm{DS_0}|\hat{H}|^1\mathrm{TT}\rangle = -\sqrt{3}(h_A h_B|l_A l_B), \tag{7.23}$$

$$\langle \mathrm{DS_0}|\hat{H}|\mathrm{S_1}S_0\rangle = \sqrt{2}\left[(l_A|\hat{F}|h_A) + (h_A l_A|l_A l_A) - (h_A l_A|h_A h_A)\right], \tag{7.24}$$

$$\langle \mathrm{DS_0}|\hat{H}|\mathrm{CA}\rangle = \sqrt{2}(l_A h_A|l_A l_B), \tag{7.25}$$

$$\langle \mathrm{DS_0}|\hat{H}|\mathrm{AC}\rangle = -\sqrt{2}(l_A h_A|h_A h_B), \tag{7.26}$$

$$\langle \mathrm{DS_0}|\hat{H}|\mathrm{S_0D}\rangle = \langle \mathrm{S_0D}|\hat{H}|\mathrm{DS_0}\rangle = 0. \tag{7.27}$$

Equations 7.12-7.17 and 7.23-7.27 complete the electronic Hamiltonian of the seven-state model. Using the same grid of the displaced co-planar ethylene dimer (Figure 7.3), the coupling between DS_0 and S_1S_0, ^{1}TT, CA and AC diabatic states is represented in Figure 7.5.

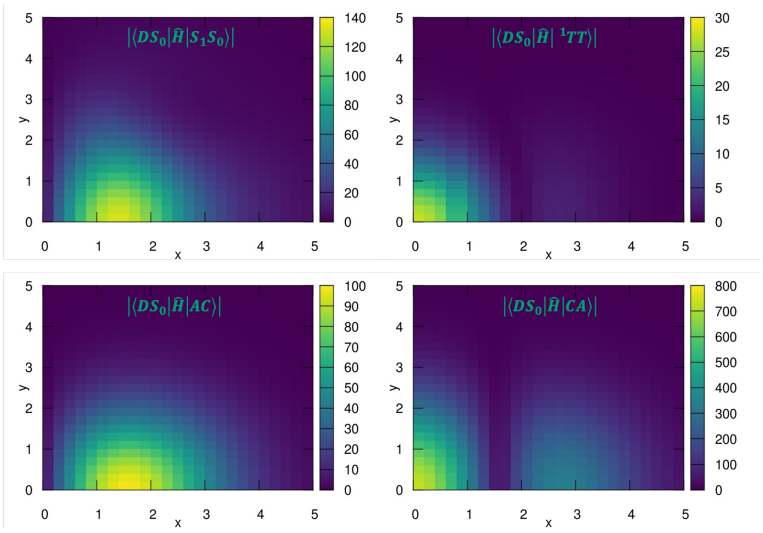

Figure 7.5: Absolute electronic couplings (in meV) between DS_0 and S_1S_0, ^{1}TT, CA, and AC diabats for the stacked ethylene dimer computed at a constant vertical separation (z = 3.5 Å) and different longitudinal (x in Å) and horizontal (y in Å) displacements as shown in Figure 7.3

The doubly excited localized state shows sizeable couplings with S_1S_0, ^{1}TT, CA, and AC states. The DS_0/S_1S_0 couplings present the strongest interaction at the longitudinal displacement (y = 0.0 Å), with eclipsed alternate carbons, where the electronic interaction is 133 meV. The couplings of DS_0 to AC and CA show

very similar conformational profiles, with the strength of the interaction to CA being larger than for S_1S_0 and about twice the coupling to AC. Interestingly, the couplings to the triplet-pair state are maximum at the eclipsed structure, since it simultaneously maximizes the overlaps between localized HOMOs and LUMOs (Equation 7.23). The computed interaction at the D_{2h} arrangement (~ 30 meV) is considerably stronger than the optimal coupling between S_1S_0 and ^{1}TT (Figure 7.4). This result can be rationalized by comparing Equations 7.12 and 7.23, where the former corresponds to the difference between two bielectronic integrals, resulting in a rather small overall interaction.

7.3.2 Singlet fission couplings

Even if the D state lies energetically above the optical transition, it can be directly or indirectly involved in the SF process, likewise charge separated configurations are able to catalyze the formation of the ^{1}TT state through the CT-mediated mechanism.

Normally, the reaction rate for the formation of the triplet-pair can be approximated by the Fermi's Golden Rule:(33)

$$k_{SF} = \frac{2\pi}{\hbar}|V_{SF}|^2\delta(E_I - E_F), \tag{7.28}$$

where I and F subscripts refer to initial and final states, respectively, and $\delta(E_I - E_F)$ ensures energy conservation. The electronic coupling in SF (V_{SF}) can be perturbatively expanded to second order to take into account the participation of one mediator state, which corresponds to the CT (CA and AC) states (five-state model). To model the case in which both states, CT and D (or S_0S_1), can act as mediator, the V_{SF} can be expanded to third order:

$$V_{SF} = \sum_{n=1}^{\infty} V_{IF}^{(n)}, \tag{7.29}$$

$$V_{IF}^{(1)} \equiv V_{IF} = \langle I|\hat{H}|F\rangle, \tag{7.30}$$

$$V_{IF}^{(2)} = \sum_{K\neq I,F} \frac{V_{IK}V_{KF}}{(E_I + E_F)/2 - E_K}, \tag{7.31}$$

$$V_{IF}^{(3)} = \sum_{K,L\neq I,F} \frac{V_{IK}V_{KL}V_{LF}}{(E_I - E_K)(E_F - E_L)} - V_{IF}\sum_{K\neq I,F} \frac{V_{IK}V_{KF}}{(E_I - E_K)(E_F - E_K)}, \tag{7.32}$$

where $E_K = \langle K|\hat{H}|K\rangle$. Such expression has been employed in SF to discern between different mechanisms for the formation of the triplet-pair state depending on the energy distribution of electronic states and the coupling between them. The direct transition from initial state ($n = 1$) depends only on the direct coupling between ^{1}TT and S_1S_0; in our model system $<S_1S_0|\hat{H}|^1TT>$ is maximized when the ethylene

dimer is slipped in the x-axis. On the other hand, the mediated mechanism through virtual states (K states can be CT and D) is described when $n = 2$. In fact, the mediated mechanism has shown to be dominant in many systems, in which the CT states (CA and AC) act as virtual mediators due to the strong couplings with S_1 and ^{1}TT states. In Figure 7.4 it can be noticed that the couplings with CT states are considerably larger than the direct one. Additionally, in the seven-state model the L and K can be CT (AC and CA) and D. In this way, Equation 7.32 represents the mechanism mediated simultaneously by both states.

If D is the lowest molecular excited state, the first step of SF can occur directly from it, in this case the activation of D occurs as consequence of the fast exciton decay after photoabsorption by the optical state (S*) populating the D state and then the formation of ^{1}TT state as:

$$S^* \longrightarrow D \overset{S_1, CT}{\rightleftharpoons} {}^1TT. \tag{7.33}$$

Generation of ^{1}TT from D can take place through different microscopic mechanisms, that can involve, or not, other electronic states if they are close in energy. Furthermore, as observed with the CT states, the S*-CT-^{1}TT couplings determine their participation in SF process. The possibility and the relative importance of different decay paths was explored by computing the total couplings (Equation 7.29-7.32) for the conformational space of the co-planar ethylene dimer considering different relative energetic ordering of states.

First, if D and ^{1}TT states are much lower than the rest of singlet excitations in the system, second (and third) order terms in Equation 7.29 can be disregarded, and the only available channel is the direct transfer from D to the triplet-pair state. In that case, the rate of ^{1}TT formation is expected to be controlled by the direct coupling, which is favored in the eclipsed conformation (Figure 7.5). It is worth noticing that the eclipsed form also corresponds to the most stable arrangement of excimeric states,(34) since it produces the strongest exciton coupling ($\langle S_1S_0|\hat{H}|S_0S1\rangle$ in Figure 7.4). Therefore, if the S_1 state is not much higher in energy than the D and ^{1}TT states, the excimer formation could compete with SF from D state. The respective feasibility of excimer and triplet-pair state formation will be largely controlled by the relative energies of S_1 and D states of the chromophore.

Alternatively, if there are other excitations lying not too high in energy, such as the local exciton (S_1) or CT states, they could mediate the SF mechanism from D state (Figure 7.6).

Despite that DS_0/S_1S_0 couplings are rather strong (Figure 7.5), mediation by S_1 state is effectively hindered by the weak $S_1S_0/^1$TT interaction, and SF from D with low-lying S_1 state is still dominated by the direct mechanism (Figure 7.6a). On the other hand, the presence of low-energy CT states has an important impact

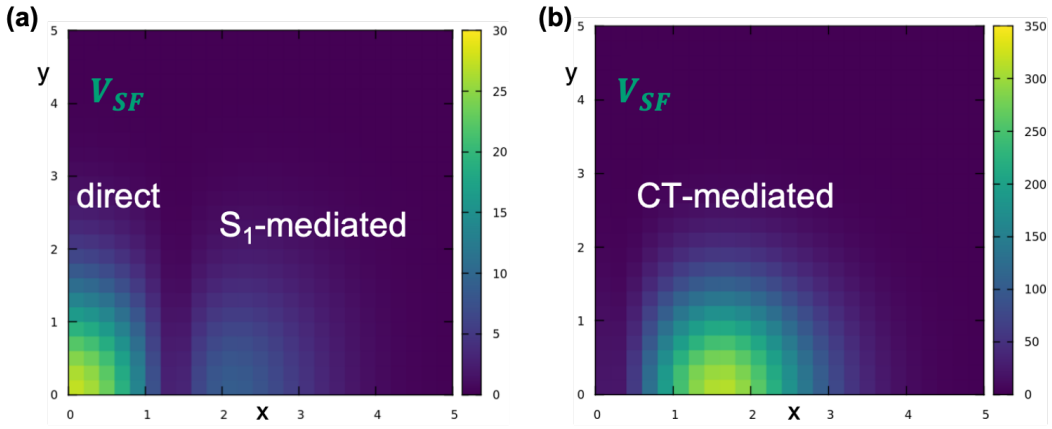

Figure 7.6: Absolute total SF couplings (in meV) between DS_0 and ^1TT with $E(DS_0) - E(^1TT) = 0.25$ eV, and S_1S_0/S_0S_1 and CT states at 0.4 and 20 eV (a), and 20 and 0.4 eV (b) above the D state, for the stacked ethylene dimer computed at a constant vertical separation ($z = 3.5$ Å) and different longitudinal (x in Å) and horizontal (y in Å) displacements as shown in Figure 7.3.

on SF. If CA and AC configurations are energetically close to D (Figure 7.6b), the CT-mediated mechanism is expected to be the main channel to populate ^1TT, with optimal couplings for slip-stacked conformations along the x-axis having a maximum absolute value of ~ 320 meV. If both CT and S_1 states are energetically close to D, the third order couplings simultaneously involving CT and S_1 (CT,S_1-mediated mechanism) contribute to an important increase of the total SF coupling of slip-stacked conformations of ~ 110 meV with respect to the (second order) CT-mediated couplings (Figure 7.7).

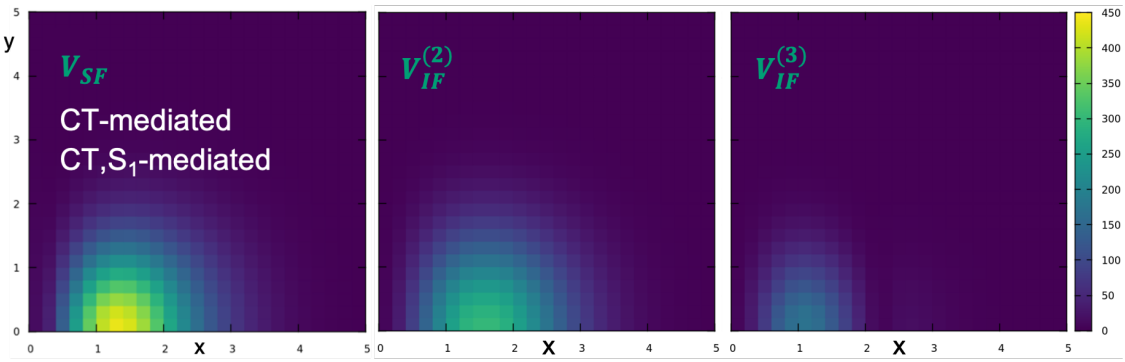

Figure 7.7: Absolute total, second and third order SF couplings (in meV) between DS_0 and ^1TT with $E(DS_0) - E(^1TT) = 0.25$ eV, and S_1S_0/S_0S_1 and CT states at 0.4 and 0.4 eV above the D state, for the stacked ethylene dimer computed at a constant vertical separation ($z = 3.5$ Å) and different longitudinal (x in Å) and horizontal (y in Å) displacements as shown in Figure 7.3.

Probably, the case with small D/S_1 gaps, and CT states a few eVs above them might represent a realistic energy distribution of molecular dimers, aggregates or crystal structures of organic chromophores with the D state below S_1. Interestingly, in that situation we might have both SF mechanisms available, with direct transition from D favored for eclipsed dimers and CT-mediated formation of ^{1}TT in displaced arrangements (Figure 7.8).

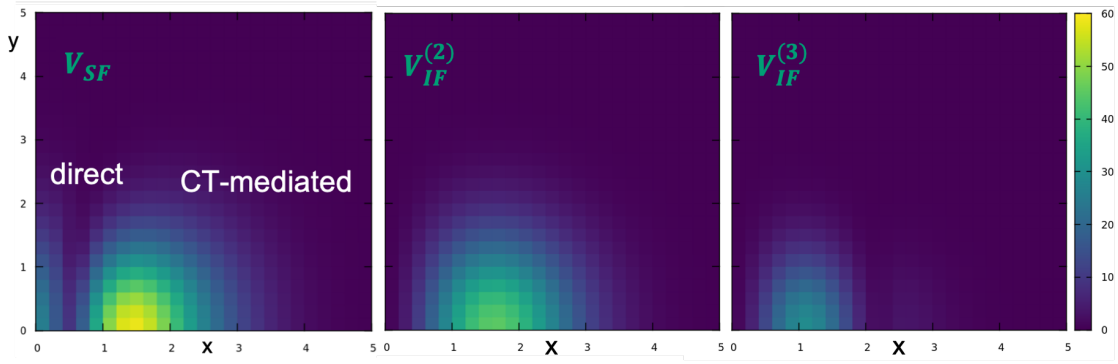

Figure 7.8: Absolute total, second and third order SF couplings (in meV) between DS_0 and ^{1}TT with $E(DS_0) - E(^1TT) = 0.25$ eV, and S_1S_0/S_0S_1 and CT states at 0.4 and 3.4 eV above the D state, for the stacked ethylene dimer computed at a constant vertical separation ($z = 3.5$ Å) and different longitudinal (x in Å) and horizontal (y in Å) displacements as shown in Figure 7.3.

The fact that the D state cannot be connected to the ground state through the dipole moment operator (dark state) might be an advantage for the SF reaction. Contrary to singlet fission from the HOMO→LUMO optical singlet (S_1), radiative decay to the ground state (fluorescence) cannot compete with the formation of the triplet-pair, potentially resulting in increased fission efficiencies.

In many organic chromophores the doubly excited state lies above the S_1 excitation as in class II chromophores. Hence, the SF photophysical reaction will occur from the S_1 exciton, while the D state, if energetically not too high, might play an indirect role as a virtual state catalyzing the formation of the triplet-pair state, similar to the CT-mediated SF mechanism:

$$S_1 \rightleftharpoons^{D,CT} {}^1TT \tag{7.34}$$

Direct S_1 to ^{1}TT coupling (Figure 7.4) is of the order of tens of meV or weaker, with a maximum at the alternate conformation (with x displacement of half of the carbon-carbon bond distance, ~ 0.8 Å). Our calculations confirm that doubly excited states can mediate the transition to ^{1}TT through second order contributions (Equation 7.31). Interestingly, both direct and D-mediated mechanisms are

maximum and in phase at the alternate geometry (with second order D-mediated couplings being stronger than $S_1/^1TT$ direct interactions), in which they cooperatively assist the formation of the triplet-pair state with a rather strong overall SF coupling ($\sim$ 60 meV in Figure 7.9a).

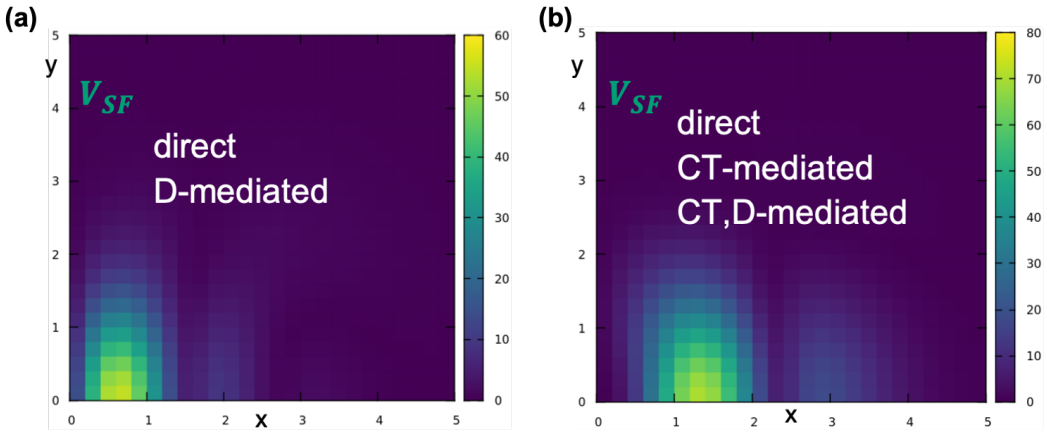

Figure 7.9: Absolute total SF couplings (in meV) between S_1S_0 and ^1TT with $E(S_1S_0) - E(^1TT) = 0.25$ eV, and DS_0/S_0D and CT states at 0.4 and 20 eV (a), and 0.4 and 3.4 eV (b) above the S_1 state, for the stacked ethylene dimer computed at a constant vertical separation ($z = 3.5$ Å) and different longitudinal (x in Å) and horizontal (y in Å) displacements as shown in Figure 7.3.

If D state is energetically close to S_1, but CT is higher in energy (by a few eVs), the CT-mediated channel is still responsible for the stronger contribution to SF couplings, with direct and CT,D-mediated paths also contributing, although to a lesser degree (Figure 7.9b). Concretely, the direct interaction exhibits the opposite sign, effectively decreasing the overall $|V_{SF}|$ values, in particular for $x < 1$ Å. The third order CT,D-mediation is also out-of-phase with respect to superexchange for $0 \leq x \leq 0.8$ Å, but in-phase for $x > 0.8$ Å structures, resulting in a maximum coupling shifted to higher longitudinal displacements with respect to the CT-mediated mechanism alone.

As shown in numerous occasions,(23; 25; 14; 24; 35) CT-mediated SF can be rather efficient, with strong SF couplings achieved through superexchange, *i.e.*, second order contributions to the $S_1/^1TT$ coupling. When CT states are close to S_1, $|V_{SF}|$ is as high as 706 meV (Figure 7.10a at 1.0 Å). Due to the strength of S_1/CT and $CT/^1TT$ couplings, second order CT terms largely determine the overall SF couplings when both D and CT states are energetically low (Figure 7.10b), with virtually no difference with the $|V_{SF}|$ profile obtained with high energy D state in Figure 7.10a.

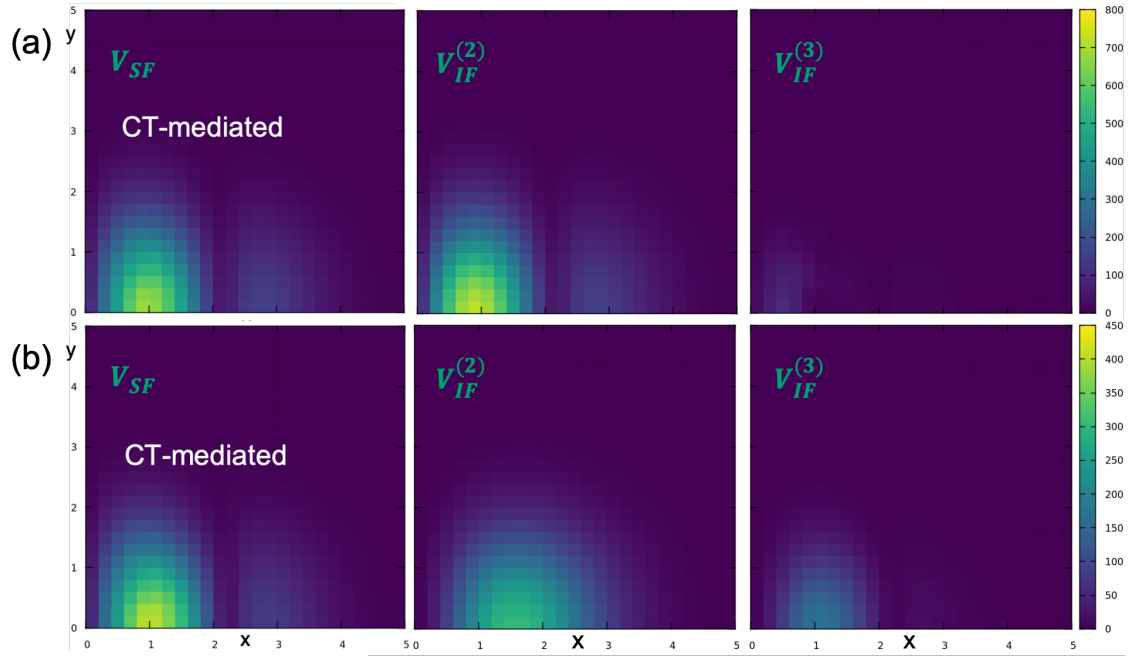

Figure 7.10: Absolute total SF couplings (in meV) between S_1S_0 and ^{1}TT with $E(S_1S_0) - E(^1TT) = 0.25$ eV, and DS_0/S_0D and CT states at 20 and 0.4 eV (a), 0.4 and 0.4 eV (b) and above the S_1 state, for the stacked ethylene dimer computed at a constant vertical separation (z = 3.5 Å) and different longitudinal (x in Å) and horizontal (y in Å) displacements as shown in Figure 7.3.

7.3.3 Singlet fission dynamics with D state

The potential impact of the D state in the SF dynamics, either as being the initial state for the transition to ^{1}TT or as a mediator state, was evaluated by computing the time evolution of the density matrix of excitonic states through the second order time convolutionless quantum master equation (TCL QME) expressed as:

$$\frac{d}{dt}\rho_{ex}(t) = -i\left[H_{ex}, \rho_{ex}(t)\right] + \sum_{\omega,K} \gamma_K(\omega,t)\left(A_K(\omega)\rho_{ex}(t)A_K^\dagger(\omega) - \frac{1}{2}\left\{A_K^\dagger(\omega)A_K(\omega), \rho_{ex}(t)\right\}\right), \tag{7.35}$$

where $\rho_{ex}(t)$ is the density matrix at time t, H_{ex} is the excitonic Hamiltonian in Equation 7.11, and $A_I(\omega)$ is the I-diabat transition matrix defined as:

$$A_I(\omega) = \sum_{K',L'} |K'\rangle\langle K'|I\rangle\langle I|L'\rangle\langle L'|\delta(E_{L'} - E_{K'} - \hbar\omega), \tag{7.36}$$

where prime indices K' and L' run over adiabatic states with energies $E_{K'}$ and $E_{L'}$, and $\gamma_K(\omega,t)$ is the relaxation rate that becomes time independent in the Markov

approximation and can be written as:

$$\gamma_I(\omega) = \begin{cases} 2\pi J_I(\omega)(1 + n(\omega, T));\ \omega > 0 \\ \frac{4\lambda_I k_B T}{\Omega_I};\ \omega = 0 \\ 2\pi J_I(-\omega) n(-\omega, T);\ \omega < 0 \end{cases} \tag{7.37}$$

with the spectral density $J_I(\omega)$ approximated by an Ohmic function with a Lorentz-Drude cutoff:(36; 37)

$$J_I(\omega) = \frac{1}{\pi} \frac{2\omega\lambda_I\Omega_I}{\omega^2 + \Omega_I^2}, \tag{7.38}$$

where k_B is the Boltzman constant, and $n(\omega, T)$ the Bose-Einstein distribution at temperature T. In the following, I use $\lambda_I = 50$ meV and $\Omega_I = 180$ meV for all diabats I, corresponding to the stretching modes in acene molecules.(35)

In order to evaluate the time evolution, H_{ex} from specific structural conformations of the ethylene dimer previously computed were employed to evaluate Equation 7.35. To simplify, the states labelled as S_1, D and CT are simultaneously referred to S_1S_0/S_0S_1, DS_0/S_0D and AC/CA pair of states, respectively.

SF dynamics from D

For the stacked eclipsed disposition of the two chromophores, direct coupling between dark state and ^{1}TT is maximum, while couplings to S_1 and CT states become zero (Figure 7.5).

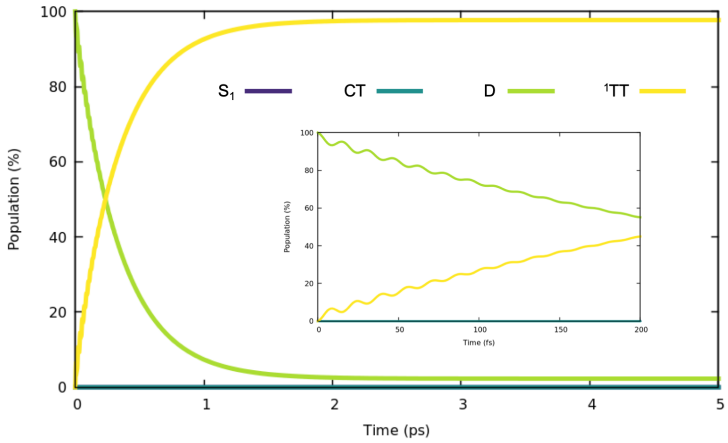

Figure 7.11: Time evolution of state population (in %) for two co-planar eclipsed ethylene molecules ($z = 3.5$ Å) from DS_0 state, with $E(DS_0) - E(^1TT) = 0.25$ eV, and S_1S_0/S_0S_1 and CT states at 0.4 and 3.4 eV. D, S_1 and CT indicate the total population of DS_0/S_0D, S_1S_0/S_0S_1 and CA/AC, respectively. Early time evolution shown in the inset.

Thus, at this arrangement of the molecular dimer, generation of the triplet-pair state can only follow a direct mechanism, as shown in Figure 7.11, in which the population of the D state is directly transferred to ^{1}TT. The first order $DS_1/^1TT$

coupling at the D_{2h} symmetry is in the order of 30 meV, resulting in a rather fast formation of ^{1}TT, which is completed with less than 2 ps.(38)

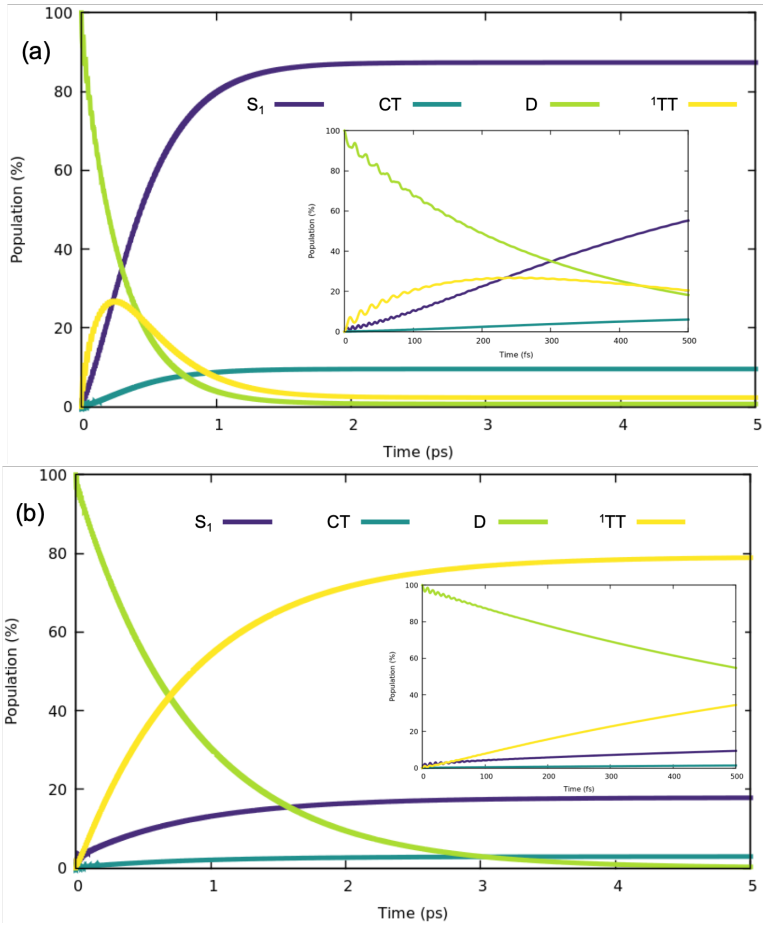

Figure 7.12: Time evolution of state population (in %) for two co-planar ethylene molecules ($x = 0.2$, $y = 0.0$, $z = 3.5$ Å) from DS_0 state, with $E(DS_0) - E(^1TT)$ equals to (a) 0.25 eV and (b) 0.55 eV, and S_1S_0/S_0S_1 and CT states at 0.4 and 3.4 eV. D, S_1 and CT indicate the total population of DS_0/S_0D, S_1S_0/S_0S_1 and CA/AC, respectively. Early time evolution shown in the inset.

In reality, the symmetry restrictions on the interstate couplings imposed at the eclipsed disposition can be alleviated due to static or dynamic disorder. Small distortions lowering the D_{2h} symmetry can allow the interaction of D states with CT and S_1 configurations. To simulate such disorder effects, we perform the time evolution for a small longitudinal displacement between the two molecules (with $x =$ 0.2 Å in Figure 7.12a). Initially, the system evolves towards the triplet-pair state, as in the ideal D_{2h} symmetry, but very rapidly the D (and ^{1}TT) state follows internal conversion to the S_1 state. At the nearly eclipsed (and eclipsed) conformation, the exciton and superexchange interactions are rather strong (in the order of 500 meV or larger), stabilizing the formation of an excimer-like adiabatic state that delocalizes over the two molecules, and exhibits strong S_1 character and sizeable symmetric contributions of CT configurations ($\sim 10\%$). This state acts as a trap state blocking

the formation of ^{1}TT. The decay to an excimeric trap state can be circumvented in chromophores with a larger relative energy gap between S_1 and ^{1}TT. In Figure 7.12b we simulate the exciton dynamics corresponding to the same situation as in Figure 7.12a, but with a larger exothermicity for the SF process from the dark state, that is from 0.25 eV to 0.55 eV as evaluated with the state energies of the monomer ($E(\mathrm{D}) - 2E(\mathrm{T}_1)$). Now, excimer stabilization due to exciton (S_1S_0/S_0S_1) and superexchange (S_1/CT) couplings is not large enough to overcome the $S_1/^1$TT diabatic energy gap, and the triplet-pair is the lowest adiabatic state. It is worth noticing that in this case ^{1}TT mixes with S_1 ($\sim 18\%$) and CT ($\sim 3\%$) configurations.

As illustrated in Figure 7.5, slip-stack configurations do not favor the direct coupling, and as a consequence the direct mechanism is also unfavorable. On the other hand, the dark state presents quite strong interactions with excitonic (S_1) and CT states, with S_1/CT couplings also being strong. Overall, SF couplings predict CT and S_1 mediated processes (Figure 7.6). As a result, the excited state time evolution from the dark state in the $x = 1.4$ Å dimer exhibits a rather different population profile than in the eclipsed case (Figure 7.13). At early times, both excitonic and CT states are involved in the decay of the dark state. Initially, especially in the first 50 fs, the D state shows intense population oscillations coherent with the fluctuations in the total excitonic population. The S_1 occupation reaches $\sim 20\%$, and rapidly decays to $\sim 3\%$. The fast depopulation of S_1 coincides with the modest raise of CT population. Moreover, the steep formation of ^{1}TT occurs from the very beginning, suggesting an intricate participation of D, S_1 and CT states in the SF mechanism. Notably, the $DS_0 \rightarrow {}^1$TT photophysical reaction is nearly completed within 0.5 ps, faster than in the direct case.

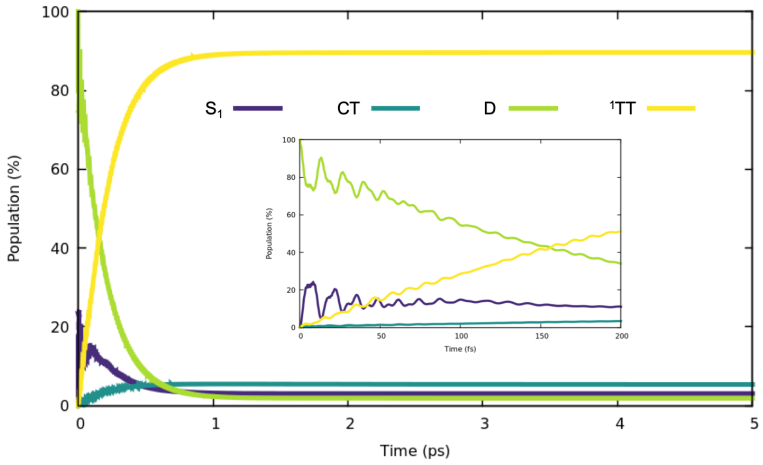

Figure 7.13: Time evolution of state population (in %) for two co-planar ethylene molecules ($x = 1.4$, $y = 0.0$, $z = 3.5$ Å) from DS_0 state, with $E(DS_0) - E(^1\mathrm{TT}) = 0.25$ eV, and S_1S_0/S_0S_1 and CT states at 0.4 and 3.4 eV. D, S_1 and CT indicate the total population of DS_0/S_0D, S_1S_0/S_0S_1 and CA/AC, respectively. Early time evolution shown in the inset.

To confirm the simultaneous participation of S_1 and CT states, we simulate the SF dynamics without AC/CA (Figure 7.14a) and without S_1S_0/S_0S_1 (Figure 7.14b) configurations. In both cases the dynamics of the process change. The SF reaction becomes slower without S_1 states, especially in the absence of CT states. Without the presence of AC and CA configurations at relatively low energies, the initial DS_0 state strongly interacts with S_1S_0, producing a mixed D ($\sim 80\%$) and S_1 ($\sim 20\%$) population in the first few fs. From there, the formation of the triplet-pair state is achieved through the simultaneous direct transition from D and S_1 states, with a faster reaction rate from the dark state. The changes observed without excitonic states are less extreme and mainly related with the evolution at early times. The formation of ^{1}TT is nearly completed at 2 ps, which is twice the time required when S_1 states are energetically close (Figure 7.13), demonstrating the simultaneous mediation of CT and excitonic states.

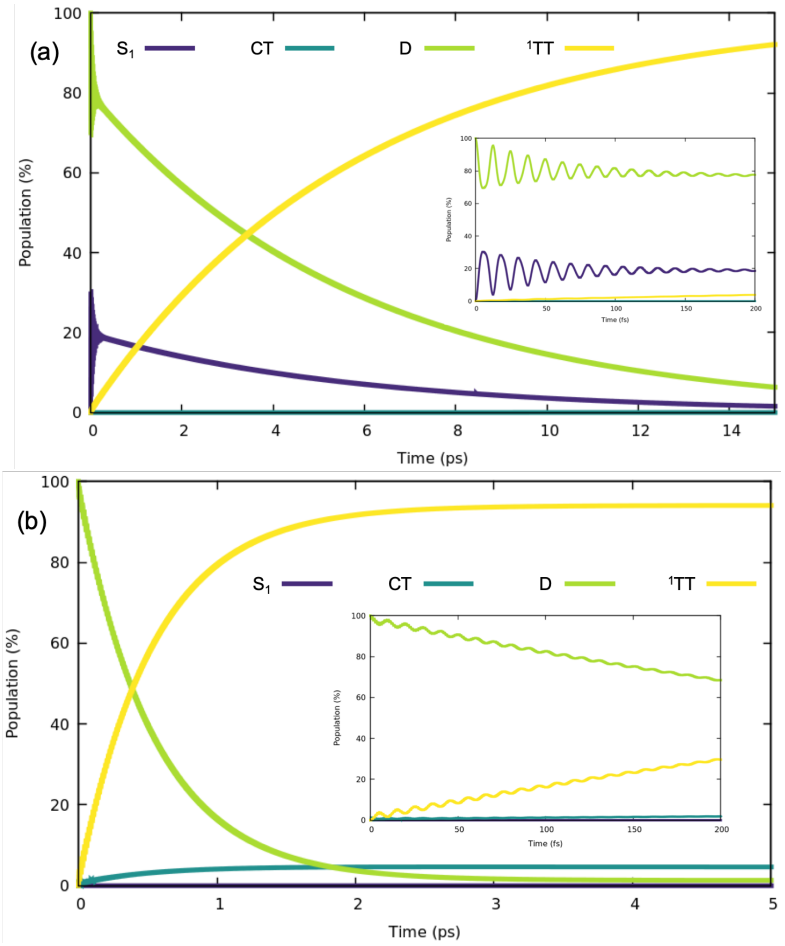

Figure 7.14: Time evolution of state population (in %) for two co-planar ethylene molecules ($x = 1.4$, $y = 0.0$, $z = 3.5$ Å) from DS_0 state, with $E(DS_0) - E(^1TT) = 0.25$ eV, and (a) S_1S_0/S_0S_1 states at 0.4 eV (no CT states) and (b) CT states at 3.4 eV (no S1 states). D, S_1 and CT indicate the total population of DS_0/S_0D, S_1S_0/S_0S_1 and CA/AC, respectively. Early time evolution shown in the inset.

D-mediator SF dynamics

In this section, we explore the potential mediator role of the dark state in the SF dynamics with S_1S_0 as the initial state, and by considering two different coupling hot spots in the configurational space of two co-planar ethylene molecules.

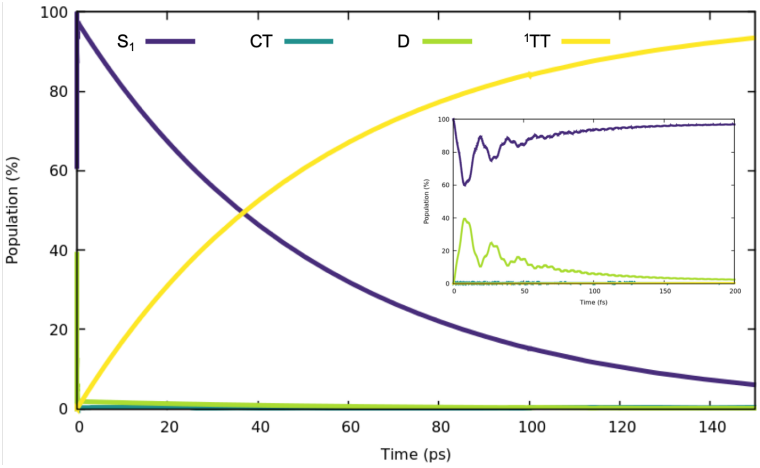

Figure 7.15: Time evolution of state population (in %) for two co-planar ethylene molecules ($x = 0.8$, $y = 0.0$, $z = 3.5$ Å) from S_1S_0 state, with $E(S_1S_0) - E(^1TT) = 0.55$ eV, and DS_0/S_0D and CT states at 0.4 and 20 eV. D, S_1 and CT indicate the total population of DS_0/S_0D, S_1S_0/S_0S_1 and CA/AC, respectively. Early time evolution shown in the inset.

The first case corresponds to the x-axis displaced conformation. Figure 7.9 illustrates the quite strong direct and D-mediated (second order) SF couplings, which are expected to dominate the excited state dynamics if CT states lie energetically high. This situation is represented with the simulation of exciton dynamics for the $x = 0.8$ Å conformation, suggesting a direct $S_1 \rightarrow {}^1TT$ mechanism (Figure 7.15). At this molecular arrangement, the coupling between S_1S_0 and DS_0 (106 meV) is about an order of magnitude stronger than the $S_1S_0/{}^1TT$ interaction (17 meV). As a consequence, the S_1S_0 state initially interacts with the dark state, which reaches a population as high as 40%, but vanishes after less than 200 fs, while S_1 is totally recovered. During the first 200 fs the triplet-pair remains depopulated. At later times the S_1 and ^1TT populations simultaneously decay and grow,respectively, following a first order kinetics. Thus, in this case, the D state is not actually mediating the formation of the triplet-pair state, but assisting exciton delocalization, that is from S_1S_0 to S_1S_0+S_0S_1, prior to the (direct) S_1 to ^1TT transition.

Finally, I present the simulation of the SF dynamics for the ethylene dimer structural conformer with a long axis displacement of 1.4 Å, and D and CT states at 0.4 and 3.4 eV with respect to S_1 (Figure 7.16), for which SF couplings predict the possibility of direct, CT-mediated and CT,D-mediated contributions to the total coupling (Figure 7.9b). The formation of the triplet-pair state is very fast, *i.e.*,

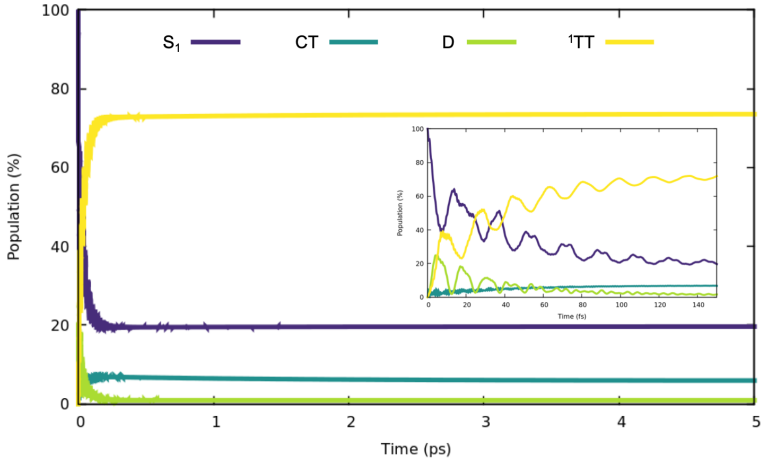

Figure 7.16: Time evolution of state population (in %) for two co-planar ethylene molecules ($x = 1.4$, $y = 0.0$, $z = 3.5$ Å) from S_1S_0 state, with $E(S_1S_0) - E(^1TT) = 0.25$ eV, and DS_0/S_0D and CT states at 0.4 and 3.4 eV. D, S_1 and CT indicate the total population of DS_0/S_0D, S_1S_0/S_0S_1 and CA/AC, respectively. Early time evolution shown in the inset.

completed within 140 fs, although the final ^1TT state is strongly mixed with S_1 (20%) and CT (6%) configurations. D and CT states are largely involved in the early exciton dynamics, with strong oscillations between $S_1/D/^1TT$. The initial decay of S_1 is concomitant to the raise of D, immediately followed by the increase in the ^1TT population. Although the occupation of the CT state remains always quite low due to its higher energy, it seems to also affect the time evolution of ^1TT.

Internal conversion to the triplet-pair becomes nearly an order of magnitude slower if the CT states are removed from the system (Figure 7.17a). The D state strongly interacts with S_1 and presents sizeable occupation at early times (0-60 fs), coinciding with a raise of ^1TT. The population of the dark state considerably diminishes approximately at 60-80 fs, just when the increase of ^1TT decelerates. This profile indicates a short-time D-mediated SF mechanism followed by the direct $S_1 \rightarrow ^1TT$ transition. Alternatively, if the dark state is very high in energy (Figure 7.17b), the formation of ^1TT is dominated by the CT-mediation, as it becomes evident when compared to the slower dynamics obtained when only the direct mechanism is taken into account (Figure 7.17c). Overall, despite that in this case the sole presence of the direct mechanism results in a rather fast ^1TT generation, the different mediation mechanism through D and CT states are more efficient and are expected to dominate SF in slip-stacked conformations.

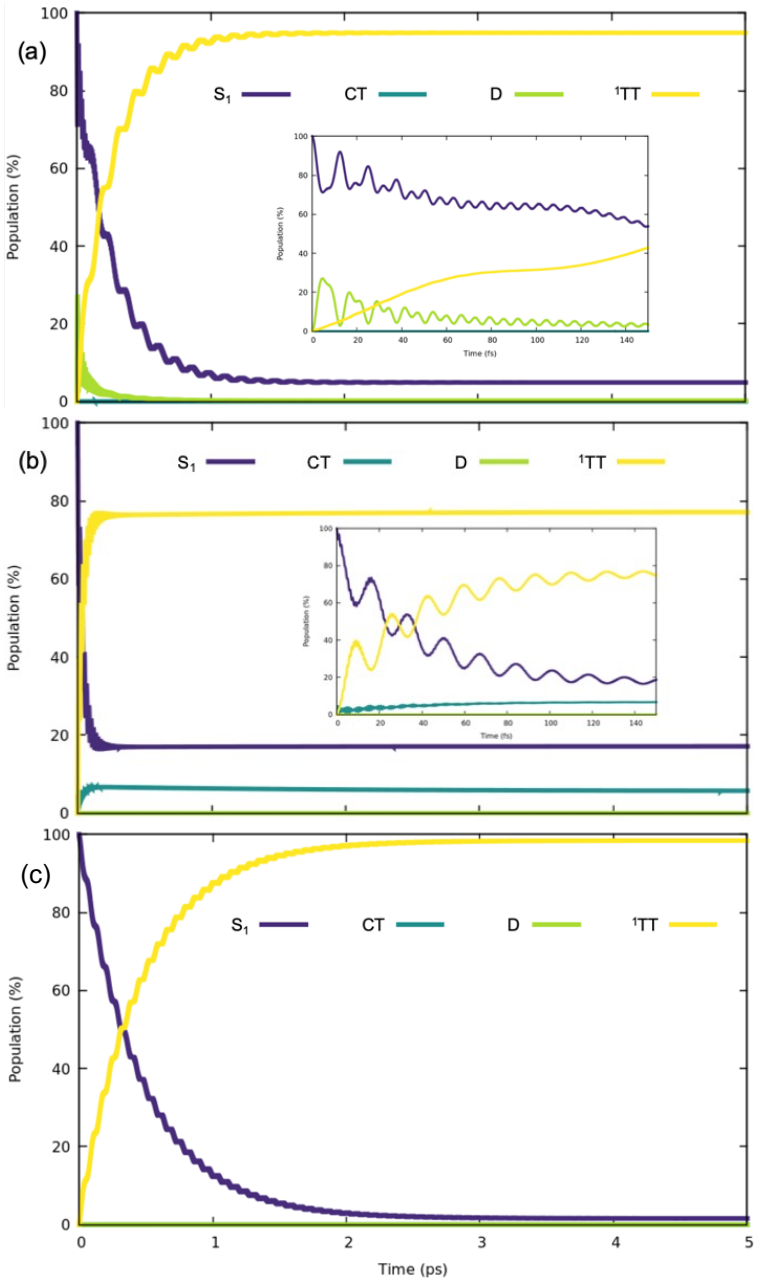

Figure 7.17: Time evolution of state population (in %) for two co-planar ethylene molecules ($x = 1.4$, $y = 0.0$, $z = 3.5$ Å) from S_1S_0 state, with $E(S_1S_0) - E(^1TT) = 0.25$ eV, and (a) DS_0/S_0D at 0.4 eV (no CT states), (b) CT states at 3.4 eV (no DS_0/S_0D states), and (c) no CT and DS_0/S_0D states. D, S_1 and CT indicate the total population of DS_0/S_0D, S_1S_0/S_0S_1 and CA/AC, respectively. Early time evolution shown in the inset.

7.4 Appendix

7.4.1 Computational details

Molecular geometry of each ethylene molecule has been frozen at the MP2/cc-pVTZ ground state D_{2h} optimized structure, with CC and CH bond lengths of 1.33 and 1.08 Å, respectively, and HCC angle of 121.3°. Electronic couplings between diabatic states have been computed using orthonormalized orbitals localized on each of the two ethylene molecules. Fragment orbitals have been obtained as linear combinations of canonical (ground state) Hartree-Fock orbitals of the dimer as described in subsection 3.3.2.1. The 6-31G basis set has been employed in all electronic structure calculations. These calculations have been performed with a development version of the Q-Chem program.(39)

The TCL QME equation has been solved by means of the fourth-order Runge-Kutta approach at $T = 300$ K. Excited to ground state radiative decays have not been included in the exciton dynamic simulations. Singlet fission exciton dynamics calculations have been done with an in-house program developed by the group.

Bibliography

[1] S. Singh, W. J. Jones, W. Siebrand, B. P. Stoicheff, and W. G. Schneider, "Laser generation of excitons and fluorescence in anthracene crystals," *The Journal of Chemical Physics*, vol. 42, no. 1, pp. 330–342, 1965.

[2] N. Geacintov, M. Pope, and F. Vogel, "Effect of magnetic field on the fluorescence of tetracene crystals: Exciton fission," *Physical Review Letters*, vol. 22, no. 12, pp. 593–596, 1969.

[3] R. C. Johnson and R. E. Merrifield, "Effects of magnetic fields on the mutual annihilation of triplet excitons in anthracene crystals," *Physical Review B*, vol. 1, no. 2, pp. 896–902, 1970.

[4] R. E. Merrifield, "Theory of magnetic field effects on the mutual annihilation of triplet excitons," *The Journal of Chemical Physics*, vol. 48, no. 9, pp. 4318–4319, 1968.

[5] A. Suna, "Kinematics of exciton-exciton annihilation in molecular crystals," *Physical Review B*, vol. 1, no. 4, pp. 1716–1739, 1970.

[6] C. E. Swenberg, M. A. Ratner, and N. E. Geacintov, "Energy dependence of optically induced exciton fission," *The Journal of Chemical Physics*, vol. 60, no. 5, pp. 2152–2157, 1974.

[7] M. C. Hanna and A. J. Nozik, "Solar conversion efficiency of photovoltaic and photoelectrolysis cells with carrier multiplication absorbers," *J. Appl. Phys.*, vol. 100, no. 7, p. 074510, 2006.

[8] W. Shockley and H. J. Queisser, "Detailed balance limit of efficiency of p-n junction solar cells," *Journal of Applied Physics*, vol. 32, no. 3, pp. 510–519, 1961.

[9] M. B. Smith and J. Michl, "Recent advances in singlet fission," *Annual Review of Physical Chemistry*, vol. 64, no. 1, pp. 361–386, 2013.

[10] M. B. Smith and J. Michl, "Singlet fission," *Chemical Reviews*, vol. 110, no. 11, pp. 6891–6936, 2010.

[11] D. Casanova, "Theoretical modeling of singlet fission," *Chemical Reviews*, vol. 118, no. 15, pp. 7164–7207, 2018.

[12] N. J. Thompson, D. N. Congreve, D. Goldberg, V. M. Menon, and M. A. Baldo, "Slow light enhanced singlet exciton fission solar cells with a 126% yield of electrons per photon," *Applied Physics Letters*, vol. 103, no. 26, p. 263302, 2013.

[13] J. Xia, S. N. Sanders, W. Cheng, J. Z. Low, J. Liu, L. M. Campos, and T. Sun, "Singlet fission: Progress and prospects in solar cells," *Advanced Materials*, vol. 29, no. 20, p. 1601652, 2017.

[14] D. Casanova, "Electronic structure study of singlet fission in tetracene derivatives," *Journal of Chemical Theory and Computation*, vol. 10, no. 1, pp. 324–334, 2014.

[15] E. Kumarasamy, S. N. Sanders, M. J. Y. Tayebjee, A. Asadpoordarvish, T. J. H. Hele, E. G. Fuemmeler, A. B. Pun, L. M. Yablon, J. Z. Low, D. W. Paley, J. C. Dean, B. Choi, G. D. Scholes, M. L. Steigerwald, N. Ananth, D. R. McCamey, M. Y. Sfeir, and L. M. Campos, "Tuning singlet fission in π-bridge-π chromophores," *Journal of the American Chemical Society*, vol. 139, no. 36, pp. 12488–12494, 2017.

[16] D. Casanova, "Theoretical modeling of singlet fission," *Chem. Rev.*, vol. 118, no. 15, pp. 7164–7207, 2018.

[17] P. M. Zimmerman, Z. Zhang, and C. B. Musgrave, "Singlet fission in pentacene through multiexciton quantum states," vol. 2, no. 8, pp. 648–652, 2010.

[18] H. Kim and P. M. Zimmerman, "Coupled double triplet state in singlet fission," vol. 20, no. 48, pp. 30083–30094, 2018.

[19] W.-L. Chan, M. Ligges, A. Jailaubekov, L. Kaake, L. Miaja-Avila, and X. Y. Zhu, "Observing the multiexciton state in singlet fission and ensuing ultrafast multielectron transfer," *Science*, vol. 334, no. 6062, p. 1541, 2011.

[20] A. M. Müller, Y. S. Avlasevich, W. W. Schoeller, K. Müllen, and C. J. Bardeen, "Exciton fission and fusion in bis(tetracene) molecules with different covalent linker structures," *J. Am. Chem. Soc.*, vol. 129, no. 46, pp. 14240–14250, 2007.

[21] K. Miyata, F. S. Conrad-Burton, F. L. Geyer, and X. Y. Zhu, "Triplet pair states in singlet fission," *Chem. Rev.*, vol. 119, no. 6, pp. 4261–4292, 2019.

[22] M. B. Smith and J. Michl, "Recent advances in singlet fission," *Annu. Rev. Phys. Chem.*, vol. 64, no. 1, pp. 361–386, 2013.

[23] W.-L. Chan, T. C. Berkelbach, M. R. Provorse, N. R. Monahan, J. R. Tritsch, M. S. Hybertsen, D. R. Reichman, J. Gao, and X. Y. Zhu, "The quantum coherent mechanism for singlet fission: Experiment and theory," *Acc. Chem. Res.*, vol. 46, no. 6, pp. 1321–1329, 2013.

[24] T. Zeng, R. Hoffmann, and N. Ananth, "The low-lying electronic states of pentacene and their roles in singlet fission," *J. Am. Chem. Soc.*, vol. 136, no. 15, pp. 5755–5764, 2014.

[25] D. Beljonne, H. Yamagata, J. L. Brédas, F. C. Spano, and Y. Olivier, "Charge-transfer excitations steer the davydov splitting and mediate singlet exciton fission in pentacene," *Phys. Rev. Lett.*, vol. 110, p. 226402, 2013.

[26] M. Schreiber, M. R. Silva-Junior, S. P. A. Sauer, and W. Thiel, "Benchmarks for electronically excited states: Caspt2, cc2, ccsd, and cc3," vol. 128, no. 13, p. 134110, 2008.

[27] M. R. Silva-Junior, M. Schreiber, S. P. A. Sauer, and W. Thiel, "Benchmarks for electronically excited states: Time-dependent density functional theory and density functional theory based multireference configuration interaction," vol. 129, no. 10, p. 104103, 2008.

[28] K. Schulten and M. Karplus, "On the origin of a low-lying forbidden transition in polyenes and related molecules," *Chem. Phys. Lett.*, vol. 14, no. 3, pp. 305–309, 1972.

[29] T. H. Dunning, R. P. Hosteny, and I. Shavitt, "Low-lying π-electron states of transbutadiene," *J. Am. Chem. Soc.*, vol. 95, no. 15, pp. 5067–5068, 1973.

[30] R. P. Hosteny, T. H. Dunning, R. R. Gilman, A. Pipano, and I. Shavitt, "Ab initio study of the πelectron states of transbutadiene," *J. Chem. Phys.*, vol. 62, no. 12, pp. 4764–4779, 1975.

[31] A. Amirav, U. Even, and J. Jortner, "Butterfly motion of the isolated pentacene molecule in its first-excited singlet state," *Chem. Phys. Lett.*, vol. 72, no. 1, pp. 21–24, 1980.

[32] A. M. Griffiths and P. A. Freedman, "Out-of-plane vibrations of isolated tetracene and pentacene molecules," *J. Chem. Soc., Faraday Trans. 2*, vol. 78, no. 2, pp. 391–398, 1982.

[33] P. A. M. Dirac and N. H. D. Bohr, "The quantum theory of the emission and absorption of radiation," *Proc. R. Soc. London, Ser. A*, vol. 114, no. 767, pp. 243–265, 1927.

[34] N. E. Swenberg, C. E.; Geacintov, *Organic molecular photophysics*. No. v. 1 in A Wiley-Interscience publication, J. Wiley, 1973.

[35] T. C. Berkelbach, M. S. Hybertsen, and D. R. Reichman, "Microscopic theory of singlet exciton fission. iii. crystalline pentacene," *J. Chem. Phys.*, vol. 141, no. 7, p. 074705, 2014.

[36] T. C. Berkelbach, M. S. Hybertsen, and D. R. Reichman, "Microscopic theory of singlet exciton fission. ii. application to pentacene dimers and the role of superexchange," vol. 138, no. 11, p. 114103, 2013.

[37] F. Mirjani, N. Renaud, N. Gorczak, and F. C. Grozema, "Theoretical investigation of singlet fission in molecular dimers: The role of charge transfer states and quantum interference," *J. Phys. Chem. C*, vol. 118, no. 26, pp. 14192–14199, 2014.

[38] E. G. Fuemmeler, S. N. Sanders, A. B. Pun, E. Kumarasamy, T. Zeng, K. Miyata, M. L. Steigerwald, X. Y. Zhu, M. Y. Sfeir, L. M. Campos, and N. Ananth, "A direct mechanism of ultrafast intramolecular singlet fission in pentacene dimers," *ACS Central Science*, vol. 2, no. 5, pp. 316–324, 2016.

[39] Y. Shao, Z. Gan, E. Epifanovsky, A. T. B. Gilbert, M. Wormit, J. Kussmann, A. W. Lange, A. Behn, J. Deng, X. Feng, D. Ghosh, M. Goldey, P. R. Horn, L. D. Jacobson, I. Kaliman, R. Z. Khaliullin, T. Kus, A. Landau, J. Liu, E. I. Proynov, Y. M. Rhee, R. M. Richard, M. A. Rohrdanz, R. P. Steele, E. J. Sundstrom, H. L. Woodcock, P. M. Zimmerman, D. Zuev, B. Albrecht, E. Alguire, B. Austin, G. J. O. Beran, Y. A. Bernard, E. Berquist, K. Brandhorst, K. B. Bravaya, S. T. Brown, D. Casanova, C.-M. Chang, Y. Chen, S. H. Chien, K. D. Closser, D. L. Crittenden, M. Diedenhofen, R. A. DiStasio, H. Do, A. D. Dutoi, R. G. Edgar, S. Fatehi, L. Fusti-Molnar, A. Ghysels, A. Golubeva-Zadorozhnaya, J. Gomes, M. W. D. Hanson-Heine, P. H. P. Harbach, A. W. Hauser, E. G. Hohenstein, Z. C. Holden, T.-C. Jagau,

H. Ji, B. Kaduk, K. Khistyaev, J. Kim, J. Kim, R. A. King, P. Klunzinger, D. Kosenkov, T. Kowalczyk, C. M. Krauter, K. U. Lao, A. D. Laurent, K. V. Lawler, S. V. Levchenko, C. Y. Lin, F. Liu, E. Livshits, R. C. Lochan, A. Luenser, P. Manohar, S. F. Manzer, S.-P. Mao, N. Mardirossian, A. V. Marenich, S. A. Maurer, N. J. Mayhall, E. Neuscamman, C. M. Oana, R. Olivares-Amaya, D. P. O'Neill, J. A. Parkhill, T. M. Perrine, R. Peverati, A. Prociuk, D. R. Rehn, E. Rosta, N. J. Russ, S. M. Sharada, S. Sharma, D. W. Small, A. Sodt, T. Stein, D. Stuck, Y.-C. Su, A. J. W. Thom, T. Tsuchimochi, V. Vanovschi, L. Vogt, O. Vydrov, T. Wang, M. A. Watson, J. Wenzel, A. White, C. F. Williams, J. Yang, S. Yeganeh, S. R. Yost, Z.-Q. You, I. Y. Zhang, X. Zhang, Y. Zhao, B. R. Brooks, G. K. L. Chan, D. M. Chipman, C. J. Cramer, W. A. Goddard, M. S. Gordon, W. J. Hehre, A. Klamt, H. F. Schaefer, M. W. Schmidt, C. D. Sherrill, D. G. Truhlar, A. Warshel, X. Xu, A. Aspuru-Guzik, R. Baer, A. T. Bell, N. A. Besley, J.-D. Chai, A. Dreuw, B. D. Dunietz, T. R. Furlani, S. R. Gwaltney, C.-P. Hsu, Y. Jung, J. Kong, D. S. Lambrecht, W. Liang, C. Ochsenfeld, V. A. Rassolov, L. V. Slipchenko, J. E. Subotnik, T. Van Voorhis, J. M. Herbert, A. I. Krylov, P. M. W. Gill, and M. Head-Gordon, "Advances in molecular quantum chemistry contained in the q-chem 4 program package," *Mol. Phys.*, vol. 113, no. 2, pp. 184–215, 2015.

Chapter 8

Spiroconjugated dimers

Spiro-linked compounds are defined by the IUPAC as compounds having one atom (usually a quaternary carbon) as the only common member of two rings.(1) If both halves are constituted by π-electron systems, they are named spiroconjugated compounds.(2) Then, spiroconjugation is the term used to describe the indirect interaction between two systems of π-orbitals in perpendicular planes and linked together through a non-conjugated atom, *i.e*, an sp^3 carbon.(3).

Spiroconjugated systems present unusual molecular properties associated with the relative orientation of their constitutive halves. First, the orthogonality and rigidity provided by the spiro-linkage prevents sterical hindrance between π-systems, and increase the stability and solubility with respect to any other dimer arrangement. This special molecular geometry minimizes electronic interactions, and the relative orientation of the monomeric transition dipole moments excludes the possibility of excimer formation and energy splitting of excited states as a consequence of molecular aggregation. These properties make them materials with potential applications in optoelectronic devices. They have been extensively investigated and used in field-effect transistors, solar cells, photodiodes and phototransistors, light-emitting devices, etc.(4; 5) It is only very recently that spiroconjugated systems have been considered as potential SF materials. By means of transient absorption spectroscopy, Kumarasamy et al. obtained fast SF rates and slow triplet pair recombination in a dimer of spiro-pentacene.(6)

In this chapter, spiroconjugated systems are studied as promising materials fulfilling the requirements to carry out two photophysical process to generate triplet excitons. In the first section, an exhaustive theoretical study of the suitability of proposed spiroconjugated dimers to undergo the SF process is reported. The potential to be good SF sensitizers of a family of pro-spiro chromophores is investigated. Then, the modelling of the SF intricacies in spiroconjugated dimers in terms of the nature of electronic states, interstate couplings, and SF mechanisms, as well, the

effect of vibrational distortions is presented to obtain a rather complete picture of the process. An alternative photophysical process to generate exciton triplets is the intersystem crossing (ISC). In collaboration with the group of Prof. Jinquan Chen from the East China Normal University, we explored the assistance of charge resonance to an efficient singlet to triplet conversion featured by a different family of spiro-conjugated systems. In the last part of this chapter, in-depth characterization of the radical character in spiro compounds is provided.

8.1 Spiroconjugated dimers in singlet fission

8.1.1 Chromophores pro-spiro

In the design of spiroconjugated compounds suitable for SF, it is necessary to consider monomers with the proper energetics (section 7.1). The full characterization of SF chromophores expose their electronic features in order to determine if they are or not able to fulfill the SF requirements, *i.e.*, $E(S_1) \geq 2E(T_1)$, $E(T_2) > 2E(T_1)$, etc. In this case, two conjugated scaffolds were considered, namely 2,7-disubstituted-fluorene **Fn** and 2,7-disubstituted-5,10-dihydro-dibenzopentalene **DBPn**, containing one and two sp^3 (pro-spiro) carbon atoms, respectively, combined with two substituents: diemethylene (**1**) and dycyanomethylene group (**2**), see Figure 8.1.

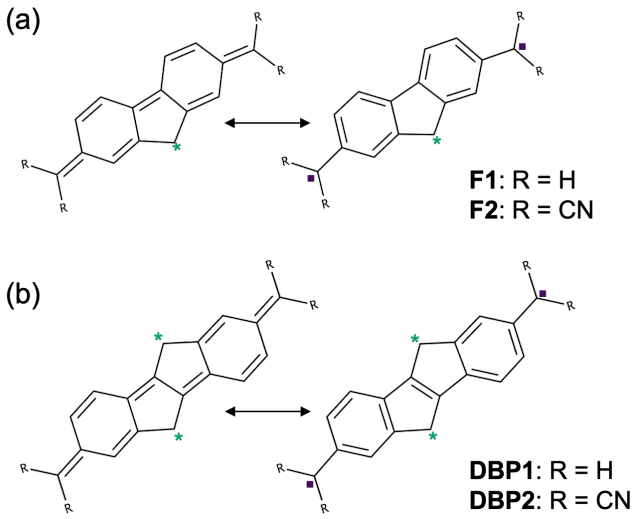

Figure 8.1: Quinoidal (left) and diradical (right) electromers of the studied chromophores: **F1**: 2,7-dimethylene-fluorene, **F2**: 2,7-bis(dicyanomethylene)-fluorene (a), **DBP1**: 2,7-dimethylene-5,10-dihydro-dibenzopentalene and **DBP2**: 2,7-bis(dicyanomethylene)-5,10-dihydro-dibenzopentalene (b). Starred position indicate pro-spiro atoms.

Both structures present two planar resonance forms, namely quinoidal (closed-shell) and aromatic (diradical), exhibiting tendency to have diradical character. In the ground state both, **Fn** and **DBPn**, are planar with C_{2v} and C_{2h} molecular symmetry, respectively.

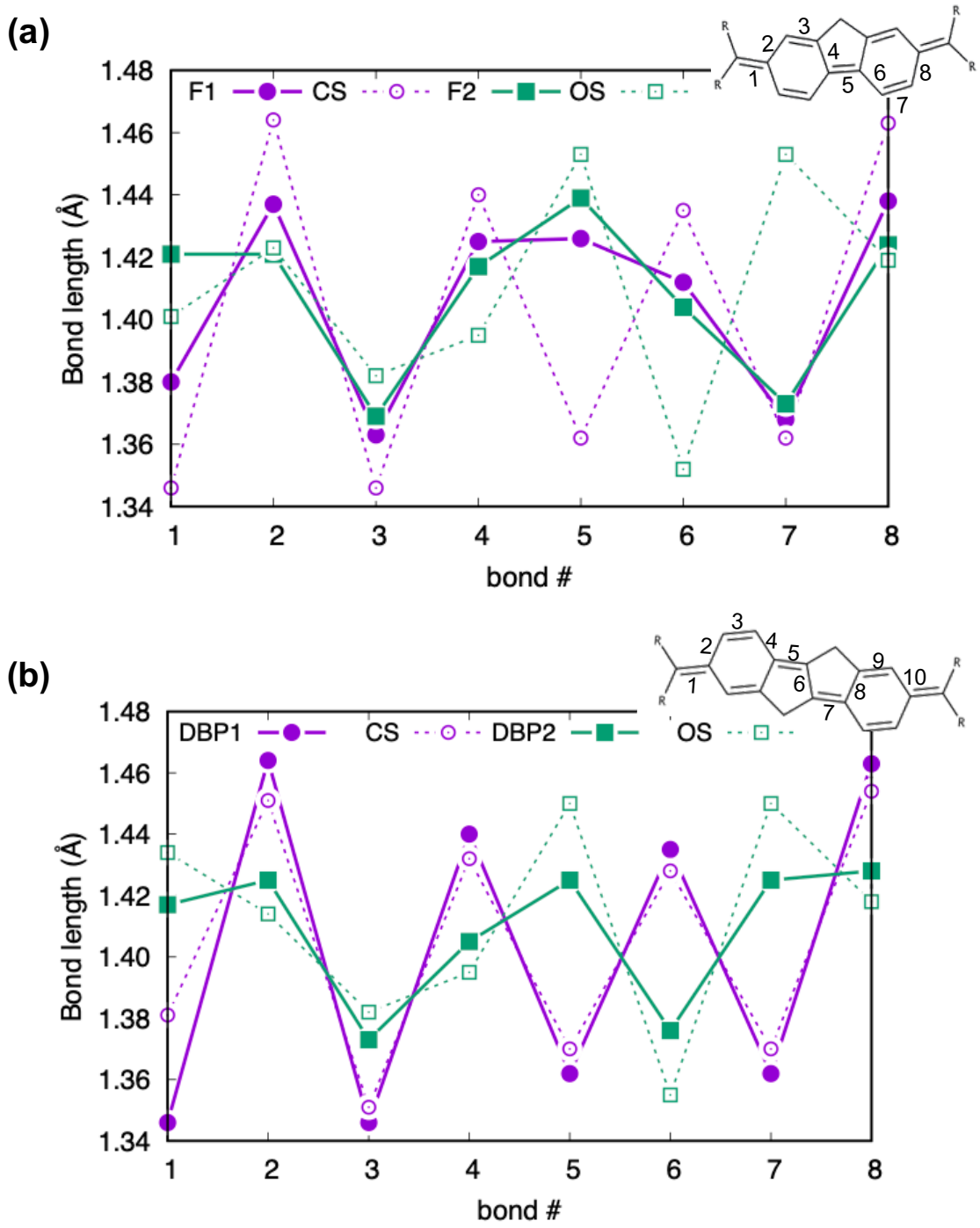

Figure 8.2: Bond length alternation of ground state optimized geometries of **Fn** (a) and **DBPn** (b) compared to the purely closed-shell (CS) and diradical (OS) structures. CS corresponds to the restricted singlet and OS to the unrestricted triplet for R = H.

The effect of the electron withdrawing power of the dicyano groups permits the

recovery of local aromaticity of the six-member of rings, leading to the apparition of diradicaloid character. As illustrated in Figure 8.2 **F1** and **F2** have a similar bond length distribution that resembles the aromatic-like pattern within the benzene rings of the open-shell structure (diradical structure), pointing that **F1** holds some diradical character. Contrarily, the minimum of **DBP1** is clearly quinoidal-like and corresponds to the closed-shell geometry, since its radical form is destabilized by the ring strain around the vinylene group shared by two pentagons, as seen in the study of carbon-bridged phenylenevinylene oligomers.(7)

Computed singlet-triplet energy gaps give an idea of the diradicaloid character of these monomers. Further, as mentioned before, the relative energy of the first excited singlet and triplet states determines the suitability of a compound to experience SF. Table 8.1 illustrates the intermediate diradical character of **F2** and **DBP2** ($y_0 = 0.44$ and $y_0 = 0.46$, respectively), which agrees with the small ΔE_{ST}^{ad}. The spatial representation of the FOD density in the ground state (Figure 8.3 b) captures the diradical stabilization effect by the CN groups through delocalization of unpaired electrons. The radical index of **F1** is close to that of its analogous cyano-derivative, in line with their similar bond pattern, while the singlet-triplet energy gap is around twice the computed one for **F2**. On the other hand, **DBP1** shows rather mild diradical character as indicated by the larger ΔE_{ST}^{ad} and its quite small diradical index ($y_0 = 0.17$), in conjunction with a quinoidal-like structure.

	F1	**F2**	**DBP1**	**DBP2**
ΔE_{ST}^{ad}	10.0	5.5	19.3	5.4
y_0	0.39	0.44	0.17	0.46
N_u	0.92	0.99	0.51	1.05

Table 8.1: Adiabatic singlet-triplet energy gaps (ΔE_{ST}^{ad}) computed at CAM-B3LYP level (in kcal/mol) and ground state diradical index (y_0) and number of unpaired electrons (N_u) obtained with RAS-SF of **Fn** and **DBPn** molecules.

HOMO and LUMO of the monomers are π-orbitals delocalized over the entire backbone but the sp^3 carbon atom (Figure 8.3 a). As expected, this pro-spiro atom plays an structural role helping to maintain the rigidity and planarity of the π-systems in both halves.

Computed low-lying excited states are summarized in Table 8.2. The main contributions to the electronic structure of T_1 and the two lowest excited singlets involve the HOMO and LUMO frontier orbitals (Figure 8.3). While S_1 is mainly described by the $HOMO^2 \rightarrow LUMO^2$ transition, the most important configuration in S_2 corresponds to the HOMO-to-LUMO excitation. HOMO-1 $\rightarrow$ LUMO and/or HOMO $\rightarrow$ LUMO+1 configurations contributes to both excited singlets. In the T_2

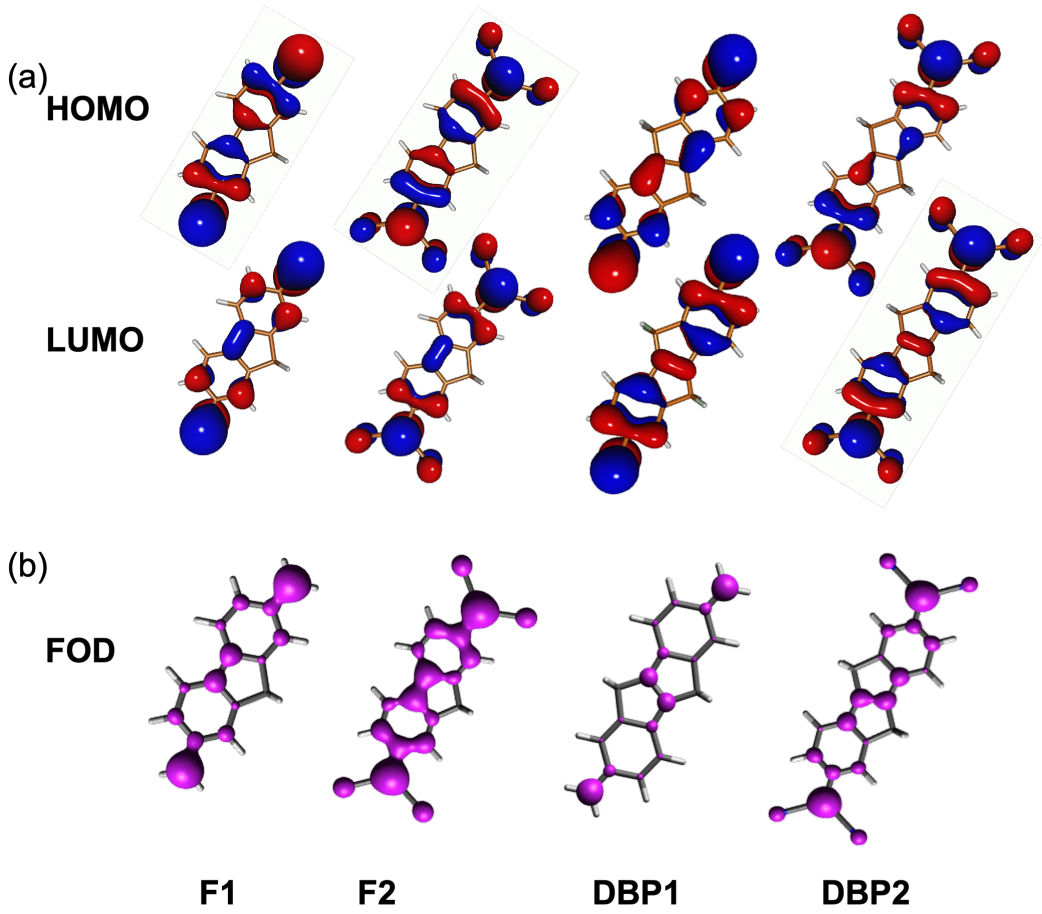

Figure 8.3: Frontier molecular orbitals (a) and FOD (b) of **Fn** and **DBPn** monomers.

state electronic excitation from HOMO-1 and HOMO to LUMO and LUMO+1 are involved. Vertical energies to the lowest triplet preserve the trend obtained for the adiabatic energies at the DFT level and dictated by the diradicaloid character of the molecules. In chromophores with the dicyano group, T_1 is considerably lower than in **F1** and **DBP1** (Table 8.1). Calculated excitations predict the presence of a dipole forbidden transition ($f \sim 0$) to a singlet state located just below the optical excitation, which holds an important double excitation character. This state ordering is in agreement with the 2^1A_g state lying below 1^1B_u in the closely related diphenylpolyenes.(8; 9; 10) The optical state is S_2, $^1B_2$ and ^1B_u for **Fn** and **DBPn**, respectively, corresponds mainly to the HOMO-to-LUMO single electron promotion. This dipole allowed transition lies about 3 eV above the ground state of the dimethylene substituted monomers, while it is notably redshifted upon CN substitution, in agreement with the excitation energies predicted by TD-DFT(11) (2.03 eV) and with the reported absorption maximum in solution (1.98 eV).(12)

molecule	state	ΔE	f	contributions (%)
F1	$^3B_2$	0.78	-	H $\rightarrow$ L (91)
	$2\times{}^3B_u$	1.57		
	$^1A_1$	2.75	0.008	$H^2 \rightarrow L^2$ (46)
				H-1 $\rightarrow$ L (20)
	$^1B_2$	3.11	2.096	H $\rightarrow$ L (48)
				H-1 $\rightarrow$ L/H $\rightarrow$ L (25)
	$^3A_1$	3.44	-	H-1 $\rightarrow$ L (45)
				H-1 $\rightarrow$ L+1 (16)
F2	$^3B_2$	0.41	-	H $\rightarrow$ L (94)
	$2\times{}^3B_u$	0.82		
	$^1A_1$	2.17	0.005	$H^2 \rightarrow L^2$ (41)
				H-1 $\rightarrow$ L (29)
	$^1B_2$	2.51	2.124	H $\rightarrow$ L (50)
				H-1 $\rightarrow$ L/H $\rightarrow$ L (28)
	$^3A_1$	2.82	-	H-1 $\rightarrow$ L (66)
				H-1 $\rightarrow$ L+1 (12)
DBP1	^3B_u	1.41	-	H $\rightarrow$ L (87)
	$2\times{}^3B_u$	2.82		
	^1A_g	2.97	0.000	$H^2 \rightarrow L^2$ (42)
				H $\rightarrow$ L+1 (15)
	^1B_u	3.05	2.726	H $\rightarrow$ L (52)
				H-1 $\rightarrow$ L/H $\rightarrow$ L (19)
	^3A_g	2.94	-	H $\rightarrow$ L+1 (35)
				H-1 $\rightarrow$ L (34)
DBP2	^3B_u	0.35	-	H $\rightarrow$ L (93)
	$2\times{}^3B_u$	0.70		
	^1A_g	1.85	0.000	$H^2 \rightarrow L^2$ (38)
				H-1 $\rightarrow$ L (28)
	^1B_u	2.28	2.393	H $\rightarrow$ L (42)
				H-1 $\rightarrow$ L/H $\rightarrow$ L (35)
	^3A_g	2.37	-	H-1 $\rightarrow$ L (60)
				H-1 $\rightarrow$ L+1 (18)

Table 8.2: Vertical excitation energies (ΔE in eV), oscillator strengths (f), and electronic transition contributions (in %) to the low-lying excited singlet and triplet states of **Fn** and **DBPn** computed at the RAS(4,4)-*sr*VWN level. For the sake of comparison we include twice the energy of the lowest triplet. H = HOMO, L = LUMO.

Data in Table 8.2 and diradical character (Table 8.1) give all the important quantities to establish relationships between excited states and draw preliminary conclusion about the feasibility of SF in these compounds. Since $2E(T_1) < E(S_1)$, SF for the four pro-spiro chromophores would be an exothermic process. Additionally, the second triplet state is energetically higher than twice the energy of T_1, *i.e.*, $2E(T_1) < E(T_2)$, which is beneficial for SF since it hinders the efficient recombination of the fission triplets to the triplet manifold as a competing decay channel. Nevertheless, there is a large difference in **F1**, **F2** and **DBP2** regarding the $2T_1$ energy and the excitation to the lowest singlets (S_1 and S_2), which predict a kinetically unfavorable SF photophysical reaction ($E(S_1)$-$2E(T_1) > 1$ eV). On the other hand, transition energy to the lowest excited singlets in **DBP1** are rather close to twice the S_0 to T_1 gap (0.1-0.2 eV above $2E(T_1)$), satisfying thermodynamic and kinetic conditions for an efficient SF process.

These results are computed at the Franck-Condon (FC) region, thus the relaxation on the excited state potential energy surface (PES) has not been taken into account. The relative energy between both S_1 and T_1 states should be evaluated at the minima of the potential energy surface since the fission rate is slower than the vibration relaxation rate. Before the generation of the multiexcitonic state (^{1}TT state), the ^1B_u state is expected to follow a vibrational relaxation to the minimum in its PES in an ultrafast process that can lead to unfavorable energy gaps between S_2 and T_1. Geometry optimization of **DBP1** on the excited ^1B_u PES systematically lowers the excitation energies with respect to the gaps at the ground state structure as shown in Table 8.3. The ordering of states remains the same as in the FC geometry. With the relaxation of ^1B_u, the ^3B_u state is also stabilized while the energy of ^3A_g is not significantly affected. Importantly, the SF exothermicity increases upon the relaxation of the state, which could be beneficial in order to inhibit the reverse SF reaction once the triplets are formed.

state	S_0 geom.	^1B_u geom.
^3B_u	1.41	1.02
^1A_g	2.97	2.55
^1B_u	3.05	2.87
^3A_g	2.94	2.83
$2 \times {}^3B_u$	2.85	2.03

Table 8.3: RAS(4,4)-*sr*VWN vertical transition energies (in eV) to low-lying excited states of **DBP1** at the CAM-B3LYP ground and ^1B_u optimized geometries. For the sake of comparison we include twice the energy of the lowest triplet.

All these results point towards **DBP1** as the most promising candidate for

efficient SF. In the following, the possibility of SF in the *spiro*-**DBP1**is investigated.

8.1.2 Spiroconjugated DBP1 dimer

The spiro-system is obtained by fusion of two **DBP1** monomers through the pro-spiro carbon atom. The ground state characterization shows that the properties (N_u, y_0, etc.) are obtained as twice the values in the monomer. As an example, Figure 8.4 shows the comparison between **DBP1** and its spiro derivative. Both monomers in the dimer are equivalent and the bond length alternation remains the same as in **DBP1**. In general, the formation of the spirocompound implies a rather small separation between chromophores and the sp^3-hybridization of the spiro-atom forces the orthogonality between the two π-systems. Additionally, the bond lengths related to the spiro-linkage, as well as the C-C$_{spiro}$-C angle are marginally distorted with respect to the ones in the pro-spiro chromophore (Figure 8.4b).

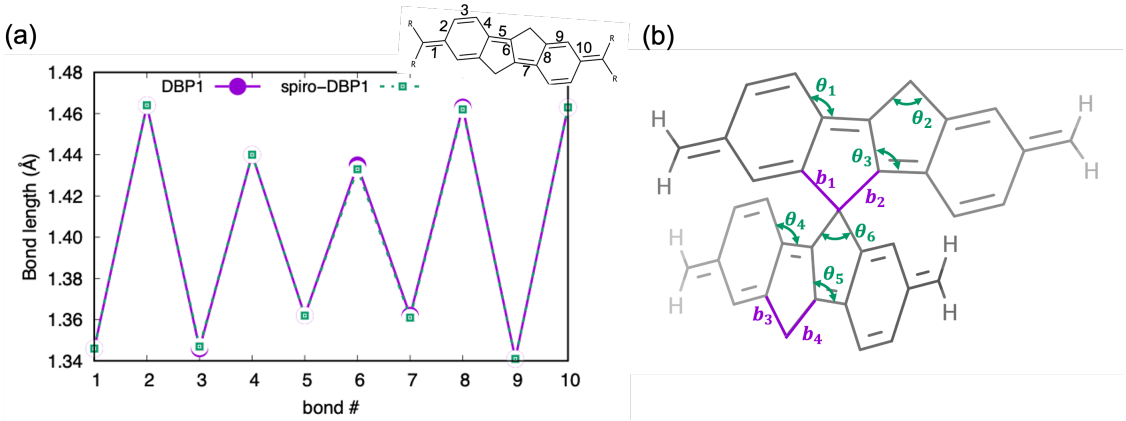

Figure 8.4: Bond length variation of **DBP1** and *spiro*-**DBP1** (a), and distortion leaded by the spiro-link in *spiro*-**DBP1** (b): $\theta_1 = 132.6^o(132.5^o)$, $\theta_2 = 101.9^o(101.9^o)$, $\theta_3 = 108.6^o(111.0^o)$, $\theta_4 = 132.4^o(132.5^o)$, $\theta_5 = 111.0^o(111.0^o)$, $\theta_6 = 100.6^o(101.9^o)$, $b_1 = 1.54(1.52)$, $b_2 = 1.50(1.50)$, $b_3 = 1.52(1.52)$, $b_4 = 1.50(1.50)$, the values in parenthesis correspond to **DBP1**.

The *spiro*-**DBP1** dimer contains a 2-fold rotation axis (C_2 symmetry point group) that goes through the spiro atom in the direction resulting from the sum of the normal vectors of the two monomeric planes. Although in the dimer the two π-electron systems are perpendicular to each other, they can effectively interact contingent upon their local symmetry.(3; 2) More concretely, only those orbitals from the monomer that are simultaneously antisymmetric to the two perpendicular reflexion planes in the dimer have the right symmetry to interact. In the case of π-orbitals it corresponds to those orbitals invariant under a C_2 rotation around the axis in the molecular plane that goes through the spiro atom and is parallel to the

short monomeric axis (pseudo C_{2v} in Figure 8.5). Here, this condition has to be considered only approximatively, since the **DBP1** is not invariant under such C_2 rotation. In this sense, the LUMO of **DBP1** is locally (around the spiro atom) C_2 symmetric, while the HOMO is antisymmetric. As a result, the two HOMOs of *spiro*-**DBP1** are degenerate (non-interacting monomeric HOMOs) and the LUMO and LUMO+1 present a small energy splitting (Δ_L = 54 meV). Considering the poor intermonomer orbital overlap, such orbital spliting can be approximated as twice the two-electron exchange integral of the LUMO on the two chromophores (K_{ll}):

$$\Delta_L \approx 2K_{ll}. \tag{8.1}$$

From such distribution of the frontier molecular orbitals, a moderate redshift of the transition energies to the lowest excited states with respect to the monomer must be predicted. It is also worth noticing the lack of electron density on the spiro atom in all the frontier molecular orbitals, which suggests that the bridging sp^3 carbon is not directly involved in the electronic structure of the low-lying states, and that its impact in the relative energies and couplings is merely structural.

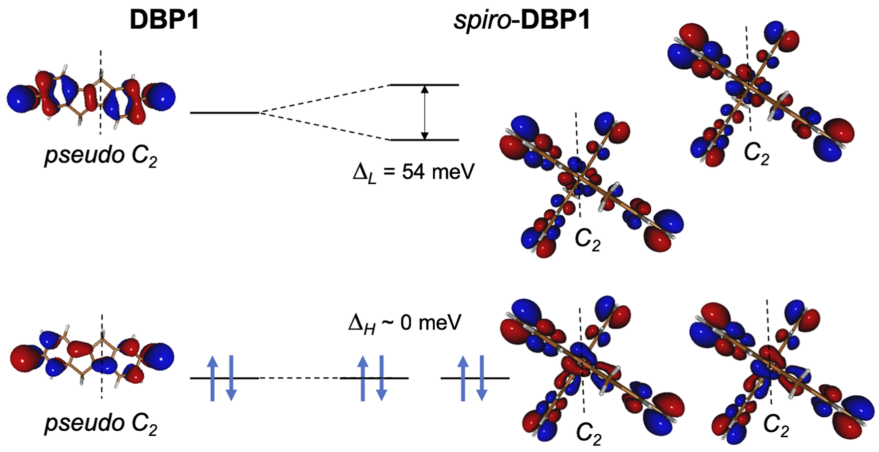

Figure 8.5: Frontier molecular orbital energy diagram of **DBP1** (left) and *spiro*-**DBP1** (right). The vertical dashed line on **DBP1** indicates the *pseudo*-C_{2v} rotation discussed in the text. The vertical dashed line on *spiro*-**DBP1** corresponds to the C_{2v} symmetry axis.

8.1.2.1 Electronic states of *spiro*-DBP1

Energy distribution of the lowest-lying electronic excited singlet states of the *spiro*-**DBP1** are shown in Table 8.4. Pairs of quasi-degenerate excited states can be observed, which is in good agreement with the idea of two chromophores weakly interacting. Furthermore, as predicted from the Δ_L, there is a very small redshift

of the transition energies with respect to the monomeric excited states. The nature of all these excited states (adiabatic states) can be characterized in terms of coupling of monomeric states (diabats). Then, the wave function of every excited state can be expressed in terms of local and collective excitons. In Table 8.4, the composition of the adiabatic states (herein labeled in boldface) reflects the main electronic character. Note that the SS contribution includes all possible combinations of S_iS_j with $i,j = 0,1,2,...$ configurations. Note that computed adiabatic states of spiroconjugated molecules are labelled in capital boldface letters, while regular capital characters are used for electronic states of monomers and diabatic states in spiro-dimers.

State	*Symm*	ΔE	f	ω^{SS}	ω^{CT}	ω^{TT}	N_u
^{1}**TT**	A	2.83	0.000	0.09	2.94	96.97	4.29
$\mathbf{S}_1$	B	2.94	0.013	98.35	1.64	0.01	3.63
$\mathbf{S}_{1'}$	A	2.95	0.002	89.60	9.75	0.65	3.63
$\mathbf{CR}_1$	B	3.02	0.089	3.50	96.07	0.43	2.79
$\mathbf{CR}_2$	A	3.04	0.021	10.65	86.80	2.55	2.74
$\mathbf{S}_2$	B	3.05	2.604	96.70	3.29	0.01	2.83
$\mathbf{S}_{2'}$	A	3.09	2.643	98.54	1.44	0.02	2.89

Table 8.4: Excitation energies (ΔE in eV), oscillator strengths (f), and composition contributions with singlet-singlet (ω^{SS}), charge transfer (ω^{CT}), and multiexcitonic (ω^{TT}) character in % of *spiro*-**DBP1** computed at the RAS-*sr*VWN level.

The lowest-lying excited state of the *spiro*-**DBP1** has an excitation energy (2.93 eV), very close to twice the lowest triplet in the monomer (2.92 eV). This transition has a multiexcitonic character, that can be assigned to a pair of triplets localized in each monomer and coupled as an overall singlet, as can be reflected in the large number of unpaired electrons ($N_u = 4.29$).

The ^{1}**TT** state exhibits a 96.97 % triplet-triplet character, but charge transfer also contributes to it, suggesting that there is a weak electronic interaction between both triplets. Indeed, following the triplet-triplet energy binding approximation:

$$E_b = E(^5\mathrm{TT}) - E(^1\mathrm{TT}) = -42 \text{ meV}, \tag{8.2}$$

results in a very small triplet-triplet interaction. At the RAS(8,8)-2SF/6-311+G(d,p) level, ^{1}**TT** is higher in energy than ^{5}**TT** (E_b is negative). Triplet-pair in this situation is named unbound biexciton and indicates that triplet separation will be exothermic.(13)

Since the electronically coupled triplet-pair state typically exhibits characteristic transitions in the excited state spectra,(14; 15) electronic transitions from ^{1}**TT**

in **DBP1** were characterized to further investigate the nature of the SF precursor (Table 8.5). Computed high-energy states and their transition dipole moments from the ^{1}**TT** state, indicate that excited state optically allowed transitions correspond to excitations to $^1\mathbf{T}_1\mathbf{T}_i$ associated to $T_1 \rightarrow T_i$ transitions in the **DBP1** monomer (Table 8.6), and hence predict the lack of additional transient absorptions other than those corresponding to triplet-triplet transitions. All these results point towards the formation of a spin coherent triplet-pair state with very small electronic coupling between the localized triplets. Such state has been labeled by Pensack and coworkers as $^1(\mathbf{T}\cdots\mathbf{T})$.(16)

State	Excitation energy (eV)	Oscillator strength	N_u
T_2	1.41	0.003	2.25
T_3	2.93	0.000	3.42
T_4	3.39	0.000	2.49
T_5	3.71	1.858	2.35

Table 8.5: **DBP1** transitions from T_1 to higher excited triplets computed at RAS-SF/6-31G** using an active space of 4 electrons into 4 π-orbitals.

State	Excitation energy (eV)	Transition dipole moment	N_u
$^1\mathbf{T}_1\mathbf{T}_2$	1.42	0.003	4.40
$^1\mathbf{T}_2\mathbf{T}_1$	1.44	0.001	4.25
$^1\mathbf{T}_2\mathbf{T}_2$	2.83	0.000	4.47
$^1\mathbf{T}_1\mathbf{T}_3$	2.94	0.000	5.43
$^1\mathbf{T}_3\mathbf{T}_1$	2.95	0.000	5.41
$^1\mathbf{T}_1\mathbf{T}_4$	3.40	0.000	5.04
S	3.65	0.052	3.31
$^1\mathbf{T}_1\mathbf{T}_5$	3.70	1.852	4.53
$^1\mathbf{T}_5\mathbf{T}_1$	3.73	1.231	4.51

Table 8.6: *spiro*-**DBP1** transitions from $^1\mathbf{T}_1\mathbf{T}_1$ to higher excited states computed at RAS-SF/6-31G** using an active space of 8 electrons into 8-π orbitals. **S** is a computed state that does not correspond to the TT character.

About 0.1 eV above ^{1}**TT** lie a pair of near-degenerate singlet dark states with A and B symmetries resulting from the coupling of two local S_1 (^1A_g) excitations on each moiety ($\mathbf{S}_1$ and $\mathbf{S}_{1'}$). Both states exhibit LE/CT mixings, especially the C_2-symmetric transition ($\mathbf{S}_{1'}$) for which charge separation configurations represent almost 10% of the transition. Similarly, the two linear combinations of the monomeric

bright state (S_2) on each **DBP1** moiety are very close in energy. Excitations to $\mathbf{S}_2$ and $\mathbf{S}_{2'}$ exhibit transition dipole moments perpendicular (B symmetry) and parallel (A symmetry) to the molecular rotational axis, in agreement with the dipole-dipole interaction model of Kasha.(17) The small energy gap between these states and ^{1}**TT** suggests that an efficient SF reaction might occur from $\mathbf{S}_1/\mathbf{S}_{1'}$ or $\mathbf{S}_2/\mathbf{S}_{2'}$.

At the same transition energies as the $\mathbf{S}_i$ excitonic states ($\sim$ 3 eV), two novel excitations appear that cannot be directly associated with any of the electronic transitions of the monomer. Decomposition of their electronic wave function characterizes them as symmetric combinations of CT configurations between the two DBP1 fragments, that is charge resonant states(18) ($\mathbf{CR}_1$ and $\mathbf{CR}_2$) belonging to the A and B representations of the molecular symmetry. Charge transfer or resonance states have been extensively studied as mediators in the SF process. In the case of not too high CT energies ($\sim$ 1 eV above $S_1/^1$TT), the charge separation configurations act as virtual states assisting the formation of the triplet-pair (super-exchange), leading to the commonly referred CT-mediated SF, which is the most commonly invoked SF mechanism.(19; 20; 21; 22; 23; 24) In *spiro*-**DBP1**, these states appear rather low in energy compared to CT energies computed for other SF materials, as in covalent dimers of pentacene.(25) The presence of such low-energy CR states can be rationalized by the $1/R$ dependence of the energy of separated charges and the rather short distance between **DBP1** fragments in the dimer, which is approximately 2.5 Å in *spiro*-**DBP1**, 3.7-3.8 Å in crystalline tetracene and pentacene and 3.1 Å in efficient SF tetracene covalent, dimers(26; 27) as measured by the shortest inter-monomer C-C distance. More importantly, in this case $\mathbf{CR}_1$ and $\mathbf{CR}_2$ are virtually isoenergetic to the lowest singlets, which could potentially facilitate the efficient formation of ^{1}**TT**. On the other hand, the existence of very low CT states could eventually provide a nonradiative decay channel back to the ground state, possibly through the formation of trap states,(28; 29; 30; 27) and hence being detrimental to SF.

8.1.2.2 Singlet fission mechanism

Results presented until this point suggest that, indeed, the spiro-dimers are promising candidates to carry out SF. On one hand, the selection of the chromophore with the optimum excited state distribution is necessary for an efficient process. In addition, the weak interaction between monomers in spiro-compounds does not importantly modify the electronic structure of the monomer, and additionally, the short distance between them makes the lower charge transfer/resonance states available to play a (significant) role in the SF mechanism.

The first step in the SF reaction is completed with the formation of the multiexcitonic state (Equation 7.1). Here, the presence of the large number of excited states

in a small range of energy allows all them to participate in the formation of $^1\mathbf{TT}$. The relative rates of formation from different electronic states ($r_{1,i}$) are evaluated by means of the kinetic model based on the transition state theory modification of the Fermi golden rule developed by Feng et al.(31)

$$r_{1,i}[\mathbf{S}_i/\mathbf{CR}_i \rightarrow {}^1\mathbf{TT}] \approx |V|^2 e^{-\alpha\Delta G_i/kT}, \tag{8.3}$$

where i is the first or second singlet excitonic state or charge resonance state, V is the nonadiabatic coupling between initial and final states, α is the free energy approach coefficient accounting for the magnitude of the activation energy, as suggested previously, $\alpha = 0.5$ is used, ΔG_i is the free energy difference between initial and final states, k is the Boltzmann constant, and T is the temperature.(31) This equation has been simplified by approximating the nonadiabatic coupling V (Equation 8.3) to the norm of the symmetrized one-particle transition density matrix indicated as γ(32) in Equation 8.4, and the ΔG_i by the electronic energy difference between states (ΔE_i).(13; 27; 31)

$$|V| \propto \frac{||\gamma_i||}{\Delta E_i}. \tag{8.4}$$

The transition between excitonic and CR states will be much faster than the formation of $^1\mathbf{TT}$. Therefore, we assume that after absorption the excited states population follows a Boltzmann distribution among $\mathbf{S}_{i'}$, $\mathbf{CR}_i$, and $\mathbf{S}_i$. Then, the overall rate of the first step in SF is approximated as the sum of the contributions from the set of rapidly populated states:

$$r_1 \approx \sum_i p_i r_{1,i}, \tag{8.5}$$

where p_i is the Boltzmann's factor of state i. In order to evaluate the importance of each transition to the final product ($^1\mathbf{TT}$), the factor f_i is defined as:

$$f_i \equiv p_i r_{1,i}. \tag{8.6}$$

The values for these parameters are reported in Table 8.7 resumes ts. As pointed out by the energy distribution of excited states, ΔE_i goes from 0.1 to $\sim$ 0.3 eV. At a given temperature (300 K here), the population of the lowest excited states is considerably larger than in higher states, as indicated by the Boltzmann's factors, suggesting the fast internal conversion to $\mathbf{CR}_i$ and later to $\mathbf{S}_1/\mathbf{S}_{1'}$ states after photoexcitation to the bright states. The strongest coupling ($||\gamma_i||^2$) is obtained between $\mathbf{CR}_i$ and the triplet-triplet pair. Actually, these states contribute to more than the 50% to r_1 despite they holding less than 4% of population. Nonadiabatic couplings of $\mathbf{S}_2$ and $\mathbf{S}_{2'}$ with $^1\mathbf{TT}$ are at least one order of magnitude smaller with respect to the CR/TT ones. This is in good agreement with previous studies reporting that the CR/TT coupling in SF materials is significantly stronger than the S_i/TT

interaction.(32) The two lowest excitonic states have more than 90% of the total electronic population. Nevertheless, $||\gamma_{S_1,{}^1TT}||^2$ and f_i of $\mathbf{S}_1$ are rather small. On the other hand, $\mathbf{S}_1$**'** contributes to the formation of ^{1}**TT** with close to 40%. This can be rationalized as a result of the contribution of the CT configurations ($\sim$ 10 %) to its wave function. Bright states play a marginal role in the SF mechanism, pointing up that the direct transition from S_2 to TT is not favorable in *spiro*-**DBP1**.

state	*Sym.*	ΔE_i	p_i	$\|\|\gamma_i\|\|^2$	f_i
$\mathbf{S}_1$	B	0.11	0.590	0.004	0.072
$\mathbf{S}_{1'}$	A	0.12	0.363	0.034	0.383
$\mathbf{CR}_1$	B	0.19	0.023	0.296	0.335
$\mathbf{CR}_2$	A	0.21	0.014	0.263	0.205
$\mathbf{S}_2$	B	0.22	0.008	0.026	0.003
$\mathbf{S}_{2'}$	A	0.26	0.002	0.016	0.003

Table 8.7: Electronic energy gap ΔE_i (in eV), Boltzmann's factor p_i (T = 300 K), squared norm of γ_i and contribution to r_1 (f_i) for the transition from excitonic and $\mathbf{CR}_i$ excitations to the triplet-pair state in *spiro*-**DBP1**.

These results highlight the crucial role of CT contributions in spiroconjugated dimers. SF in *spiro*-**DBP1** is predicted to occur mainly through the population of low-lying excited states with strong CR character ($\mathbf{CR}_i$) and through the lowest excitonic states with important mixing with CT configuration.

Interestingly, $\mathbf{S}_1$ and $\mathbf{S}_{1'}$ are dark states in which the main transition is HOMO^2 $\rightarrow$ LUMO^2, meaning that they are mostly the doubly ("D") excited state described in previous chapter. Energetically, the situation of the *spiro*-**DBP1** could be described by the couplings in Figure 7.7, but the relative orientation of the monomers in the dimer is different in each case, *i.e.*, (slip-)stacked in ethylene and orthogonal in *spiro*-**DBP1**.

The complete SF photophysical reaction requires the splitting of ^{1}**TT** into two independent triplets. The relative rate of this reaction can be evaluated via the binding energy (E_b) as:

$$r_2[^1\mathbf{TT} \rightarrow \mathbf{T}_1 + \mathbf{T}_1] \approx e^{-\alpha E_b/kT} \tag{8.7}$$

It is expected that the weak electronic interaction between the two triplets in ^{1}**TT**, given by the negative sign of E_b (-42 meV), results in $r_1 << r_2$. However, rates are computed taking account different approximations and comparison between them is not possible. Still, it is safe to conclude that the formation of the ^{1}**TT** will be the rate limiting step for the SF fission efficiency in *spiro*-**DBP1**, and probably

in general for spiroconjugated compounds with triplet and singlet energies suitable for singlet fission.

8.1.3 Vibronic couplings

Even with the rigidity of the dimeric scaffold provided by the spiro-atom, some vibrational modes can distort the ground state and favour a deactivation path different from SF or modify the mechanism in which it occurs. Actually, it has been shown that vibrational distortions can change the interaction between two moieties in spiroconjugated systems.(33) So far, the Franck-Condon geometry has been explored, suggesting the suitability of the *spiro*-**DPB1** to perform SF. This static picture does not consider the structural variation that can occur due to finite temperature effects or via the energy relaxation of the photoactivated system on the excited state PES. The former is related to low-frequency modes and corresponds to geometrical distortions within the kT energy range that can modify the relative orientation and, as a consequence, interaction between the two moieties. On the other hand, the structural rearrangement of excited molecules from the ground state geometry to the excited state minima might involve much larger energy changes, triggering the movement of high-frequency vibrations. This is the typical case in conjugated systems, for which $\pi \rightarrow \pi^*$ electron promotions couple to CC stretching modes in the order of 1400-1600 cm^{-1}.

In the following, the effect of low- and high-frequency vibrations in the SF capabilities of *spiro*-**DBP1** will be explored.

8.1.3.1 Low-energy vibrational modes

In order to investigate the impact of the thermal activation of the excited vibrational levels of low-frequency molecular modes, I explored the distortion along the five lowest-energy vibrational modes of *spiro*-**DBP1**. The aim is not to exhaustively analyze all vibrations; rather, I considered the five molecular modes $[Q_i(\Gamma),\ i = 1,5,\ \Gamma = A,B]$ with harmonic frequencies < 50 cm^{-1} (Figure 8.6), which mostly corresponds to symmetric (A) and antisymmetic (B) bending deformations between the two monomers modifying their relative disposition (dihedral angle).

To infer the potential role of these modes, I evaluated excited state energies and interstate couplings ($||\gamma||$) at the distorted geometries of the dimer following each $Q_i(\Gamma)$ deformation, implying an energy change of the order of kT ($T = 300$K). Overall, the relative energies of low-lying states of *spiro*-**DBP1** do not change very much with respect to the ground state distribution. The low-lying states remain within a rather small energy range (0.1-0.3 eV) for the five distortions with the ^{1}**TT**

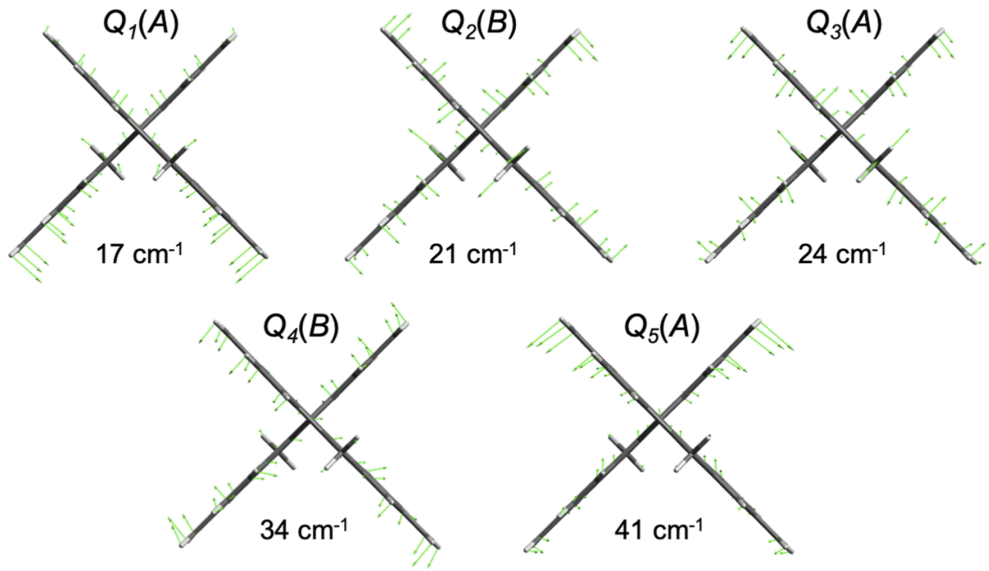

Figure 8.6: Lowest frequency modes of *spiro*-**DBP1** computed at the CAM-B3LYP level.

state systematically being the lowest excited singlet (Figure 8.7a). Additionally, the geometrical changes induce small modifications of the interstate couplings ($||\gamma||^2$ in Figure 8.7b). The only exception is the distortion along the $Q_3(A)$ mode, which exhibits reduced relative energies with respect to ^{1}**TT** and sizable modifications of the computed couplings.

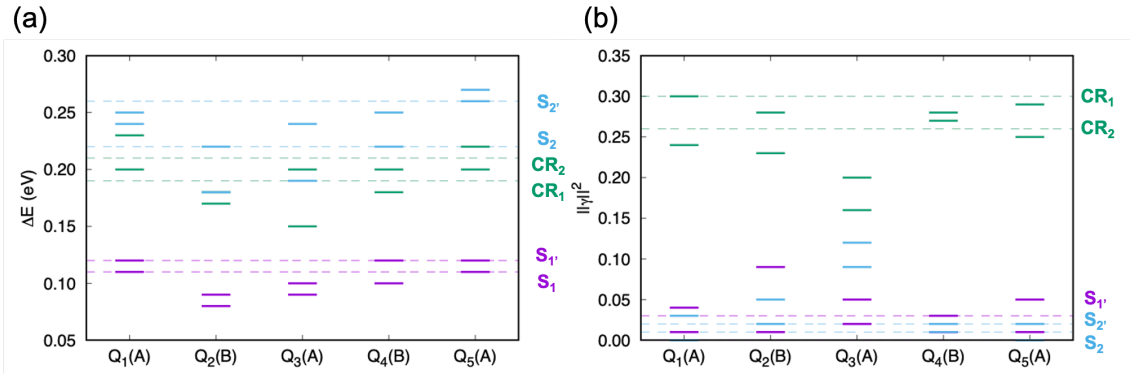

Figure 8.7: Excited state energy diagram (in eV) with respect to ^{1}**TT** (a) and $||\gamma||^2$ values to ^{1}**TT** (b) at the $Q_i(\Gamma)$-distorted structures of *spiro*-**DBP1** computed at the RAS(8,8)-*sr*VWN level. Dashed lines indicate the values at the Franck-Condon geometry.

These changes can be rationalized by means of the electronic composition of states in terms of diabatic contributions. The distorted geometry induced by the symmetric $Q_3(A)$ bending mode exhibits a quite different composition of the low-

state	$Sym.$	ΔE_i	p_i	$\|\|\gamma_i\|\|^2$	f_i
$\mathbf{S}_1$	B	0.09	0.512	0.021	0.211
$\mathbf{S}_{1'}$	A	0.10	0.410	0.055	0.442
$\mathbf{CR}_1$	B	0.15	0.054	0.198	0.245
$\mathbf{CR}_2$	A	0.20	0.009	0.165	0.064
$\mathbf{S}_2$	B	0.24	0.002	0.090	0.028
$\mathbf{S}_{2'}$	A	0.19	0.013	0.119	0.011

Table 8.8: Electronic energy gaps with respect to $^1\mathbf{TT}$ (ΔE_i, in eV), Boltzmann's factors p_i ($T = 300$ K), squared norms of γ_i, contributions to r_1 (f_i) for the transition from excitonic and $\mathbf{CR}_i$ excitations to the triplet-pair state for the $Q_3(A)$-distorted *spiro*-**DBP1** computed at the RAS(8,8)-*sr*VWN level.

lying states with increased degrees of CT configurations into the triplet-pair and excitonic states (Figure 8.8), which explains the increased $||\gamma||^2$ values between $^1\mathbf{TT}$ and excitonic states.

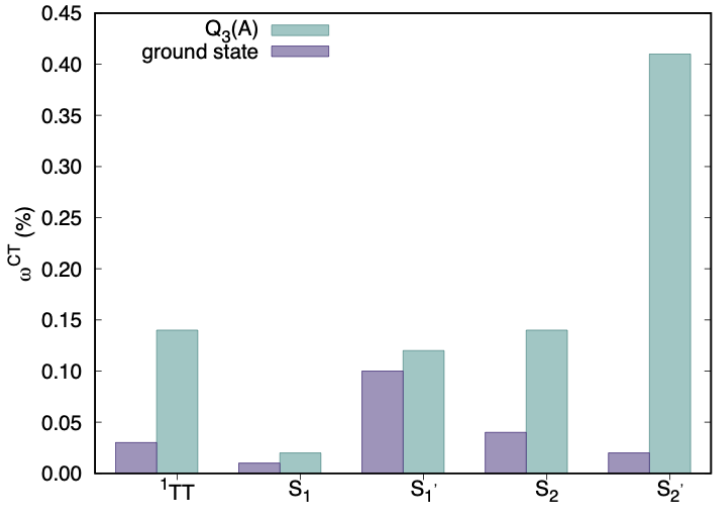

Figure 8.8: CT contributions ω^{CT} (in %) of low-lying states of *spiro*-**DBP1** at the ground state and $Q_3(A)$-distorted structures computed at the RAS-*sr*VWN level.

Changes in the interstate couplings might affect the SF mechanism. Indeed, the slight energy lowering of excitonic states with respect to $^1\mathbf{TT}$ and the increase of electronic couplings notably modify the weight of the different SF paths (Table 8.8), with the transition from $\mathbf{S}_{1'}$ becoming the main path toward the triplet-pair state and with a notably larger overall rate of formation, *i.e.*, $r_1(Q_3)/r_1(FC) = 1.54$ ($\sim 50\%$ increase).

The increase of the TT/CT mixing also modifies the triplet-triplet interaction

in ^{1}**TT**, stabilizing the spin-singlet coupling of the two triplets with respect to ^{5}**TT**. At the $Q3(A)$-distorted geometry, the two spin multiplicities become virtually degenerate ($\Delta E_b \sim 0$ meV), reducing the ground state exoergicity for the triplet-triplet decoupling.

Although these results do not predict major modifications of the photophysics of *spiro*-**DBP1** with temperature, the change in state population can help to improve the SF process and its efficiency.

8.1.3.2 High-energy vibrational modes

Now, the possible impact that high-energy structural distortions might have on the SF reaction in *spiro*-**DBP1** is considered. Here, I focus my attention on molecular vibrational modes involving stretching of carbon-carbon bonds (Figure 8.9). At 1359 and 1361 cm^{-1}, two modes corresponding to the symmetric and antisymmetric stretching of C-C single bonds in the quinoidal form of **DBP1** moieties ($Q_{s1}(\Gamma)$,$\Gamma = A, B$) can be indentified while symmetric/antisymmetric C=C stretchings ($Q_{s2}(\Gamma)$,$\Gamma = A, B$) appear at higher frequencies (1585 cm^{-1}).

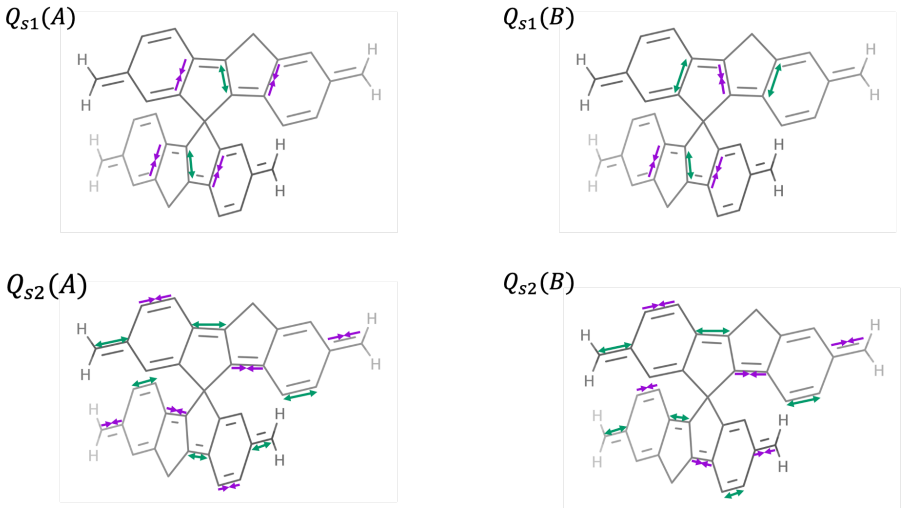

Figure 8.9: Symmetric (A) and antisymmetric (B) CC stretching vibrational modes of *spiro*-**DBP1**.

These vibrational modes allow *spiro*-**DBP1** to relax on the PES of the low-lying excited states. The symmetric $Q_{s1}(A)$ vibration towards the simultaneous shortening of the bonds shared by the two pentagons in each **DBP1** monomer (negative displacements in Figure 8.10a) stabilizes the singlet excited states, while in the opposite direction of $Q_{s1}(A)$ all low-lying singlets are strongly destabilized with respect to their Franck-Condon energies. These energy trends can be rationalized as the result of increasing and decreasing the π bonding and antibonding interac-

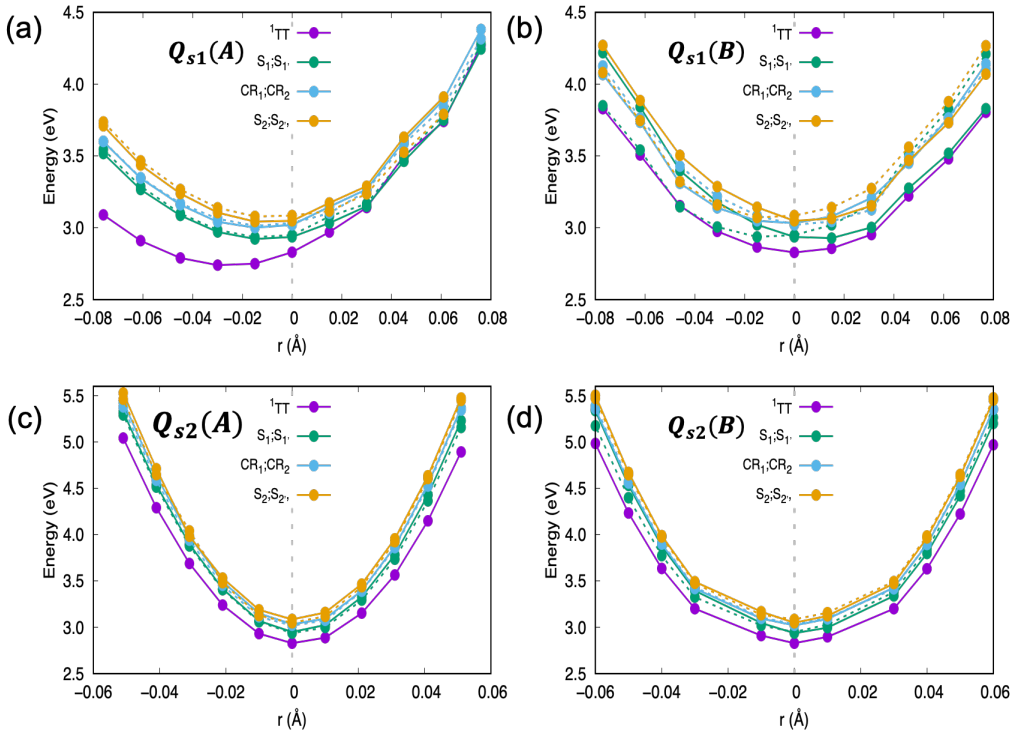

Figure 8.10: Excited state energy profiles (in eV) along the $Q_{s1}(A)$ (a), $Q_{s1}(B)$ (b), $Q_{s2}(A)$ (c), and $Q_{s2}(B)$ (d) stretching bonds in Figure 8.9 computed at the RAS(8,8)-*sr*VWN level.

tions in the frontier MOs, which can differently stabilize/destabilize the HOMO and LUMO of the monomers (Figure 8.3). Importantly, due to the simultaneous electron promotion to both monomeric LUMOs, energy stabilization upon $Q_{s1}(A)$ is more pronounced in ^{1}**TT** than for excitonic and CR states. This result is in line with the SF exothermicity increase observed in the excited state optimization of **DBP1** (Table 8.3). Moreover, the relative stability of ^{1}**TT** comes with a diminution of its CT character, which reduces from 3% at the Franck-Condon geometry to <0.5% for a 0.08 Å decrease in the central CC bond lengths. The $Q_{s1}(B)$ stretching breaks the C_2 symmetry of the dimer, generating inequivalent **DBP1** units. Both directions of the vibrational distortion stabilize (destabilize) the HOMO (LUMO) of one of the monomers, while destabilize (stabilize) the HOMO (LUMO) of the other **DBP1** fragment. As a result, ^{1}**TT** presents a rather flat and symmetric PES around the ground state geometry. On the other hand, excitonic states tend to localize on one of the two chromophores and CR contributions become unbalanced CT excitations with neat charge separation character (Figure 8.10b). Moreover, $Q_{s1}(B)$ distortion diminishes the energy gap between the lowest excitonic state and ^{1}TT, which might facilitate the formation of the triplet-pair.

Double bond stretchings in $Q_{s2}(\Gamma)$ systematically increase the energy of all low-lying singlets. Both symmetric, $Q_{s2}(A)$, and antisymmetric, $Q_{s2}(B)$, distortions

largely preserve the relative state energies (Figure 8.10c and d, respectively); hence, they are not expected to have a strong impact on the SF capabilities.

In summary, this investigation points out that spiroconjuged dimers are suitable materials to carry out SF. **DBP1** is a promising chromophore with the proper excited state distribution to make SF process efficient. The spiro linkage favors the presence of low-lying charge resonance states, which play a major role in the formation of the triplet-pair state. Overall, these results suggest that spiroconjugated dimers are potentially good candidates to efficiently generate independent triplet states through SF.

8.2 Spin orbit charge transfer - intersystem crossing in spiroconjugated dimers

Triplet excited states play an important role in excited states dynamics as they can provide a deactivation path. Differently from excited singlet states, triplets have long-lifetime and can reach longer diffusion lengths.(34; 35; 36) Excited triplet states have application in organic optoelectronic devices as OLEDs, photodynamic therapy, organic memory devices, sensors, among other electronic, magnetic and medical applications.(34; 37; 38) In addition, diradical character associated with the relative ΔE_{ST}, as has been exposed through these pages, entails interesting molecular properties for potential use in organic photovoltaics. Electronic transition from S_0 to T_1 is not spin allowed since there is a net change in the state multiplicity, *i.e.*, $\Delta S \neq 0$. Nevertheless, the population of the excited triplet states can be reached from the deactivation of higher singlet excited states through the radiativeless process of intersystem crossing (ISC).(39) ISC is the transition process between states of different multiplicities, from singlet to triplet, or triplet to singlet as it is the case in reverse-ISC. In principle, this transition is forbidden by spin symmetry selection rule, but the process is facilitated by the spin-orbit coupling (SOC) effect that mixes the angular orbital moment L with the spin S of the singlet and triplet states represented by the wave functions, Ψ_S and Ψ_T, as $\langle \Psi_S | \hat{S} \cdot \hat{L} | \Psi_T \rangle$. To enhance the SOC, it is important to have a small energy gap between both states. Also, large atomic numbers result in large orbital and spin magnetic moments, which favors the spin reorientation, *i.e.*, from β to α in order to obtain the triplet state. The dependence of the SOC strength with the atomic number is named "heavy atom effect" (HAE).(40; 41) Modifications to organic scaffolds have been made to include atoms able to provide HAE (P, S, Te, Se, P or transition metals) for studying ISC in organic molecules.(42; 43; 44; 40)

Another inducing ISC is through charge resonance process. To this end, donor-

aceptor moieties of a system must ideally be well separated, and the molecular overlap of both halves rather poor.(39) The spin-flip is facilitated since the orbital angular momentum tends to change during the electron migration in the CR process. As the SOC is enhanced by the CT states, this mechanism is called *spin-orbit charge transfer intersystem crossing* (SOCT-ISC, Figure 8.11).

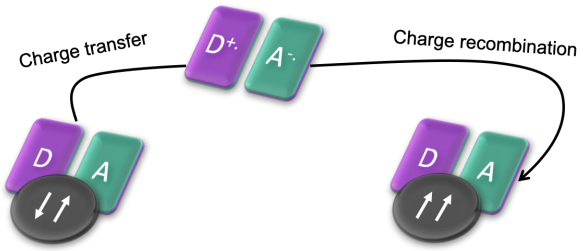

Figure 8.11: ISC process assisted by CT states in a donor-acceptor system. After its formation, the charges in the cationic/anionic monoradical pair are recombined promoting the spin-flip to form a triplet state. Figure adapted from reference(39).

Little is known about this mechanism, but some studies have provided the basis for enhancing its efficiency.(45; 46) A large dihedral angle between π-systems, orthogonal molecular orbitals, and of course a low energy CT state are desirable. All these requirements can be fulfilled owing to the spiro-linkage as exposed in the previous section. Actually, the reverse-ISC process has been studied in spiroconjugated systems recently.(47) Herein, I present the computational characterization of the SOCT-ISC mechanism in a family of spiroconjugated systems designed and experimentally studied by the group of Prof. Jinquan Chen from the East China Normal University. In the following I will discuss the theoretical aspects and results of this study. Complete experimental characterization of the photophysics of these spiro-conjugated dimers can be found in reference.(48)

Four 2,7-substituted benzophenone moieties are used as building blocks for the spirocompounds (**m0** - **3** in Figure 8.12a). All monomers are characterized having a singlet ground state with closed-shell structure. Computation of singlet and triplet excited states was performed with different methods (see the details in reference (48)). While T_1 in **m0** is a $\pi\pi^*$ transition, it has $n\pi^*$ character in **m1** and **m2**, and an intramonomer charge transfer (iCT) character ($\pi\pi*$) in **m3**, for which the $n\pi^*$ transition corresponds to T_2. On the other hand, the first excited singlet is a dipole forbidden transition with $n\pi^*$ character, and the bright state ($f > 0$) with $\pi\pi^*$ character is higher in energy. At the CAM-B3LYP level, the excitation energies are $T_1 \sim 3.3$ eV, $S_1 \sim 4.0$ for all the monomers, and bright state of **m0**, **m2** - **3** (S_2) is around 4.5 eV and 5.3 eV for **m1** (S_4). The relative energies between S_n and T_1 are quite small, which discards **m0** - **3** as potential singlet fission chromophores.

The permanent dipole moment in the ground state is modulated by the acceptor-

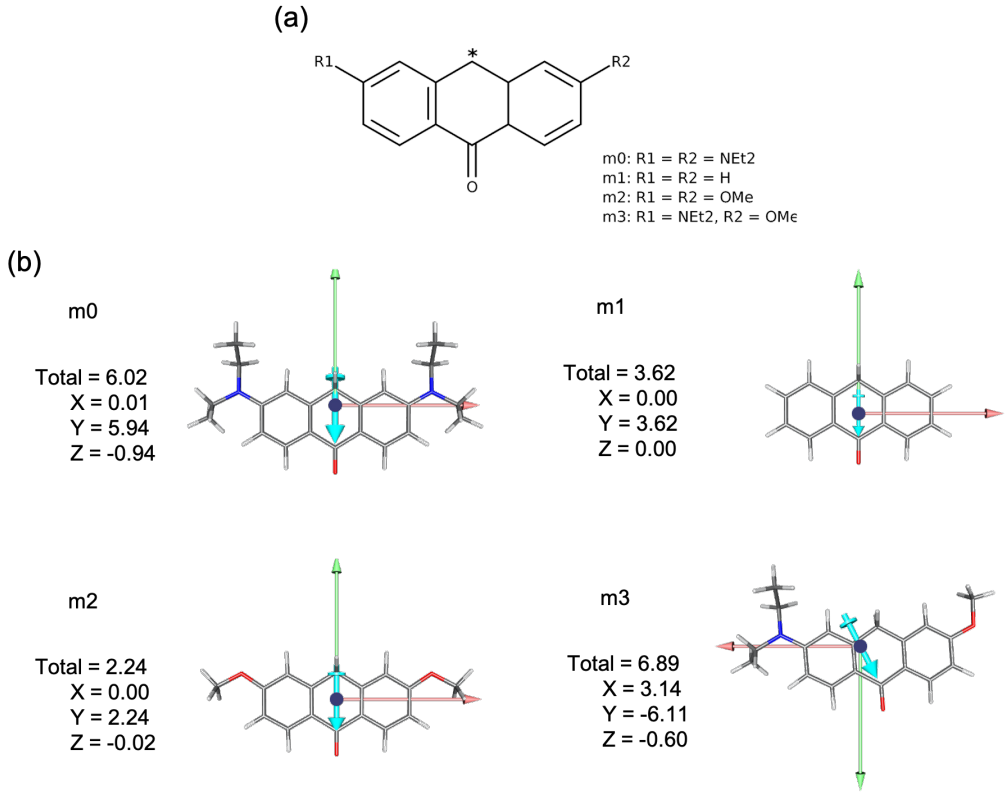

Figure 8.12: Structure of 2,7-substituted benzophenone (a) and permanent dipole moment (b) of **m0** - **3**.

donor character of the susbtituents, and is oriented along the short molecular axis pointing to the dione group with the exception of **m3**, where it is slightly tilted due to the molecular asymmetry 8.12b).

8.2.1 Spiro[bisanthracene]dione analogues

The three spiroconjugated dimers, **SF1** - **3**, respectively, were obtained by the combination of **m0** with **m1** - **3** (Figure 8.13). As expected from the spiro-linkage, monomers are oriented perpendicularly to each other.

Frontier molecular orbitals of **SF1** - **3** can be correlated to molecular orbitals of the monomers. HOMO and LUMO orbitals of the dimer are localized on one constituting monomer; more specifically, while the HOMO is over the **m0** moiety, the LUMO is over **m1-3** (Figure 8.14 a). The total dipole moment is given by the vector summation of the dipole moment of both monomers, towards the dione group of **m0** (Figure 8.14b).

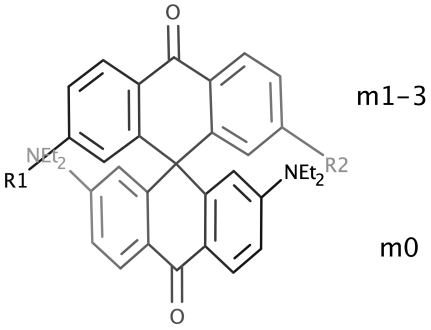

Figure 8.13: Structure of 2,7-substituted benzophenone. Bottom part is **m0**, combined with **m1-3** monomers to produce **SF1-3**. Figure adapted from reference(48).

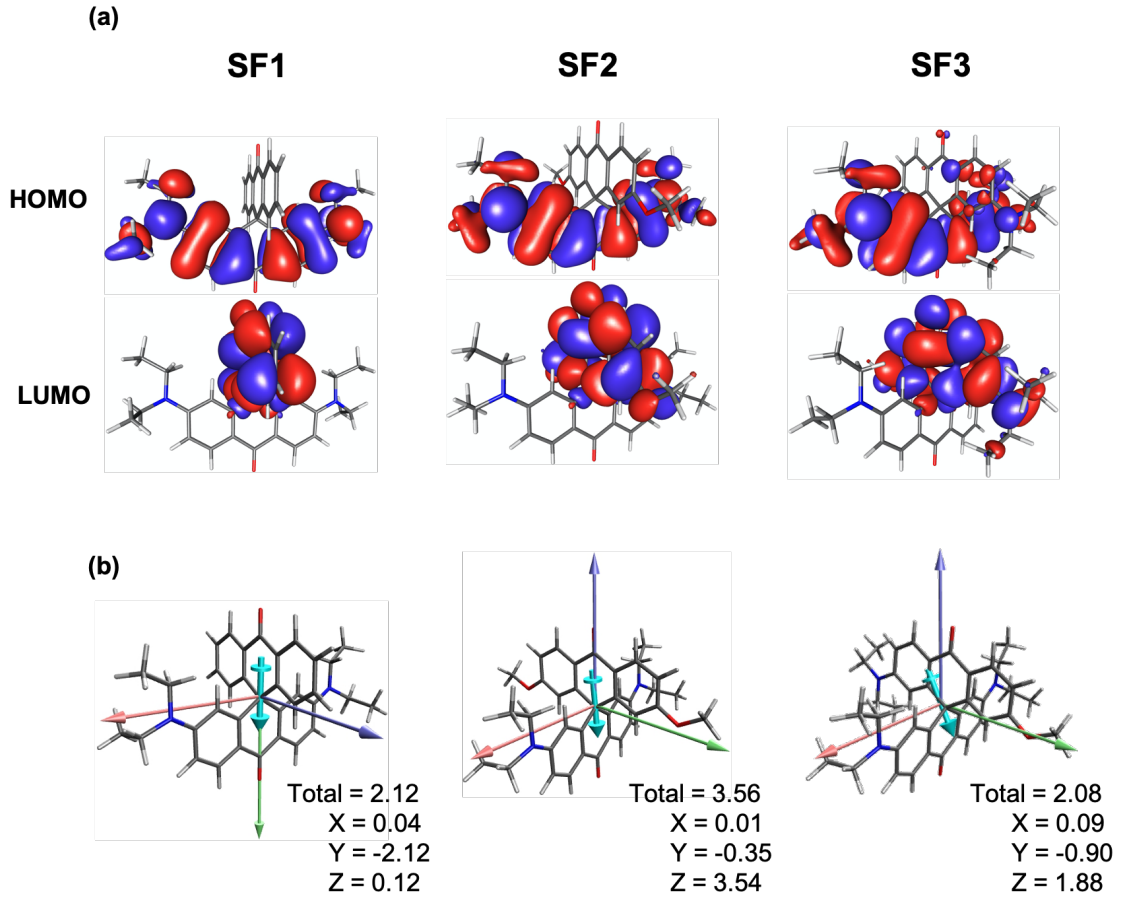

Figure 8.14: HOMO and LUMO orbitals (a) and permanent dipole moment in Debye (b) of **SF1-3**. Figure adapted from reference(48).

8.2.2 Photophysics of Spiro[bisanthracene]dione

Experimentally, the variation of the solvent polarity, from the non-polar cyclohexane to the polar acetonitrile going through the 2-methyltetrahydrofuran, shifts pro-

portionally the main absorption band of the **SFn** to lower energies (Figure 2 of reference(48)). The absorption spectra of spirocompounds were simulated in gas phase (Figure 8.15), reproducing nicely the experimental observations.

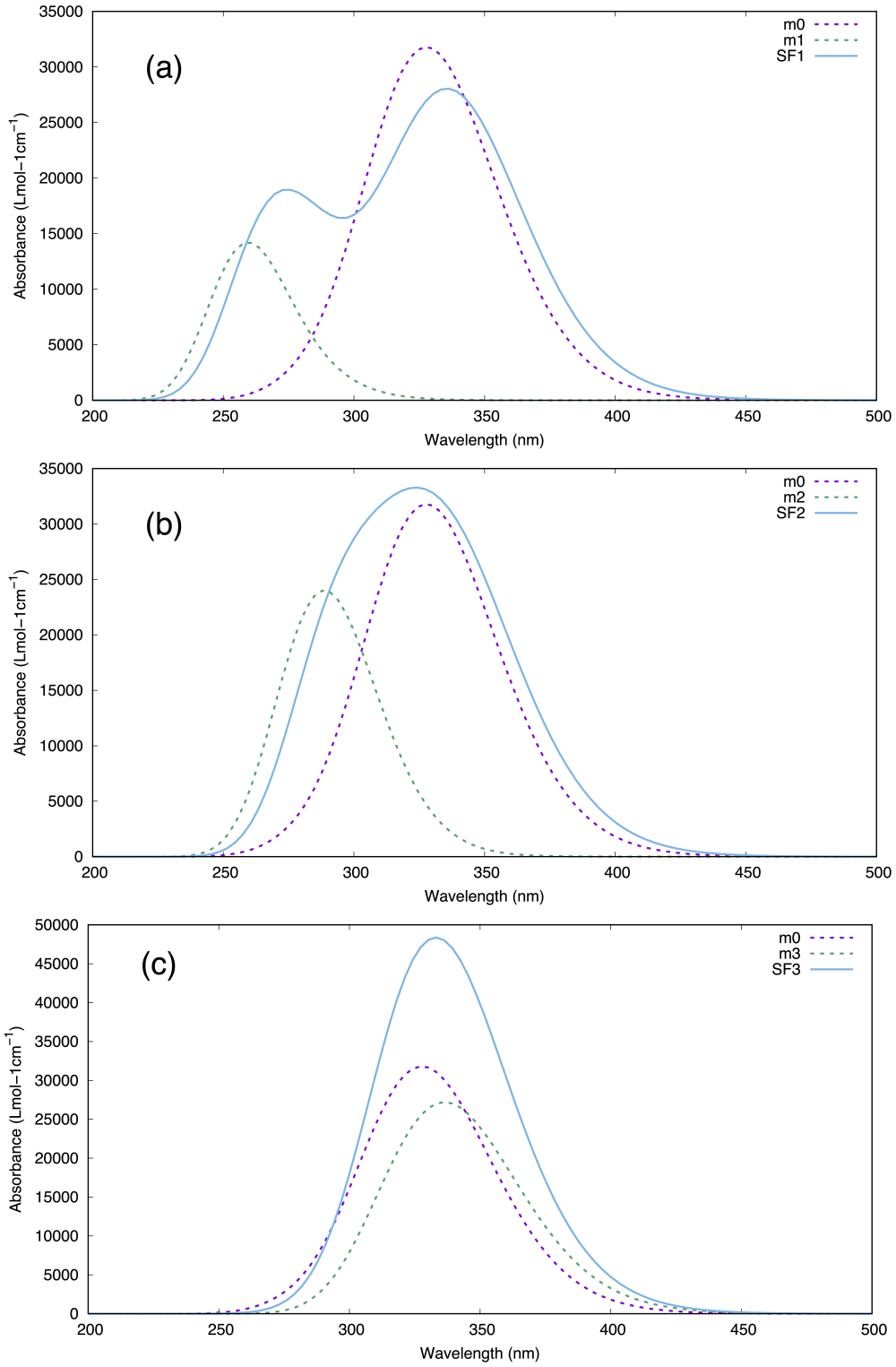

Figure 8.15: Simulated UV-VIS spectra of **SF1-3** (a-c) with the contributions of excitations of each monomer. Figure adapted from reference(48).

Calculations showed a large number of triplet excitations (5 at least, as illustrated in Table 8.9) lying energetically below the excited singlets. Both, low-lying triplets and singlets correspond to $\pi\pi^*$ and nπ^* transitions for all systems, while an iCT appears for **SF3**, directly related to the iCT state in **m3**. T_1 is characterized as a $\pi\pi^*$ transition (since iCT in **m3** is a $\pi\pi^*$ state) and has an excitation energy of $\sim$ 3.2 eV. The bright singlet is computed around 4.2 eV and also possesses a $\pi\pi^*$ character. The most intense band corresponds to the optical transition of the monomer **m0** (4.48 eV), while the local excitations in **m1 - 3** are higher in energy and weaker in intensity. As in the *spiro*-**DBP1** homodimer, the properties of the monomer are conserved and the small redshift from **m0** to **SFn** can be rationalizated as the weak interaction between monomers in the spiro-compound. Optically active and dark states can be analysed in terms of the contribution of the monomeric excitations. Interestingly, all states computed in the energy range of the bright state (S^*, *i.e.*, S_4 of **SF1** and S_3 of **SF2** and **SF3**) have small contributions, and less than 1 eV above the S^* lies a state with $\sim$ 90% charge transfer character from **m0** to **m1-3** (transitions from **m1-3** to **m0** are energetically higher).

State	ΔE	f	Character	Transition	Composition (%)
SF1					
T_1	3.28	-	LE/CT	m0($\pi\pi^*$)/m0 $\rightarrow$ m1	76.9/7.9
T_2	3.30	-	LE/CT	m0($\pi\pi^*$)/m0 $\rightarrow$ m1	74.7/17.3
T_3	3.38	-	LE/CT	m1(nπ^*)/m0 $\rightarrow$ m1	89.1/5.6
T_4	3.57	-	LE/CT	m0(nπ^*)/m1 $\rightarrow$ m0	76.6/10.7
T_5	3.66	-	LE/CT	m0($\pi\pi^*$)/m1 $\rightarrow$ m0	65.6/11.7
S_1	3.86	0.000	LE/CT	m1(nπ^*)/m0 $\rightarrow$ m1	85.0/6.4
S_2	4.03	0.000	LE/CT	m0(nπ^*)/m1 $\rightarrow$ m0	79.0/10.5
S_3	4.14	0.001	CT	m0 $\rightarrow$ m1	97.5
S_4	4.24	0.864	LE	m0 ($\pi\pi^*$)	91.0
S_5	4.46	0.000	CT	m0 $\rightarrow$ m1	97.9
SF2					
T_1	3.29	-	LE/CT	m0($\pi\pi^*$)/m0 $\rightarrow$ m2	82.3/4.8
T_2	3.31	-	LE/CT	m0($\pi\pi^*$)/m0 $\rightarrow$ m2	82.1/7.6
T_3	3.51	-	LE/CT	m2($\pi\pi^*$)/m0 $\rightarrow$ m2	69.5/5.1
T_4	3.52	-	LE/CT	m2(nπ^*)/m0 $\rightarrow$ m2	87.6/7.4
T_5	3.56	-	LE/CT	m2($\pi\pi^*$)/m0 $\rightarrow$ m0	70.2/5.9
S_1	3.99	0.000	LE/CT	m2(nπ^*)/m0 $\rightarrow$ m2	88.2/8.2
S_2	4.03	0.000	LE/CT	m0($\pi\pi^*$)/m0 $\rightarrow$ m2	82.1/7.2

Continued on next page

State	ΔE	f	Character	Transition	Composition (%)
S_3	4.26	0.848	LE	m0($\pi\pi^*$)	91.0
S_4	4.42	0.020	CT	m0 $\rightarrow$ m2	94.5
S_5	4.70	0.316	LE/CT/LE	m2($\pi\pi^*$)/m0 $\rightarrow$ m2/m0($\pi\pi^*$)	46.1/19.4/12.8
SF3					
T_1	3.21	-	iCT/CT	m3($\pi\pi^*$)/m0 $\rightarrow$ m3	68.9/5.0
T_2	3.28	-	LE/CT	m0($\pi\pi^*$)/m0 $\rightarrow$ m3	74.9/4.5
T_3	3.31	-	LE/CT	m0($\pi\pi^*$)/m0 $\rightarrow$ m3	75.1/14.2
T_4	3.56	-	LE/CT	m3(nπ^*)/m0(n) $\rightarrow$ m3(π^*)	66.8/20.0
T_5	3.58	-	LE/CT	m0(nπ^*)/m3(n) $\rightarrow$ m0(π^*)	70.4/15.0
S_1	4.02	0.000	LE/CT	m3(nπ^*)/m0(n) $\rightarrow$ m3(π^*)	77.2/14.3
S_2	4.04	0.000	LE/CT	m0(nπ^*)/m3 $\rightarrow$ m0	72.3/14.8
S_3	4.24	0.845	LE	m0($\pi\pi^*$)	88.7
S_4	4.33	0.677	iCT/CT	m3($\pi\pi^*$)/m0 $\rightarrow$ m3	70.7/14.6
S_5	4.62	0.030	CT/iCT	m0 $\rightarrow$ m3/m3(iCT)	76.4/16.1

Table 8.9 Vertical excitation energies (in eV), oscillator strengths (f), excited character, transitions and orbital composition to the low-lying excited states of **SF1-3** computed at the ground state geometry. Character of the transition has been indicated in % for the main orbital contributions.

Large differences are observed in the emission spectra with the change of the polarity of the solvent. A main band at about 400 nm is identified for all **SFn** as the radiative decay from the S* state. A new band appears at lower energy ($>$ 500 nm), which broadens with the increase of in solvent polarity. This new broad emission feature is associated to the stabilization of interchromophore charge transfer. In the emission spectrum of each **SFn**, the optical features of each monomer can be distinguished. The most intense band corresponds to the energy de-excitation of the $\pi\pi^*$ state of **m0**, while in the CT minimum this state is strongly stabilized, actually being the lowest excited state. Fluorescence from the CT state is then allowed by Kasha's rule. For instance, at the CT minimum, the geometry of **SF1** is distorted and the CT character is maximized up to 96 % of **m0** $\rightarrow$ **m1**. Notice that, due to the lack of molecular symmetry, CT states are not degenerate. The role of **m0** as a donor stabilizes the charge separation, then E(**m0** $\rightarrow$ **m1-3**) $<$ E(**m1-3** $\rightarrow$ **m0**). The stabilization of CT states is modulated by the substituents, in **SF2** and **SF3**. MeO and Net_2 are electron donating groups, that reduce the charge transfer between both halves compared with **SF1**, as reflected by the high mixing with $\pi\pi^*$

configurations in the minimum of CT PES (Table 8.10).

State	ΔE	f	character	%
SF1	3.23	0.004	m0 $\rightarrow$ m1	96.1
SF2	3.44	0.000	m2(nπ^*)/m0 $\rightarrow$ m2	70.9/22.6
SF3	3.47	0.000	m3(nπ^*)/m0 $\rightarrow$ m3	83.7/9.6

Table 8.10: Vertical de-excitation energy (in eV), oscillator strength (f), and state character from the energy minimum of the lowest CT state of **SF1-3** computed at the CT state geometry.

8.2.3 Spin-orbit coupling

8.2.3.1 A brief experimental background

The fast generation of long-life triplets (9.22, 3.84 and 4.04 μs in **SF1-3**, respectively) has been detected experimentally by femtosecond transient absorption. In cyclohexane a long-lived excited-state absorption (ESA) signal is observed for **SF1-3**, which decays in about 200 ns in **SF1**; similar results are obtained in **SF2** and **SF3**. This signal is associated with the formation of a $\pi\pi^*$ triplet. With the increase in polarity of the solvent (up to DMSO), the ESA band associated with the triplet gradually disappears and only remains present in **SF3** (about 4 ns after excitation). A ground-state bleach signal is observed before the signal of triplet formation, indicating the presence of another state that acts as an intermediate in the triplet generation. According to the computational characterization presented in Table 8.9, the excited states that are energetically accessible from S* have important contributions of CT configurations. Figure 8.16 illustrates the excited state dynamics suggested **SF3** by experimental observations and computational predictions. After the population of the $\pi\pi^*$ bright state, the CT state is formed and generates the triplet state by charge recombination.

In summary, a fast conversion from singlet to triplet that depends on the stabilization of CT states by the solvent is detected experimentally. The ISC rate constant (k_{ISC}) can be approximated by the Marcus form of the Fermi's golden rule:

$$k_{ISC} = \frac{2\pi}{h} < \Psi^0_{CT}|H_{SO}|\Psi^0_T >^2 (4\pi\lambda RT)^{-\frac{1}{2}} \times e^{\frac{(\Delta E+\lambda)^2}{4\lambda RT}}, \tag{8.8}$$

where H_{SO} is the spin-orbit Hamiltonian, λ is the reorganization energy, and ΔE is the splitting between CT and triplet state.

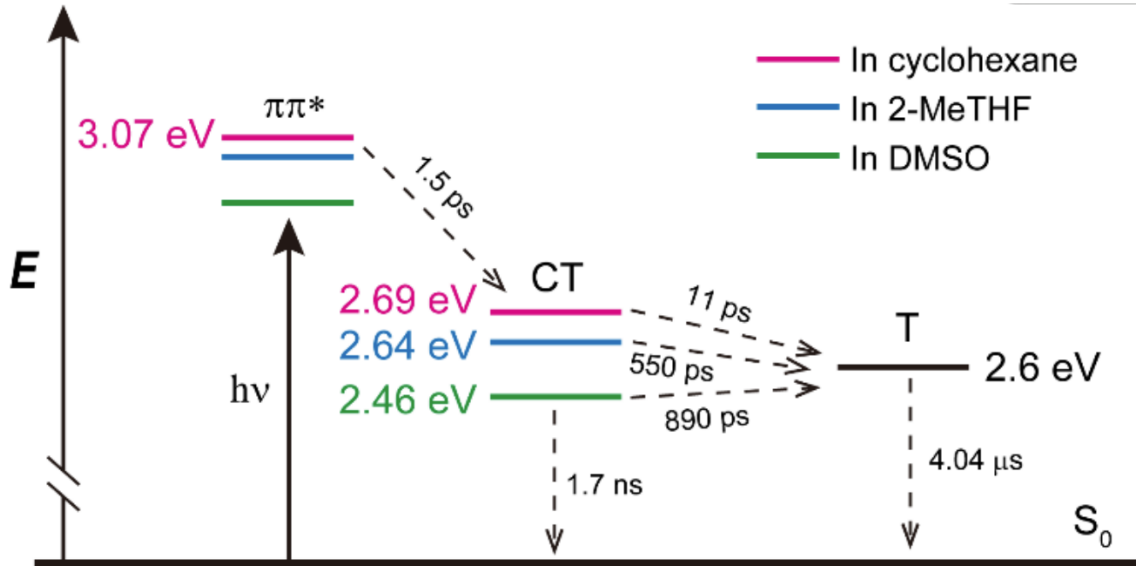

Figure 8.16: Simplified Jablonski diagram of the photophysical processes involved in the excited state dynamics of **SF3**. Figure taken from reference(48).

To describe the generation of triplets via CT states, the spin-orbit coupling between them was computed at the equilibrium structure of the CT state.

Table 8.11 shows that, at this geometry, there are several triplets close in energy with $< CT|H_{SO}|T_n > \neq 0$. Large H_{SO} couplings are found with triplets that have large mix of configuration with CT states. The family of spiro-compounds investigated here are characterized by their tunable SOCT-ISC as a function of the solvent polarity. In non-polar environments, the CT state assist the SOCT-ISC, providing rate constants that can vary by 2 orders of magnitude according to the electron withdrawing or donating character of the substituent group. In polar solvents, the CT state is stabilized and can act as a trap state favoring other deactivation pathways than the triplet formation.

State	ΔE	SOC	Character	%
SF1				
T_1	-0.16	1.00	m1($n\pi^*$)/m0 → m1	72.3/9.3
T_2	-0.12	1.62	m0($\pi\pi^*$)/m0 → m1	70.6/10.2
T_3	-0.06	0.77	m0 → m1/m1($n\pi^*$)	73.3/15.0
T_4	0.06	0.18	m0($\pi\pi^*$)/m0 → m1	68.5/5.1
T_5	0.09	0.40	m1($\pi\pi^*$)/m0 → m1/m1($n\pi^*$)	70.4/4.6
SF2				

Continued on next page

State	ΔE	SOC	Character	%
T_1	-0.47	0.89	m2($n\pi^*$)/m2 $\rightarrow$ m0	69.7/21.7
T_2	-0.43	58.06	m2 $\rightarrow$ m0	78.7
T_3	-0.15	0.12	m0($\pi\pi^*$)/m0 $\rightarrow$ m2	75.8/4.7
T_4	-0.13	0.69	m0($\pi\pi^*$)/m0 $\rightarrow$ m2	74.0/7.7
T_5	-0.08	1.96	m2($\pi\pi^*$)/m2 $\rightarrow$ m0	76.0/5.4
T_6	0.13	0.02	m0($n\pi^*$)/m2 $\rightarrow$ m0	87.5/6.4
SF3				
T_1	-0.61	49.70	m3(iCT)/m0 $\rightarrow$ m3	75.3/5.9
T_2	-0.47	2.13	m3($n\pi^*$)/m0 $\rightarrow$ m3	81.5/9.6
T_3	-0.20	27.25	m3(iCT)	76.6
T_4	-0.20	0.69	m0($\pi\pi^*$)/m3 $\rightarrow$ m0	74.3/4.6
T_5	-0.17	1.61	m0($\pi\pi^*$)/m3(iCT)/m3($n\pi^*$)/m3 $\rightarrow$ m0	68.8/7.4
T_6	0.10	0.01	m0($n\pi^*$)/m3 $\rightarrow$ m0	74.0/15.3

Table 8.11 Relative energies (in eV) and spin-orbit couplings (in cm^{-1}) between the lowest CT singlet and low-lying triplet states of **SF1-3** computed at the CT state geometry. Character of the transition has been indicated in % for the main orbital contributions.

These results highlight the main role of the low energy CT states assisting and promoting the fast S $\rightarrow$ T conversion.

8.3 Spiroconjugation of a diradicaloid-pair

As exposed in the first section of this Chapter, *spiro*-**DBP1** has suitable electronic features to carry out efficient SF. A good excited state distribution in the monomers is predicted, with a small and positive $E(S^*) - 2E(T_1)$ value. On the other hand, **Fn** and **DBP2** chromophores can be regarded as diradicaloids (see Table 8.1), meaning that the energy of T_1 is considerably low with respect to S^* excitation energy, and the singlet fission process is not favored. Interestingly, the tetra-phenyl substituted **DBP2** has been synthesized and theoretically and experimentally characterized,(12) whit a reported value of ΔE_{ST} = 5.68 kcal/mol at B3LYP/6-31G(d,p), that is in good agreement with our calculations (8.07 kcal/mol). In the same study, an extended version of **DBP2** (Figure 8.17c) was shown to hold a strong diradical character (ΔE_{ST} = 2.12 kcal/mol, determined by SQUID measurements, and 1.83 kcal/mol at B3LYP/6-31G(d,p) level). Recently, the experimental group of Professor Eiichi Nakamura from The University of Tokyo achieved the synthesis of *spiro*-**DBP2**,(49)

while the group of the University of Malaga lead by Prof. Juan Casado characterized its spectroscopic features. My contribution to this collaboration consists in the description and rationalization of the electronic structure of this compounds.

Through this chapter, it has been suggested that the main role of the spiro linkage is structural, allowing both halves to be together in a rigid conformation with weak interaction as a consequence of the orthogonality of the π-backbones, which also results in a low-lying pair of charge transfer states. This signifies, that the final properties of the spiro system are largely dictated by the electronic structure of the "independent" monomers. Hence, is it reasonable to envisage the *spiro*-**DBP2** as a pair of independent diradicaloids? Or that the diradicaloid character of **DBP2** can lead to an interaction between both fragments to form a tetraradicaloid?

Here, I will present the theoretical and computational investigation of the electronic structure of *spiro*-**DBP2**. For the sake of comparison, the pro-spiro, spiro and an extended monomer were analyzed at the same level of theory (see the Appendix). In order to differentiate between **DBP2** and *spiro*-**DBP2**, hydrogen atoms in the pro-spiro position where replaced by phenyl groups. In the following, the pro-spiro chromophore will be named *ph***DBP2**, its extended version, based on bis(dibenzo)pentalene (*ph***BDP2**), **ex***ph***DBP2**, and the spiro dimer spiro-*ph***DBP2** (Figure 8.17).

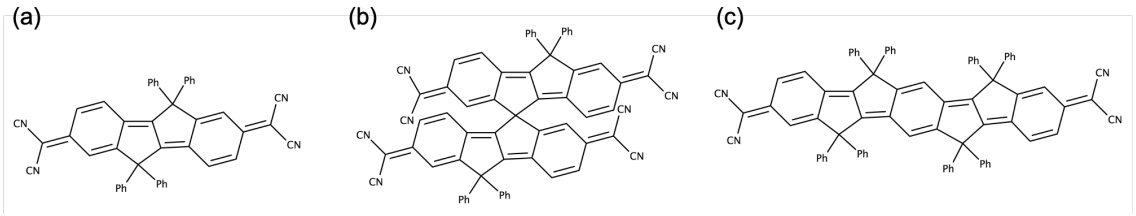

Figure 8.17: Structure of *ph***DBP2** (a), the spiro dimer *spiro-ph***DBP2** (b), and **ex***ph***BDBP2** (c).

At the DFT level of theory all of them hold a singlet open-shell ground state. The closed-shell singlet is higher in energy, with open-shell to closed-shell gaps following the *ph***DBP2** < *spiro-ph***DBP2** < **ex***ph***BDBP2** tendency. Adiabatic energy gaps computed with the B3LYP functional in kcal/mol, are 5.79 and 1.78 for *ph***DBP2** and **ex***ph***DBP2**, respectively, and 3.48 kcal/mol and 0.78 kcal/mol are obtained with ωB97X-D, respectively. There is a noticeable drop of ΔE_{ST}^{ad}, *i.e.*, a substantially growth of diradical character, from *ph***DBP2** to *ph***BDBP2**. This can be explained by the decreased interaction between radicals on the molecular ends through the π-conjugated system due to the larger molecular size. Interestingly, the adiabatic quintet state of *spiro-ph***DBP2** is computed at 10.9 (6.69 kcal/mol with ωB97X-D) kcal/mol above the ground state open-shell singlet. This result

indirectly indicates the presence of two triplets, one in each *ph***DBP2** unit of the spiro-compound. Further characterization of the radical nature of these compounds is presented in Table 8.12.

Geometry	Compound	state	ΔE	N_u	y_0	y_1
B3LYP	*ph***DBP2**	S_0	-	0.94	0.40	0.06
		T_1	10.10	2.10	1.00	0.04
	*spiro-ph***DBP2**	S_0	-	2.02	0.44	0.43
		T_1	9.11	3.10	0.98	0.46
		T_2	9.16	3.11	0.97	0.46
		Q_1	18.36	4.19	1.00	1.00
	ex*ph***DBP2**	S_0	-	1.68	0.80	0.04
		T_1	0.58	2.08	1.00	0.03
ωB97X-D	*ph***DBP2**	S_0	-	1.13	0.51	0.05
		T_1	6.66	2.08	1.00	0.03
	*spiro-ph***DBP2**	S_0	-	2.39	0.54	0.53
		T_1	6.02	3.29	0.90	0.64
		T_2	6.09	3.29	0.90	0.64
		Q_1	12.15	4.17	1.00	1.00
	ex*ph***DBP2**	S_0	-	1.75	0.84	0.03
		T_1	0.21	2.06	1.00	0.02

Table 8.12: Low-lying state relative energies (ΔE in kcal/mol), number of unpaired electrons (N_u), and diradical (y_0) and tetraradical (y_1) indices of *ph***DBP2**, *spiro-ph***DBP2** and **ex***ph***DBP2** computed at the RAS-SF/6-31G(d,p) level for the ground state geometry optimized at B3LYP and ωB97X-D functionals.

The following discussion will be done using the results obtained with the B3LYP optimized geometry, but it is worth noting that conclusions are qualitatively the same with geometries obtained with ωB97X-D. Large N_u values of S_0 of the three compounds reaffirm their open-shell character. As mentioned before, *ph***DBP2** is a moderate diradicaloid, with $y_0 = 0.40$. After construction of *spiro-ph***DBP2**, two vertical triplets, T_1 and T_2, are calculated close to the energy of the T_1 of *ph***DBP2**; these states are the $\pm$ linear combinations of the configurations that localize the triplet in one or another *ph***DBP2** unit. Additionally, the Q_1 state is $\sim 2T_1$ of *ph***DBP2**. This small energy difference can be associated with the diradical-diradical interaction through the spiro-connection (as discussed in Figure 8.5 and Equation 7.18). This result points towards the rise of a system with ~ 4 unpaired electrons, *i.e.*, a tetraradical.

On the other hand, the ground state of *spiro-ph***DBP2** holds 2.02 unpaired

electrons, that are approximately twice the monomer value. Moreover, while they both exhibit a similar y_0 value (about 0.4), *spiro-ph***DBP2** has a $y_1 = 0.43$), meaning that it should be named tetraradicaloid instead of diradicaloid. **ex***ph***DBP2** S_0 and T_1 states are almost degenerate with an energy gap smaller than 1 kcal/mol, and a diradical index y_0 larger than 0.8. Clearly, **ex***ph***DBP2** holds the strongest diradical character, while *spiro-ph***DBP2** is the only tetraradicaloid of the series.

The radical character of *spiro-ph***DBP2** was determined through experiments of molar magnetic susceptibility ($\chi_M T - T$). Three main signals are characterized as one singlet, triplet, and quintet that can be assigned to the S_0 (ground state), $T_{1,2}$, and Q_1 in Table 8.12, respectively. A small amount of an impurity with diradical character is also detected ($\Delta E_{ST} = 0.09$ kcal/mol). The impurity is predicted to be produced by the strong interaction between two spiro-compounds when they are close to each other. Due to steric hindrance, the π-π stacking between two monomeric backbones is not possible. However, radicals localized at the molecular ends can interact covalently to form a σ-bond, (Figure 8.18a).

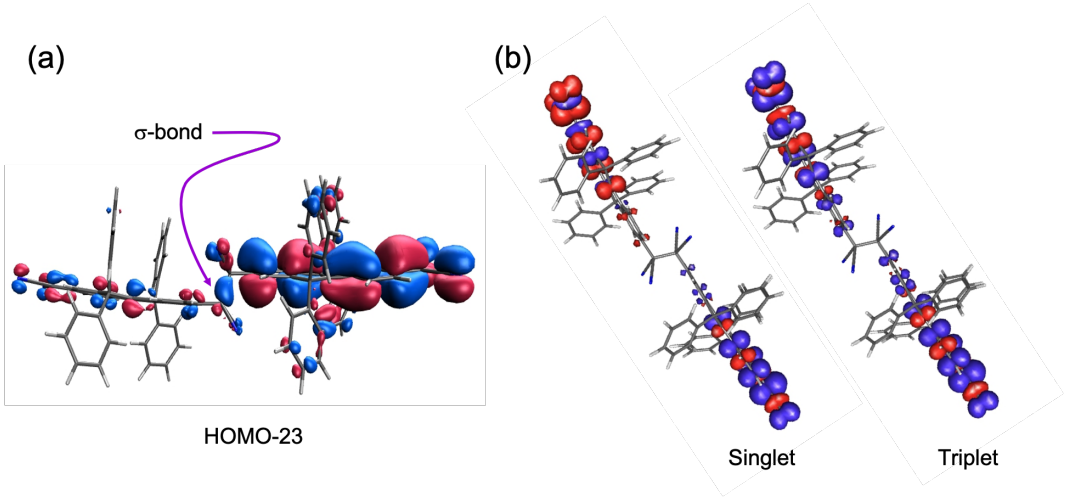

Figure 8.18: σ-bonding orbital (HOMO-23) (a) and spin density representation of the lower singlet and triplet (b) of the σ-dimer at the ωB97X-D/6-31G(d).

This situation was evaluated in a σ-bonded dimer of *ph***DBP2**. The computed electronic binding energy between two monomers is $\sim$ 25.3 kcal/mol. Two unpaired electrons are localized one at each extreme of the σ-dimer (Figure 8.18b shows the spin density of lowest singlet and triplet states). Due to the large distance between both radicals, their interaction fades away and the singlet-triplet energy gap tends to zero ($\Delta E_{ST} < 0.03$ kcal/mol), in good agreement with the aforementioned singlet-triplet energy gap experimentally determined (0.09 kcal/mol).

8.4 Appendix

8.4.1 Computational details

Molecular structures have been optimized within the density functional theory (DFT) in conjunction with the CAM-B3LYP(50) energy functional.

The ground state diradical character (y_0) has been quantified as the occupation number of the lowest unoccupied natural orbital (LUNO).(51) The number of unpaired electrons of electronic states has been evaluated according to the linear Head-Gordon index (N_u).(52)

All calculations were performed with the Q-Chem program.(53) Molecular orbitals (MOs), RAS-*sr*VWN natural orbitals (NOs) and FODs(54; 55) have been plotted with a homemade version of Avogadro (Version 1.2).(56)

8.4.1.1 Spiroconjugated dimers in singlet fission

Optimized geometries were confirmed to be minima on the ground state potential energy surface (PES) by means of frequency analysis within the harmonic approximation. Raw frequencies are 17.68, 22.21, 24.86, 35.70, 42.42 cm^{-1}.

Excited states have been computed employing the restricted active space configuration interaction method with the *hole* and *particle* approximation and the spin-flip excitation operator (RAS-SF),(57; 58) and with the inclusion of short-range DFT correlation through a range-separation scheme (RAS-*sr*DFT).(59) Short-range exchange and correlation effects have been taken into account with the short-range version of the Slater-Dirac and Vosko-Wilk-Nussair(60) functionals, respectively (61) and here is named RAS-*sr*VWN. The lowest restricted open-shell Hartree-Fock (ROHF) high-spin triplet (quintet) state is used as the reference configuration for all RAS-*sr*VWN calculations of the studied monomers (spiro dimers) with 4 (8) electrons into 4 (8) π-orbitals in the RAS II space. RAS I and RAS III subspaces include all virtual and doubly occupied orbitals, respectively.

Characterization of electronic excited states of spiroconjugated compounds in terms of local excitations (LE), charge transfer (CT) or resonance (CR), and triplet-triplet configurations (TT), i.e. diabatic states, has been carried out by the decomposition of the adiabatic state wave functions and density matrices.(62; 63) CT diabatic states have been also computed with the constrained-DFT (C-DFT).(64)

8.4.1.2 SOCT-IC

Vertical excitation energies at different molecular geometries (ground, excited and CT states) were calculated with the LR-TDDFT with the Tamm-Dancoff approximation (TDA) and with the CAM-B3LYP functional due to its ability to properly describe electronic transitions with weak electron/hole overlaps, such as in charge transfer (CT) excitations, and the basis set 6-311G(d,p). RAS-SF calculations were performed with the high-spin quintet as the reference configuration, with 4 electrons in 4 orbitals in the RAS II space, all occupied (virtual) orbitals in the RAS I (RAS III) space, and the 6-31G(d,p) basis set.

Geometry relaxation on the excited states potential energy surfaces were performed with B3LYP and CAM-B3LYP functionals for different excited triplet and singlet states. Solvation effects of cyclohexane and DMSO solvents were included through the SMD solvation model. Inter-state spin orbit couplings between low-energy singlets and triplets were computed at the same electronic structure level (CAM-B3LYP/6-311G(d,p)) taking into account one-electron contributions to the Breit-Pauli spin-orbit Hamiltonian.

8.4.1.3 spiro-DBP2

Molecular geometries of ground state open- and closed-shell configurations and the lowest triplet state have been optimized within the density functional theory (DFT) in combination with the ω-B97XD and B3LYP and in addition to CAM-B3LYP, and the 6-31G(d,p) basis set. Formation of the σ-dimer has been simulated by a pair of Q_1 molecules at the ωB97X-D/6-31G(d) computational level. Restricted active space spin-flip (RAS-SF) calculations were done by including all doubly occupied and virtual orbitals in RAS I and RAS III subspaces, respectively. In the active space are included 4 electrons in the 4 frontier π-orbitals, and 4 electrons in the 5 orbitals in the σ-dimer; while RAS II in the spiro-compound included 8 electrons in 8 orbitales. The high spin triplet (monomers) and quintet (spiro and σ-dimer) Hartree-Fock determinants were used as the reference configurations. The 6-31G(d,p) basis set was used in all RAS-SF calculations.

Vertical excitation energies to the lowest excited states where obtained with the time dependent (linear response) version of DFT (TDDFT), and with the ω-B97X-D functional and 6-31G(d,p) basis set.

Bibliography

[1] I. U. of Pure and A. Chemistry, "Iupac compendium of chemical terminology – the gold book," 2009.

[2] H. Dürr and R. Gleiter, "Spiroconjugation," *Angewandte Chemie International Edition in English*, vol. 17, no. 8, pp. 559–569, 1978.

[3] H. E. Simmons and T. Fukunaga, "Spiroconjugation," *Journal of the American Chemical Society*, vol. 89, no. 20, pp. 5208–5215, 1967.

[4] Y.-H. Tseng, P.-I. Shih, C.-H. Chien, A. K. Dixit, C.-F. Shu, Y.-H. Liu, and G.-H. Lee, "Stable organic blue-light-emitting devices prepared from poly[spiro(fluorene-9,9'-xanthene)]," *Macromolecules*, vol. 38, no. 24, pp. 10055–10060, 2005.

[5] Y.-H. Tseng, P.-I. Shih, C.-H. Chien, A. K. Dixit, C.-F. Shu, Y.-H. Liu, and G.-H. Lee, "Stable organic blue-light-emitting devices prepared from poly[spiro(fluorene-9,9'-xanthene)]," *Macromolecules*, vol. 38, no. 24, pp. 10055–10060, 2005.

[6] E. Kumarasamy, S. N. Sanders, M. J. Y. Tayebjee, A. Asadpoordarvish, T. J. H. Hele, E. G. Fuemmeler, A. B. Pun, L. M. Yablon, J. Z. Low, D. W. Paley, J. C. Dean, B. Choi, G. D. Scholes, M. L. Steigerwald, N. Ananth, D. R. McCamey, M. Y. Sfeir, and L. M. Campos, "Tuning singlet fission in π-bridge-π chromophores," *Journal of the American Chemical Society*, vol. 139, no. 36, pp. 12488–12494, 2017.

[7] P. M. Burrezo, X. Zhu, S.-F. Zhu, Q. Yan, J. T. López Navarrete, H. Tsuji, E. Nakamura, and J. Casado, "Planarization, fusion, and strain of carbon-bridged phenylenevinylene oligomers enhance π-electron and charge conjugation: A dissectional vibrational raman study," *Journal of the American Chemical Society*, vol. 137, no. 11, pp. 3834–3843, 2015.

[8] B. E. Kohler, C. Spangler, and C. Westerfield, "The 2 1ag state in the linear polyene 2,4,6,8,10,12,14,16[U+2010]octadecaoctaene," *The Journal of Chemical Physics*, vol. 89, no. 9, pp. 5422–5428, 1988.

[9] R. L. Christensen, M. G. I. Galinato, E. F. Chu, J. N. Howard, R. D. Broene, and H. A. Frank, "Energies of low-lying excited states of linear polyenes," *The journal of physical chemistry. A*, vol. 112, no. 49, pp. 12629–12636, 2008.

[10] B. Küpper, M. Kleinschmidt, K. Schaper, and C. M. Marian, "On the photophysics of 1,6-diphenyl-1,3,5-hexatriene isomers and rotamers," *ChemPhysChem*, vol. 12, no. 10, pp. 1872–1879, 2011.

[11] Y.-Q. Qiu, W.-Y. Wang, N.-N. Ma, C.-H. Wang, M.-Y. Zhang, H.-Y. Zou, and P.-J. Liu, "Computational investigation on redox-switchable nonlinear optical properties of a series of polycyclic p-quinodimethane molecules," *Journal of Molecular Modeling*, vol. 19, no. 12, pp. 5479–5487, 2013.

[12] X. Zhu, H. Tsuji, K. Nakabayashi, S.-i. Ohkoshi, and E. Nakamura, "Air- and heat-stable planar tri-p-quinodimethane with distinct biradical characteristics," *Journal of the American Chemical Society*, vol. 133, no. 41, pp. 16342–16345, 2011.

[13] M. H. Farag and A. I. Krylov, "Singlet fission in perylenediimide dimers," *The Journal of Physical Chemistry C*, vol. 122, no. 45, pp. 25753–25763, 2018.

[14] M. T. Trinh, A. Pinkard, A. B. Pun, S. N. Sanders, E. Kumarasamy, M. Y. Sfeir, L. M. Campos, X. Roy, and X.-Y. Zhu, "Distinct properties of the triplet pair state from singlet fission," *Science Advances*, vol. 3, no. 7, 2017.

[15] S. Khan and S. Mazumdar, "Diagrammatic exciton basis theory of the photophysics of pentacene dimers," *The Journal of Physical Chemistry Letters*, vol. 8, no. 18, pp. 4468–4478, 2017.

[16] R. D. Pensack, E. E. Ostroumov, A. J. Tilley, S. Mazza, C. Grieco, K. J. Thorley, J. B. Asbury, D. S. Seferos, J. E. Anthony, and G. D. Scholes, "Observation of two triplet-pair intermediates in singlet exciton fission," *The Journal of Physical Chemistry Letters*, vol. 7, no. 13, pp. 2370–2375, 2016.

[17] M. Kasha, "Characterization of electronic transitions in complex molecules," *Discuss. Faraday Soc.*, vol. 9, pp. 14–19, 1950.

[18] A. V. Luzanov and V. F. Pedash, "Interpretation of excited states using charge-transfer numbers," *Theor. Exp. Chem.*, vol. 15, no. 4, pp. 338–341, 1980.

[19] C. E. Miller, M. R. Wasielewski, and G. C. Schatz, "Modeling singlet fission in rylene and diketopyrrolopyrrole derivatives: The role of the charge transfer state in superexchange and excimer formation," *J. Phys. Chem. C*, vol. 121, no. 19, pp. 10345–10350, 2017.

[20] M. B. Smith and J. Michl, "Recent advances in singlet fission," *Annu. Rev. Phys. Chem.*, vol. 64, no. 1, pp. 361–386, 2013.

[21] D. Beljonne, H. Yamagata, J. L. Brédas, F. C. Spano, and Y. Olivier, "Charge-transfer excitations steer the davydov splitting and mediate singlet exciton fission in pentacene," *Phys. Rev. Lett.*, vol. 110, p. 226402, 2013.

[22] W.-L. Chan, T. C. Berkelbach, M. R. Provorse, N. R. Monahan, J. R. Tritsch, M. S. Hybertsen, D. R. Reichman, J. Gao, and X. Y. Zhu, "The quantum coherent mechanism for singlet fission: Experiment and theory," *Acc. Chem. Res.*, vol. 46, no. 6, pp. 1321–1329, 2013.

[23] T. C. Berkelbach, M. S. Hybertsen, and D. R. Reichman, "Microscopic theory of singlet exciton fission. iii. crystalline pentacene," *J. Chem. Phys.*, vol. 141, no. 7, p. 074705, 2014.

[24] T. Zeng, R. Hoffmann, and N. Ananth, "The low-lying electronic states of pentacene and their roles in singlet fission," *J. Am. Chem. Soc.*, vol. 136, no. 15, pp. 5755–5764, 2014.

[25] E. G. Fuemmeler, S. N. Sanders, A. B. Pun, E. Kumarasamy, T. Zeng, K. Miyata, M. L. Steigerwald, X. Y. Zhu, M. Y. Sfeir, L. M. Campos, and N. Ananth, "A direct mechanism of ultrafast intramolecular singlet fission in pentacene dimers," *ACS Cent. Sci.*, vol. 2, no. 5, pp. 316–324, 2016.

[26] N. V. Korovina, S. Das, Z. Nett, X. Feng, J. Joy, R. Haiges, A. I. Krylov, S. E. Bradforth, and M. E. Thompson, "Singlet fission in a covalently linked cofacial alkynyltetracene dimer," *J. Am. Chem. Soc.*, vol. 138, no. 2, pp. 617–627, 2016.

[27] X. Feng, D. Casanova, and A. I. Krylov, "Intra- and Intermolecular Singlet Fission in Covalently Linked Dimers," *J. Phys. Chem. C*, vol. 120, no. 34, pp. 19070–19077, 2016.

[28] H. Marciniak, M. Fiebig, M. Huth, S. Schiefer, B. Nickel, F. Selmaier, and S. Lochbrunner, "Ultrafast exciton relaxation in microcrystalline pentacene films," *Phys. Rev. Lett.*, vol. 99, p. 176402, 2007.

[29] H. Marciniak, I. Pugliesi, B. Nickel, and S. Lochbrunner, "Ultrafast singlet and triplet dynamics in microcrystalline pentacene films," *Phys. Rev. B*, vol. 79, p. 235318, 2009.

[30] V. M. Nichols, M. T. Rodriguez, G. B. Piland, F. Tham, V. N. Nesterov, W. J. Youngblood, and C. J. Bardeen, "Assessing the potential of peropyrene as a singlet fission material: Photophysical properties in solution and the solid state," *J. Phys. Chem. C*, vol. 117, no. 33, pp. 16802–16810, 2013.

[31] A. B. Kolomeisky, X. Feng, and A. I. Krylov, "A simple kinetic model for singlet fission: A role of electronic and entropic contributions to macroscopic rates," *The Journal of Physical Chemistry C*, vol. 118, no. 10, pp. 5188–5195, 2014.

[32] S. Matsika, X. Feng, A. V. Luzanov, and A. I. Krylov, "What we can learn from the norms of one-particle density matrices, and what we can't: Some results for

interstate properties in model singlet fission systems," *The Journal of Physical Chemistry A*, vol. 118, no. 51, pp. 11943–11955, 2014.

[33] N. A. van Dantzig, D. H. Levy, C. Vigo, and P. Piotrowiak, "Vibronic coupling and energy transfer in bichromophoric molecules: The effect of symmetry," *The Journal of Chemical Physics*, vol. 103, no. 12, pp. 4894–4906, 1995.

[34] S. Guo, S. Liu, K. Y. Zhang, W. Huang, and Q. Zhao, "Utilization of triplet excited states in organic semiconductors," *Journal of Semiconductors*, vol. 40, no. 7, p. 070402, 2019.

[35] M. Zubiria-Ulacia, J. M. Matxain, and D. Casanova, "The role of ct excitations in pdi aggregates," *Phys. Chem. Chem. Phys.*, vol. 22, pp. 15908–15918, 2020.

[36] S. K. Lower and M. A. El-Sayed, "The triplet state and molecular electronic processes in organic molecules," *Chemical Reviews*, vol. 66, no. 2, pp. 199–241, 1966.

[37] W. Wang, N. Xie, L. He, and Y. Yin, "Photocatalytic colour switching of redox dyes for ink-free light-printable rewritable paper," *Nature Communications*, vol. 5, no. 1, p. 5459, 2014.

[38] P. Tao, Y. Miao, H. Wang, B. Xu, and Q. Zhao, "High-performance organic electroluminescence: Design from organic light-emitting materials to devices," *The Chemical Record*, vol. 19, no. 8, pp. 1531–1561, 2019.

[39] D. Sasikumar, A. T. John, J. Sunny, and M. Hariharan, "Access to the triplet excited states of organic chromophores," *Chem. Soc. Rev.*, vol. 49, pp. 6122–6140, 2020.

[40] P. Xue, P. Wang, P. Chen, B. Yao, P. Gong, J. Sun, Z. Zhang, and R. Lu, "Bright persistent luminescence from pure organic molecules through a moderate intermolecular heavy atom effect," *Chem. Sci.*, vol. 8, pp. 6060–6065, 2017.

[41] J. C. Koziar and D. O. Cowan, "Photochemical heavy-atom effects," *Accounts of Chemical Research*, vol. 11, no. 9, pp. 334–341, 1978.

[42] D. R. Lee, K. H. Lee, W. Shao, C. L. Kim, J. Kim, and J. Y. Lee, "Heavy atom effect of selenium for metal-free phosphorescent light-emitting diodes," *Chemistry of Materials*, vol. 32, no. 6, pp. 2583–2592, 2020.

[43] K. N. Solovev and E. A. Borisevich, "Intramolecular heavy-atom effect in the photophysics of organic molecules," *Physics-Uspekhi*, vol. 48, no. 3, pp. 231–253, 2005.

[44] S. M. Winter, R. T. Oakley, A. E. Kovalev, and S. Hill, "Spin-orbit effects in heavy-atom organic radical ferromagnets," *Phys. Rev. B*, vol. 85, p. 094430, 2012.

[45] T. Okada, I. Karaki, E. Matsuzawa, N. Mataga, Y. Sakata, and S. Misumi, "Ultrafast intersystem crossing in some intramolecular heteroexcimers," *The Journal of Physical Chemistry*, vol. 85, no. 26, pp. 3957–3960, 1981.

[46] Z. E. X. Dance, S. M. Mickley, T. M. Wilson, A. B. Ricks, A. M. Scott, M. A. Ratner, and M. R. Wasielewski, "Intersystem crossing mediated by photoinduced intramolecular charge transfer: julolidine-anthracene molecules with perpendicular π systems," *The Journal of Physical Chemistry A*, vol. 112, no. 18, pp. 4194–4201, 2008.

[47] H. Ohkuma, T. Nakagawa, K. Shizu, T. Yasuda, and C. Adachi, "Thermally activated delayed fluorescence from a spiro-diazafluorene derivative," *Chemistry Letters*, vol. 43, no. 7, pp. 1017–1019, 2014.

[48] M. Lv, Y. Yu, M. E. Sandoval-Salinas, J. Xu, Z. Lei, D. Casanova, Y. Yang, and J. Chen, "Engineering the charge-transfer state to facilitate spin-orbit charge transfer intersystem crossing in spirobis[anthracene]diones," *Angewandte Chemie International Edition*, vol. 59, no. 49, pp. 22179–22184, 2020.

[49] H. Hamada, Y. Itabashi, R. Shang, and E. Nakamura, "Axially chiral spiroconjugated carbon-bridged p-phenylenevinylene congeners: Synthetic design and materials properties," *Journal of the American Chemical Society*, vol. 142, no. 4, pp. 2059–2067, 2020.

[50] T. Yanai, D. P. Tew, and N. C. Handy, "A new hybrid exchange–correlation functional using the coulomb-attenuating method (cam-b3lyp)," *Chemical Physics Letters*, vol. 393, no. 1, pp. 51–57, 2004.

[51] K. Yamaguchi, *Self-Consistent Field: Theory and Applications*, pp. 727–828. Elsevier, 1990.

[52] M. Head-Gordon, "Characterizing unpaired electrons from the one-particle density matrix," *Chem. Phys. Lett.*, vol. 372, no. 3-4, pp. 508–511, 2003.

[53] Y. Shao, Z. Gan, E. Epifanovsky, A. T. B. Gilbert, M. Wormit, J. Kussmann, A. W. Lange, A. Behn, J. Deng, X. Feng, D. Ghosh, M. Goldey, P. R. Horn, L. D. Jacobson, I. Kaliman, R. Z. Khaliullin, T. Kus, A. Landau, J. Liu, E. I. Proynov, Y. M. Rhee, R. M. Richard, M. A. Rohrdanz, R. P. Steele, E. J. Sundstrom, H. L. Woodcock, P. M. Zimmerman, D. Zuev, B. Albrecht, E. Alguire, B. Austin, G. J. O. Beran, Y. A. Bernard, E. Berquist,

K. Brandhorst, K. B. Bravaya, S. T. Brown, D. Casanova, C.-M. Chang, Y. Chen, S. H. Chien, K. D. Closser, D. L. Crittenden, M. Diedenhofen, R. A. DiStasio, H. Do, A. D. Dutoi, R. G. Edgar, S. Fatehi, L. Fusti-Molnar, A. Ghysels, A. Golubeva-Zadorozhnaya, J. Gomes, M. W. D. Hanson-Heine, P. H. P. Harbach, A. W. Hauser, E. G. Hohenstein, Z. C. Holden, T.-C. Jagau, H. Ji, B. Kaduk, K. Khistyaev, J. Kim, J. Kim, R. A. King, P. Klunzinger, D. Kosenkov, T. Kowalczyk, C. M. Krauter, K. U. Lao, A. D. Laurent, K. V. Lawler, S. V. Levchenko, C. Y. Lin, F. Liu, E. Livshits, R. C. Lochan, A. Luenser, P. Manohar, S. F. Manzer, S.-P. Mao, N. Mardirossian, A. V. Marenich, S. A. Maurer, N. J. Mayhall, E. Neuscamman, C. M. Oana, R. Olivares-Amaya, D. P. O'Neill, J. A. Parkhill, T. M. Perrine, R. Peverati, A. Prociuk, D. R. Rehn, E. Rosta, N. J. Russ, S. M. Sharada, S. Sharma, D. W. Small, A. Sodt, T. Stein, D. Stuck, Y.-C. Su, A. J. W. Thom, T. Tsuchimochi, V. Vanovschi, L. Vogt, O. Vydrov, T. Wang, M. A. Watson, J. Wenzel, A. White, C. F. Williams, J. Yang, S. Yeganeh, S. R. Yost, Z.-Q. You, I. Y. Zhang, X. Zhang, Y. Zhao, B. R. Brooks, G. K. L. Chan, D. M. Chipman, C. J. Cramer, W. A. Goddard, M. S. Gordon, W. J. Hehre, A. Klamt, H. F. Schaefer, M. W. Schmidt, C. D. Sherrill, D. G. Truhlar, A. Warshel, X. Xu, A. Aspuru-Guzik, R. Baer, A. T. Bell, N. A. Besley, J.-D. Chai, A. Dreuw, B. D. Dunietz, T. R. Furlani, S. R. Gwaltney, C.-P. Hsu, Y. Jung, J. Kong, D. S. Lambrecht, W. Liang, C. Ochsenfeld, V. A. Rassolov, L. V. Slipchenko, J. E. Subotnik, T. Van Voorhis, J. M. Herbert, A. I. Krylov, P. M. W. Gill, and M. Head-Gordon, "Advances in molecular quantum chemistry contained in the q-chem 4 program package," *Mol. Phys.*, vol. 113, no. 2, pp. 184–215, 2015.

[54] C. A. Bauer, A. Hansen, and S. Grimme, "The fractional occupation number weighted density as a versatile analysis tool for molecules with a complicated electronic structure," *Chemistry–A European Journal*, vol. 23, no. 25, pp. 6150–6164, 2017.

[55] S. Grimme and A. Hansen, "A practicable real-space measure and visualization of static electron-correlation effects," *Angewandte Chemie International Edition*, vol. 54, no. 42, pp. 12308–12313, 2015.

[56] M. D. Hanwell, D. E. Curtis, D. C. Lonie, T. Vandermeersch, E. Zurek, and G. R. Hutchison, "Avogadro: an advanced semantic chemical editor, visualization, and analysis platform," *J. Cheminf.*, vol. 4, no. 1, p. 17, 2012.

[57] D. Casanova, "Electronic structure study of singlet fission in tetracene derivatives," *Journal of Chemical Theory and Computation*, vol. 10, no. 1, pp. 324–334, 2014.

[58] D. Casanova, "Efficient implementation of restricted active space configuration interaction with the hole and particle approximation," *J. Comput. Chem.*, vol. 34, no. 9, pp. 720–730, 2013.

[59] D. Casanova, "Short-range density functional correlation within the restricted active space ci method," *The Journal of Chemical Physics*, vol. 148, no. 12, p. 124118, 2018.

[60] S. H. Vosko, L. Wilk, and M. Nusair, "Accurate spin-dependent electron liquid correlation energies for local spin density calculations: a critical analysis," *Can. J. Phys.*, vol. 58, no. 8, pp. 1200–1211, 1980.

[61] J. Toulouse, A. Savin, and H.-J. Flad, "Short-range exchange-correlation energy of a uniform electron gas with modified electron–electron interaction," *Int. J. Quantum Chem.*, vol. 100, no. 6, pp. 1047–1056, 2004.

[62] A. V. Luzanov, D. Casanova, X. Feng, and A. I. Krylov, "Quantifying charge resonance and multiexciton character in coupled chromophores by charge and spin cumulant analysis," *J. Chem. Phys.*, vol. 142, no. 22, p. 224104, 2015.

[63] D. Casanova and A. I. Krylov, "Quantifying local exciton, charge resonance, and multiexciton character in correlated wave functions of multichromophoric systems," *J. Chem. Phys.*, vol. 144, no. 1, p. 014102, 2016.

[64] Q. Wu and T. V. Voorhis, "Constrained density functional theory and its application in long-range electron transfer," *J. Chem. Theory Comput.*, vol. 2, no. 3, pp. 765–774, 2006.

Chapter 9

General conclusions

This chapter does not pretend to summarize again in detail the individual conclusions of each chapter but rather give a general picture of the achievements of the work presented. The results exposed throughout these pages present the full characterization of the radical character of organic systems by means of adequate electronic structure methods. More specifically, the origin of the diradical (polyradical) character was rationalized for each system and put in relation with the most remarkable molecular properties associated with the presence of unpaired electrons.

To highlight the structure-diradical character relationships established in this work, the radical characters of **[6]Ac**, **[6]CC**, and **2** can be used as an example (Chapter 4). All of them are composed by six fused benzene rings having zigzag-edges. When rings are fused following a one dimensional pattern, the experimentally well-known **[6]Ac** holds a moderate diradicaloid character. If this linear arrangement is closed in a belt shape, one obtains the **[6]CC** compound that exhibits a stronger diradicaloid character, resulting in a severe chemical instability, which has prevented its synthesis. Finally, the triangular arrangement of six fused rings in **2** presents a triplet-spin ground state and can be considered a perfect diradical.

Besides these purely topological considerations, a relationship between the radical character of a system and the spatial arrangement of the radical sites within the molecular structure can be drawn. This has been demonstrated in Chapter 6, where the radical-radical interaction (ferromagnetic or antiferromagnetic) is modulated by the characteristics of the bridge linking the individual units that carry an unpaired electron, namely its flexibility, length and nature of π-conjugation. Alternatively, the controlled tuning of radical character in organic molecules can be achieved through chemical modifications of the molecular structure, as addressed in Chapter 4. More specifically, heteroatom substitution, which has been shown to affect the spin multiplicity of the ground state, provides a viable strategy to design new stable (di)radicaloid systems.

The establishment of the aforementioned structure-properties relationships called for methods incorporating strong correlation effects to achieve the proper description of the radical nature of the systems. Concretely, the characterization of (poly)radical systems of small to large size reported in this thesis mainly rely on the use of the powerful RAS-SF family of methods. Indeed, these approaches provide a multiconfigurational wave function able to deal with several strongly correlated electrons. Moreover, this accurate treatment is achieved at reasonable computational cost as evidenced from the study of the large macrostructures reported in Chapter 6. The theoretical-experimental synergy in which some parts of this thesis has been carried out highlights the crucial role of such quantum chemistry methods in the understanding of radical systems. In this context, I have been able to provide an interpretation of the spectroscopic features of newly synthesized stable diradical dianions oligothiophene derivatives and illustrate at the molecular level their peculiar ability to stabilize polaron-pairs (Chapter 5). In the same chapter, I have rationalized the temperature related interconversion between two stable conformers with different diradical character.

With a more applied aspect in mind, and from the understanding gained from the previous chapters, it is evident that key photophysical processes at stake in organic based devices can beneficiate from the presence of radicals. In this regard, I have focused my interest on the unique spin-allowed singlet fission (SF) process that is currently considered as one of the most promising approaches in the development of the next generation photovoltaic technologies. Among the requirements for this process to occur efficiently, the control of the singlet-triplet energy gap, which can be modulated indirectly via the alteration of the radical character, is crucial. From the theoretical point of view, I have extended the well-established five state model to describe SF by including doubly excited states. The obtained results from the application of the new model show that indeed these states can potentially play an important role in the SF mechanism as the initial or mediator states (Chapter 7). In particular, I have identified the parameters, *i.e.*, relative energy of states and adequate electronic couplings, controlling the involvement of the doulby excited states in the SF process, and I have explored the optimal conditions for the fast and efficient generation of the triplet-pair state.

Ultimately, the last chapter is devoted to the in-depth exploration of spiro-conjugated molecules on the basis of the structure-diradical relationships and photophysical processes derived from the previous chapters. These systems hold a very unique chromophoric arrangement (*i.e.*, two weakly interacting perpendicular chromophores close in space) via the spiro atom. Spiro-compounds exhibit low energy charge-transfer (CT) states, which makes them promising candidates for CT-mediated photophysical processes such as SF or intersystem crossing.

Chapter 10

Full list of publications

Publications included in this thesis:

- S. Rivero[+], R. Shang[+], **M. E. Sandoval-Salinas**[+], H. Hamada, K. Nakabayashi, S. Ohkoshi. D. Casanova, E. Nakamura, J. Casado, "A spiro-driven tetraradical", submitted.
- **M. E. Sandoval-Salinas**, D. Casanova, "The doubly excited state in singlet fission", *ChemPhotoChem*, accepted, DOI: 10.1002/cptc.202000211.
- M LV[+], Y. Yu[+], **M. E. Sandoval-Salinas**[+], J. Xu, Z. Lie, D. Casanova, Y. Yang, J. Chen, "Engineering the charge-transfer state to facilitate spin-orbit charge transfer intersystem crossing in spirobis[anthracene]diones", *Angew. Chem. Int. Ed.*, 2020, 59, 22179-22184.
- **M. E. Sandoval-Salinas**, A. Carreras, J. Casado, D. Casanova, "Singlet fission in spiroconjugated dimers", *J. Chem. Phys.*, 2019, 150, 204306.
- **M. E. Sandoval-Salinas**, A. Carreras, D. Casanova, "Triangular graphene nanofragments: open-shell character and doping", *Phys. Chem. Chem. Phys.*, 2019, 21, 9069-9076.
- Y. Ni, **M. E. Sandoval-Salinas**, T. Tanaka, H. Phan, T. S. Herng, T. Y. Gopalakrishna, J. Ding, A. Osuka, D. Casanova, J. Wu, "[n]Cyclo-para-biphenylmethine polyradicaloids: [n]annulene analogues and unusual valence tautomerization", *Chem*, 2019, 5, 108-121.
- A. Perez-Guardiola[+], **M. E. Sandoval-Salinas**[+], D. Casanova, E. San Fabián, A. J. José Pérez-Jiménez, J. C. Sancho-Garcia, "The role of topology in organic molecules: origin and comparison of the radical character in linear and cyclic oligoacenes and related oligomers", *Phys. Chem. Chem. Phys.*, 2018, 20, 7112-7124.

- D. Yuan, S. Medina, P. Mayorga, L. Ren, **M. E. Sandoval-Salinas**, S. J. Grabowski, D. Casanova, X. Zhu, J. Casado, "Thieno[3,4-c]pyrrole-4,6-dione oligothiophenes have two crossed paths for electron delocalization", *Chem. Eur. J.*, 2018, 24, 13523-13534.

- S. Medina, P. Mayorga, **M. E. Sandoval-Salinas**, T. Li, F. J. Ramírez, D. Casanova, X. Wang and J. Casado, "Isomerism, diradical signature, and raman spectroscopy: underlying connections in diamino oligophenyl dications", *ChemPhysChem* 2018, 19, 1465-1470.

- C. Liu, **M. E. Sandoval-Salinas**, Y. Hong, T. Y. Gopalakrishna, H. Pan, N. Aratani, T. S. Herng, J. Ding, H. Yamada, D. Kim, D. Casanova, J. Wu, "Macrocyclic polyradicaloids with unusual super-ring structure and global aromaticity",*Chem*, 2018, 4, 1-10.

- J. Wang, G. Kim, **M. E. Sandoval-Salinas**, H. Phan, T. Y. Gopalakrishna, X. Lu, D. Casanova, D. Kim, J. Wu, "Stable 2D anti-ferromagnetically coupled fluorenyl radical dendrons", *Chem. Sci.*, 2018, 9, 3395-3400.

Note: $^{+}$ equal contribution.

Publications not included in this thesis:

- I. Buyanova, C. Phansa, **M. E. Sandoval-Salinas**, D. Casanova, W. Myers, N. Greenham, A. Rao, W. Chen, Y.Huang, "Competition between formation of dark intermediate triplet pair states and excimer-like recombination hotspots controls singlet fission yield", *Cell Reports Physical Science*, accepted.

- A. Perez-Guardiola, R. Ortiz-Cano, **M. E. Sandoval-Salinas**, J. Fernandez-Rossier, D. Casanova, A. J. José Pérez-Jiménez, J. C. Sancho-Garcia, "From Cyclic Nanorings to Single-Walled Carbon Nanotubes: Disclosing the Evolution of their Electronic Structure with the Help of Theoretical Methods", *Phys. Chem. Chem. Phys.*, 2019, 21, 2547-2557.

- X. Lu, S. Lee, Y. Hong, H. Phan, T. Y. Gopalakrishna, T. Seng Herng, T. Tanaka, **M. E. Sandoval-Salinas**, W. Zeng, J. Ding, D. Casanova, A. Osuka, D. Kim, J. Wu, "Fluorenyl Based Macrocyclic Polyradicaloids", *J. Am. Chem. Soc.*, 2017, 139,13173-13183.